



UNIVERSITEIT VAN PRETORIA
UNIVERSITY OF PRETORIA
YUNIBESITHI YA PRETORIA

Novel air monitoring technologies for volatile and semi-volatile organic compounds for sustainable development

by

Genna-Leigh Geldenhuys

Submitted in partial fulfilment of the requirements for the degree

Doctor of Philosophy (Chemistry)
In the Faculty of Natural & Agricultural Sciences
University of Pretoria
Pretoria

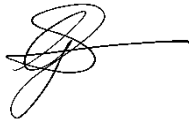
Supervisor: Professor Patricia B.C. Forbes

March 2023

Declaration

I, Genna-Leigh Geldenhuys declare that the thesis, which I hereby submit for the degree Doctor of Philosophy at the University of Pretoria, is my own work and has not previously been submitted by me for a degree at this or any other tertiary institution.

Signature:

A handwritten signature in black ink, appearing to be 'Genna-Leigh Geldenhuys', written in a cursive style with a long horizontal stroke extending to the right.

Date:

March 2023

Acknowledgements

This thesis benefited from the encouragement and guidance of so many individuals. Special thanks are given to:

- Professor Patricia Forbes, my supervisor and mentor, for your constant support and guidance throughout my post-graduate career and for all the opportunities you have given me to grow as a researcher. You have become my special, life long friend.
- Impala Platinum Ltd for your support, involvement and financial resources throughout my career.
- National Research Foundation and the University of Pretoria for financial assistance.
- My colleagues in Munich, Dr Jürgen Orashe, Dr Gert Jakobi, Dr George Dragan, Dr Nadine Gawlitta and Dr Vesta Kohlmeier.
- Prof Ralf Zimmermann, for the opportunity to collaborate with your research groups and for all the support throughout our project.
- Dr Yvette Naudé for all things GC. I appreciate all your time and patience and your constant willingness to share your knowledge.
- Restek (USA) for providing GC resources and Leco Corp. for your training and use of software.
- Mr David Masemula for all his assistance in the lab and his gentle and kind demeanour.
- My UP family: thank you to each individual in our research group who made my time on campus so enjoyable and for endless chats and encouragement.
- My parents, Sandy and Chris Geldenhuys and my sister Candice for their unconditional love and support.
- Ricardo Ribeiro, my rock, for enduring the toughest times with me and giving me the love and support (and bottomless tea) that I needed to succeed.

Summary

Environmental protection and the search for cleaner, more sustainable fuels are two of the most important concerns modern society is facing. This research aims to determine whether a transition from fossil fuels to the use of biofuels will significantly lead to reductions in air emissions of potentially harmful substances, and thus to healthier, sustainable development. In this regard, assessing combustion emissions from key sectors and developing and testing novel monitoring technologies, such as a graphene-based sampler that offers sustainable advantages over currently available options, can facilitate extensive monitoring and management of volatile and semi-volatile atmospheric pollutants in a cost effective and efficient manner.

Polycyclic aromatic hydrocarbons (PAHs) have been used as markers of environmental combustion pollutants as they are ubiquitous airborne pollutants arising from various anthropogenic sources such as biomass burning and diesel combustion emissions and are specifically of concern due to their significant adverse human health and environmental impacts. Airborne PAHs coexist in two phases and the need for both gas and particle sampling is vital for accurate calculation of emission inventories and risk assessments to guide air quality management plans as well as reduction and abatement strategies.

Traditional PAH sampling methods require large sampling volumes and extended sampling times which introduce unwanted sampling artefacts resulting from analyte breakthrough, adsorption effects (of gas phase analytes onto collected particles) and filter blow off which results in unreliable quantification. Additionally, large amounts of toxic solvents are required for sample clean up and extraction which generates waste and may cause adverse environmental impacts. However, the portable multi-channel polydimethylsiloxane (PDMS) denuder devices used in this study overcome these limitations as they are of open geometry with low back pressure and they require low flow rates and short sampling intervals. In addition, they have the advantage of being able to be thermally desorbed preventing the need for time consuming and environmentally unfriendly solvent extraction steps. A drawback of these samplers is that they are limited to non-polar semi-volatile organic compounds.

The initial phase of the study aimed at gaining more insight into diesel combustion PAH air emissions and the partitioning thereof using the PDMS portable denuder devices for sampling. Here, an engine dynamometer experiment was conducted with a light duty diesel engine to determine emission factors under two different engine operating modes, representative of idling and severe real-world, developing country conditions. Results indicated that PAH

emission factors differed significantly for the different modes of engine operation with the highest emission factor being for idle mode with a total PAH emission factor of 1181.14 $\mu\text{g kg}^{-1}$. A total of ten PAHs were quantified and over 80 % of PAHs were found in the gas phase which emphasized the need for this study seeing that numerous other studies tend to focus only on particulate matter in the determination of PAH emission factors. This work emphasised the importance of characterizing the EFs of PAHs and the phase partitioning of these compounds for accurate air quality control as well as the protection of the health of the general public. This study allowed for a better understanding of the denuder operating mechanisms and can provide useful guidelines as well as potential limitations which should be considered in future sampling applications with these samplers.

The next phase of the project encompassed key economic industries in South Africa, the one being the mining industry, as a substantial fossil fuel user, and the other being the sugar cane industry as a contributor to atmospheric air pollution but also a potential feedstock producer for biofuel production. The aim of providing a link between the bioeconomy and resource management was achieved via the monitoring of PAH air pollutants at various sites in the sugar cane and platinum mining industry. The former industry practices the pre-harvest burning of sugar cane which is a significant anthropogenic source of air pollution resulting in atmospheric emissions, including PAHs, that have may have adverse impacts on air quality and human health on a local, regional and even a global scale. The mining industry is a major source of combustion emissions from trackless mobile diesel machinery that are used in critical operations underground. These combustion emissions contribute to gas and particulate PAH pollutant levels which is a cause for concern from an environmental standpoint but also from a human health perspective, especially due to the confined working environments underground which results in an increased risk of occupational exposure to harmful and carcinogenic pollutants.

Air pollutant monitoring was carried out during the preharvest burning of sugarcane crop residues in South Africa, at five different locations in Kwa-Zulu Natal, to bring to light the resultant PAH emissions and to better understand overall environmental impact. In this study, the total gas and particle phase PAH concentrations ranged from 0.05-9.85 $\mu\text{g m}^{-3}$ per individual burn event where nine PAHs were quantified. Over 85% of all PAHs were found to exist in the gas phase and the PAH fingerprints were substantially different between each burn event indicating the vital role that prevailing weather conditions as well as the nature of the burn and the crop have on emissions and the gas-particle partitioning thereof. This study may

aid in the refinement of current best practice in sugar cane harvesting towards enhancing greater sustainability. One consideration in this respect is the exploration of a combustion alternative and the conversion of biomass waste into biofuels, whilst simultaneously minimizing the emission of harmful air pollutants.

The feasibility of a transition to alternative fuels was then investigated in an underground platinum mine. During this sampling campaign, air pollutants emitted from a load haul dump (LHD) engine exhaust were compared when operated on pure diesel, rapeseed methyl ester (RME) biodiesel or gas-to-liquid (GTL) fuels. These selected test fuels have the potential of being generated locally with sustainable feedstocks for first or second generation biofuel such as by using sugar cane, sunflower oil ester or waste biomass for production of biomass-to-liquid (BTL) fuel. The influence of emissions on air quality in the mines was investigated as one feasibility indicator in this study whereas the others included: the functional performance of the engine when operated on alternate fuels as well as the cost, socio-economic and environmental implications of implementation. Monitoring results showed that total toxic PAH concentrations from combustion emissions from a high idling load haul dump vehicle decreased dramatically when substituting the diesel fuel with gas-to-liquid or biodiesel fuels (total PAH gas phase concentrations of 42; 18 and 11 $\mu\text{g m}^{-3}$ for diesel, gas-to-liquid and rapeseed methyl ester respectively) and no substantial hinderance on engine performance or power was reported by mining staff. This study therefore further supports GTL and RME as cleaner fuel alternatives to petroleum derived diesel. Cost and sensitivity analysis revealed that the production and use of biomass-to liquid and biodiesel is a potentially feasible solution towards sustainable development in South African underground platinum mines.

During the aforementioned sampling campaigns, all of which employed PDMS denuders, it became evident that there is a need for a sampler that can sorb volatile organic compounds and more polar SVOCs to broaden the scope of analytes which are sampled. It is for this reason that research was conducted which focused on novel monitoring technologies whereby a graphene-based sampler was developed which is in the process of being patented (Schoonraad and Forbes 2019a & 2019b). The graphene wool (GW) material was synthesised by non-catalytic chemical vapour deposition using a high-purity quartz wool substrate. The *in-situ* synthesis method avoids post-growth transfer and isolation steps and allows the graphene to be directly synthesised into graphene wool. In the absence of a catalyst during graphene growth, the cracking of methane and nucleation is not as efficient, resulting in graphene defects which can be minimised by optimising the growth conditions. The roles of the methane and hydrogen

flow rates in the synthesis of the graphene wool were investigated, as was the effect of growth temperature, growth time and cooling rates. The precursor flow rates and growth temperature were found to be the most vital parameters. The best quality graphene wool showed a minimum ratio of disordered carbon relative to graphitic carbon (ID/IG & 0.8) with a calculated crystallite grain size of 24 nm. The morphology of the optimised graphene wool was flake-like, and the X-ray photoelectron spectroscopy analysis revealed a surface composition of 94.05 at % C 1s and 5.95 at % O 1s. With this new material, the integrity of the synthesised graphene surface is preserved in use and it has the added advantage of structural support from the quartz substrate. Unlike many other forms of graphene, this fibrous graphene wool is flexible, malleable and compressible, allowing for a wealth of potential applications including in electronics, energy storage, catalysis, and gas sorption, storage, separation and sensing applications.

In line with the aims of the overarching project, the air pollutant sampling capabilities of the GW were of interest. The optimal packing weight of GW inside a glass tube (178 mm, i.d. 4 mm, o.d. 6 mm) was investigated by the adsorption of vaporized alkane standards onto the GW, using a condensation aerosol generator in temperature-controlled chamber with subsequent detection by a flame ionization detection. The optimized weight was found to be 120 mg with a bed length of 5 cm at a flow rate of 500 mL min⁻¹, which provided a gas collection efficiency of >90 % for octane, decane and hexadecane. The humidity uptake of the sampler was found to be less than 1 % (m/m) for ambient relative humidities <70 %. Breakthrough studies showed the favourable adsorption of polar molecules which is attributed to the defective nature of the graphene and the inhomogeneous coating of the graphene layers on the quartz wool, suggesting that the polar versus non-polar uptake potential of the GW can be tuned by varying the graphene layering on the quartz wool substrate during synthesis. The GW traps were conditioned with nitrogen gas between subsequent experiments to successfully demonstrate the reusability and reproducibility of the material.

The GW traps were applied in a combustion sampling campaign to monitor trace levels of organic compounds ranging in volatility (80.1 – 404 °C) and were compared to other samplers, including PDMS denuder devices and activated charcoal. The GW samplers proved to be comparable to PDMS denuders in terms of sampling and thermal desorption of non-polar semi-volatile organic compounds. The total alkane concentrations were found to be 17.96±13.27 µg m⁻³ and 18.30±16.42 µg m⁻³ for the GW and PDMS, respectively. The GW sampler was found to be more effective than PDMS in retaining the lighter, more volatile n-alkanes such as n-

octane and n-nonane. These findings, in conjunction with the results from the GW collection efficiency and breakthrough studies, demonstrates the fitness for use of this material in sampling a wide scope of analytes ranging in volatility. GW proved to be an effective sampling medium comparable to currently available technologies with additional advantages such as surface chemistry tunability. In line with sustainability, novel GW provides a new, exciting possibility for the monitoring of organic air pollutants with numerous advantages, including high sampling efficiencies, simple and cost-effective synthesis of the thermally stable GW, solvent-free and environmentally friendly analysis, and potential reusability of samplers.

In conclusion, this project sheds new light on current environmental and human health issues of global interest and may aid regulatory bodies as well as related industries in planning long-term bio-economical and resource management strategies. One of which would be the promotion of a circular economy whereby a collaboration between key sectors would assist in closing the loop between feedstock producers, the refining industry and fuel users in the country which would lead to more environmentally friendly solutions.

Project Outputs

Patents

Graphene wool and manufacture thereof, PCT International Application PCT/ZA2020/050005, G. Schoonraad and P.B.C. Forbes; filed on 24 January 2020.

System and method for manufacturing graphene wool, SA provisional patent application 2019/00675; G. Schoonraad and P.B.C. Forbes; filed on 1 February 2019 (a).

Air pollutant trap, SA provisional patent application 2019/00674; G. Schoonraad and P.B.C. Forbes; filed on 1 February 2019 (b).

***Note: surname changed from Schoonraad back to maiden name Geldenhuys in 2020.**

Publications and Manuscripts

This thesis is based on the following journal papers:

Geldenhuys, G., Wattrus, M. and Forbes, P.B.C. 2022. Gas and particle phase polycyclic aromatic hydrocarbon emission factors from a diesel vehicle engine: Effect of operating modes in a developing country context. *Atmospheric Environment: X*. 13: 100158. DOI: <https://doi.org/10.1016/j.aeaoa.2022.100158>.

Geldenhuys, G., Orasche, J., Jakobi, G., Zimmermann, R. and Forbes, P.B.C. 2022. Characterization of gaseous and particulate phase polycyclic aromatic hydrocarbons emitted during pre-harvest burning of sugar cane in different regions of Kwa-Zulu Natal, South Africa. *Environmental Toxicology and Chemistry*, Accepted for publication. DOI: <https://doi.org/10.1002/etc.5579>.

Geldenhuys, G., Wattrus, M. and Forbes, P.B.C. 2022. Transition to sustainable alternative fuels in an underground platinum mining environment: Efficiency, emissions, safety and cost considerations. *Energy for Sustainable Development*, Submitted.

Schoonraad, G., Madito, J.M., Manyala, N. and Forbes, P.B.C. 2020. Synthesis and optimisation of a novel graphene wool material by atmospheric pressure chemical

vapour deposition. *Journal of Materials Science*. 55: 545-564. DOI: <https://doi.org/10.1007/s10853-019-03948-0>

Geldenhuis, G., Mason, Y., Dragan, G.C., Zimmermann, R., Forbes, P.B.C. 2021. Novel graphene wool gas adsorbent for volatile and semi-volatile organic compounds. *ACS Omega*. 6(38):24765-76. DOI: <https://doi.org/10.1021/acsomega.1c03595>.

Mason, Y.C., Schoonraad, G., Orasche, J., Bisig, C., Jakobi, G., Zimmermann, R., and Forbes, P.B.C. 2020. Comparative sampling of gas phase volatile and semi-volatile organic fuel emissions from a combustion aerosol standard system. *Environmental Technology & Innovation*. 19: 100945. DOI: <https://doi.org/10.1016/j.eti.2020.100945>.

Two additional papers were produced as a contributing co-author and are provided in Appendix A and B:

Geitner, V., Orasche, J., Dragan, G.C., Jakobi, G., Schnelle-Kreis, J., Geldenhuis, G.L., Forbes, P.B.C., Karg, E.W., Breuer, D. and Zimmermann, R. 2021. Feasibility study of portable sampling techniques for combustion related airborne particulates in a platinum mine. *Gefahrstoffe Reinhaltung Der Luft*. 81(9-10): 386-396.

Gawlitta; N., Orasche; J., Geldenhuis; G., Jakobi; G., Wattrus, M., Jennerwein; M., Michalke; B., Gröger; T., Forbes; P.B.C. and Zimmermann, R. 2022. A study on the chemical profile and the derived health effects of heavy-duty machinery aerosol with a focus on the impact of alternative fuels. *Air Quality, Atmosphere & Health* :1-17. DOI: <https://doi.org/10.1007/s11869-022-01287-9>.

Conference Presentations

Oral Presentations

Schoonraad, G., Madito J.M., Wojno, Y. and Forbes, P.B.C. 2019. Synthesis and characterisation of a novel graphene wool sampler for the determination of organic air pollutants. 4th International Mass Spectrometry School, 15-20 September 2019, Sitges, Barcelona, Spain.

Schoonraad, G., Dragan, G.C., Orasche, J., Kohlmeier, V., Zimmermann, R., Rohwer, E.R., Pretorius, C., Forbes, P.B.C. 2018. Multi-channel polydimethylsiloxane denuder devices for the determination of gas and particulate phase polycyclic aromatic hydrocarbons in underground mines. Analitika 2018 Conference, 22-25 July 2018, Limpopo, South Africa. **Best student oral presentation awarded by ChromSA.*

Poster Presentations

Schoonraad, G., Madito, J.M., Wojno, Y., Manyala, N., Dragan, G.C., Zimmerman, R. and Forbes, P.B.C. 2019. Synthesis and characterisation of a novel graphene wool sampler for organic air pollutants. 63rd International Conference on Analytical Sciences and Spectroscopy, 25-28 June 2019, Montreal, QC, Canada. **Best student presentation awarded.*

Schoonraad, G., Pretorius, C., and Forbes, P.B.C. 2018. Application of a multi-channel polydimethylsiloxane denuder device for the determination of PAHs in diesel exhaust emissions. 42nd International Symposium on Capillary Chromatography and 15th GCxGC Symposium, 14-19 May 2018, Riva Del Garda, Italy

Table of Contents

| | |
|---|------|
| Declaration | ii |
| Acknowledgements | iii |
| Summary | iv |
| Project Outputs | ix |
| Conference Presentations..... | xi |
| Table of Contents | xii |
| Abbreviations | xiii |
| List of Tables | xvii |
| List of Figures | xx |
| Chapter 1: Introduction | 1 |
| 1.1 Background | 1 |
| 1.2 Problem statement and justification for the study..... | 2 |
| 1.3 Aims and objectives | 3 |
| 1.4 Thesis outline | 4 |
| 1.5 References | 6 |
| Chapter 2: PAH Emission factors (Paper 1) | 9 |
| Chapter 3: Emissions assessment: Sugar cane industry (Paper 2) | 23 |
| Paper 2 Supplementary Information | 39 |
| Chapter 4: Feasibility study: Platinum mine industry (Paper 3) | 44 |
| Paper 3 Supplementary Information | 86 |
| Chapter 5: Development of a novel sample based on graphene wool (Paper 4) | 92 |
| Chapter 5: Development of a novel sample based on graphene wool (Paper 5)..... | 113 |
| Chapter 5: Development of a novel sample based on graphene wool (Paper 6) | 126 |
| Paper 6 Supplementary Information | 139 |
| Chapter 6: Conclusions and Recommendations for Future Work | 148 |
| 6.1 Conclusions | 148 |
| 6.2 Recommendations for future work..... | 152 |
| Appendix A: Co-authored paper 1..... | 153 |
| Appendix B: Co-authored paper 2..... | 165 |
| Appendix C: Certificate of analysis of the PAH mix..... | 183 |

Abbreviations

Abbreviations from all chapters have been listed below. Abbreviations in the Appendix are not listed here, unless used elsewhere in the thesis, as they are fully defined in the respective paper.

| | |
|-------------------|---|
| APCVD | Atmospheric pressure chemical vapour deposition |
| BaP _{eq} | Benzo[a]pyrene equivalent |
| BTEX | Benzene, toluene, ethylbenzene and xylene |
| BTL | Biomass-to-liquid |
| BP | Back pressure |
| BV | Breakthrough volume |
| CAPEX | Capital expenditure |
| CAST | Combustion aerosol standard system |
| CIS | Cooled injection system |
| CMS | Comprehensive Molecular Analytics |
| CTL | Coal-to-liquid |
| CVD | Chemical vapour deposition |
| DB | Dry bulb |
| DCM | Dichloromethane |
| DEE | Diesel exhaust emissions |
| DFT | Density functional theory |
| DME | Department of Minerals and Energy |
| DOC | Diesel oxidation catalyst |
| DPF | Diesel particulate filter |
| DPM | Diesel particulate matter |
| DRME | Department of Minerals, Resources and Energy |
| DW | Downwind |
| eBC | Equivalent black carbon |
| EC | Elemental carbon |
| ECM | Engine control module |
| EF | Emission factor |
| EGR | Exhaust gas recirculation |
| F | Filter |
| FAME | Fatty acid methyl ester |

| | |
|------------------|---|
| FID | Flame ionisation detector |
| FT-IR | Fourier transform infrared spectroscopy |
| FWHM | Full width half maximum |
| GC | Gas chromatograph |
| GC x GC | Two-dimensional gas chromatography |
| GC-MS | Gas chromatography-mass spectrometry |
| GHG | Greenhouse gas |
| GTL | Gas-to-liquid |
| GW | Graphene wool |
| HACA | Hydrogen abstraction-C ₂ H ₂ addition |
| HC | Hydrocarbon |
| HEFA | Hydrotreated esters and fatty acid |
| HI | High idle mode |
| HPLC | High performance liquid chromatography |
| IARC | International Agency for Research on Cancer |
| IR | Infrared |
| ISO | International Organisation for Standardisation |
| I _{Std} | Internal standard |
| KIT | Karlsruhe Institute of Technology |
| KZN | Kwa-Zulu Natal |
| LCOF | Levelized cost of fuel |
| LDV | Light duty vehicle |
| LHD | Load haul dump vehicle |
| LN ₂ | Liquid nitrogen |
| LNT | Lean nitrous oxide trap |
| LOD | Limit of detection |
| LOQ | Limit of quantification |
| LPG | Low pressure gas |
| MDHS | Methods for the determination of hazardous substances |
| NRF | National Research Foundation |
| OC | Organic carbon |
| OPEX | Operating expenditure |
| PAH | Polycyclic Aromatic Hydrocarbon |
| PASE | Plunger assisted solvent extraction |

| | |
|-------------------|--|
| PCA | Principal component analysis |
| PD | Pure diesel |
| PDMS | Polydimethylsiloxane |
| PEMS | Portable emissions measurement system |
| PM | Particulate matter |
| PM _{2.5} | Particulate matter with aerodynamic diameter < 2.5 µm |
| PT | Primary trap |
| PTFE | Polytetrafluoroethylene |
| PUF | Polyurethane foam |
| QFF | Quartz fiber filter |
| QW | Quartz wool |
| RME | Rapeseed methyl ester |
| ROR | Rate of return |
| RSD | Relative standard deviation |
| SA | South Africa |
| SASA | South African Sugar Association |
| SCR | Selective catalytic reduction |
| SEM | Scanning electron microscopy |
| S/N | Signal to noise |
| ST | Secondary trap |
| SVOC | Semi-volatile organic compound |
| TC | Total carbon |
| TC | Test cycle mode |
| TD | Thermal desorption |
| TD-GCxGC-ToF-MS | Thermal desorption-two-dimensional gas chromatography-time-of-flight mass spectrometry |
| TDS | Thermal desorption system |
| TEF | Toxic equivalence factor |
| TEM | Transmission electron microscopy |
| TEQ | Toxic equivalence quotient |
| THC | Total hydrocarbon |
| TMM | Trackless mobile machinery |
| ToF-MS | Time-of-flight mass spectrometry |
| ULS | Ultra-low sulphur |

| | |
|--------|---|
| US EPA | United States Environmental Protection Agency |
| UV | Ultraviolet |
| UV | Utility vehicle |
| UW | Upwind |
| VOC | Volatile organic compound |
| WB | Wet bulb |
| WHO | World Health Organisation |
| XPS | X-ray photoelectron spectroscopy |

List of Tables

Chapter 2 (Paper 1)

| | |
|---|----|
| Table 1: Sixteen US EPA priority PAHs and their corresponding abbreviations, molar masses and boiling points..... | 11 |
| Table 2: Test engine operation mode..... | 12 |
| Table 3: Test engine specifications..... | 12 |
| Table 4: Test fuel specifications..... | 12 |
| Table 5: Detected PAH abbreviations and coefficients of variation for trap and filter calibration curves..... | 16 |
| Table 6: LOD and LOQ values for PAHs in gas phase and particulate phase..... | 17 |
| Table 7: Concentration of PAHs in raw and dilute exhaust streams in $\mu\text{g}/\text{m}^3$ | 17 |
| Table 8: Calculated emission factors for PAHs emitted per kg fuel burned during idle and maximum power mode..... | 19 |
| Table 9: Comparison of PAH EFs (in $\mu\text{g}/\text{kg}$ fuel burned) obtained from various studies done on light duty vehicles (LDVs)..... | 20 |

Chapter 3 (Paper 2)

| | |
|--|----|
| Table 1: Sample site, location crop information and meteorological sampling details for each sampled burn event..... | 28 |
| Table 2: Analytes investigated in this study including 15 of the 16 US EPA priority PAHs and their corresponding abbreviations, molar masses and boiling points..... | 30 |
| Table 3: Limits of detection and limits of quantification for individual PAHs detected in PDMS trap and QFF samples (ng m^{-3})..... | 30 |
| Table 4: TEF values for PAHs and the calculated TEQ values for total gas and particle PAHs ($\mu\text{g m}^{-3}$)..... | 34 |
| Table 5: Mean and median eBC concentrations determined via Aethalometer readings during different sugar cane burn events..... | 36 |

(Paper 2) Supplementary Information

| | |
|---|----|
| Table S1: Quantified PAHs ($\mu\text{g m}^{-3}$) as the sum of the primary trap (PT), filter (F) and secondary trap (ST) for each burn event..... | 39 |
|---|----|

| | |
|--|----|
| Table S2: Data processing parameters for ChromaTOF Tile (Version v1.01.00.0, Leco, USA)..... | 40 |
| Table S3: Chemical components with highest loadings towards the three classes of samples namely the primary trap, filter and secondary trap..... | 42 |

Chapter 4 (Paper 3)

| | |
|--|----|
| Table 1: Properties of the diesel, RME and GTL fuel used in the underground sampling campaign..... | 55 |
| Table 2: LHD engine specifications..... | 56 |
| Table 3: Analytes investigated in this study including fifteen of the sixteen US EPA priority PAHs and their corresponding abbreviations, molar masses and boiling points..... | 59 |
| Table 4: Comparative qualitative observations of LHD engine performance parameters when operated on neat diesel, GTL and RME fuels..... | 68 |
| Table 5: Advantages and disadvantages of the use of biodiesel over diesel..... | 69 |
| Table 6: Diesel consumption and power usage in hybrid and fully mechanised mining operations..... | 72 |
| Table 7: Comparison of environmental, economic and social impacts pertaining to the use of alternate fuels. The plus symbols indicate the extent of the positive impact and the minus symbols represent the negative impact..... | 74 |

(Paper 3) – Supplementary Information

| | |
|--|----|
| Table S1 Sample details for underground platinum mine campaign..... | 87 |
| Table S2 ChromaTOF Tile list of chemical features contributing to variances between gas phase LHD PDMS samples for PD, RME and GTL fuel..... | 89 |

Chapter 5 (Paper 5)

| | |
|--|-----|
| Table 1: Density, mass, and volume of GW packed into a glass tube for the optimization study..... | 118 |
| Table 2: Moisture uptake of GW traps at various levels of humidity (n = 3)..... | 120 |
| Table 3: BVs of QW, GW, and PDMS along with the boiling points, molecular masses, and densities of the compounds at the inlet temperature of 250 °C..... | 122 |

(Paper 6)

Table 1: Mean FID results for the sampling events of the undiluted fuel emissions over each 10 min sampling period..... 132

Table 2: The relative advantages and disadvantages of GW, PDMS and charcoal samplers for the sampling of the selected VOCs, PAHs and n-alkanes at trace levels.....133

(Paper 6) – Supplementary Information

Table S1: Standards and internal standards used in this study..... 140

Table S2: Ambient conditions at the start of sampling events for this study..... 141

Table S3: Mean FTIR results for the sampling events of the undiluted fuel emissions over each 10 min sampling period..... 141

Table S4: Concentrations of target analytes detected upon analysis of blank samplers..... 143

Table S5: Concentrations of target analytes detected upon thermal desorption of GW samplers after sampling the emissions of CAST combustion of different fuels with associated standard deviations between sampling duplicates..... 144

Table S6: Concentrations of target analytes detected upon thermal desorption of PDMS samplers after sampling the emissions of CAST combustion of different fuels with associated standard deviations between sampling duplicates..... 145

Table S7a: LODs and LOQs (ng) of target analytes for different samplers, namely PDMS, GW and activated charcoal. PDMS and GW samplers were directly thermally desorbed whilst the activated charcoal extract was first extracted with CS₂ and the extract was injected into the GC port..... 146

Table S7b: LODs and LOQs (ng.m⁻³) of target analytes for different samplers, namely PDMS, GW and activated charcoal. PDMS and GW samplers were directly thermally desorbed whilst the activated charcoal extract was first extracted with CS₂ and 1 µL of the 3 mL extract was injected into the GC port..... 147

List of Figures

Chapter 2 (Paper 1)

| | |
|--|----|
| Figure 1: (a) Schematic of test cell setup indicating the undiluted, raw and diluted sample positions, (b) cross section of diluted sample position in the exhaust duct and (c) a photograph of the test cell setup..... | 13 |
| Figure 2: Schematic of multi-channel trap denuder sampling devices used for PAH Sampling..... | 14 |
| Figure 3: Torque measurements as a function of temperature..... | 14 |
| Figure 4: Variation in engine emission dilution factors as a function of sampling distance from the tailpipe outlet..... | 15 |
| Figure 5: Concentration of emitted pollutants as a function of engine power..... | 16 |
| Figure 6: Total gas and particulate PAH concentrations for raw and dilute samples..... | 18 |
| Figure 7: Idle mode (M_A) PAH profiles for raw (left) and dilute (right) samples..... | 18 |
| Figure 8: Max power mode (M_B) PAH profiles for raw (left) and dilute (right) samples.... | 18 |
| Figure 9: Comparison of particulate PAH EFs (in $\mu\text{g}/\text{kg}$ fuel burned) obtained from various studies done on LDVs where this study represents a sum of gas and particle phase..... | 20 |

Chapter 3 (Paper 2)

| | |
|---|----|
| Figure 1: (a) Sampling locations in the SA sugar belt.in Kwa-Zulu Natal Province in South Africa (adapted from SASA,(nd)) (b) the sampling setup during burning events..... | 27 |
| Figure 2: Schematic of the denuder sampling device consisting of a primary trap, filter and secondary trap for simultaneous gas and particulate sampling..... | 29 |
| Figure 3: Box plot representing the sum of PAHs detected on the primary trap, filter and secondary trap per burn event in upwind (UW) and downwind (DW) samples..... | 31 |
| Figure 4: Upwind (left) and downwind (right) total PAH concentrations found on the primary trap, filter and secondary trap of the denuder device per burn event (1-5)..... | 32 |
| Figure 5: Individual PAH concentrations detected during each burn event on the primary trap, filter and secondary trap of the denuder sampling device..... | 33 |
| Figure 6: Loading plot (left) and scores plot (right) for total PAH concentrations (DW gas + particle phase) between the different burn events..... | 35 |

Figure 7: Biplot for sampling and meteorological variables relating to individual burn events. Total DW PAHs on primary trap, filter and secondary trap per burn event were used for the plot..... 35

(Paper 2) – Supplementary Information

Figure S1: ChromaTOF Tile scores (top) and loading (bottom) plot for sampling and meteorological variables relating to individual burn events..... 41

Figure S2: Correlation between total PAH and black carbon (BC) emissions at each of the five burn events..... 43

Chapter 4 (Paper 3)

Figure 1: Biofuel generation based on different feedstocks..... 49

Figure 2: (a) Multi-channel trap denuder sampling devices secured on sampling table underground (b) Position of the multi-channel trap denuder sampling devices relative to the LHD exhaust (c) Schematic of multi-channel trap denuder sampling devices used for PAH sampling..... 57

Figure 3: (Top left) Total PAH concentrations on the primary and secondary trap for the LHD engine exhaust samples during high idle mode using diesel, RME and GTL fuels (Top right) Total PAH concentrations on the primary and secondary trap for the LHD engine exhaust samples during test cycle mode using diesel, RME and GTL fuels and (bottom) hierarchical tree map chart of total PAH concentrations for different tested fuels during both cycles.... 64

Figure 4: PCA Loading Plot of the PDMS trap samples for LHD operated on pure diesel, rapeseed methyl ester and gas-to -liquid fuels..... 66

Figure 5: PCA Loading Plot of the PDMS trap samples for LHD operated on pure diesel, rapeseed methyl ester and gas-to -liquid fuels..... 66

(Paper 3) – Supplementary Information

Figure S1: Photograph of load haul dump vehicle used for underground mining operations 91

Chapter 5 (Paper 4)

- Figure 1: a Temperature profile of the CVD process as measured by a series of thermocouples and b schematic of the non-catalytic direct growth mechanism of CVD graphene on quartz wool substrate..... 95
- Figure 2: G intensity map (a), I_D/I_G ratio map (b) and I_{2D}/I_G ratio map (c) for GW grown at 800 °C. G intensity map (d), I_D/I_G ratio map (e) and I_{2D}/I_G ratio map (f) for GW grown at 1200 °C. G intensity map (g), I_D/I_G ratio map (h) and I_{2D}/I_G ratio map (i) for GW grown at 1300 °C. Comparison of the D, G and 2D peaks in the Raman spectra (j) and graph representing G intensity and I_D/I_G and I_{2D}/I_G ratios (k)..... 98
- Figure 3: SEM images for pristine quartz wool (a), GW grown at 800 °C (b), 1200 °C (c) and 1300 °C (d)..... 99
- Figure 4: G intensity map (a), I_D/I_G ratio map (b) and I_{2D}/I_G ratio map (c) for GW that was cooled slowly at -0.4 °C s^{-1} . G intensity map (d), I_D/I_G ratio map (e) and I_{2D}/I_G ratio map (f) for GW that was cooled rapidly at -14.5 °C s^{-1} . Comparison of the D, G and 2D peaks in the Raman spectra (g) and graph representing G intensity and I_D/I_G and I_{2D}/I_G ratios (h)..... 100
- Figure 5: SEM images for pristine quartz wool (a), GW grown and cooled slowly at a rate of -0.4 °C s^{-1} (b) and GW grown and cooled rapidly at a rate of -14.5 °C s^{-1} (c) at 200 nm range..... 101
- Figure 6: G intensity map (a), I_D/I_G ratio map (b) and I_{2D}/I_G ratio map (c) for GW grown with 20 sccm CH_4 . G intensity map (d), I_D/I_G ratio map (e) and I_{2D}/I_G ratio map (f) for GW grown with 50 sccm CH_4 . G intensity map (g), I_D/I_G ratio map (h) and I_{2D}/I_G ratio map (i) for GW grown with 100 sccm CH_4 . G intensity map (j), I_D/I_G ratio map (k) and I_{2D}/I_G ratio map (l) for GW grown with 150 sccm CH_4 . G intensity map (m), I_D/I_G ratio map (n) and I_{2D}/I_G ratio map (o) for GW grown with 200 sccm CH_4 102
- Figure 7: Comparison of the D, G and 2D peaks in the Raman spectra (a) and graph representing G intensity and I_D/I_G and I_{2D}/I_G ratios (b) for GW grown at different methane flow rates..... 103
- Figure 8: SEM images for pristine quartz wool (a) and GW grown with methane flow rates of 20 sccm (b), 50 sccm (c), 100 sccm (d), 150 sccm (e) and 200 sccm (f)..... 104
- Figure 9: G intensity map (a), I_D/I_G ratio map (b) and I_{2D}/I_G ratio map (c) for GW grown with 0 sccm H_2 . G intensity map (d), I_D/I_G ratio map (e) and I_{2D}/I_G ratio map (f) for GW grown at 250 sccm H_2 . G intensity map (g), I_D/I_G ratio map (h) and I_{2D}/I_G ratio map (i) for GW grown

| | |
|--|-----|
| with 500 sccm H ₂ . Comparison of the D, G and 2D peaks in the Raman spectra (j) and graph representing G intensity and I _D /I _G and I _{2D} /I _G ratios (k)..... | 105 |
| Figure 10: SEM images for pristine quartz wool (a) and GW grown with hydrogen flow rates of 0 sccm (b), 250 sccm (c) and 500 sccm (d)..... | 106 |
| Figure 11: G intensity map (a), I _D /I _G ratio map (b) and I _{2D} /I _G ratio map (c) for GW grown for 30 min. G intensity map (d), I _D /I _G ratio map (e) and I _{2D} /I _G ratio map (f) for GW grown for 60 min. G intensity map (g), I _D /I _G ratio map (h) and I _{2D} /I _G ratio map (i) for GW grown for 90 min. Comparison of the D, G and 2D peaks in the Raman spectra (j) and graph representing G intensity and I _D /I _G and I _{2D} /I _G ratios (k)..... | 107 |
| Figure 12: SEM images for pristine quartz wool (a) and GW grown for 30 min (b), 60 min (c) and 90 min (d)..... | 108 |
| Figure 13: G intensity map (a), I _D /I _G ratio map (b) and I _{2D} /I _G ratio map (c), full width half maximum (FWHM) of 2D peak (d) and grain size (L _a) (e) for GW that was grown using optimised experimental conditions..... | 108 |
| Figure 14: TEM images for the graphene wool grown under optimised experimental conditions (500:500:100 sccm, Ar/H ₂ /CH ₄ at 1200 °C and cooled at - 14.5 °C s ⁻¹)..... | 109 |
| Figure 15: The XPS spectra: a wide scan spectrum, b C 1s and c O 1s core-level spectra obtained from the optimised graphene wool..... | 110 |

(Paper 5)

| | |
|--|-----|
| Figure 1: Experimental setup for the determination of gas collection efficiency on the GW trap (a) and schematic of the experimental setup (b)..... | 115 |
| Figure 2: Experimental setup for the determination of humidity uptake on GW traps (a) and schematic of the experimental setup (b)..... | 116 |
| Figure 3: Experimental setup within the GC oven for the determination of breakthrough volume (a) and schematic of the experimental setup (b)..... | 117 |
| Figure 4: (a) Octane collection efficiency of GW traps as a function of increasing mass of GW but constant bed length, in comparison to PDMS and charcoal traps and (b) octane collection efficiency of GW traps as a function of packing density which was varied by altering the bed length (mm) of the GW inside the glass tube with the error bars showing standard deviation for n = 3..... | 119 |
| Figure 5: Average gas collection efficiency of C ₈ , C ₁₂ , and C ₁₆ alkanes on GW traps A–C (a). Individual collection efficiency of octane (b), dodecane (c), and hexadecane (d) on three | |

| | |
|---|-----|
| different GW traps. Desorption of octane over a period of 30 min (e) and 5 h (f) and of hexadecane over 15 h (g). The total concentration desorbed versus the total concentration loaded of dodecane on the GW trap over a period of 8 h (h)..... | 119 |
| Figure 6: Overlaid chromatograms illustrating the differing retention of methanol at 25 °C for samplers used in the breakthrough study..... | 121 |
| Figure 7: Breakthrough volume curves for the 0.120 g QW (left), 0.141 g GW (middle), and 0.365 g PDMS (right) samplers at various isothermal temperatures..... | 122 |
| Figure 8: Concentration of C ₁₀ –C ₂₀ alkanes in RME biodiesel combustion emissions on GW and PDMS samplers that were thermally desorbed and analyzed by GC–MS..... | 123 |

(Paper 6)

| | |
|--|-----|
| Figure 1: Schematic diagram of the CAST generator sampling set-up..... | 130 |
| Figure 2: Schematic of the sampler setup where numbers 1, 2 and 3 illustrate the positions of the activated charcoal, GW and PDMS samplers, respectively, during CAST sampling events..... | 131 |
| Figure 3: Detected concentrations of (a) VOCs, (b) PAHs and (c) n-alkanes from the combustion of fuel types B0, GTL and RME sampled from the CAST generator exhaust using PDMS and GW samplers. The error bars are based on the standard deviation (SD) of duplicate measurements and abbreviations can be found listed in Tables S7a and S7b..... | 134 |
| Figure 4: Relative abundance ($\mu\text{g m}^{-3}$) of various compounds detected upon analysis of the GW sampler after sampling the gas phase emissions from B0, GTL and RME combustion: (a) benzene and toluene, (b) naphthalene, (c) VOCs, (d) PAHs and (e) n-alkanes..... | 135 |
| Figure 5: PM filtered from (a) B0, (b) GTL and (c) RME CAST emissions prior to gas phase sampling..... | 136 |

(Paper 6) – Supplementary Information

| | |
|---|-----|
| Figure S1: Graphene wool sampler showing the GW of 60 mm bed length housed in a glass tube with glass end caps held in place by Teflon sleeves..... | 139 |
| Figure S2: Photograph of the CAST generator sampling set-up..... | 139 |
| Figure S3: Photograph of the sampler setup for the activated charcoal, GW and PDMS samplers, respectively, during CAST sampling events..... | 140 |
| Figure S4: Comparison of sampling event replicates for B0 a), GTL b) and RME c)..... | 142 |

Chapter 1: Introduction

1.1 Background

Two of the most important concerns that modern society faces are the search for cleaner, more sustainable energy and the protection of the environment. Air quality is a fundamental aspect pertaining to sustainable development in terms of human and environmental health and the ability to fully characterise and understand toxic compounds contributing to atmospheric pollution is vital for any method of mitigation. Anthropogenic sources, such as diesel combustion emissions, are major contributors to air pollution and should be considered the highest priority with respect to implementing change, especially since they are directly in our control.

Fossil fuel reserves are being depleted and will not be able to sustain the world's energy demand, and as a result consumers and industry are at the mercy of volatile oil prices. It is due to these concerns that there has been a substantial increase in interest regarding the use of alternative fuels and biofuels which are sustainably produced. Biofuels are attractive from an environmental and human health perspective as they can potentially decrease emissions associated with fuel combustion such as particulate matter (PM), polycyclic aromatic hydrocarbons (PAHs) and other volatile and semi-volatile organic compounds (SVOCs).

Given the possibility of the use of alternative fuels in engines currently fuelled by diesel, it is necessary to evaluate and quantify emission benefits and liabilities of these fuels by monitoring and characterizing pollutants using efficient and feasible sampling methodology. In South Africa (SA), large industries, such as mining and sugar cane farming, are major anthropogenic sources of combustion pollutants due to automotive emissions and biomass burning respectively, which have negative impacts on the environment and human health. The link between sugar cane biomass and cleaner fuel is the potential for the biomass to be used as a feedstock for biofuel production as opposed to the current practice of it being burnt. The ability to sample and quantify toxic compounds from the burning process is crucial in motivating a change to more sustainable solutions.

The wide use of mobile and stationary diesel machinery in underground mines poses a risk to the health and safety of employees due to exposure to diesel exhaust emissions (DEE), which

as a whole were classified as being carcinogenic to humans (Group 1) by the International Agency for Research on Cancer (IARC) which forms part of the World Health Organization (IARC 2012, 2014). Evidence reveals that exposure is associated with an increased risk of lung cancer as well as other health complications such as respiratory and cardiovascular diseases (Lewtas 2007, Kim et al. 2013). The same problem also arises in the communities that are in close proximity to sugar cane fields in the province of Kwa-Zulu Natal in SA, due to pre-harvest field burning which produces extensive plumes of PM and other hazardous air emissions resulting from open burning of agricultural waste.

1.2 Problem statement and justification for the study

The intensifying demand for energy and the current over dependence on fossil fuels have made energy security a critical issue worldwide (Ambaye, Vaccari et al. 2021). Although the economic impact may be immobilizing, the adverse environmental impacts associated with the use of fossil fuels are far more concerning and will influence the planet and all future generations to come. There is a pressing need for sustainable development and a transition to alternative fuels can lead to a reduction in emissions of harmful pollutants and greenhouse gases and can be a possible immediate solution to the aforementioned problems. Such a transition must be accompanied by a comprehensive risk management strategy, one aspect of which is that the resultant emissions that arise from the combustion of these fuels are required to be fully characterised and quantified.

Volatile and semi-volatile organic compounds, such as PAHs that are commonly used as environmental pollution markers, require trace sampling technologies that are selective, sensitive, cost effective and most importantly can be used in an environmentally friendly manner devoid of toxic solvents. Traditional PAH sampling methods require large sampling volumes and extended sampling times which introduce unwanted sampling artefacts resulting from analyte breakthrough, adsorption effects (of gas phase analytes onto collected particles) and filter blow off. Miniature portable denuder devices comprised of two multi-channel polydimethylsiloxane (PDMS) rubber traps separated by a quartz fibre filter have been demonstrated to overcome these limitations as they are of open geometry with low back pressure and they require low flow rates and short sampling intervals (Forbes et al. 2012). They also offer the added advantage of being able to be thermally desorbed preventing the need for time consuming and environmentally unfriendly solvent extraction (Forbes et al. 2009, Forbes,

2015, Geldenhuys 2014, Geldenhuys et al. 2015, Munyeza et al. 2019). PDMS denuders are limited to the sampling of non-polar SVOCs and as such, there is a continuous need for the development of practical and sustainable sampling methodologies that cater for the sampling of a larger scope of analytes with higher polarities and volatilities and, very importantly, are readily available in developing countries.

1.3 Aim and objectives

The influence of atmospheric pollutants on human health is an important aspect of the research into environmentally-related diseases. This project aims to address air quality monitoring for sustainable development by characterising selected volatile and semi-volatile organic compounds emitted from key South African industries (namely the platinum mining and sugar industries) using portable denuder devices as well as by the development and validation of novel sampling technologies to increase the scope of analytes which can be sampled and thereby enhance environmental applications.

The aim will be achieved by meeting the following objectives:

- To determine gas and particle phase PAH emission factors for a diesel vehicle engine using portable denuder samplers that overcome traditional sampling drawbacks and bottlenecks (Chapter 2). These experiments will be done on an aged diesel engine under different operating modes that are representative of the fleet performance in a developing country.
- To characterize and quantify gaseous and particulate phase polycyclic aromatic hydrocarbons emitted during pre-harvest burning of sugar cane and to determine the influence that meteorological, crop and burn conditions have on PAH emissions as well as PAH partitioning between the two phases.
- To determine the feasibility of a transition from fossil fuel to the use of greener fuel in the platinum mining industry by evaluating four key aspects:
 - Reduction of engine emissions: to characterise, quantify and compare PAHs emitted from trackless mobile machinery in an underground platinum mine when fuelled with diesel, rapeseed methyl ester biodiesel and gas-to-liquid fuel, respectively, using an

optimised thermal desorption and comprehensive two-dimensional gas chromatography technique coupled to time-of-flight mass spectrometry.

- Engine functional performance: to review the effects that biofuels have on engine performance reported in the literature and to compare this to feedback obtained from underground operators during this sampling campaign.
 - Cost and sensitivity analysis: to review literature regarding biofuel production costs and to estimate the current costs incurred for diesel usage in hybrid and fully mechanised platinum mines.
 - Environmental and socio-economic factors: to compare environmental, economic and social impacts pertaining to the use of diesel, biodiesel and GTL/BTL respectively.
- To develop and test a novel graphene-based sampling technology for the monitoring of volatile and semi-volatile organic compounds (Chapter 5) by achieving the following:
 - To synthesise and fully characterise a graphene wool material.
 - To test GW adsorbents in terms of trap assembly, gas-phase collection efficiencies, breakthrough volumes, and humidity uptake.
 - To conduct controlled laboratory experiments based on a combustion aerosol standard system in order to further elucidate the fundamental operating mechanisms of the GW samplers and to compare them to other samplers, namely the PDMS denuder devices and commercial activated charcoal traps.

1.4 Thesis Outline

This research incorporates various aspects and studies, which involved numerous collaborations across multiple academic disciplines. The chapters of this thesis are based on published and submitted manuscripts. Each paper commences with a concise literature review therefore a separate literature review chapter was not included in this thesis. Various review articles were consulted for the overarching aspect of the prevalence of PAHs in the atmosphere and the analytical techniques used for the monitoring thereof (Pandey et al. 2011, Kim et al. 2013, Forbes 2015).

Chapter 2 (**Paper 1**): initiates the research by determining the status quo regarding diesel vehicle emissions as a basis for further investigations into emissions arising from alternative

fuels. The paper summarizes the methods, results and discussion of diesel engine dynamometer experiments. Here, PAH profiles and emission factors from a light duty vehicle under different operating modes, representative of developing country conditions, are presented and discussed. This sampling was achieved using PDMS denuders that were effectively able to sample both phases and analysis was performed using thermal desorption coupled to comprehensive two-dimensional gas chromatography with time-of-flight mass spectrometric detection (TD-GCxGC-ToF-MS). Gas and particle phase PAH profiles and EFs at each of the modes tested are then compared to other reported studies using alternative measurement methods (such as tunnel and roadside samples) in order to assess the advantages and disadvantages of the adopted test measurement strategy and identify potential areas of further development.

In order to shed more light on anthropogenic sources of PAHs in SA, whilst assessing a key contributing sector, Chapter 3 (**Paper 2**) details the methods, results and discussion of the sampling of air emissions during pre-harvest burning of sugar cane in Kwa-Zulu Natal. Here, gas and particle phase PAHs arising from pre-harvest sugar cane burning were characterized and quantified. The influence of weather, crop and burn conditions on emissions is discussed. This study, and others like it, are important to be able to inform the establishment of best practice in sugar cane harvesting and related air quality monitoring, and thereby strive towards enhancing the environmental benefits of the sugar cane industry and its sustainability. The emission inventory of biomass burning reported in this study can be compared to the bio-economical exploitation of crop residues for biofuel generation, as discussed in the following Paper 3, with the aim of promoting a circular economy in SA.

Based on the findings in Chapter 2 and 3 that evaluated source specific emissions, specifically those of PAHs, further investigations into alternative fuels and practices were warranted. Chapter 4 (**Paper 3**) summarizes the methods, results and discussion of an underground platinum mine air sampling campaign whereby the feasibility of a transition to alternative fuels, with focus on biodiesel and biomass-to-liquid fuel, is considered. Herein, the evaluation of this transition was carried out according to four indicators namely: the functional performance of biofuel versus diesel, potential reductions in air emissions of potentially harmful substances, as well as cost, socio-economic and environmental implications of implementation. In line with the focus of the research presented in this thesis, emphasis was given to the air emission indicator. Gas and particulate PAHs emitted from an underground LHD engine exhaust, when operated on pure diesel, RME or GTL, were characterized in order to evaluate if the use of

biofuels will significantly lead to reductions in air emissions of potentially harmful substances, and thus to healthier, sustainable development. Each of the other indicators are reviewed and discussed and contribute to the overall feasibility of transitioning to alternate fuels. This chapter builds on the findings of Paper 1 & 2 and presents holistic and realistic solutions for sustainable development in SA, whereby key industries such as the sugar cane and mining sectors join forces to create a circular economy as feedstock producers and fuel users respectively and subsequently lessen the environmental burden of anthropogenic combustion emissions (as investigated in the aforementioned studies).

Numerous organic air pollutants arise from fuel and biomass combustion and current sampling methodologies have limitations in terms of the scope of compounds that can be sampled. In line with sustainable development, a novel graphene wool sampler was developed for this purpose. Chapter 5 (**Paper 4**) details the method of atmospheric pressure chemical vapour deposition (CVD) synthesis of graphene on a high-purity quartz wool substrate and investigates the roles that experimental parameters (namely methane and hydrogen flow rates, growth temperature, growth time and cooling rates) have on the quality of the synthesised graphene wool. **Paper 5** reports on the optimised GW trap assembly, gas-phase collection efficiencies, breakthrough volumes, and humidity uptake in order to evaluate their use as air samplers for VOCs and SVOCs. Following on from paper 5, the application of the optimised GW samplers is demonstrated in **Paper 6** by means of comparative sampling of gas phase volatile and semi-volatile organic fuel emissions from a combustion aerosol standard system. In Chapter 6, specific and general conclusions of the study are made and recommendations for future work are proposed.

1.5 References

- Ambaye, T. G., M. Vaccari, A. Bonilla-Petriciolet, S. Prasad, E. D. van Hullebusch and S. Rtimi. 2021. Emerging technologies for biofuel production: a critical review on recent progress, challenges and perspectives. *Journal of Environmental Management*. 290: 112627. DOI: <https://doi.org/10.1016/j.jenvman.2021.112627>.
- Forbes, P. (2015). *Monitoring of Air Pollutants: Sampling, Sample Preparation and Analytical Techniques*. (Vol. 70): Elsevier. Netherlands.

- Forbes, P.B.C., Karg, E.W., Zimmermann, R. & Rohwer, E.R. 2012. The use of multi-channel silicone rubber traps as denuders for polycyclic aromatic hydrocarbons. *Analytica Chimica Acta*. 730: 71-79. DOI: <https://doi.org/10.1016/j.aca.2011.11.013>.
- Forbes, P.B.C. & Rohwer, E.R. 2009. Investigations into a novel method for atmospheric polycyclic aromatic hydrocarbon monitoring. *Environmental Pollution*. 157(8-9): 2529-2535. DOI: <https://doi.org/10.1016/j.envpol.2009.03.004>.
- Geldenhuis, G. 2014. Characterization of diesel emissions with respect to semi-volatile organic compounds in South African platinum mines and other confined environments (Masters dissertation, University of Pretoria).
- Geldenhuis, G., Rohwer, E.R., Naudé, Y., & Forbes, P.B.C. 2015. Monitoring of atmospheric gaseous and particulate polycyclic aromatic hydrocarbons in South African platinum mines utilising portable denuder sampling with analysis by thermal desorption–comprehensive gas chromatography–mass spectrometry. *Journal of Chromatography A*. 1380: 17-28. DOI: <https://doi.org/10.1016/j.chroma.2014.12.062>.
- International Agency for Research on Cancer (IARC), World Health Organization (WHO). 2012. IRAC: Diesel Engine Exhaust Carcinogenic (press release). Available at https://www.iarc.fr/en/media-centre/pr/2012/pdfs/pr213_E.pdf.
- International Agency for Research on Cancer (IARC), World Health Organization (WHO). 2014. Diesel and gasoline engine exhausts and some nitroarenes (volume 105). Available at <http://monographs.iarc.fr/ENG/Monographs/vol105/mono105.pdf>.
- Kim, K.H., Jahan, S.A., Kabir, E. and Brown, R.J.C. 2013. A review of airborne polycyclic aromatic hydrocarbons (PAHs) and their human health effects. *Environment International*. 60: 71–80. DOI: <https://doi.org/10.1016/j.envint.2013.07.019>.
- Lewtas J. 2007. Air pollution combustion emissions: characterization of causative agents and mechanisms associated with cancer, reproductive, and cardiovascular effects. *Mutation Research/Reviews in Mutation Research*. 636 (1-3): 95-133. doi: 10.1016/j.mrrev.2007.08.003. Epub 2007 Aug 17. PMID: 17951105. DOI: <https://doi.org/10.1016/j.mrrev.2007.08.003>.
- Munyeza, C.F., Kohlmeier, V., Dragan, G.C., Karg, E.W., Rohwer, E.R., Zimmermann, R. and Forbes, P.B.C. 2019. Characterisation of particle collection and transmission in a polydimethylsiloxane based denuder sampler. *Journal of Aerosol Science*. 130: 22-31. DOI: <https://doi.org/10.1016/j.jaerosci.2019.01.001>.

Pandey, S.K., Kim, K.H. and Brown, R.J. 2011. A review of techniques for the determination of polycyclic aromatic hydrocarbons in air. *TrAC Trends in Analytical Chemistry*, 30(11): 1716-1739. DOI: <https://doi.org/10.1016/j.trac.2011.06.017>.

Chapter 2: PAH Emission Factors (Paper 1)

Determination of gas and particle phase polycyclic aromatic hydrocarbon emission factors from a diesel vehicle engine under different operating mode is presented in this chapter.

This chapter was published in the Journal Atmospheric Environment: X.

Geldenhuis, G., Wattus, M. and Forbes. P.B.C. 2022. Gas and particle phase polycyclic aromatic hydrocarbon emission factors from a diesel vehicle engine: Effect of operating modes in a developing country context. *Atmospheric Environment: X.* 13: 100158. DOI: <https://doi.org/10.1016/j.aeaoa.2022.100158>.

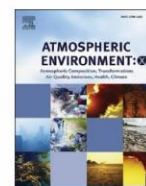
Author contributions

G. Geldenhuis: Methodology, Investigation, Formal analysis, Writing – original draft. **M. Wattus:** Methodology, Resources, Investigation, Formal analysis, Writing – review & editing. **P.B.C. Forbes:** Conceptualization, Methodology, Investigation, Formal analysis, Writing – review & editing, Supervision, Project administration, Resources, Funding acquisition.



Contents lists available at ScienceDirect

Atmospheric Environment: X

journal homepage: www.journals.elsevier.com/atmospheric-environment-x

Gas and particle phase polycyclic aromatic hydrocarbon emission factors from a diesel vehicle engine: Effect of operating modes in a developing country context

G. Geldenhuys^{a,b}, M. Wattrus^c, P.B.C. Forbes^{a,*}

^a Department of Chemistry, University of Pretoria, Lynnwood Road, Hatfield, Pretoria, 0001, South Africa

^b Impala Platinum Ltd, Processing Laboratory, 123 Bethlehem Drive, Rustenburg, 0299, South Africa

^c Sasol Fuels Application Centre (SFAC), 81 Bridge Place Capricorn Park, Muizenberg, Western Cape, South Africa

ARTICLE INFO

Keywords:

Polycyclic aromatic hydrocarbon
Emission factor
Diesel exhaust emission
Light duty vehicle
Denuder
Dynamometer

ABSTRACT

Airborne polycyclic aromatic hydrocarbons (PAHs) arising from diesel exhaust emissions are of concern due to their significant human health and environmental impacts. Engine dynamometer experiments with a light duty diesel engine were conducted to measure PAH emissions representative of developing country conditions, and thereby determine emission factors at two different engine operating modes that are representative of idling and severe real-world conditions, respectively. We employed a portable denuder device for the simultaneous sampling of gaseous and particulate PAH emissions, the components of which were subsequently individually thermally desorbed and analysed by two-dimensional gas chromatography with time-of-flight mass spectrometric detection (TD-GC×GC-ToF-MS). Results indicated that PAH emission factors differed significantly for the different modes of engine operation with the highest emission factor being for idle mode with a total PAH emission factor of 1181.14 µg/kg. Under real-world conditions, it is expected that further variance in emission factors will be introduced as a result of brake and tyre wear, different engine technologies, engine age and maintenance, as well as fuel quality and measurement methods.

1. Introduction

Air pollution emissions from mobile sources need to be monitored to evaluate the efficiency of regulatory measures, maintain accurate emission inventories and also to assess the potential impact that transportation has on human and environmental health. Diesel exhaust emissions (DEE), in particular, have been classified as being carcinogenic based on comprehensive laboratory experimental findings and epidemiological studies that have reported strong associations between vehicle emissions and adverse health impacts (Kim et al., 2013; Rengarajan et al., 2015; Samet et al., 2000; Shen et al., 2014, US EPA, 2004, 2014). Notably, the International Agency for Research on Cancer (IARC) has established that diesel emissions may induce lung cancer and be associated with an increased risk of bladder cancer (IARC 2012).

DEE comprises of a complex mixture of compounds and its composition is dependent on various parameters such as engine technology, fuel type, temperature, humidity, mode of engine operation and maintenance (Weitekamp et al., 2020). The gaseous fraction of DEE consists

of carbon monoxide, carbon dioxide, nitrogen oxides, sulphur oxides, and volatile organic compounds. The particulate fraction includes elemental and organic carbon (EC and OC), sulphates, and metals. As a result, diesel combustion emissions contribute to ambient particulate and gaseous air pollutant levels, including those of polycyclic aromatic hydrocarbons (PAHs) (Ono-Ogasawara and Smith, 2004).

PAHs are semi-volatile organic compounds that can be distributed over both fractions of the exhaust, depending on operating and environmental conditions (Vione et al., 2004). Some PAHs have been found to be toxic and even carcinogenic to humans, and therefore their regulation and quantification in each phase is crucial (Rohr and Wyzga, 2012 (Reşitoğlu et al. 2015)). The United States Environmental Protection Agency (US EPA) has identified 16 priority PAHs as illustrated in Table 1 and the World Health Organization (WHO) added 17 additional PAHs to make a total of 33 PAHs under its regulation (Poster et al., 2006, WHO, 2014). The different sources of PAHs in diesel vehicle exhaust include unburned fuel, lubricating oil and pyrosynthesis from lower molecular weight aromatics originating from the fuel (Rhead and Pemberton,

* Corresponding author.

E-mail address: patricia.forbes@up.ac.za (P.B.C. Forbes).

<https://doi.org/10.1016/j.aeoa.2022.100158>

Received 6 July 2021; Received in revised form 17 January 2022; Accepted 7 February 2022

Available online 9 February 2022

2590-1621/© 2022 The Authors.

Published by Elsevier Ltd.

This is an open access article under the CC BY-NC-ND license

(<http://creativecommons.org/licenses/by-nc-nd/4.0/>).

Table 1

Sixteen US EPA priority PAHs and their corresponding abbreviations, molar masses and boiling points (PubChem database, Available at <https://pubchem.ncbi.nlm.nih.gov/compound>).

| | Formula | PAH Name | Abbreviation | Molar Mass (g/mol) | Boiling point (°C) |
|----|---------------------------------|------------------------|--------------|--------------------|--------------------|
| 1 | C ₁₀ H ₈ | Naphthalene | Nap | 128 | 218 |
| 2 | C ₁₂ H ₈ | Acenaphthylene | Acy | 152 | 265 |
| 3 | C ₁₂ H ₁₀ | Acenaphthene | Ace | 154 | 278 |
| 4 | C ₁₃ H ₁₀ | Fluorene | Flu | 166 | 295 |
| 5 | C ₁₄ H ₁₀ | Phenanthrene | Phe | 178 | 339 |
| 6 | C ₁₄ H ₁₀ | Anthracene | Ant | 178 | 340 |
| 7 | C ₁₆ H ₁₀ | Fluoranthene | FluAn | 202 | 375 |
| 8 | C ₁₆ H ₁₀ | Pyrene | Pyr | 202 | 360 |
| 9 | C ₁₈ H ₁₂ | Benz[a]anthracene | BaA | 228 | 435 |
| 10 | C ₁₈ H ₁₂ | Chrysene | Chy | 228 | 448 |
| 11 | C ₂₀ H ₁₂ | Benzo[b]fluoranthene | BbF | 252 | 481 |
| 12 | C ₂₀ H ₁₂ | Benzo[k]fluoranthene | BkF | 252 | 481 |
| 13 | C ₂₀ H ₁₂ | Benzo[a]pyrene | BaP | 252 | 495 |
| 14 | C ₂₂ H ₁₂ | Benzo[ghi]perylene | BghiP | 276 | 536 |
| 15 | C ₂₂ H ₁₂ | Indeno[1,2,3-cd]pyrene | I123P | 276 | 536 |
| 16 | C ₂₂ H ₁₄ | Dibenz[ah]anthracene | DbahA | 278 | 524 |

1996). PAHs in unburned diesel fuel have been shown to be the primary contributor of lighter 2–3 ringed PAHs in diesel exhaust. For example, 24% of naphthalene in the exhaust was found to be sourced from naphthalene in the fuel that survived combustion (Marr et al., 1999). It was also concluded that the presence of higher molecular weight PAHs in diesel exhaust, not present in the fuel, originate from other sources such as lubricating oil or pyrosynthesis (Marr et al., 1999).

Vehicle emission factors (EFs) are functional relationships that predict the quantity of an emitted pollutant as a function of the activity causing the emission (Phuleria et al., 2006; Riccio et al., 2016). EFs are significantly influenced by factors such as vehicle type; engine age and maintenance; fuel type and composition, as well as driver behaviour and travel speed. Poor fuel quality, aging vehicle fleet, and lack of road-worthy emission tests and operational maintenance are the reasons for the lack of standard compliance and for higher than normal transport emissions in developing countries (Ayeter et al., 2021). It is for this reason that there continues to be a need to characterize the potential health risks from older engines which are prevalent in developing countries, and it is also vital assess health and environmental effects associated with exposure to diesel exhaust as a whole (Weitekamp et al., 2020).

EFs have been measured using a number of different methods, including vehicle chassis dynamometer studies (Yanowitz et al., 1999; Kostenidou et al., 2021), remote sensing (Burgard et al., 2003; Guo et al., 2007; Schifter et al., 2003; Zhang et al., 1995), twin-site experiments (Gietl et al., 2010; Oliveira et al., 2010; Pey et al., 2010), roadway tunnel studies (Phuleria et al., 2006; Kristensson et al., 2004; Handler et al., 2008; Mancilla and Mendoza, 2012; Weingartner et al., 1997; Abu-Alaban et al., 2002; Wang et al., 2021) and on-road chase experiments (Wang et al., 2011) each of which have their advantages and limitations which are comprehensively reviewed by Vicente Franco et al. (2013).

Riccio et al. determined PAH emission factors from an urban tunnel experiment in Naples, Italy whereby they placed two mobile measuring stations at the entrance and exit of the tunnel and took PM₁₀ samples every hour onto 47 mm borosilicate glass filters (Riccio et al., 2016). The authors found PAH concentrations as high as 1450 ng/m³, with benzo(a)pyrene having an EF of 2.7 µg/km, which was three times higher than expected based on other studies. Lower molecular weight PAHs, i.e., 3-ring PAHs, were abundant at both the tunnel entrance and exit, while

the most prevalent PAHs were the 4-ring pyrene and benzo(a)anthracene and the 6-ring dibenzopyrenes (Riccio et al., 2016).

Tunnel measurements of PAHs lack resolution on individual vehicle contributions as they represent the overall vehicle fleet emissions in a specific tunnel and sources are not limited to exhaust emissions alone but also include emissions from other sources such as grassland fires, domestic fires and industry emissions. Additionally, transient ambient tunnel sampling methods only cover limited traffic circumstances and are influenced by changes in the local meteorological and environmental conditions and the results may not be generally applicable to open roadways (Ning et al., 2008). Another consideration to be made in tunnel EF studies is that the sampled air mass may be fresh or aged, or a mixture of the two, which will impact the speciation of pollutants (Forbes et al., 2013).

Zheng et al. (2017) employed a portable emissions measurement system (PEMS) to collect real-world particle samples from diesel vehicles in China. DPM samples were collected onto 47 mm quartz fiber filters with a cyclone filter impactor with inlet flow rate of 5 L/min. Fourteen in-use heavy-duty diesel vehicles were employed in the study to measure the species-resolved particulate PAH emissions under real-world driving conditions and 15 priority PAHs were characterized by gas chromatography-mass spectrometry (GC-MS). The authors found that 3 and 4-ring PAHs accounted for 95% of the total measured particulate PAH emission factors for all vehicles. They also noted that the average particulate emission factor of 15 PAHs for electronically controlled fuel injection engines was 187 ± 80 µg/kg which was a 76% reduction when compared to 782 ± 378 µg/kg for mechanical pump fuel injection engines, which clearly indicated the influence that engine technology has on emission factors (Zheng et al., 2017).

For a study to determine EFs to be effective and accurate, it should be performed under realistic driving conditions where the inputs from other sources are minimized. Modern dynamometers can realistically vary load on the vehicle or engine to simulate real world driving and can produce realistic brake wear when driven through a transient driving cycle, however a limitation of this type of study is that a controlled laboratory environment will never fully represent real-world driving conditions (Cocker et al., 2004; Zheng et al., 2016). Another consideration is that dynamometer studies cannot fully replicate other inevitable non-exhaust emissions such as those from the wear of brake linings, tyre wear and re-suspended road dust, all of which will contribute to roadside emissions (Abu-Alaban et al., 2003; Allen et al., 2001; Morawska and Zhang, 2002).

In a recent study, PM emitted from diesel vehicles operated under different driving conditions on a chassis dynamometer revealed that the emissions were dominated by the organic carbon fraction whereby the PAH analysis results revealed that 4 and 5-ring PAHs were the most prevalent (Wang et al., 2021). The sum of particulate PAH EFs ranged widely from 0.41 to 18.60 mg/kg for the different vehicles tested in the study, of which most of were Euro 4 and 5 compliant (Wang et al., 2021).

In a comprehensive review of literature, whereby exposure to both filtered and whole diesel exhaust was considered, it was found that the gas fraction of diesel exhaust plays a significant role when considering health-related endpoints (Weitekamp et al., 2020). The numerous studies cited in this article, and others found in the literature, have primarily paid attention to the toxicity of particulate matter and soot emissions, but it has been found that many PAHs are emitted predominantly in the gas phase (Geldenhuys, 2014; Geldenhuys et al., 2015). The methods cited in literature use sampling methods that require larger sampling volumes and extended sampling times to accurately quantify trace level of PAHs in ambient air, after which a highly sensitive analytical system must be employed after complicated and time consuming pre-treatment and analyte concentration procedures (Pandey et al., 2011). All of the aforementioned sampling strategies introduce unwanted sampling artefacts and increase the risk of analyte breakthrough and blow off resulting in vital PAH partitioning

information being lost. It is for this reason that it is vital to overcome these sampling bottlenecks and include a simplified sampling method that is able to adopt low flow rates, short sampling intervals and simultaneous sampling of gas and particle phase PAHs in a manner in which their partitioning is unaffected by sampling conditions. Correspondingly, the aim of this study is to determine gas and particulate phase PAH emission factors from a light duty diesel engine, in a controlled test cell facility, which is operated at two different modes representative of different engine operating conditions. It is the first time that both gas and particle PAH EFs have been simultaneously determined for different engine operating modes using small portable denuder sampling devices that minimise sampling artefacts and avoid time consuming and environmentally unfriendly sample preparation techniques. These phase specific EF values will be useful in the calculation of more accurate emission inventories and can be used to guide air quality management plans as well as reduction and abatement strategies. Gas and particle phase PAH profiles and EFs at each of the modes tested are then compared to other reported studies using other measurement methods (such as tunnel and roadside samples) in order to assess the advantages and disadvantages of the adopted test measurement strategy and identify potential areas of further development.

2. Methodology

Controlled testing was carried out at the Sasol Fuels Application Centre in Cape Town, South Africa. Vehicle emissions were simulated and tested in a test cell equipped with a Euro 2 compliant, 1.6 L test engine, fitted with a close-coupled diesel oxidation catalyst (DOC). Diagnostic checks were carried out on the engine prior to testing to ensure performance was as per specification. It must be noted that poor fuel quality, an aging vehicle fleet, and lack of mandatory roadworthy emission tests are reasons which can contribute to the lack of standard compliance in developing countries in Africa (Ayeter et al., 2021). It is for this reason that a Euro 2 compliant engine was chosen to be representative of the average fleet in developing countries, and the emissions arising from this engine would have significance in, for example, South Africa where the Euro 2 Vehicle Emission Standard is adopted.

The test fuel contained less than 10 ppm sulphur and the test engine operation modes, dynamometer details and fuel specifications are listed in Tables 2–4 respectively. An electrical engine dynamometer was coupled to the test engine to simulate and control engine operation parameters, including speed, torque and throttle and all the testbed data as well as engine control module (ECM) parameters were logged by the test cell automation system at a frequency of 10 Hz. Fig. 1 shows a schematic of the test cell setup. Fuel consumption was measured using a mass flow meter employing a Coriolis mass flow sensor and fuel temperature conditioning unit (AVL models 735S and 753C, respectively).

The test engine was operated in 2 different operating modes as detailed in Table 2. These modes represent varying torque (power) conditions. M_A represents a vehicle idling whilst M_B represents a vehicle exerted to maximum power and speed i.e., driving uphill whilst pulling a load. The actual operating modes of vehicles on the road would fall within the range of these test modes, seeing that M_B is a severe operating mode, allowing for a predicted range of emissions to be estimated.

2.1. Test engine

The test engine was a 1.6 L engine which is used in light duty

Table 2
Test engine operation modes.

| | Dyno Speed (rev/min) | Brake Power (kW) | Dyno Torque (Nm) | Engine Throttle Position (%) | Fuel Mass Flow Rate (kg/h) | Intake Air Mass Flow (kg/h) | Exhaust Mass Flow Rate (kg/h) |
|-------|----------------------|------------------|------------------|------------------------------|----------------------------|-----------------------------|-------------------------------|
| M_A | 780 | 4.19 | 10 | 27.4 | 3.13 | 232 | 235 |
| M_B | 4000 | 78 | 187 | 100 | 18.4 | 399 | 417 |

Table 3
Test engine specifications.

| Parameter | Detail |
|---------------------------|--|
| Model year | 2010 |
| Cylinders | 4 |
| Capacity | 1,595 cm ³ |
| Compression ratio | 16.5 : 1 |
| Induction | Turbocharged with intercooler |
| Fuel System | Common rail direct injection using piezo injectors |
| Exhaust gas recirculation | Cooled exhaust gas recirculation (EGR) for NO _x control |
| Transmission | 5-speed manual |
| Max Power | 77 kW @ 4400 rpm |
| Max Torque | 250 Nm @ 1500–2500 rpm |
| Emission control | Close-coupled diesel oxidation catalyst (DOC) |
| Emission level | Euro 2 |
| CO ₂ emissions | 109 g/km |

Table 4
Test fuel specifications.

| Carcal RF-06-03 | |
|---|--------|
| Cetane number | 53.5 |
| Density at 15 °C (g/mL) | 0.8363 |
| Aromatics (% volume) | 26.9 |
| Flash point (°C) | 83 |
| Polycyclic aromatic hydrocarbons (% mass) | 5.0 |
| Viscosity at 40 °C (mm ² /s) | 2.75 |
| Sulphur (mg/kg) | 1.2 |
| Lubricity at 60 °C (µm) | 376 |
| Water content (mg/kg) | 70 |
| Carbon content (% mass) | 86.70 |
| Hydrogen content (% mass) | 13.30 |

passenger vehicles and it is Euro 2 emission level compliant. The engine was set up using a production standard engine Electronic Control Unit and exhaust system. The engine was fitted with a Diesel Oxidation Catalyst (DOC) which is typical for a Euro 2 emission level engine as used in vehicle fleets found in developing countries. Further details of the test engine are shown in Table 3.

2.2. Test fuel

For the test cell experiments, an ultra-low sulphur (ULS) diesel fuel that contained less than 10 ppm sulphur was used during testing (Carcal RF 06–03). This certification test fuel was sourced from Europe, and is EN590 compliant. The specifications of the test fuel are presented in Table 4.

2.3. Laboratory analytical equipment

Undiluted exhaust gas was sampled using a Horiba MEXA series 7000 exhaust gas analyser to measure concentrations of NO_x (nitrogen oxides), CO (carbon monoxide), THC (total hydrocarbons), and CO₂ (carbon dioxide). Real-time measurements of soot concentration in the undiluted exhaust were performed by means of a photo-acoustic soot sensor (AVL483 Micro Soot Sensor). Soot measured in this way corresponds to the insoluble or non-volatile portion of the particulate matter (primarily elemental carbon). DPM emissions are typically expressed in grams of particulate matter per unit of mechanical energy delivered by the engine, such as g/kWh. This approach normalises DPM with

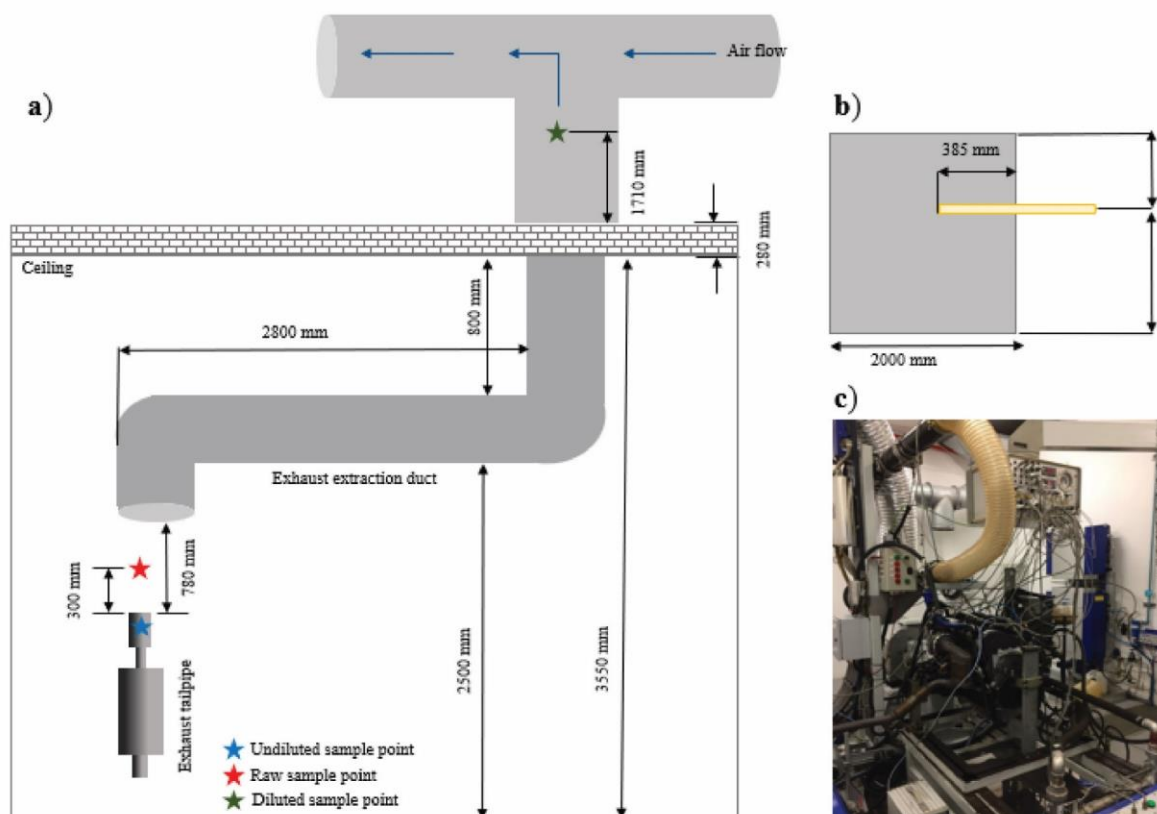


Fig. 1. (a) Schematic of test cell setup indicating the undiluted, raw and diluted sample positions, (b) cross section of diluted sample position in the exhaust duct and (c) a photograph of the test cell setup.

mechanical energy and thus removes any variability between tests introduced by variable exhaust flow rates or engine power differences. No correction for thermophoretic or diffusional losses has been applied to the measured results. These instruments for the measurement of exhaust emissions are done according to international standard methods. The humidity and ambient pressure in the test cell were determined with a Kestrel portable weather station.

On-line instruments sample undiluted exhaust gas from the inside of the tailpipe. In addition, a sampling point was positioned at a distance of 0.3 m away from the tailpipe exit. This optimum distance of 0.3 m was determined by measuring the soot and gas emissions at different distances from the tailpipe outlet in order to balance variability in dilution ratio while satisfying the concentration and temperature range of the sampling devices. The samplers that were positioned 0.3 m away from the tailpipe outlet, were named “Raw” as opposed to the measurements that were taken directly in the tailpipe to measure undiluted exhaust emissions which were named “Undiluted”.

A select number of measurements were taken in the exhaust extraction duct of the facility. The raw exhaust passed into the exhaust extraction duct before it was emitted to the outside atmosphere. The diluted measurements were taken directly in the exhaust duct with minimal adjustments and they represent a more aged and equilibrated air mass (Fig. 1). Samples were taken after ~4 min equilibration in each mode. A background air sample was also taken from the inlet air that was supplied to the test cell after it had passed through fabric filters. The position of the sample was approximately 0.3 m inside the inlet ducting.

2.4. Sampling methodology

PAH sampling was performed at two positions during each mode: 1) On a stand parallel to exhaust flow at a distance of 0.3 m from the tailpipe exit, denoted “Raw”, and 2) On a probe in the exhaust extraction duct perpendicular to air flow denoted “Diluted”.

Particle and gas phase PAH sampling was performed using multi-channel silicone rubber trap denuders (Fig. 2). The PAH samples were collected at a flow rate of 500 mL/min for 10 min, using Gilair Plus personal sampling pumps (Sensidyne), to obtain a final sampling volume of 5 L.

The denuder consisted of two multi-channel silicone rubber traps (each trap: 178 mm long glass tube, 6 mm o.d., 4 mm i.d.) each containing 22 parallel PDMS tubes (55 mm long, 0.3 mm i.d., 0.6 mm o.d.) separated by a 6 mm diameter quartz fibre filter (QFF), held in position by a Teflon connector. This configuration allows for both gas and particulate phase sampling (Forbes et al., 2012; Forbes and Rohwer, 2009, 2015; Munyeza et al., 2019). In the denuder, the gas phase SVOCs are trapped by the first (primary) trap as the polydimethylsiloxane serves as a solvent for these compounds, and the particles are trapped downstream on the quartz fiber filter. The post filter trap (secondary trap) collects any PAHs that break through from the primary trap or have blown off from the filter. Fig. 2 illustrates the sampler setup.

2.5. Instrumental analysis

Offline analysis of the denuders was performed by means of a LECO Pegasus 4D GCxGC-ToFMS instrument (LECO, St. Joseph, MI, USA) that was equipped with an Agilent Technologies 7890 GC (Palo Alto, CA, USA), a quad jet dual-stage modulator and a secondary oven. Data acquisition and processing was executed by ChromaTOF software version 4.0 (LECO Corp., St. Joseph, MI). A Gerstel 3 Thermal Desorption System (TDS) was employed for sample introduction. Synthetic air was used for the hot jets and liquid nitrogen (LN₂) was used to cool nitrogen gas for the cold jets with an AMI Model 186 liquid level controller to maintain sufficient levels. The GC column set consisted of a Restek Rxi-1MS nonpolar phase 100% dimethyl polysiloxane; (30 m, 0.25 mm i.d., 0.25 μm df) as the first dimension (1D) and a Rxi-17Sil MS, midpolar 5% phenyl 95% methylsiloxane (0.79 m, 0.25 mm i.d., 0.25

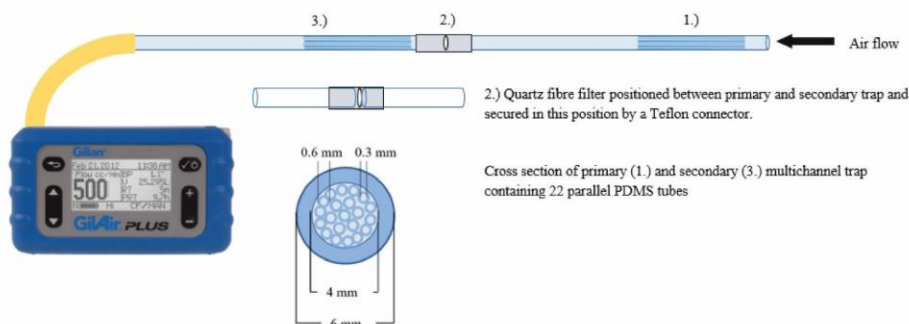


Fig. 2. Schematic of multi-channel trap denuder sampling devices used for PAH sampling.

$\mu\text{m df}$) as the second dimension (2D). Thermal desorption was carried out from 30 °C to 280 °C at 60 °C/min and held for 5 min after which the analytes were cryogenically focused via a cooled injection system (CIS) at –50 °C using liquid nitrogen. The temperature was ramped at 12 °C/s to 280 °C and the inlet purge time was 3 min. The desorption flow rate was 100 mL/min and the TDS transfer line was at 280 °C. The primary oven was ramped at 10 °C/min from 40 °C to 315 °C which was held for 5 min. The secondary oven was offset by +5 °C and the modulator temperature was offset by 30 °C. The modulation period was 4 s with a hot pulse time of 1 s. The MS transfer line temperature was set to 280 °C and mass acquisition ranged from 50 to 500 Da at 100 spectra/s. The electron energy was 70 eV and the ion source temperature was 200 °C.

2.6. Matrix matched calibration standards

Calibration was performed by using a certified standard PAH mix solution (Supelco, St Louis, MO), containing 15 priority PAHs (Table 1 with the exception of benzo[k]fluoranthene). The nominal concentration of each compound in the mixture dissolved in methylene chloride was 2000 $\mu\text{g/mL}$. The names and abbreviations of the PAHs included are given in Table 1. Stock solutions at a concentration of 100 $\mu\text{g/mL}$ were prepared in toluene and working solutions were prepared by appropriate dilutions of the stock solutions before use. All solvents used for standard preparation and cleaning of syringes, traps and filters, were of analytical grade (99% purity) including toluene, DCM and n-hexane which were purchased from Sigma Aldrich. Acetone was obtained from Associated Chemical Enterprises, (ACE South Africa). Deuterated internal standards (I_{Std}), d8-naphthalene, d10-phenanthrene, d10-pyrene and d12-chrysene were obtained from Isotec Inc (Sigma Aldrich, Bellefonte, USA) and used in all standards and samples.

Calibration curves were generated in order to quantify gas and particle phase PAHs. For gas phase PAHs, quantification was achieved by analysing individual conditioned PDMS traps that were spiked with 1 μL of the following concentrations of mixed PAH standard in toluene: 1.0, 2.0, 5.0, 10.0 and 15.0 $\text{ng}/\mu\text{L}$. Similarly, to quantify particle bound PAHs, clean 35 mm QFF punches were spiked with 1 μL of 0.5, 1.0, 2.0, 3.0, 5.0 and 10 $\text{ng}/\mu\text{L}$ mixed PAH standards in toluene. The I_{Std} mixture, containing d8-naphthalene, d10-phenanthrene, d10-pyrene and d12-chrysene (1 $\text{ng}/\mu\text{L}$), was spiked onto all samples prior to analysis and calibration curves were derived using the area ratio of target analyte: I_{Std} . The I_{Std} correction accounted for any instrument variability or matrix effects. Linear regression analyses were performed after blank correction, using the Data Analysis Toolkit in Excel. The limit of detection (LOD) of each target compound was calculated as a response at three times the signal to noise (S/N) ratio and the limit of quantitation (LOQ) as ten times the S/N ratio.

2.7. Test cell measurements

Temperature and air flow within the test cell were monitored via online sensors. Air flow was measured using a thermal mass flow sensor

(ABB Sensyflow) connected to the engine air intake and the exhaust flow rate was calculated on the basis of the conservation of mass, by adding the intake air and fuel mass flow rates together. The temperature sensors included a wall mounted sensor for an overall test cell temperature, a sensor at the intake filter of the engine and a sensor in the exhaust stream at the sample point 0.3 m away from the tailpipe (raw sample point). Fig. 3 depicts the temperature as a function of varying engine power. The humidity in the test cell was 46% and the ambient pressure was 1021 Pa.

The distance of 0.3 m from the tailpipe was selected as it was close enough to the source for stable engine readings based on monitored CO_2 and NO_x emission dilution factors (less variability as depicted in Fig. 4) and was far enough from the tailpipe for sampling devices to withstand elevated temperatures from the exhaust. The temperature at the sampling point (inlet of denuder) ranged from 46 °C at 50% load to 53 °C after running for a short while at maximum load, which later increased to 210 °C. Fig. 4 depicts the decreasing engine variability at distances from –0.1 m (penetrating the tailpipe) to 0.5 m from the tailpipe for CO_2 and NO_x emissions.

Fig. 5 shows the emission of common pollutants as a function of engine power. It is clearly visible for each pollutant, that the engine operation mode significantly influences the concentration of pollutants emitted which are largely governed by the high temperatures and pressures of the combustion process as well as the air-to-fuel ratio, which varies due to the lean-burning nature of diesel engines. Total hydrocarbons are found in highest concentration in idle mode which is characterized by oxygen rich conditions and the lowest at the maximum power mode. The opposite trend was seen for soot emissions where concentrations were elevated to approximately 44 mg/m^3 during maximum power mode which can be attributed to the increase in temperature and oxygen deficient conditions. The NO_x emissions reveal a similar progressive increase in emissions as the engine torque is increased as this causes an increase in temperature which increases NO formation kinetics (Eiguren-Fernandez and Miguel, 2012). CO_2 emissions increase purely as a function of the amount of fuel burned and

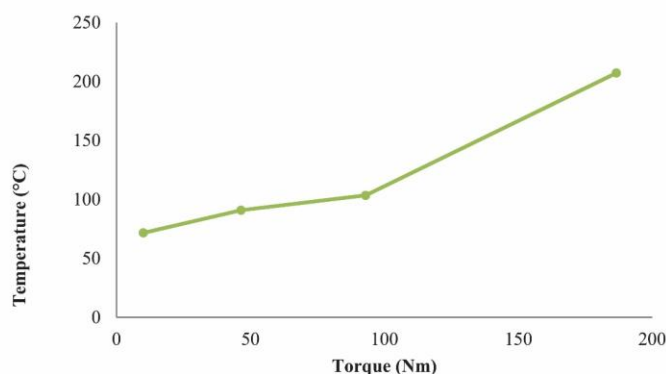


Fig. 3. Torque measurements as a function of temperature.

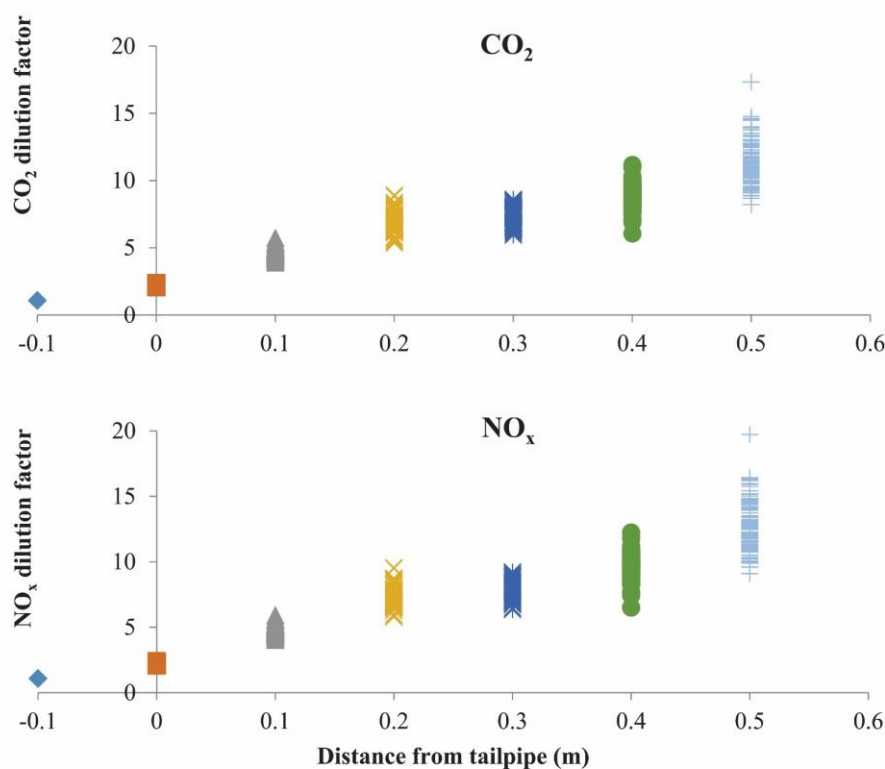


Fig. 4. Variation in engine emission dilution factors as a function of sampling distance from the tailpipe outlet.

since the engine load is progressively increased, the amount of fuel burned and therefore CO_2 emitted also increases. In Section 3.2 these results are correlated to PAH emissions to gain a better understanding of the concentrations emitted and the phase partitioning thereof.

3. Results and discussion

3.1. Calibration results

Table 5 represents the 10 out of 15 priority PAHs that were detected in the gas and particle phase samples with their abbreviations. The R^2 values show good linearity but were affected by variation in TD efficiency.

Table 6 shows the limits of detection and quantitation for PAHs on the multi-channel PDMS traps (gas phase PAHs) and on quartz fibre filter (particulate phase PAHs). The LOD and LOQ are given in pg on trap as well as ng/m^3 based on a sample volume of 5 L. The limit of detection (LOD) of each target compound was calculated as three times the signal to noise (S/N) ratio and the limit of quantitation (LOQ) as ten times the S/N ratio. These values were found to have similar orders of magnitude to the values reported in another study that saw the application of the denuder devices in an underground platinum mine (Geldenhuys et al., 2015). The limit of detection for the gas phase PAHs range from $0.3 \text{ ng}/\text{m}^3$ for 2 ringed naphthalene to $79.3 \text{ ng}/\text{m}^3$ for 6-ring benzo(ghi)perylene. The LOD for the particulate bound PAHs ranged from $0.3 \text{ ng}/\text{m}^3$ for naphthalene to $18.5 \text{ ng}/\text{m}^3$ for dibenz(a,h)anthracene.

3.2. Total gas and particulate PAH concentrations

Total PAH emissions from the raw exhaust were 6.3 and $33.9 \text{ } \mu\text{g}/\text{m}^3$ for M_A (idle mode) Raw and M_B (max power mode) Raw, respectively and 0.2 and $21.7 \text{ } \mu\text{g}/\text{m}^3$ for the dilute samples as seen in Table 7. From Fig. 6 it can be seen that PAHs were predominantly found in the gas phase (80–100% in the raw exhaust stream as well as in the dilute (aged)

samples). There were no ambient PAHs detected in the background samples.

The raw M_A sample showed that over 90% of PAHs were detected on the primary trap and only 10% on the secondary trap, with no particulate PAHs, whilst the diluted sample revealed that $0.25 \text{ } \mu\text{g}/\text{m}^3$ of PAHs were detected solely on the primary trap. The raw M_B sample showed gas and particulate PAHs which is consistent with denuder theory in which the primary PDMS trap acted as a solvent for the gas phase analytes and analytes that were associated with particles passed through the trap and were collected on the downstream filter and either remained on the filter or subsequently experienced blow off and were then trapped on the secondary trap. Blow off (or loss by volatilization) is a well-documented phenomenon, whereby loss of particle phase analyte is caused by the pressure (and temperature) gradient existing through the filter (Kumari and Lakhani 2018). The loss due to blow off is expected to be minimal due to low sampling flow rates and sampling times, however it can still occur and should be taken into account via the use of a second trap in this case. In addition, the low back pressure across the denuder sampling device throughout this sampling interval reduced the potential for such effects to occur.

M_B showed much higher PAH concentration than the idle M_A which is expected as the engine was under load (full throttle and full torque). The raw sample showed higher concentrations of PAHs on the secondary trap than the primary trap which is due to blow off from the filter and PAHs that are transiently associated with particles when exiting the exhaust since there is not sufficient time to equilibrate. The gas/particle partitioning of PAHs is complex and is also further influenced by the high temperatures of the exerted engine in M_B , which perturbs the equilibration between phases.

Particulate emissions were the highest for M_B which correlated to the highest soot and carbon dioxide emissions in the test cell measurements (Fig. 5) which suggests that soot measurements may be used as a proxy to estimate particulate PAHs levels in diesel emissions. During sampling for M_B , less than 1 L of raw emissions were sampled due to pump failure

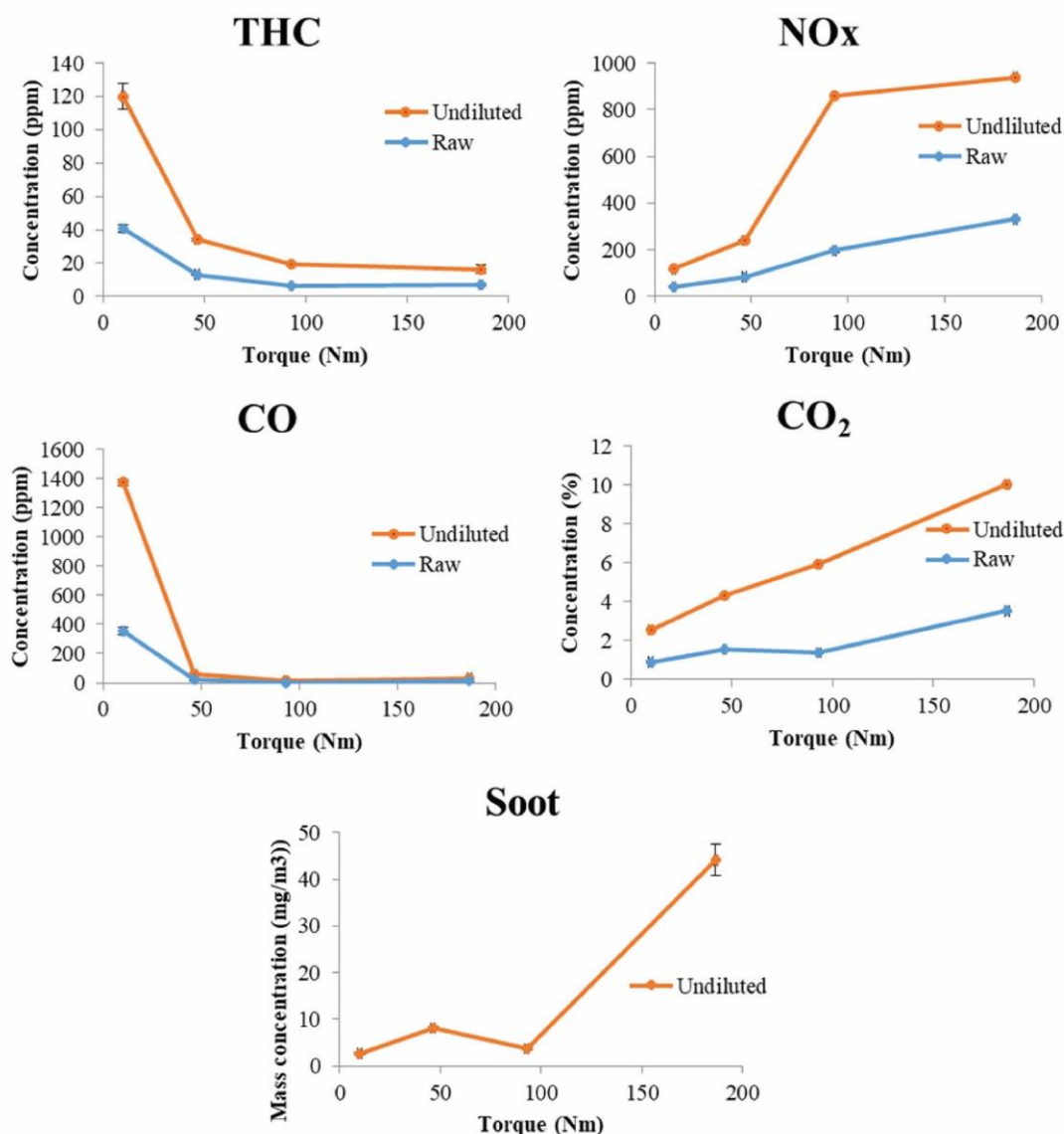


Fig. 5. Concentration of emitted pollutants as a function of engine power.

Table 5

Detected PAH abbreviations and coefficients of variation for trap and filter calibration curves.

| PAH | Abbr. | m/z | Trap | Filter |
|-------------------------|-------|-----|----------------|----------------|
| | | | R ² | R ² |
| <i>Naphthalene-d8</i> | IS | 136 | | |
| Naphthalene | Nap | 128 | 0.9349 | 0.9321 |
| Acenaphthylene | Acy | 152 | 0.9998 | 0.9056 |
| Acenaphthene | Ace | 154 | 0.9864 | 0.9255 |
| <i>Phenanthrene-d10</i> | IS | 188 | | |
| Fluorene | Flu | 166 | 0.9874 | 0.9677 |
| Phenanthrene | Phe | 178 | 0.9854 | 0.9224 |
| Anthracene | Ant | 178 | 0.9410 | 0.9583 |
| Fluoranthene | FluAn | 202 | 0.9252 | 0.9883 |
| Pyrene | Pyr | 202 | 0.9607 | 0.9777 |
| Benz(a)anthracene | BaA | 228 | 0.8284 | 0.9430 |
| Benzo(a)pyrene | BaP | 252 | 0.9419 | 0.9734 |

at high PM loading and possibly also due to the high temperature of 210 °C at the sampling point, this was however corrected for as exact sampling volumes were used to calculate the concentration per m³.

The dilution effects were more evident in M_A, with a significant

difference between the raw and dilute samples. The dilution factors for M_A and M_B, based on total PAH concentrations, were found to be 22.4 and 0.8 respectively. The formation of PAH derivatives in post emission reactions as well as equilibration and particle losses due to impaction along the exhaust extraction ducting can be contributing factors to the noted dilution effects when comparing raw and dilute samples. The post emission reactions would include the formation of alkylated and oxygenated PAHs as well as nitrated PAHs due to the presence of NO_x emissions from the diesel engine. These profiles are reported to be dominated by nitro-naphthalene, 1-nitropyrene and 9-nitroanthracene (Correa et al., 2021; Huang et al., 2015; Kostenidou et al., 2021). The PAH derivative compounds were not quantified in this study although formation of these compounds during dilution and aging would result in lower concentrations of parent PAHs. The particulate PAHs in M_B were 6.36 and 6.19 µg/m³ for the raw and dilute sample respectively which shows that there was only a small amount of particulate loss which is likely due to impaction in the exhaust ducting. The secondary trap PAH concentration for the raw M_B (15.7 µg/m³) sample is comparable to the primary trap PAH concentration in the M_B dilute sample (14.8 µg/m³) which is consistent with the theory that PAHs are transiently associated with particles in the raw exhaust stream and consequently pass through the primary trap. Once these emissions are aged, or have had sufficient

Table 6
LOD and LOQ values for PAHs in gas phase (top) and particulate phase (bottom).

| PAH (trap) | pg (trap) | | Calculated air sample (ng/m ³) | |
|--------------|-----------|--------|--|-------|
| | LOD | LOQ | LOD | LOQ |
| Nap | 1.4 | 4.8 | 0.3 | 1.0 |
| Acy | 3.3 | 11.1 | 0.7 | 2.2 |
| Ace | 2.8 | 9.3 | 0.6 | 1.9 |
| Flu | 5.1 | 16.9 | 1.0 | 3.4 |
| Phe | 8.8 | 29.3 | 1.8 | 5.9 |
| Ant | 5.5 | 18.4 | 1.1 | 3.7 |
| Pyr | 11.1 | 36.8 | 2.2 | 7.4 |
| FluAn | 11.1 | 36.9 | 2.2 | 7.4 |
| BaA | 53.8 | 179.3 | 10.8 | 35.9 |
| Chy | 51.8 | 172.6 | 10.4 | 34.5 |
| BbF | 76.3 | 254.3 | 15.3 | 50.9 |
| BaP | 160.2 | 534.1 | 32.0 | 106.8 |
| IcdP | 255.2 | 850.6 | 51.0 | 170.1 |
| BghiP | 396.6 | 1322.1 | 79.3 | 264.4 |
| DahA | 243.2 | 810.6 | 48.6 | 162.1 |
| PAH (filter) | pg (QFF) | | Calculated air sample (ng/m ³) | |
| | LOD | LOQ | LOD | LOQ |
| Nap | 1.7 | 5.7 | 0.3 | 1.1 |
| Acy | 2.3 | 7.5 | 0.5 | 1.5 |
| Ace | 5.7 | 18.9 | 1.1 | 3.8 |
| Flu | 2.5 | 8.2 | 0.5 | 1.6 |
| Phe | 3.0 | 9.9 | 0.6 | 2.0 |
| Ant | 2.2 | 7.2 | 0.4 | 1.4 |
| Pyr | 1.5 | 5.1 | 0.3 | 1.0 |
| FluAn | 1.3 | 4.3 | 0.3 | 0.9 |
| BaA | 7.4 | 24.8 | 1.5 | 5.0 |
| Chy | 5.8 | 19.2 | 1.2 | 3.8 |
| BbF | 13.1 | 43.6 | 2.6 | 8.7 |
| BaP | 38.8 | 129.4 | 7.8 | 25.9 |
| IcdP | 71.9 | 239.8 | 14.4 | 48.0 |
| BghiP | 69.6 | 232.0 | 13.9 | 46.4 |
| DahA | 92.6 | 308.7 | 18.5 | 61.7 |

time to equilibrate, the PAHs partition from the particulate phase into the more favorable gas phase especially for low molecular weight PAHs, which is then collected on the secondary trap of the raw stream sample and then downwind on the primary trap in the exhaust extraction ducting, respectively.

3.3. PAH profiles

The PAH profiles for M_A and M_B differed significantly in terms of the number, type and concentration of PAHs for both gas and particulate phases. Naphthalene was found to be the most abundant PAH in the raw exhaust stream for both M_A and M_B with a total of 9 PAHs detected in M_A and only 4 in M_B.

Fig. 7 shows that PAHs emitted during idle mode, M_A, ranged from the lighter 2-ringed acenaphthylene to the heavier 4-ringed benzo(a)anthracene and pyrene which were present in the highest concentrations (excluding Nap), none of which were associated with particles.

For M_B (Fig. 8) only lighter 2–3 ringed PAHs up to fluorene were found in the raw exhaust stream but phenanthrene, anthracene, fluoranthene and pyrene were found in the dilute sample stream which were partitioned between gas and particulate phases after mixing with air and having had time to condense and equilibrate. The presence of the lighter PAHs at higher concentrations in the M_B raw stream likely arose from unburnt diesel fuel as during this mode when the throttle is increased there is more fuel introduced into the engine than in idle mode and combustion occurs under more oxygen deficient conditions.

The PAHs emitted during maximum power were found to be predominantly on the filter and secondary trap indicating that they are associated with particles whereas the idle mode produced predominantly gas phase PAH emissions, which was consistent with the soot measurements as seen in Fig. 5 that showed the highest soot concentrations of approximately 44 mg/m³ during maximum power operation,

Table 7
Concentration of PAHs in raw and dilute exhaust streams in µg/m.³.

| | PAH | M _A Raw | M _B Raw | M _A Dil | M _B Dil | |
|----------------|-----------|--------------------|--------------------|--------------------|--------------------|------|
| Primary trap | Nap | 2.77 | 6.99 | 0.03 | 13.27 | |
| | Acy | 0.22 | 2.46 | ND | ND | |
| | Ace | 0.25 | ND | 0.22 | ND | |
| | Flu | 0.24 | 2.35 | ND | 0.21 | |
| | Phe | 0.30 | ND | ND | 0.26 | |
| | Ant | 0.17 | ND | ND | 0.60 | |
| | FluAn | 0.21 | ND | ND | ND | |
| | Pyr | 0.77 | ND | ND | 0.46 | |
| | BaA | 0.67 | ND | ND | ND | |
| | BaP | ND | ND | ND | ND | |
| | Sum | 5.59 | 11.80 | 0.25 | 14.81 | |
| | Filter | Nap | <DL | 6.36 | <DL | 4.99 |
| | | Acy | ND | ND | ND | ND |
| | | Ace | ND | ND | ND | ND |
| Flu | | ND | ND | ND | ND | |
| Phe | | ND | ND | ND | 0.25 | |
| Ant | | ND | ND | ND | 0.25 | |
| FluAn | | ND | ND | ND | ND | |
| Pyr | | ND | ND | ND | 0.70 | |
| BaA | | ND | ND | ND | ND | |
| BaP | | ND | ND | ND | ND | |
| Sum | | 0.00 | 6.36 | 0.00 | 6.19 | |
| Secondary trap | | Nap | <DL | 8.93 | <DL | 0.15 |
| | | Acy | 0.22 | 2.28 | ND | ND |
| | | Ace | 0.20 | 2.24 | ND | ND |
| | Flu | 0.27 | 2.28 | ND | ND | |
| | Phe | ND | ND | ND | 0.23 | |
| | Ant | ND | ND | ND | 0.12 | |
| | FluAn | ND | ND | ND | 0.03 | |
| | Pyr | ND | ND | ND | 0.17 | |
| | BaA | ND | ND | ND | ND | |
| | BaP | ND | ND | ND | ND | |
| | Sum | 0.69 | 15.72 | 0.00 | 0.70 | |
| | Total sum | 6.28 | 33.88 | 0.25 | 21.7 | |

implying an increased number of adsorption sites for PAHs and thus an increase in transient particle association. The opposite is seen during idle mode where the soot concentrations were negligible thus all PAHs were solely found in the gas phase and were collected on the primary trap.

The PAH profiles in this study were found to be consistent with that of other diesel engine emission studies reported in the literature. In a chassis dynamometer study where vehicle exhaust emissions were sampled under different driving cycles, it was reported that the sum of two-ring, three-ring and four-ring PAHs accounted for ~87% of the total gaseous PAH concentrations (Wei et al., 2015). Dandajeh et al. also reported that the most abundant exhaust PAHs, in a study investigating fuel ignition and injection, were found in the gas phase and consisted of predominantly 2 and 3-ring PAHs (Dandajeh et al., 2019). These findings were consistent with what was reported by other authors, as Hu et al. confirmed that PAHs in the gas phase dominated the total PAH (gas + particle phases) emissions for all the test vehicles in their investigation carried out using a chassis dynamometer under different driving cycles. The authors found that 99% of the 2-ring, 98% of the 3-ring, 97% of the 4-ring and 95% of the carcinogenic PAHs were all found in the gas phase after a diesel particle filter (DPF) which demonstrates the need for gas phase PAH characterisation and quantification (Hu et al., 2013).

3.4. PAH emission factors

Emission factors for M_A and M_B were calculated for each detected PAH in both gas and particulate phases as it was demonstrated in this study that over 80% of PAHs were found in the gas phase, even for the larger 4-ring PAHs.

Light duty vehicle EFs were determined directly from the engine dynamometer measurements using the equation below where the

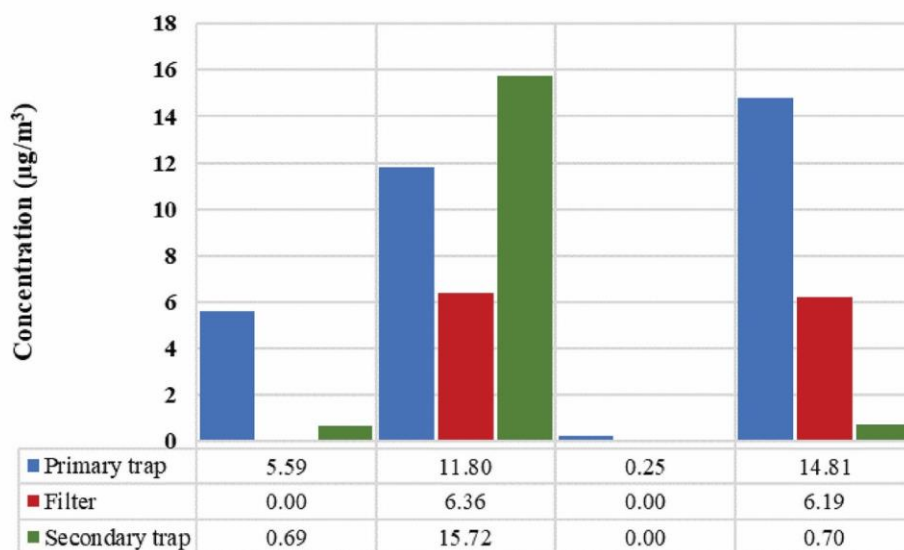


Fig. 6. Total gas and particulate PAH concentrations for raw and dilute samples.

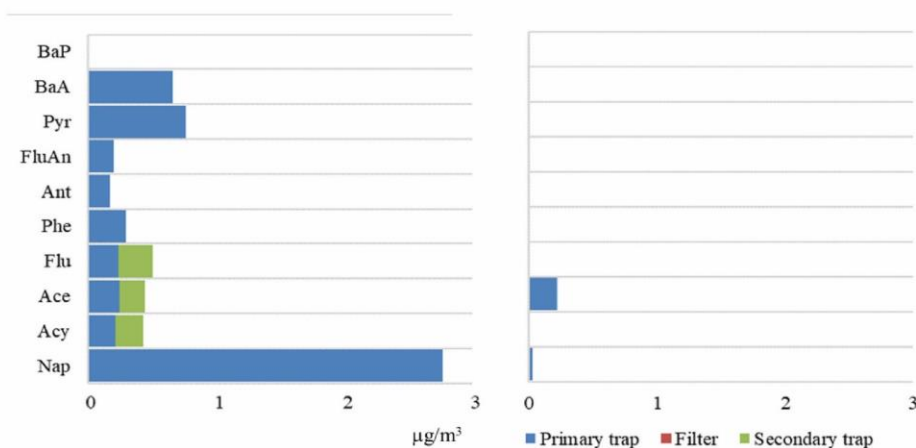


Fig. 7. Idle mode (M_A) PAH profiles for raw (left) and dilute (right) samples.

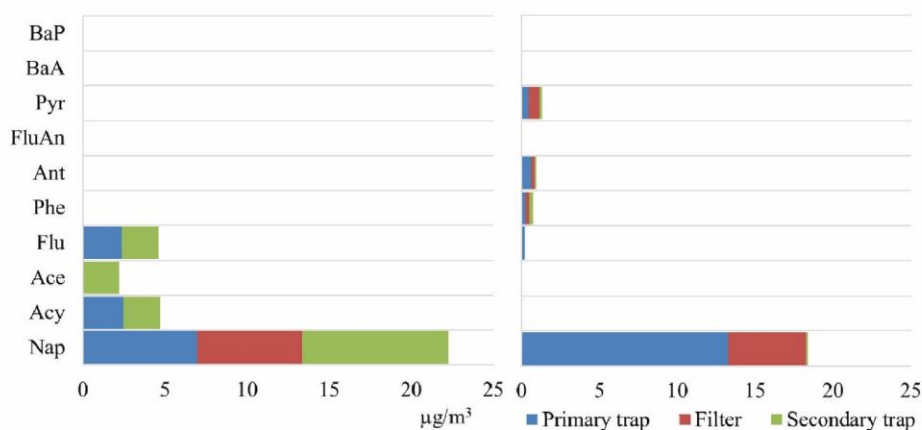


Fig. 8. Max power mode (M_B) PAH profiles for raw (left) and dilute (right) samples.

difference in $[CO_2]$ in the undiluted exhaust stream and the sampling point was used to determine the dilution ratio. The sampling points included dilute emissions in the exhaust duct where there was no in-line CO_2 monitor, therefore the conventional dilution ratio determination approach, using CO_2 as a tracer, could not be adopted. The total air flow

that was sampled was also accounted for after the sampling flow rate was taken into account. The sampling correction factor was introduced to correct for the total flow at the sampling point (i.e., what portion of the total air flow was sampled). Otherwise, it would imply that all of the PAHs derived from the fuel combusted were sampled.

Our EFs calculated in this way are noted as being indicative in nature due to the lack of a controlled dilution system for sampling.

Calculation of EFs

$$EF = \frac{[\text{PAH}] \cdot (\text{Dilution ratio}) \cdot (\text{Sampling time conversion factor})}{(\text{Ratio of total air sampled}) \cdot (\text{Fuel consumption})}$$

$$EF_{\text{PAH}} = \frac{[\text{PAH}] \cdot [\text{CO}_2 \text{ undiluted}] \cdot [\text{Sampling flow rate}] \cdot [\text{time conversion factor}]}{[\text{CO}_2 \text{ sampling point}] \cdot [\text{Total exhaust flow rate}] \cdot [\text{Fuel flow rate}]}$$

$$= EF \text{ (}\mu\text{g/kg)}$$

Where:

[PAH] = total mass of PAH (μg) on the trap or filter determined from the calibration curve

[CO₂ undiluted] = concentration (%) of CO₂ in undiluted exhaust

[CO₂ diluted] = concentration (%) of CO₂ at sampling point

Total exhaust flow rate = average total exhaust mass flow rate (kg/hr).

Sampling flow rate = sampling flow rate (0.5 L per min equates to 0.03 m³/h atmospheric sampling at 101,8 kPa and temperature at each mode was logged as:

Idle: 25.7 °C.

Max power: 207.2 °C).

Time factor = factor of 6 used to convert 10 min sampling time to 1 h.

Fuel flow rate = fuel consumption measured by Sasol automated system:

Idle: 0.300 kg/h.

Max power: 18.400 kg/h.

EF_{PAH} = the PAH emission factor (μg of PAH emitted per kg of fuel burned).

From Table 8 and previous results and discussion, it is evident that the mode of engine operation has a significant influence on the type and number of PAHs emitted. The idle mode resulted in a total PAH EF of 1181.14 $\mu\text{g/kg}$ which is significantly higher than the total PAH EF of 592.10 $\mu\text{g/kg}$ determined during maximum power mode. The vast differences in parameters between the two engine operational modes play a major role on the resultant EF i.e., the maximum power mode required

Table 8
Calculated emission factors for PAHs emitted per kg fuel burned during idle and maximum power mode.

| Idle mode | PAH | [$\mu\text{g}/\text{m}^3$] | EF ($\mu\text{g}/\text{kg}$) | | |
|----------------|---------|------------------------------|--------------------------------|--------------------------------|--------|
| 1° trap | Nap | 2.77 | 520.15 | | |
| | Acy | 0.22 | 41.31 | | |
| | Ace | 0.25 | 46.95 | | |
| | Flu | 0.24 | 45.07 | | |
| | Phe | 0.3 | 56.33 | | |
| | Ant | 0.17 | 31.92 | | |
| | FluAn | 0.21 | 39.43 | | |
| | Pyr | 0.77 | 144.59 | | |
| | BaA | 0.67 | 125.81 | | |
| | 2° trap | Nap | – | – | |
| Acy | | 0.22 | 41.31 | | |
| Ace | | 0.2 | 37.56 | | |
| Flu | | 0.27 | 50.70 | | |
| Total | | 6.29 | 1181.14 | | |
| Max power mode | | PAH | [$\mu\text{g}/\text{m}^3$] | EF ($\mu\text{g}/\text{kg}$) | |
| | | 1° trap | Nap | 6.99 | 122.02 |
| | | | Acy | 2.46 | 42.94 |
| | | | Flu | 2.35 | 41.02 |
| | | | Nap | 6.39 | 111.54 |
| | Filter | | Nap | 8.93 | 155.88 |
| | | | Acy | 2.28 | 39.80 |
| | | | Ace | 2.24 | 39.10 |
| | | | Flu | 2.28 | 39.80 |
| | | | Total | 33.92 | 592.10 |

over 60 times more fuel, which results in a lower EF.

3.5. Comparison to other studies

The EFs in this study were compared to the EFs obtained from other studies whereby on-road methodologies were used and only particulate emissions were measured. It must be noted that this study was a stationary test using one type of fuel whereas the other studies where on-road real time tests where the average of emissions from many vehicles were therefore measured. Whilst it is acknowledged that chassis-based study results would have yielded very useful comparisons, unfortunately other studies in literature, including those for chassis studies, use distance-based EF which are thus not directly comparable to the results generated in this study. Only reported studies reporting volume based EFs (i.e., with $\mu\text{g}/\text{kg}$ units) were thus included, as they allow for direct comparison.

A comprehensive comparison of the particle associated PAHs from diesel exhaust showed that EFs reported over the past several decades span up to 8 orders of magnitude (Hays et al., 2017). It is immediately evident from the EFs in Table 9 and from Fig. 9 that there are significant differences in reported emission factors from various studies which is likely due to the way the test was conducted as well as the factors influencing the emissions such as the type of fuel that was used. The sampling volumes used in each study are substantially different and it must be noted that larger sample volumes are needed to obtain concentrations above LOD values for particle phase samples. In this study a sampling volume of 5 L with a low sampling flow rate of 500 mL/min was applied whereas high flow rates of 450 L/min, 30–450 L/min, and 50 L/min were applied for several hours in the tunnel, freeway and on-road study, respectively (Marr et al., 1999; Phuleria et al., 2006; Ning et al., 2008).

Other authors found that 95% of the total measured particulate emission factors were as a result of 3 and 4-ring PAHs (Zheng et al., 2017), which was consistent with what was found in this study where all particulate PAHs were found to be the lower molecular weight moieties. It must be noted that 89% of EFs were accounted for from gas phase PAHs during idle mode and 35% during the max power mode, of which 3 and 4-ring PAHs were also predominant although heavier PAHs such as pyrene and benz(a)anthracene were detected.

Testing an individual vehicle in a controlled setting such as in this study, or even averaging over several vehicles, can lead to very different results than a tunnel study that includes an average over thousands of vehicles equipped with numerous engine types and burning different fuels, which must be taken into consideration. A chassis dynamometer study was conducted by Wei et al. whereby PAHs in vehicular exhaust were characterized and quantified whilst the engine was operated under different driving cycles including idle and acceleration mode, such as in this study. The authors confirmed that emissions are influenced by the mode of engine operation and found that the concentration of PAHs was the highest in acceleration tests, followed by deceleration and idle tests. The sum of 2–4 ring PAHs accounted for 87% of the total gaseous PAH concentration which was consistent with this study (Wei et al., 2015). When considering EFs from vehicles within different European classes, it was found that PAH emissions vary according to the Euro standard of the vehicle, with the oldest Euro standard displaying the highest emissions. In the case of diesel private cars, ΣPAHs EF was found to be 26.78 ± 10.85 mg km⁻¹ for Euro 1, 3.09 ± 3.26 mg km⁻¹ for EURO 2, and 1.29 ± 0.49 mg km⁻¹ for Euro 3 (Perrone et al., 2014). The higher EFs reported in this study can be expected as the engine employed is older in order to represent engines in operation in developing countries, and they are thus complaint to older European engine classes and standards (Liu et al., 2017).

What is evidently conclusive from this comparison is that the gas phase EFs, which are not considered in any other study, are comparable and in some cases higher than the particulate EFs especially for lower molecular weight PAHs. Fig. 9 reveals that the PAH EF profiles are

Table 9Comparison of PAH EFs (in $\mu\text{g}/\text{kg}$ fuel burned) obtained from various studies done on light duty vehicles (LDVs).

| PAH | This study (gas + particle) | | This study (particle) | | This study (gas) | | Tunnel study ^a (particle) | | Freeway ^b (particle) | | On road ^c (particle) | |
|-------|-----------------------------|----------------|-----------------------|----------------|------------------|----------------|--------------------------------------|--------|---------------------------------|-------|---------------------------------|-------|
| | M _A | M _B | M _A | M _B | M _A | M _B | Ultrafine | Accum. | CA-110 | I-710 | 1996a | 1997a |
| Nap | 520.15 | 389.44 | | 267.42 | 520.15 | 122.02 | | | | | | |
| Acy | 82.62 | 82.74 | 41.31 | 39.80 | 41.31 | 42.94 | | | | | | |
| Ace | 84.50 | 39.10 | 37.56 | 39.10 | 46.95 | | | | | | | |
| Flu | 95.77 | 80.82 | 50.70 | 39.80 | 45.07 | 41.02 | 2.39 | 0.37 | 2.86 | 16.29 | 8.00 | 10.30 |
| Phe | 56.33 | | | | 56.33 | | | | | | | |
| Ant | 31.92 | | | | 31.92 | | | | | | | |
| FluAn | 39.43 | | | | 39.43 | | | | | | | |
| Pyr | 144.59 | | | | 144.59 | | 3.63 | 0.55 | 3.30 | 23.21 | 9.00 | 13.8 |
| BaA | 125.81 | | | | 125.81 | | 4.11 | 0.43 | 0.43 | 12.24 | 4.80 | 8.80 |
| BaP | | | | | | | 5.08 | 0.34 | 0.40 | 3.52 | 6.40 | 8.30 |

^a Phuleria et al., (2006): EF attributable to LDVs in Ultrafine (particles with aerodynamic diameters (D_p) < 0.18 μm) and Accumulation Mode (D_p < 2.5 μm).

^b Ning et al., (2008): Freeway EFs in $\text{PM}_{2.5}$ samples collected from California State Highway (CA-110: only light-duty gasoline-powered vehicles) and the Long Beach Freeway (I-710: 80% light-duty gasoline-powered vehicles).

^c Marr et al., (1999) On-Road Emission Factors for Particle-Phase PAHs for light-duty vehicles ($\mu\text{g}/\text{kg}$) for 1996 (associated with particles <1.3 μm aerodynamic diameter ($\text{PM}_{1.3}$), not background-subtracted) and 1997 (Background-subtracted PAH associated with particles <2.5 μm aerodynamic diameter ($\text{PM}_{2.5}$)).

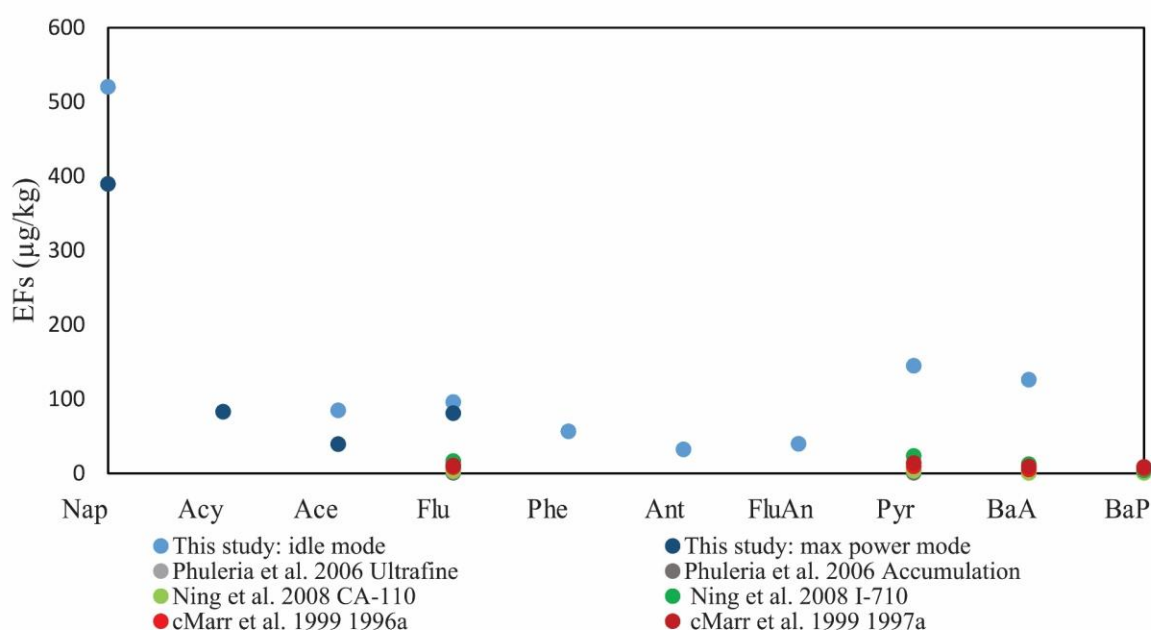


Fig. 9. Comparison of particulate PAH EFs (in $\mu\text{g}/\text{kg}$ fuel burned) obtained from various studies done on LDVs where this study represents a sum of gas and particle phase.

significantly different when the gas phase is considered whereas the profiles for all the other studies showed prevalence of heavier PAHs such as pyrene, benz(a)anthracene and benzo(a)pyrene. The fluorene EF was significantly higher in this study when compared to the tunnel study suggesting that fluorene exists in both phases.

A direct comparison is not possible due to the differences in the sampling methods and environments in which measurements were taken, however the EF profiles and the variance in the EF values demonstrate the necessity to include both gas and particulate emissions for an accurate assessment of the potential impact transportation may have on human and environmental health.

4. Conclusion

In view of the adverse environmental and health impacts of airborne PAHs that are sourced from diesel exhaust, it is crucial that accurate assessment of the effects of their concentrations be carried out and emission factors be determined to establish appropriate management and mitigation strategies. PAHs vary in physiochemical properties and they have been found to co-exist in both particulate and gas phases

which makes the sampling, extraction and analysis techniques required for the monitoring thereof somewhat challenging.

In this engine dynamometer study, the simultaneous sampling of gas and particulate PAHs from diesel exhaust emissions was successfully achieved by portable denuder devices consisting of a QFF sandwiched between two multichannel PDMS traps. The traps and filter were individually thermally desorbed and analysed by comprehensive two-dimensional gas chromatography with time-of-flight mass spectrometric detection. The sampling was rapid and effective and low limits of detection for PAHs were found for the experimental method ranging from 0.3 to 18.5 ng/m^3 for filters and 0.3–79.3 ng/m^3 for PDMS traps. Dynamometer studies have the advantage of being able to investigate vehicle emissions under different load settings in a controlled laboratory environment that is free from other sources, however a limitation to this study is that no PAH emissions arising from elsewhere on the vehicle aside from the engine are considered, such as wear of brake linings and tyres, as well as re-suspended road dust, which also have an impact on the PAH emissions from vehicle operation. It should also be noted that there was no size resolution of sampled particulate matter in this study, as total PM was collected.

The PAH profiles for each mode differed significantly in terms of the number, type and concentration of PAHs. Total PAH EFs (gas and particle phase) were determined to be 1181.14 and 592.10 µg/kg for the idle and maximum power mode respectively. Naphthalene was found to be the most abundant PAH in the raw exhaust stream for both modes and a total of 9 PAHs were detected in the idle mode and only 4 in maximum power mode. The maximum power mode revealed the highest concentration of particulate PAHs which correlated with elevated soot measurements. The presence of smaller 2–3 ringed PAHs in the exhaust may originate from unburned diesel fuel but the presence of the larger 4–6 ringed PAHs, that are not typically present in the fuel, suggest that they originate from other sources such as pyrosynthesis or the lubricating oil.

Over 80% of PAHs were found in the gas phase which emphasized the need for this study seeing that numerous other studies tend to focus only on particulate matter in the determination of PAH emission factors. Gas phase PAHs can undergo oxidation reactions producing secondary organic aerosol compounds which in some cases have been found to be more toxic than the precursor compounds (Lin et al., 2019). Therefore, characterizing the EFs of PAHs, the phase partitioning of these compounds, as well as transformations thereof, are important to air quality control as well as the health of the general public.

For future work it is recommended that a study be conducted with a controlled dilution ratio and additional tests should be carried out to more accurately determine the extent of blow off and transient phase associations at different operating modes and engine temperatures. An in-depth look into the formation of PAH derivatives and their quantification would be very valuable as low molecular weight PAHs, which were found to be more abundant, can react with NO_x in the exhaust to form highly toxic nitrated and oxygenated PAH compounds that have adverse human health and environmental effects (Keyte et al., 2016).

CRedit authorship contribution statement

G. Geldenhuys: Methodology, Investigation, Formal analysis, Writing – original draft. **M. Watrus:** Methodology, Resources, Investigation, Formal analysis, Writing – review & editing. **P.B.C. Forbes:** Conceptualization, Methodology, Investigation, Formal analysis, Writing – review & editing, Supervision, Project administration, Resources, Funding acquisition.

Declaration of competing interest

The authors declare that they have no known competing financial interests or personal relationships that could have appeared to influence the work reported in this paper.

Acknowledgements

Resources provided by the University of Pretoria and Impala Platinum (Pty) Ltd are gratefully acknowledged. Thanks to Sasol especially Sasol Fuels Application Centre (SFAC) for their valued collaboration, as well as Cecilia Pretorius and the Council for Scientific and Industrial Research (CSIR) and the Mine Health and Safety Council (MHSC).

References

- Abu-Allaban, M., Coulomb, W., Gertler, A., Gillies, J., Pierson, W., Rogers, C., Sagebiel, J., Tarnay, L., 2002. Exhaust particle size distribution measurements at the Tuscarora Mountain tunnel. *Aerosol. Sci. Technol.* 36, 771e789.
- Abu-Allaban, M., Gillies, J.A., Gertler, A.W., Clayton, R., Proffitt, D., 2003. Tailpipe resuspended road dust, and brake-wear emission factors from on-road vehicles. *Atmos. Environ.* 37, 5283e5293.
- Allen, J.O., Mayo, P.R., Hughes, L.S., Salmon, L.G., Cass, G.R., 2001. Emissions of size-segregated aerosols from on-road vehicles in the Caldecott Tunnel. *Environ. Sci. Technol.* 35, 4189–4197.
- Ayeter, G.K., Mbonigaba, Innocent, Ampofo, Joshua, Albert, Sunnu, 2021. Investigating the state of road vehicle emissions in Africa: a case study of Ghana and Rwanda. *Transportation Research Interdisciplinary Perspectives* 11, 100409.
- Burgard, D.A., Bishop, G.A., Williams, M.J., Stedman, D.H., 2003. On-road Remote Sensing of Automobile Emissions in the Denver Area: Year 4, January 2003. University of Denver.
- Cocker, D.R., Shah, S.D., Johnson, K., Miller, J.W., Norbeck, J.M., 2004. Development and application of a mobile laboratory for measuring emissions from diesel engines. 1. Regulated gaseous emissions. *Environ. Sci. Technol.* 38 (7), 2182–2189.
- Correa, S.M., Arbilla, G., da Silva, C.M., Martins, E.M., de Souza, S.L.Q., 2021. Determination of size-segregated polycyclic aromatic hydrocarbon and its nitro and alkyl analogs in emissions from diesel-biodiesel blends. *Fuel* 283, 118912.
- Dandajeh, Adamu, Hamisu, Talibi, Midhat, Ladommatos, Nicos, Paul, Hellier, 2019. Influence of combustion characteristics and fuel composition on exhaust PAHs in a compression ignition engine. *Energies* 12, 2575.
- Eiguren-Fernandez, A., Miguel, A.H., 2012. Size-resolved polycyclic aromatic hydrocarbon emission factors from on-road gasoline and diesel vehicles: temperature effect on the nuclei-mode. *Environ. Sci. Technol.* 46, 2607–2615.
- Forbes, P.B.C., Rohwer, E.R., 2009. Investigations into a novel method for atmospheric polycyclic aromatic hydrocarbon monitoring. *Environ. Pollut.* 157 (8–9), 2529–2535.
- Forbes, P.B.C., Rohwer, E.R., 2015. In: Forbes, Patricia (Ed.), Chapter 5: Denuders, in *Comprehensive Analytical Chemistry Vol. 70: Monitoring of Air Pollutants: Sampling, Sample Preparation and Analytical Techniques*, vol. 70. Netherlands: Elsevier, Netherlands, ISBN 978-0-444-63553-2, pp. 153–181.
- Forbes, P.B.C., Karg, E.W., Zimmermann, R., Rohwer, E.R., 2012. The use of multi-channel silicone rubber traps as denuders for polycyclic aromatic hydrocarbons. *Anal. Chim. Acta* 730, 71–79.
- Forbes, P.B.C., Karg, E.W., Geldenhuys, G., Nsibande, S.A., Zimmermann, R., Rohwer, E.R., 2013. Characterisation of atmospheric semi-volatile organic compounds. *Clean Air J.* 23 (1), 3–6. ISSN 1017-1703.
- Geldenhuys, G., 2014. Characterization of Diesel Emissions with Respect to Semi-volatile Organic Compounds in South African Platinum Mines and Other Confined Environments. MSc Thesis, The University of Pretoria viewed 5 March 2017. <http://hdl.handle.net/2263/46248>.
- Geldenhuys, G., Rohwer, E.R., Naudé, Y., Forbes, P.B.C., 2015. Monitoring of atmospheric gaseous and particulate polycyclic aromatic hydrocarbons in South African platinum mines utilizing portable denuder sampling with analysis by thermal desorption-comprehensive gas chromatography mass spectrometry. *J. Chromatogr. A* 1380, 17–28.
- Gietl, J.K., Lawrence, R., Thorpe, A.J., Harrison, R.M., 2010. Identification of brake wear particles and derivation of a quantitative tracer for brake dust at a major road. *Atmos. Environ.* 44, 141–146.
- Guo, H., Zhang, Q., Shi, Y., Wang, D., 2007. On-road Remote Sensing Measurements and Fuel Based Motor Vehicle Emission Inventory in Hangzhou, China, vol. 41. *Atmospheric Environment*, pp. 3095–3107.
- Handler, M., Puls, C., Zbiral, J., Marr, I., Puxbaum, H., Limbeck, A., 2008. Size and composition of particulate emissions from motor vehicles in the Kaiseröfen-Tunnel. *Atmos. Environ.* 42, 2173–2186.
- Hays, Michael D., Preston, William, J George, Barbara, J George, Ingrid, Snow, Richard, Faircloth, James, Long, Thomas, Baldauf, Richard W., McDonald, Joseph, 2017. Temperature and driving cycle significantly affect carbonaceous gas and particle matter emissions from diesel trucks. *Energy Fuels* 31, 11034–11042.
- Huang, L., Bohac, S.V., Chernyak, S.M., Batterman, S.A., 2015. Effects of fuels, engine load and exhaust after-treatment on diesel engine SVOC emissions and development of SVOC profiles for receptor modeling. *Atmos. Environ.* 102, 228–238.
- Hu, Shaohua, Jorn, D., Herner, Robertson, William, Kobayashi, Reiko, Chang, M-C Oliver, Huang, Shiou-mei, Zielinska, Barbara, Norman, Kado, Collins, John F., Paul, Rieger, 2013. Emissions of polycyclic aromatic hydrocarbons (PAHs) and nitro-PAHs from heavy-duty diesel vehicles with DPF and SCR. *J. Air Waste Manag. Assoc.* 63, 984–996.
- International Agency for Research on Cancer (IARC), 2012. Diesel Engine Exhaust Carcinogenic 2012a. Press Release, p. 213.
- International Agency for Research on Cancer (IARC), World Health Organization (WHO), 2014. Diesel and gasoline engine exhausts and some nitroarenes (volume 105). Available at: <http://monographs.iarc.fr/ENG/Monographs/vol105/mono105.pdf>.
- International Agency for Research on Cancer (IARC), World Health Organization (WHO), 2012. IRAC: Diesel Engine Exhaust Carcinogenic (press release). Available at: https://www.iarc.fr/en/media-centre/pr/2012/pdfs/pr213_E.pdf.
- Kim, K.H., Jahan, S.A., Kabir, E., Brown, R.J.C., 2013. A review of airborne polycyclic aromatic hydrocarbons (PAHs) and their human health effects. *Environ. Int.* 60, 71–80.
- Keyte, Ian J., Albinet, Alexandre, Harrison, Roy M., 2016. On-road traffic emissions of polycyclic aromatic hydrocarbons and their oxy- and nitro-derivative compounds measured in road tunnel environments. *Sci. Total Environ.* 566, 1131–1142.
- Kostenidou, E., Martinez-Valiente, A., R'мили, B., Marques, B., Temime-Roussel, B., Durand, A., André, M., Liu, Y., Louis, C., Vansevenant, B., Ferry, D., 2021. Emission factors, chemical composition, and morphology of particles emitted from Euro 5 diesel and gasoline light-duty vehicles during transient cycles. *Atmos. Chem. Phys.* 21 (6), 4779–4796.
- Kristensson, A., Johansson, C., Westerholm, R., Swietlicki, E., Gidhagen, L., Wideqvist, U., Vesely, V., 2004. Real-world traffic emission factors of gases and particles measured in a road tunnel in Stockholm, Sweden. *Atmos. Environ.* 38, 657–673.
- Kumari, K Maharaj, Lakhani, Anita, 2018. PAHs in Gas and Particulate Phases: Measurement and Control, Environmental Contaminants. Springer.
- Lin, Yuan-Chung, Ching Li, Ya, Amesho, Kassian TT., Chou, Feng-Chih, Cheng, Pei-Cheng, 2019. Characterization and quantification of PM_{2.5} emissions and PAHs

- concentration in PM_{2.5} from the exhausts of diesel vehicles with various accumulated mileages. *Sci. Total Environ.* 660, 188–198.
- Liu, Y., Martinet, S., Louis, C., Pasquier, A., Tassel, P., Perret, P., 2017. Emission characterization of in-use diesel and gasoline Euro 4 to Euro 6 passenger cars tested on chassis dynamometer bench and emission model assessment. *Aerosol Air Qual. Res.* 17, 2289–2299.
- Mancilla, Y., Mendoza, A., 2012. A tunnel study to characterize PM_{2.5} emissions from gasoline-powered vehicles in Monterrey, Mexico. *Atmos. Environ.* 59, 449–460.
- Marr, L.C., Kirchstetter, T.W., Harley, R.A., Miguel, A.H., Hering, S.V., Hammond, S.K., 1999. Characterization of polycyclic aromatic hydrocarbons in motor vehicle fuels and exhaust emissions. *Environ. Sci. Technol.* 33 (18), 3091–3099.
- Morawska, L., Zhang, J.J., 2002. Combustion sources of particles. 1. Health relevance and source signatures. *Chemosphere* 49, 1045–1058.
- Munyeza, Chiedza F., Kohlmeier, Vesta, Dragan, George C., Karg, Erwin W., Rohwer, Egmont R., Zimmermann, Ralf, Forbes, Patricia BC., 2019. 'Characterisation of particle collection and transmission in a polydimethylsiloxane based denuder sampler. *J. Aerosol Sci.* 130, 22–31.
- National Center for Biotechnology Information. PubChem database. Available at. <http://pubchem.ncbi.nlm.nih.gov/compound>.
- Ning, Z., Polidori, A., Schauer, J.J., Sioutas, C., 2008. Emission factors of PM species based on freeway measurements and comparison with tunnel and dynamometer studies. *Atmos. Environ.* 42, 3099–3114.
- Oliveira, C., Pio, C., Caseiro, A., Santos, P., Nunes, T., Mao, H., Luahana, L., Sokhi, R., 2010. Road traffic impact on urban atmospheric aerosol loading at Oporto, Portugal. *Atmos. Environ.* 44, 3147–3158.
- Ono-Ogasawara, M., Smith, T.J., 2004. Diesel exhaust particles in the work environment and their analysis. *Ind. Health* 42 (4), 389–399.
- Pandey, S.K., Kim, K., Brown, R.J.C., 2011. A review of techniques for the determination of polycyclic aromatic hydrocarbons in air. *Trends Anal. Chem.* 30 (11), 1716–1739.
- Perrone, Maria Grazia, Carbone, Claudio, Faedo, Davide, Ferrero, Luca, Maggioni, Angela, Sangiorgi, Giorgia, Bolzacchini, Ezio, 2014. 'Exhaust emissions of polycyclic aromatic hydrocarbons, n-alkanes and phenols from vehicles coming within different European classes. *Atmos. Environ.* 82, 391–400.
- Pey, J., Querol, X., Alastuey, A., 2010. Discriminating the regional and urban contributions in the North-Western Mediterranean: PM levels and composition. *Atmos. Environ.* 44, 1587–1596.
- Phuleria, H.C., Geller, M.D., Fine, P.M., Sioutas, C., 2006. Size resolved emissions of organic tracers from light- and heavy duty vehicles measured in a California roadway tunnel. *Environ. Sci. Technol.* 40 (13), 4109–4118.
- Poster, D.L., Schantz, M.M., Sander, L.C., Wise, S.A., 2006. Analysis of polycyclic aromatic hydrocarbons (PAHs) in environmental samples: a critical review of gas chromatographic (GC) methods. *Anal. Bioanal. Chem.* 386, 859–881.
- Rengarajan, T., Rajendran, P., Nandakumar, N., Lokeshkumar, B., Rajendran, P., Nishigaki, I., 2015. Exposure to polycyclic aromatic hydrocarbons with special focus on cancer. *Asian Pacific J. Tropic. Biomed.* 5 (3), 182–189. [https://doi.org/10.1016/S2221-1691\(15\)30003-4](https://doi.org/10.1016/S2221-1691(15)30003-4). ISSN 2221-1691.
- Rhead, M.M., Pemberton, R.D., 1996. Sources of naphthalene in diesel exhaust emissions. *Energy Fuel.* 10 (3), 837–843.
- Reşitoğlu, Aslan, İbrahim, Altinişik, Kemal, Ali, Keskin, 2015. The pollutant emissions from diesel-engine vehicles and exhaust aftertreatment systems. *Clean Technol. Environ. Policy* 17, 15–27.
- Riccio, A., Chianese, E., Monaco, D., Costagliola, M.A., Perretta, G., Prati, M.V., Agrillo, G., Esposito, A., Gasbarra, D., Shindler, L., Brusasca, G., Nanni, A., Pozzi, C., Magliulo, V., 2016. Real-world automotive particulate matter and PAH emission factors and profile concentrations: results from an urban tunnel experiment in Naples. Italy. *Atmos. Environ.* 141, 379–387.
- Rohr, A.C., Wyzga, R.E., 2012. Attributing health effects to individual particulate matter constituents. *Atmos. Environ.* 62, 130–152.
- Samet, J.M., Dominici, F., Curriero, F.C., Coursac, I., Zeger, S.L., 2000. Fine particulate air pollution and mortality in 20 US Cities, 1987–1994. *N. Engl. J. Med.* 343 (24), 1742–1749.
- Schifter, I., Díaz, L., Durán, J., Guzmán, E., Chávez, O., López-Salina, E., 2003. Remote sensing study of emissions from motor vehicles in the metropolitan area of Mexico City. *Environ. Sci. Technol.* 37, 395–401.
- Shen, H., Tao, S., Liu, J., Huang, Y., Chen, H., Li, W., Zhang, Y., Chen, Y., Su, S., Lin, N., Xu, Y., 2014. Global lung cancer risk from PAH exposure highly depends on emission sources and individual susceptibility. *Sci. Rep.* 4, 6561.
- U.S. Environmental Protection Agency (EPA), 2004. Air Quality Criteria for Particulate Matter. US Environmental Protection Agency, Research Triangle Park.
- U.S. National Toxicology Program (NTP), 2014. Report on Carcinogens, thirteenth ed. Available at. <http://ntp.niehs.nih.gov/pubhealth/roc/roc13>.
- Vicente Franco, V., Kousoulidou, M., Muntean, M., Ntziachristos, L., Hausberger, S., Dilara, P., 2013. Road Vehicle Emission Factors Development: A Review, vol. 70. *Atmospheric Environment*, pp. 84–97.
- Vione, D., Barra, S., de Gennaro, G., de Rienzo, M., Gilardoni, S., Perrone, M.G., Pozzoli, L., 2004. Polycyclic aromatic hydrocarbons in the atmosphere: monitoring, sources, sinks and fate. *Ann. Chim.* 94, 17–32.
- Wang, Bei, Lau, Yik-Sze, Huang, Yuhuan, Organ, Bruce, Chuang, Hsiao-Chi, Ho, Steven Sai Hang, Qu, Linli, Lee, Shun-Cheng, Ho, Kin-Fai, 2021. 'Chemical and toxicological characterization of particulate emissions from diesel vehicles. *J. Hazard Mater.* 405, 124613.
- Wang, X., Westerdahl, D., Wu, Y., Pan, X., Zhang, K.M., 2011. On-road emission factor distributions of individual diesel vehicles in and around Beijing, China. *Atmos. Environ.* 45, 503–513.
- Wei, Hu, Liu, Guangbin, Tu, Yong, Zhong, Qin, 2015. 'Emission of polycyclic aromatic hydrocarbons from different types of motor vehicles' exhaust. *Environ. Earth Sci.* 74, 5557–5564.
- Weitekamp, Chelsea A., Kerr, Lukas B., Dishaw, Laura, Nichols, Jennifer, Lein, McKayla, Stewart, Michael J., 2020. 'A systematic review of the health effects associated with the inhalation of particle-filtered and whole diesel exhaust. *Inhal. Toxicol.* 32, 1–13.
- Weingartner, E., Keller, C., Stahel, W., Burtscher, H., Baltensperger, U., 1997. Aerosol emission in a road tunnel. *Atmos. Environ.* 31 (3), 451–462.
- Yanowitz, J., Graboski, M.S., Ryan, L.B., Alleman, T.L., McCormick, R.L., 1999. Chassis dynamometer study of emissions from 21 in-use heavy-duty diesel vehicles. *Environ. Sci. Technol.* 33 (2), 209–216.
- Zhang, Y., Stedman, D.H., Bishop, G.A., Guenther, P.L., Beaton, S.P., 1995. Worldwide on-road vehicle exhaust emissions study by remote sensing. *Environ. Sci. Technol.* 29, 2286–2294.
- Zheng, X., Wu, Y., Zhang, S., Baldauf, R.W., Zhang, K.M., Hu, J., Li, Z., Fu, L., Hao, J., 2016. Joint measurements of black carbon and particle mass for heavy-duty diesel vehicles using a portable emission measurement system. *Atmos. Environ.* 141, 435–442.
- Zheng, X., Wu, Y., Zhang, S., Hu, J., Max Zhang, K., Li, Z., He, L., Hao, J., 2017. Characterizing particulate polycyclic aromatic hydrocarbon emissions from diesel vehicles using a portable emissions measurement system. *Sci. Rep.* 7 (10058), 1–12. <https://doi.org/10.1038/s41598-017-09822>.

Chapter 3: Emissions assessment: Sugar cane industry (Paper 2)

Characterization of gaseous and particulate phase polycyclic aromatic hydrocarbons emitted during pre-harvest burning of sugar cane in different regions of Kwa-Zulu Natal, South Africa is presented in this chapter.

This chapter has been accepted for publication in the Journal of Environmental Toxicology and Chemistry.

Geldenhuis, G., Orasche, J., Jakobi, G., Zimmermann, R. and Forbes, P.B.C. 2022. Characterization of gaseous and particulate phase polycyclic aromatic hydrocarbons emitted during pre-harvest burning of sugar cane in different regions of Kwa-Zulu Natal, South Africa. *Environmental Toxicology and Chemistry*. DOI: <https://doi.org/10.1002/etc.5579>.

Author contributions

G Geldenhuis: Methodology, Validation, Formal analysis, Data curation, Writing- Original draft preparation, Writing - Review & Editing; **J Orasche:** Methodology, Formal analysis, Writing - Review & Editing; **G Jakobi:** Methodology, Formal analysis, Writing - Review & Editing; **R Zimmermann:** Conceptualization, Writing - Review & Editing, Funding acquisition; **P.B.C Forbes:** Conceptualization, Visualization, Project administration, Supervision, Methodology, Formal analysis, Writing - Review & Editing, Funding acquisition.

Environmental Chemistry

Characterization of Gaseous and Particulate Phase Polycyclic Aromatic Hydrocarbons Emitted During Preharvest Burning of Sugar Cane in Different Regions of Kwa-Zulu Natal, South Africa

G. Geldenhuys,^{a,b,c} J. Orasche,^d G. Jakobi,^d R. Zimmermann,^{d,e} and Patricia B. C. Forbes^{a,*}

^aDepartment of Chemistry, Faculty of Natural and Agricultural Sciences, University of Pretoria, Pretoria, South Africa

^bProcessing Laboratory, Impala Platinum, Rustenburg, South Africa

^cSkin Rejuvenation Technologies, Irene, South Africa

^dJoint Mass Spectrometry Centre, Cooperation Group “Comprehensive Molecular Analytics,” Helmholtz Zentrum München, Neuherberg, Germany

^eJoint Mass Spectrometry Centre, Institute of Chemistry, University of Rostock, Rostock, Germany

Abstract: Biomass burning is a significant anthropogenic source of air pollution, including the preharvest burning of sugar cane. These burn events result in atmospheric emissions, including semivolatile organic compounds, that may have adverse impacts on air quality and human health on a local, regional, and even a global scale. Gaseous and particulate polycyclic aromatic hydrocarbon (PAH) emissions from various sugar cane burn events in the province of Kwa-Zulu Natal in South Africa were simultaneously sampled using a portable denuder sampling technology, consisting of a quartz fiber filter sandwiched between two polydimethylsiloxane multichannel traps. Total gas and particle phase PAH concentrations ranged from 0.05 to 9.85 $\mu\text{g m}^{-3}$ per individual burn event, and nine PAHs were quantified. Over 85% of all PAHs were found to exist in the gas phase, with smaller two- and three-ring PAHs, primarily naphthalene, 1-methyl naphthalene, and acenaphthylene, being the most dominant and causing the majority of variance between the burn sites. The PAH profiles differed between the different burn events at different sites, emphasizing the significant influence that the crop variety, prevailing weather conditions, and geographical location has on the type and number of pollutants emitted. The potential carcinogenicity of the PAH exposure was estimated based on toxic equivalency factors that showed varying risk potentials per burn event, with the highest value of 5.97 ng m^{-3} . *Environ Toxicol Chem* 2023;00:1–15. © 2023 The Authors. *Environmental Toxicology and Chemistry* published by Wiley Periodicals LLC on behalf of SETAC.

Keywords: Biomass burning; Denuder; Polycyclic aromatic hydrocarbon; Sugar cane

INTRODUCTION

Sugar cane is an essential commercial crop worldwide; it is extremely versatile, being a rich source of food, fiber, fodder, fertilizer, and numerous valuable byproducts that can be used for human and animal consumption, as well as providing a source of renewable energy (Solomon, 2011). The crop is grown in tropical or subtropical climates, with Brazil producing over 40% of the world total followed by India and China

(Flack-Prain et al., 2021; South African Sugar Association [SASA], 2019). The sugar cane industry in South Africa is ranked in the top 15 out of approximately 120 sugar-producing countries worldwide and is one of the world's leading producers of high-quality sugar with an estimated average production of 2.3 million tons/season (SASA, 2019). The industry is varied, combining the agricultural activities of sugar cane farming with the manufacture of raw and refined sugar, syrup, and a range of other by-products (SASA, 2012).

The burning of sugar cane prior to harvest is common practice in South Africa, where over 90% of the sugar cane is burnt (Pryor et al., 2017). The primary reason for burning the sugar cane is economic: most of the excess waste material is eliminated, leading to improved efficiencies of harvesting, handling, and milling. The preharvest burns also chase away the unwanted snakes and cane rats before the workers enter the fields. An alternative to burning prior to harvest is “green

This article includes online-only Supporting Information.

This is an open access article under the terms of the Creative Commons Attribution-NonCommercial-NoDerivs License, which permits use and distribution in any medium, provided the original work is properly cited, the use is non-commercial and no modifications or adaptations are made.

* Address correspondence to patricia.forbes@up.ac.za

Published online 31 January 2023 in Wiley Online Library (wileyonlinelibrary.com).

DOI: 10.1002/etc.5579

harvesting," which involves the cutting of the adult cane stalk, the removal of leaves and unwanted matter, and the covering of the plant's roots with the "trash blanket" (leaves and other residues from harvesting). This method is notoriously difficult and time consuming and results in increased harvest costs. The method does, however, have its advantages such as the preservation of soil moisture, suppressed weed growth, improved pest control, and increased soil nutrient value due to the organic matter, which also reduces field damage under wet conditions.

Besides the short-term financial benefit of the preharvest burns, there are adverse impacts on the environment that should be considered such as the emission of greenhouse gases, particulate matter, and semivolatile organic compounds (SVOCs) into the atmosphere. The smoke produced from these burning events is also hazardous to nearby road users, and the ash from the burns may end up in sensitive areas such as beaches, residential areas, and schools. The harvest season of sugar cane lasts between 5 to 6 months, and during this time a significant number of atmospheric pollutants are emitted into the atmosphere that may have a negative impact on human and environmental health (SASA, 2012).

Among the organic pollutants emitted are polycyclic aromatic hydrocarbons (PAHs), which are ubiquitous in the environment and contain two or more fused benzene rings in varying arrangements. They are formed through a pyrolytic process during incomplete combustion of organic materials and in emerging economies, such as South Africa, prominent sources include biomass burning, vehicular emissions, and indoor wood burning for heating and cooking (Dat & Chang, 2017; Forbes & Rohwer, 2009). Due to their well-researched potential carcinogenicity, teratogenicity, and genotoxicity, the US Environmental Protection Agency (USEPA) has identified 16 priority PAHs, and the World Health Organization (WHO) has added 17 additional PAHs, for a total of 33 PAHs under regulation by the WHO (Chen et al., 2017; Dat & Chang, 2017; Keith, 2015; Rengarajan et al., 2015).

Ambient PAH levels depend largely on the sources of PAHs nearby, with PAH concentrations generally being higher in industrial, urban, or residential areas compared with remote or rural sites, with PAH concentrations measured in ambient air worldwide therefore varying from less than 50 pg m^{-3} to more than $1.7 \text{ } \mu\text{g m}^{-3}$ (Dat & Chang, 2017). Furthermore, ambient PAH concentrations also depend on the prevailing meteorological conditions such as wind direction, wind speed, relative humidity, and temperature. Seasonal variation in PAH concentrations validate the importance of these meteorological parameters, although sources also vary seasonally with respect to emission rates, with higher PAH concentrations being reported in winter (Dat & Chang, 2017). A recent Iranian study found that summed PAH concentrations were $0.008\text{--}59.46$ (mean: 11.61) ng m^{-3} and $0.05\text{--}40.83$ (mean: 10.22) ng m^{-3} for the cold and warm seasons, respectively (Nadali et al., 2021).

These seasonal PAH variations can be explained by reduced radiation during winter resulting in a reduction of photo-, thermo-, and chemical oxidations in the atmosphere. In addition, a thinner planetary boundary layer and frequent thermal

inversions may trap pollutants in the lower troposphere and prevent their dispersion, resulting in higher winter values, whereas in summer seasons, lower PAH concentrations can be partially attributed to increasing PAH volatilization from particle to gas phase and better dilution and dispersion of atmospheric PAHs. Wind speed and relative humidity were also found to be significant predictors for both light and heavy PAHs because higher wind speeds may reduce PAH levels by increasing dilution and dispersion of air masses, and an inverse correlation between PAHs and wind speed was also observed by other authors (Sharma et al., 2007; Tan et al., 2006, 2011).

The contribution of various parameters such as temperature, relative humidity, rainfall, atmospheric pressure, and wind speed on total and individual PAH concentrations was investigated by Amarillo and Carreras (2016). The authors found that temperature was the meteorological parameter that affected the total and individual PAH concentrations the most, with a stronger influence on light than heavy PAHs because they are more easily partitioned into the vapor phase (Amarillo & Carreras, 2016). Masih et al. (2012) found that PAH concentrations decreased with an increase in temperature and wind speed, whereas Elorduy et al. (2016) reported a relatively low correlation between PAH concentration and humidity and concluded that temperature and wind speed might be the major meteorological factors affecting the concentration of atmospheric PAHs.

To add to the complexity of PAH emissions, they undergo various transformations in the atmosphere depending on whether the PAH is in the gas phase or if it is associated with particles, which is why it is vital that the concentration of PAHs in both phases be determined, to accurately assess the health and environmental risks they pose. The partitioning of PAHs between the gas and particle phase depends on a few aspects including the volatility of the compound, ambient temperature, and the atmospheric concentration of particles. Smaller PAHs (two- to four-ring) tend to be more present in the gas phase, and the larger PAHs (more than four rings) in the particulate phase (Godoi et al., 2004; Vione et al., 2004). Meteorological parameters such as relative humidity, precipitation, temperature and the concentration of ambient dust or particulate matter also influence the partitioning (Kural et al., 2018).

Quantification of PAHs from two municipalities in Mexico with different climatic conditions, during sugar cane harvest seasons showed that the most abundant particulate PAHs were the larger five- to six-ring PAHs, namely, indeno[1,2,3-cd]pyrene, benzo[b]fluoranthene, benzo[a]pyrene, and dibenzo[a,h]anthracene. The Σ PAHs associated with particulate matter (PM)₁₀ and PM_{2.5} ranged from 4.34 to 8.40 and 3.70 to 5.80 ng m^{-3} , respectively. That study is unique in that it accounts for the sugar cane harvest as well as the milling processes that emit pollutants into the atmosphere (Mugica-Alvarez et al., 2015). In a Brazilian study by de Andrade et al. (2010), the average ambient concentrations of total PAHs associated with atmospheric particulate matter were found to be 22.90 ng m^{-3} during August 2002 and September 2003 (falling within the annual sugar cane burn season), which was significantly higher than 2.35 ng m^{-3} for the non-burn period, indicating that the

burning of sugar cane was the main contributor to the high levels of PAHs in Araraquara, Brazil. In another Brazilian study, soot samples were collected in the sugar cane fields after burning and thereafter extracted and analyzed by gas chromatography–mass spectrometry (GC–MS) to reveal that 31 PAHs were detected; the authors concluded that their findings should serve as additional caution to workers and the general population to avoid exposure to the fly soot (Zamperlini, Silva, & Vilegas, 1997).

Due to the rise in awareness of the potential impacts of biomass burning and associated pollutants, emission factors were calculated with the aim of making source-specific emission estimates for area-wide inventories. Hall et al. (2012) reported total PAH emission factors of 7.13 ± 0.94 and $8.18 \pm 3.26 \text{ mg kg}^{-1}$ for dry leaf and whole sugar cane stalk burning, respectively, for preharvest burning in Florida. The most predominant PAH was found to be the lower molecular weight naphthalene. Ultrafine PM ($\text{PM}_{0.1}$) and particle-bound PAH emission factors were also determined in a study by Samae et al. in 2021, in which combustion of various biomasses, including sugar cane bagasse and sugar cane leaves, was carried out in a tube furnace; the emitted PM was collected using a nanosampler with size segregator. Chrysene, benzo[b]fluoranthene and benzo[k]fluoranthene were the dominant PAHs found on $\text{PM} < 0.1 \mu\text{m}$ in size, with the general finding that four- to six-ring PAH concentrations were the highest in PM samples $< 0.1 \mu\text{m}$ (Mugica-Álvarez et al., 2018; Samae et al., 2021). Sevimoglu and Rogge (2016) collected 24-h size-segregated samples for 12 months in Florida (USA), during sugar cane burning seasons using a high-volume sampler with a PM_{10} selective inlet. The authors concluded that 55%–70% of the total PAHs were associated with particles having diameters smaller than $0.49 \mu\text{m}$. The PAH levels during the burn season ranged from 3.00 to 7.36 ng m^{-3} in rural and urban regions, respectively, which were 15 times higher than during the growing season (Sevimoglu & Rogge, 2016).

Numerous other studies found in the literature pertaining to sugar cane burning have primarily paid attention to the toxicity of PAHs associated with PM, but it has been found that many anthropogenically sourced PAHs are emitted predominantly in the gas phase (Geldenhuys et al., 2015). The difficulty around the various methods used to sample semivolatile PAHs is that they require larger sampling volumes and extended sampling times to accurately quantify trace levels in ambient air, after which complicated and time consuming pretreatment and concentration procedures are employed to prepare the sample for instrumental analysis (Godoi et al., 2004; Pandey et al., 2011; Poster et al., 2006). These sampling strategies run the risk of analyte breakthrough and blow-off, and vital PAH partitioning information is lost, not to mention the introduction of unwanted sampling artifacts. Thus it is vital to overcome these sampling bottlenecks and include a simplified sampling method that is able to adopt low flow rates, short sampling intervals, and simultaneous sampling of gas and particle phase PAHs in a manner in which their partitioning is unaffected by sampling conditions.

We have characterized and quantified both gas and particulate PAH emissions from preharvest sugar cane burning events and evaluated the influence on such emissions of weather and crop conditions. To the best of our knowledge, ours is the first study to fully characterize PAHs in both phases in emissions from sugar cane burning in South Africa and also the first study to consider the influence of crop variety on the resultant PAH emissions. We collected PAHs in both gas and particle phases simultaneously using small portable denuder sampling devices that minimized sampling artifacts; each denuder component could be directly thermally desorbed, which avoids time-consuming and environmentally unfriendly sample preparation procedures. This type of sampling device has been effectively used and validated in previous studies (Forbes, 2015; Geldenhuys et al., 2015; Kohlmeier et al., 2017; Munyeza et al., 2019). Our study, and others like it, are important for establishing best practice in sugar cane harvesting and related air quality monitoring, thus helping to enhance the environmental benefits of the sugar cane industry and its sustainability.

MATERIALS AND METHODS

Sampling sites

Samples were taken at five different sites situated in the province of Kwa-Zulu Natal in South Africa (Figure 1A). The two sampling regions included the Kwa-Zulu Natal North Coast, which is a coastal region at low altitude with a warm and temperate climate, whereas the Kwa-Zulu Natal Midlands is situated more inland, at higher altitudes ($>800 \text{ m}$ above sea level), and has a more moderate maritime climate with typical warm rather than hot summers and cool to cold winters. During the month of August when sampling took place, the coastal areas experienced lower humidity of 50%–60% and less rainfall than the annual average, whereas the Midlands also experienced the lowest humidity (45.6% average relative humidity) and precipitation in August, but this was accompanied by maximum sustained winds (Climate-Data.org, nd).

Each of the farms differed in terms of size and location, as well as the age, height, and sugar cane crop variety. A total of five burn events were sampled, as summarized in Table 1. Meteorological data were extracted from fixed weather stations operating at each site and were also collected on-site using a hand-held Kestrel 4500 Pocket Weather Tracker (KestrelMeters). The burns were started along the downwind edge of the field, against wind, to reduce the speed of the burn and optimize the control thereof.

At each burn event, polydimethylsiloxane (PDMS) denuders and aethalometer samples were taken before and during the burn at a stationery point at a distance of approximately 16 m from the edge of the sugar cane field (Figure 1B). In addition, three aethalometer samplers were used as personal samplers worn by the researchers while walking around the field during the burns, which would result in measurements comparable to a farm worker's worst-case personal exposure, because the workers generally remain upwind to stay clear of the smoke.

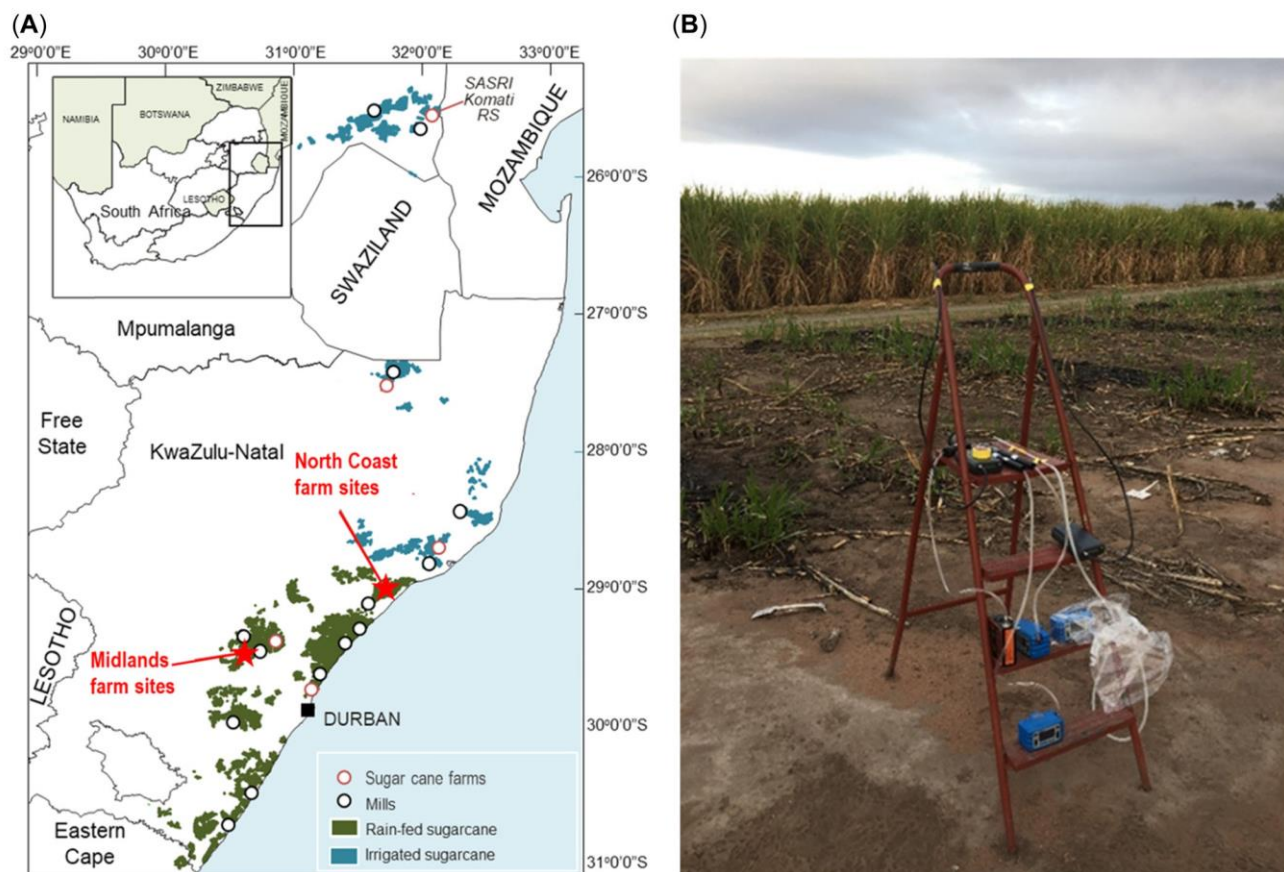


FIGURE 1: (A) Sampling locations in the South Africa sugar belt in Kwa-Zulu Natal Province in South Africa (adapted from SASA, 2022). (B) The sampling setup during burning events.

Sampling

PDMS denuder sampling devices. The PAH samples were collected with Gilair Plus personal sampling pumps (Sensidyne) attached to the denuder devices via Tygon® thermoplastic tubing. The GilAir pumps were operated at a low flow rate of 0.5 L min^{-1} to prevent breakthrough of the more volatile PAHs from the denuder traps. The denuder sampler consisted of two multichannel silicone rubber traps (each trap: 178-mm-long glass tube, 4.0-mm i.d., 6.0-mm o.d.) each containing 22 parallel PDMS tubes (55 mm long, 0.3-mm i.d., 0.6-mm o.d.) separated by a 6-mm-diameter quartz fiber filter (QFF), held in position by a Teflon connector. This configuration allows for both gas and particulate phase sampling and has been validated in numerous studies (Forbes, 2015; Forbes et al., 2012; Forbes & Rohwer, 2009; Kohlmeier et al., 2017; Munyeza et al., 2019). The gas phase SVOCs were trapped by the first (primary) trap because the PDMS served as a solvent for these compounds; the particles were then trapped downstream on the QFF. The postfilter trap (secondary trap) served to sample any blow-off. Figure 2 illustrates the sampling setup whereby each sample taken resulted in three individual samples, namely, the primary trap, the filter, and the secondary trap samples. A total of 14

samples (denuders) and two field blank samples were taken, as summarized in Table 1.

Samples were taken before and after burn events at five different sites. The upwind sample was taken prior to the burn event and represented background “clean air” that was not affected by the specific biomass burning event itself, but may have been affected by other burns in the vicinity or previous burns in the area, as well as non-biomass combustion sources of PAHs. The downwind sample was taken during the burn event in the plume of the smoke generated from the fire. This sample was taken for 10 min and thus provides a snapshot of the air quality at that specific time and position.

Field blank samples were taken at the burn events and treated in the same manner as other samples but were not connected to the sampling pump. These samples were used to determine any contamination introduced during handling and transport of samplers prior to analysis. The PAH concentrations detected on the field blanks were subtracted from all upwind and downwind samples to correct for any handling and storage contamination. The upwind samples were subtracted from the downwind samples when PAH emissions and profiles resulting from the burn event alone were considered; in the present study the upwind samples were treated as background pre-burn conditions.

TABLE 1: Sample site (farm), location of crop information, and meteorological sampling details for each sampled burn event

| Parameter | Kearsney | Gingindlovu | Glenside 23E | Glenside 57 | Glenside 58 |
|--|--|---------------------------------------|--|---|--|
| Burn event Location | 1 Kwa-Zulu Natal North Coast 170 | 2 Kwa-Zulu Natal North Coast 60 | 3 Kwa-Zulu Natal Midlands 942 | 4 Kwa-Zulu Natal Midlands 888 | 5 Kwa-Zulu Natal Midlands 882 |
| Altitude (m) | 29° 17' 42.7"S 31° 16' 13.1"E | 29° 01' 41.1"S 31° 36' 31.9"E | 29° 20' 56.7"S 30° 46' 05.8"E | 29° 21' 09.4"S 30° 46' 19.3"E | 29° 21' 17.4"S 30° 46' 16.5"E |
| Crop variety | N58: The crop residue is abundant and adhering very strongly | Mixed | N42: Light canopy. The older leaf sheaths or trash virtually cover and enclose the whole stalk | N57: Excellent canopy with fairly erect leaves (some bend near tip) of medium width. The trash is clingy and abundant | N58: The crop residue is abundant and adhering very strongly |
| Crop age (mo) | 14 | 18 | 20 | Unknown | 20 |
| Burn type and observations | Fast, hot burn, lit upwind | Slow burn | Hot burn due to dry conditions. More black particulates observed due to dryness and compact dense growth of cane (lots of leaf material). Petrol/diesel mix used to light. | Cooler burn due to early morning dew and still conditions. Plume dispersed fast with little residual smoke. Burn was fast and contained | Slow burn |
| Weather conditions | Cloudy, cool, gusty winds | Clear sky, gusty winds | Cloudy, cold, windy | Partly cloudy, no wind | Cloudy, cool, gusty winds |
| Burn start–end time | 7:00–7:45 | 15:07–16:00 | 15:37–16:30 | 7:20–8:00 | 14:48–15:32 |
| Air velocity at sampling point (m s^{-1}) | 1.6 | 4.4 | 2.4 | 0.1 | 3.5 |
| Wind direction | W | SSW | SSE | W | S |
| Barometric pressure (hPa) | 992.8 | 1012.5 | 904.7 | 910.7 | 911.6 |
| Temperature (dry bulb [DB] and wet bulb [WB], °C) | 16.9 (DB) 16.2 (WB) | 21.2 (DB) 16.8 (WB) | 14.6 (DB) 14.1 (WB) | 12.4 (DB) 10.5 (WB) | 15.2 (DB) 10.9 (WB) |
| Humidity (%) | 66.5 | 59.2 | 54.1 | 94.3 | 84.5 |
| Solar radiation (W m^{-2}) | 29.4 | 370.8 | 208.0 | 38.0 | 165.7 |
| No. of stationary samples taken | 2 | 4 | 2 | 2 | 4 |
| PDMS denuders | 2 | 2 | 2 | 2 | 2 |
| Aethalometer | 3 | 3 | 3 | 3 | 3 |
| Aethalometer | | | | | |

PDMS = polydimethylsiloxane.

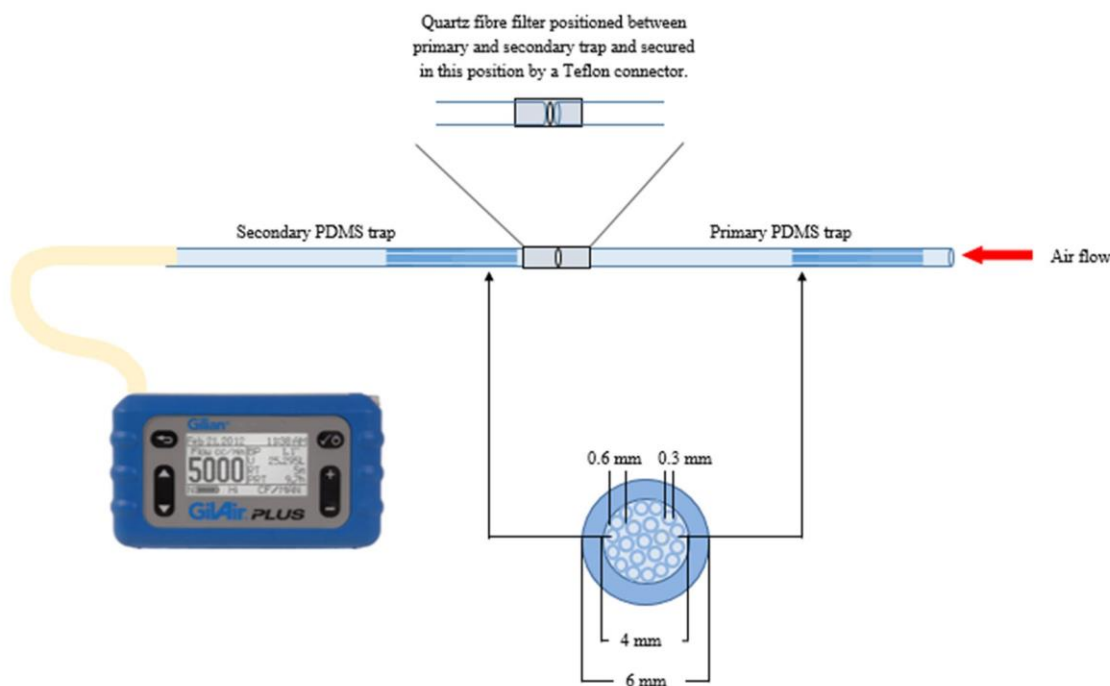


FIGURE 2: Schematic of the denuder sampling device consisting of a primary trap, filter, and secondary trap for simultaneous gas and particulate sampling (Geldenhuys et al., 2015). PDMS, polydimethylsiloxane.

Black carbon monitoring with portable aethalometers.

Portable aethalometers (microAeth[®], MA 200 series, AethLabs) were employed during all sampling events. Aethalometers are portable instruments, equipped with an internal pump, that allow for online monitoring of carbonaceous aerosol particles by measurement of their light attenuation. The aerosol particles were continuously deposited on a polytetrafluoroethylene filter tape and were monitored at five different wavelengths (375, 470, 528, 625, and 880 nm) ranging from ultraviolet to near infrared. The aethalometers were used as personal and stationary samplers as discussed in the *Sampling sites* section.

Analytical techniques

Offline analysis of each individual denuder component was performed using a LECO Pegasus four-dimensional instrument consisting of a comprehensive two-dimensional GC coupled to a time-of-flight mass spectrometer (GCxGC-TOF-MS). The instrument was equipped with an Agilent Technologies 7890 GC, a quad jet dual-stage modulator, and a secondary oven. Data acquisition and processing were executed by ChromaTOF Ver 4.0 and ChromaTOF Tile software (LECO). A Gerstel 3 thermal desorption system (TDS) was employed for sample introduction whereby the PDMS traps were directly thermally desorbed, and the filter samples were inserted into the heating zone of an empty precleaned glass tube for desorption. Synthetic air was used for the hot jets, and liquid nitrogen was used to cool nitrogen gas for the cold jets with an AMI model 186 liquid level controller to maintain sufficient levels. The GC column set consisted of a Restek Rxi-1MS nonpolar phase 100% dimethyl polysiloxane (30 m, 0.25 mm i.d., 0.25 μm df) as the first

dimension (1D) and an Rxi-17Sil MS, midpolar 50% phenyl 50%-dimethyl polysiloxane (0.79 m, 0.25 mm i.d., 0.25 μm df) as the second dimension (2D). Thermal desorption occurred from 30 to 280 $^{\circ}\text{C}$ at a rate of 60 $^{\circ}\text{C min}^{-1}$ and was held for 5 min during which the analytes were cryogenically focused via a cooled injection system at -50°C using liquid nitrogen. The temperature was ramped at 12 $^{\circ}\text{C s}^{-1}$ to 280 $^{\circ}\text{C}$, and the inlet purge time was 3 min. The desorption flow rate was 100 ml min^{-1} , and the TDS transfer line was set at 300 $^{\circ}\text{C}$. The primary oven was ramped at 5 $^{\circ}\text{C min}^{-1}$ from 40 to 315 $^{\circ}\text{C}$, which was held for 15 min. The secondary oven was offset by 5 $^{\circ}\text{C}$, and the modulator temperature was offset by 30 $^{\circ}\text{C}$. The modulation period was 3 s with a hot pulse time of 1 s. The MS transfer line temperature was set to 280 $^{\circ}\text{C}$, and mass acquisition ranged from 50 to 500 Da at 100 spectra s^{-1} . The electron energy was 70 eV, and the ion source temperature was 200 $^{\circ}\text{C}$.

Matrix-matched calibration standards

Calibration was performed using a certified standard PAH mix solution (Supelco), containing 15 priority PAHs. The nominal concentration of each compound in the mixture dissolved in methylene chloride was 2000 $\mu\text{g ml}^{-1}$. The names and abbreviations of the PAHs included are given in Table 2. A stock solution at a concentration of 100 $\mu\text{g ml}^{-1}$ was prepared in toluene, and working solutions were prepared by appropriate dilutions of the stock solutions in n-hexane before use. All solvents used for dilutions and cleaning procedures were of analytical grade (99% purity) including toluene, methanol, dichloromethane (DCM), and n-hexane (all from Sigma-Aldrich) and acetone (from Associated Chemical Enterprises). The deuterated internal standards

TABLE 2: Analytes investigated in the present study including 15 of the 16 US Environmental Protection Agency priority polycyclic aromatic hydrocarbons (PAHs) and their corresponding abbreviations, molar masses, and boiling points

| Formula | PAH name | Abbreviation | Molar mass (g mol ⁻¹) | Boiling point (°C) |
|---------------------------------|------------------------|--------------|-----------------------------------|--------------------|
| C ₁₀ H ₈ | Naphthalene | Nap | 128 | 218 |
| C ₁₁ H ₁₀ | 1-Methyl naphthalene | Nap 1 M | 142 | 240 |
| C ₁₂ H ₈ | Acenaphthylene | Acy | 152 | 265 |
| C ₁₂ H ₁₀ | Acenaphthene | Ace | 154 | 278 |
| C ₁₃ H ₁₀ | Fluorene | Flu | 166 | 295 |
| C ₁₄ H ₁₀ | Phenanthrene | Phe | 178 | 339 |
| C ₁₄ H ₁₀ | Anthracene | Ant | 178 | 340 |
| C ₁₆ H ₁₀ | Fluoranthene | FluAn | 202 | 375 |
| C ₁₆ H ₁₀ | Pyrene | Pyr | 202 | 360 |
| C ₁₈ H ₁₂ | Benz[a]anthracene | BaA | 228 | 435 |
| C ₁₈ H ₁₂ | Chrysene | Chy | 228 | 448 |
| C ₂₀ H ₁₂ | Benzo[b]fluoranthene | BbF | 252 | 481 |
| C ₂₀ H ₁₂ | Benzo[a]pyrene | BaP | 252 | 495 |
| C ₂₂ H ₁₂ | Benzo[g,h,i]perylene | BghiP | 276 | 536 |
| C ₂₂ H ₁₂ | Indeno[1,2,3-cd]pyrene | I123P | 276 | 536 |
| C ₂₂ H ₁₄ | Dibenz[a,h]anthracene | DbahA | 278 | 524 |

Data from PubChem, 2021.

(I_{Std}) d₈-naphthalene, d₁₀-phenanthrene, d₁₀-pyrene, and d₁₂-chrysene were obtained from Isotec (Sigma-Aldrich) and were used in all standards and samples.

Gas phase PAHs quantification was achieved by analyzing individual conditioned PDMS traps that were spiked with 1 µl of the following concentrations of mixed PAH standard in toluene: 0.1, 0.5, 1.0, 2.0, 5.0, 10.0, and 20.0 ng µl⁻¹. Similarly, to quantify particle bound PAHs, precleaned 6-mm QFF punches were spiked with 1 µl of 0.1, 0.5, 1.0, 2.0, 5.0, and 10 ng µl⁻¹ mixed PAH standards in toluene.

Quality assurance

The PDMS traps were conditioned prior to use at 280 °C for 16 h under hydrogen (99.999% or more purity; AFROX) with a gas flow of 100 ml min⁻¹ using a Gerstel TC 2 Tube Conditioner. Quartz fiber filter punches were rinsed twice with DCM and methanol after which they were dried in an oven at 200 °C for 2 h and stored in an amber vial in a desiccator prior to use. Immediately after sampling, the filters were stored in amber vials, and the traps were sealed with end caps. Each denuder component was individually wrapped in sterilized aluminum foil and placed in separate Ziploc bags in a cooler box containing ice packs on site. The samples were then were placed in a freezer at -18 °C between the time of collection and analysis.

Calibration was performed in duplicate, and 1 µl of an I_{Std} mixture, containing d₈-naphthalene, d₁₀-phenanthrene, d₁₀-pyrene, and d₁₂-chrysene (1 ng µl⁻¹) was spiked onto all samples and standards prior to analysis to correct for any instrument variability or matrix effects; calibration curves were derived from the area ratio of target analyte: I_{Std}. Procedural blanks were

TABLE 3: Limits of detection and limits of quantification for individual polycyclic aromatic hydrocarbons detected in polydimethylsiloxane trap and quartz fiber filter samples (ng m⁻³)

| PAH | PDMS trap | | QFF | |
|---------|-----------|-------|------|-------|
| | LOD | LOQ | LOD | LOQ |
| Nap | 0.06 | 0.19 | 0.04 | 0.15 |
| Nap 1 M | 1.15 | 3.82 | 0.20 | 0.68 |
| Acy | 1.98 | 6.61 | 0.47 | 1.57 |
| Acey | 0.89 | 2.97 | 0.86 | 2.88 |
| Flu | 1.17 | 3.89 | 2.08 | 6.94 |
| Phe | 6.58 | 21.92 | 4.32 | 14.39 |
| Ant | 4.15 | 13.84 | 1.18 | 3.92 |
| FluAn | 9.12 | 30.39 | 6.41 | 21.38 |
| Pyr | 8.56 | 28.55 | 5.46 | 18.19 |

LOD = limit of detection; LOQ = limit of quantitation; PAH = polycyclic aromatic hydrocarbon; QFF = quartz fiber filter; PDMS = polydimethylsiloxane. See Table 2 for other abbreviations.

analyzed in conjunction with the samples to ensure no carryover. Linear regression analyses were performed using the Data Analysis Toolkit in Excel, and correlation of determination values of more than 0.90 were used as a statistical measure to indicate a good linear fit and validate the analyte method. The limit of detection (LOD) of each target compound was calculated as 3 times the signal-to-noise (S/N) peak-to-peak ratio and the limit of quantitation (LOQ) as 10 times the S/N ratio using the lowest concentration calibration standard. The LOD and LOQ values for PDMS trap and QFF samples are presented in Table 3. The LOD values ranged from 0.06 to 9.12 ng m⁻³ for the PDMS traps and 0.04 to 6.41 ng m⁻³ for the QFF samples.

Statistical evaluation

Statistical evaluation, including principal component analysis (PCA), was performed using XLSTAT (Addinsoft) software and ChromaTOF Tile (LECO). A *p* value of 0.05 was used for data comparison among the primary trap, the filter, and the secondary trap, and *F* ratios were evaluated for the significant compounds (*F* ratio greater than 100). Supporting Information, Table S2, details the method parameters for the PCA analysis.

RESULTS AND DISCUSSION

The type of burn, speed of burn, and prevailing weather and crop conditions all had an influence on the resultant PAH concentration. These conditions and any significant observations are detailed in Table 1. Field blank samples were taken at burn events at which only traces of naphthalene and 1-methyl naphthalene were detected and were corrected for in the samples; the concentrations of PAHs detected on the field blank samples are reported in the Supporting Information, Table S1.

Total PAH emissions

Figure 3 depicts the ΣPAHs from all five burn events. It is immediately evident that downwind PAH concentrations were

significantly higher than the upwind samples, and it can be concluded that the preharvest burning of sugar cane biomass is a major source of PAHs in the atmosphere during a burn event. Likewise, in another similar study in Florida (USA), it was concluded that the sugar cane harvesting season resulted in 15x higher PAH concentrations than during the growing season, indicating a substantially higher exposure of the population to PAHs due to the burning events (Sevimoglu & Rogge, 2016). More recently, the same authors also positively correlated the ambient concentrations of PAHs with the biomass combustion markers levoglucosan and potassium during burn events (Sevimoglu & Rogge, 2019).

The sources of the background PAHs in the upwind samples could be attributed to the burns that were underway or had taken place in the area or from diesel exhaust emissions from vehicles operating nearby including the water truck that is required to be present during burning events in case of emergency or wildfire. Cigarette smoke from the farm workers was also documented as a potential source of PAHs in the ambient air.

In the present study, the total PAHs in the primary trap samples for all the burn events (adding up to $17.2 \mu\text{g m}^{-3}$) accounted for over 90% of total PAHs detected in the samples, signifying that the majority of PAHs were in the gas phase and that determination of PAHs associated with PM only would lead to a gross underestimation of potential environmental and human health impacts.

The majority of the samples showed the detection of both gas and particulate PAHs, which is consistent with denuder theory in which the primary PDMS trap sorbed gas phase analytes while particle-associated analytes passed through the trap and were collected on the downstream filter. Particle-bound analytes primarily remain particle bound on the filter, but should they blow

off from the filter, they are trapped on the secondary trap. Blow-off is loss of particle phase analyte caused by the pressure gradient existing through the filter (Kumari & Lakhani, 2018) and disturbance of the gas particle equilibrium (Forbes & Rohwer, 2009). In the present study, the loss due to blow-off is expected to be minimal because of low sampling flow rates and sampling intervals. In addition, the low back pressure across the denuder sampling device throughout this sampling interval reduced the potential for such effects to occur.

The upwind samples at each site showed the detection of two-ring 1-methyl naphthalene in the range of less than LOQ to $0.10 \mu\text{g m}^{-3}$. The background contribution of lighter PAHs from the secondary trap samples may be due to breakthrough of the most volatile PAHs from the primary trap, because the denuder devices are validated to have a breakthrough volume of 5 L for naphthalene at a sampling flow rate of 500 ml min^{-1} (Forbes et al., 2012; Forbes & Rohwer, 2009). Our sampling volumes were slightly higher than this, with an average sampling volume of $5.20 \pm 0.70 \text{ L}$, leading to the slight breakthrough of the two-ring PAHs. Another consideration is that these small PAHs can be transiently associated with particles and seeing that the two-ring PAHs are the most volatile, loss by volatilization from the filter may occur during sampling.

For the downwind samples, the temperatures at the sampling locations were higher than ambient temperatures, due to the burning event, and thus the breakthrough volumes would be slightly reduced because the higher temperatures reduce sorption capacity of analytes and hence reduce retention on the primary PDMS trap. Nonetheless, these PAHs would be subsequently trapped downstream on the secondary PDMS absorbent and no loss of analyte would result.

When looking at each burn event individually (Figure 4 and Supporting Information, Table S1) a distinct difference in

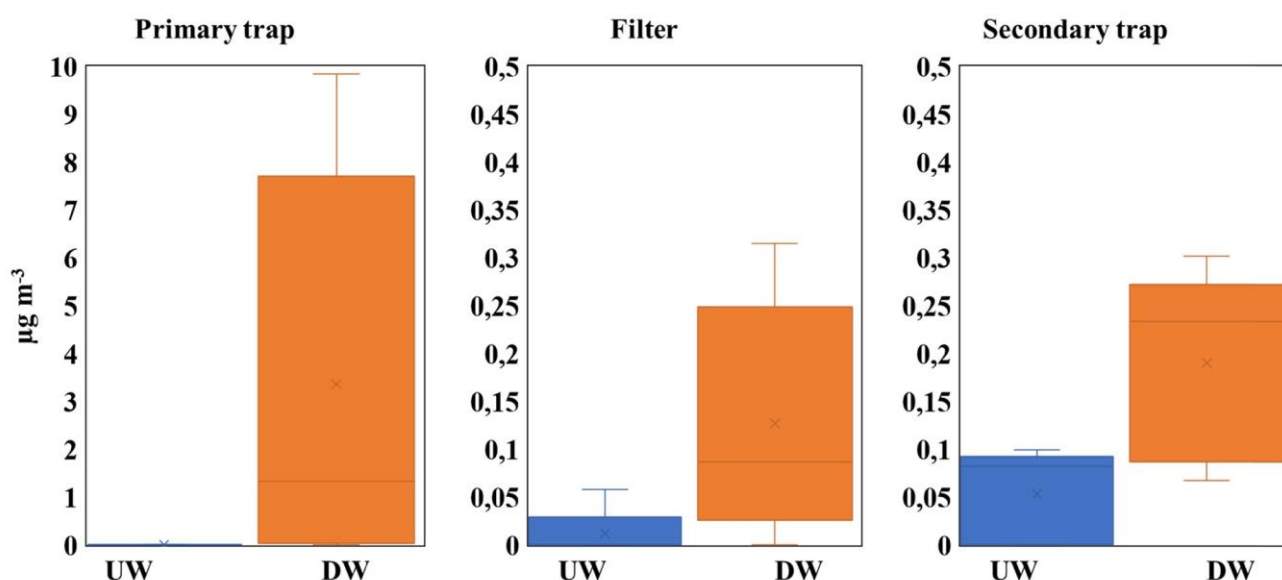


FIGURE 3: Box plot representing the sum of polycyclic aromatic hydrocarbons (PAHs) detected on the primary trap, filter, and secondary trap per burn event in upwind (UW) and downwind (DW) samples (total $n = 39$ for all plots with each plot representing $n = 5$ across the five burn events). The maximum and minimum values represent the extreme PAH concentrations found at burn events, with the area between the 25th and 75th percentiles representing the spread of PAH concentration between the other burn events.

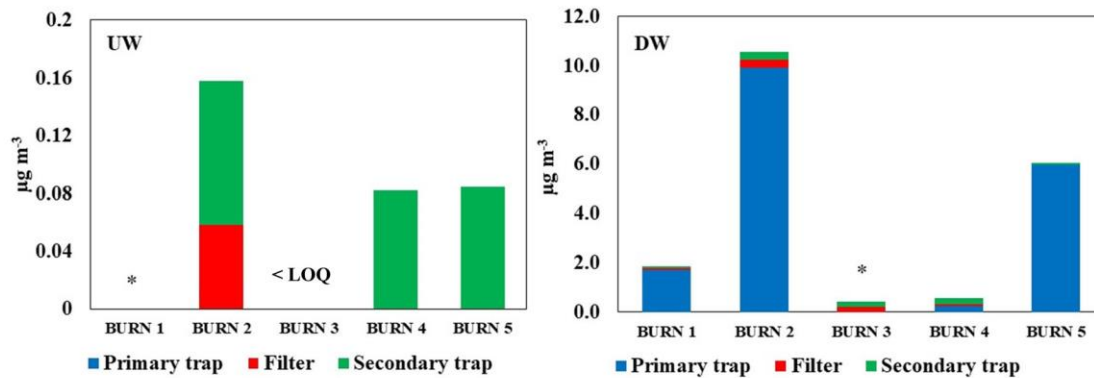


FIGURE 4: Upwind (UW; left) and downwind (DW; right) total polycyclic aromatic hydrocarbon (PAH) concentrations found on the primary trap, filter, and secondary trap of the denuder device per burn event (1–5) *Burn 1 upwind filter and secondary trap were in-field sample losses, and Burn 3 downwind primary trap was lost due to a power outage during instrumental analysis. LOQ = limit of quantitation.

concentration can be seen between each burn event that can be attributed to the prevailing weather conditions, variations in the crop variety (moisture and leaf matter), and the nature of the burn event. Figure 4 shows the variation in PAH concentration and PAH partitioning between burn events for both upwind and downwind samples. The variation emphasizes the effect that the prevailing weather, crop, and burn conditions have on the emissions. The upwind filter and secondary trap of Burn 1 fell off the sampling ladder onto the floor and were excluded from the sampling set due to possible contamination. The downwind primary trap of Burn 3 was not included due to technical complications during analysis. The lost samples were not included in subsequent calculations.

From Figure 4, it can be seen that Burn 2 had the highest total PAH concentrations in both upwind and downwind samples, with the highest portion being represented by the downwind gas phase PAHs, equating to $10.23 \mu\text{g m}^{-3}$. Burn 2 was the only burn event that was done during clear sky conditions, and it was accompanied by gusty winds. The higher ambient temperature and lower humidity compared with other burn events would be more conducive toward gas phase partitioning, which is confirmed by the largest portion of PAHs being detected on the primary trap samples. The burn event was a slow burn due to the gusty winds, which resulted in a smoldering fire, and poorer combustion conditions, and thus more combustion-associated emissions during the sampling interval.

Burn 5 also showed a significantly high gas phase PAH concentration, and this burn event was the only other burn event that was documented as a slow burn. The N58 crop variety had erect leaves with a more bare stalk compared with other varieties, and it also is characterized by abundant crop residue (South African Sugarcane Research Institute, 2022) that is strongly adhered to the stalk, which can influence the burning efficiency and may introduce a temperature gradient through the crop, leading to zones of poorer combustion efficiency and resulting in elevated PAH emissions.

Burn 4 had the lowest Σ PAH emissions in the downwind samples. This marked reduction in emissions can be partly attributed to the fact that a very narrow portion of the sugar cane

was lit to start the event, and this was when the sampling commenced; therefore the volume of sugar cane burnt was initially smaller, resulting in fewer emissions during the short sampling interval. The crop variety characterized by abundant trash significantly contributed to efficient and contained combustion, which was evident by the small amount of residual smoke produced. The still conditions, trashy crop variety, and high humidity are variables contributing toward lower PAH emissions because the burn was characterized by higher flames and a faster and more contained burn with the least amount of residual smoke produced. As a result, Burn 4 can be an indicator of more favorable preharvest burn conditions not only for reduced PAH emissions but also for better control of the fire.

Although each burn event was recorded in as much detail as possible, it must be noted that there are certain limitations for direct comparability of events. Due to the different meteorological conditions, field orientations, field shape, crop size, and age, it was difficult to standardize the burns. It was not possible to get close to the field during the burn, for safety reasons, but it would be useful to be able to view and thus compare the burn events in real time. This may be possible with drone technology for safe and accurate comparison of real-life burning campaigns.

PAH Profiles

The individual gas and particle phase PAH fingerprints are presented in Figure 5 for each burn event. These concentrations are purely as a result of the burn event, because the PAHs detected in the upwind samples were considered as background concentrations and were thus corrected for in each downwind sample by subtracting the upwind PAH concentration from the corresponding downwind PAH concentration.

The fingerprints per burn event were similar in that the majority of the emissions were found to be in the gas phase with naphthalene being the most abundant PAH in each primary trap sample except for Burn 4, whereas the sample loss in Burn 3 cannot be commented on. However, the similarities end there: the concentration and range of individual PAHs differed

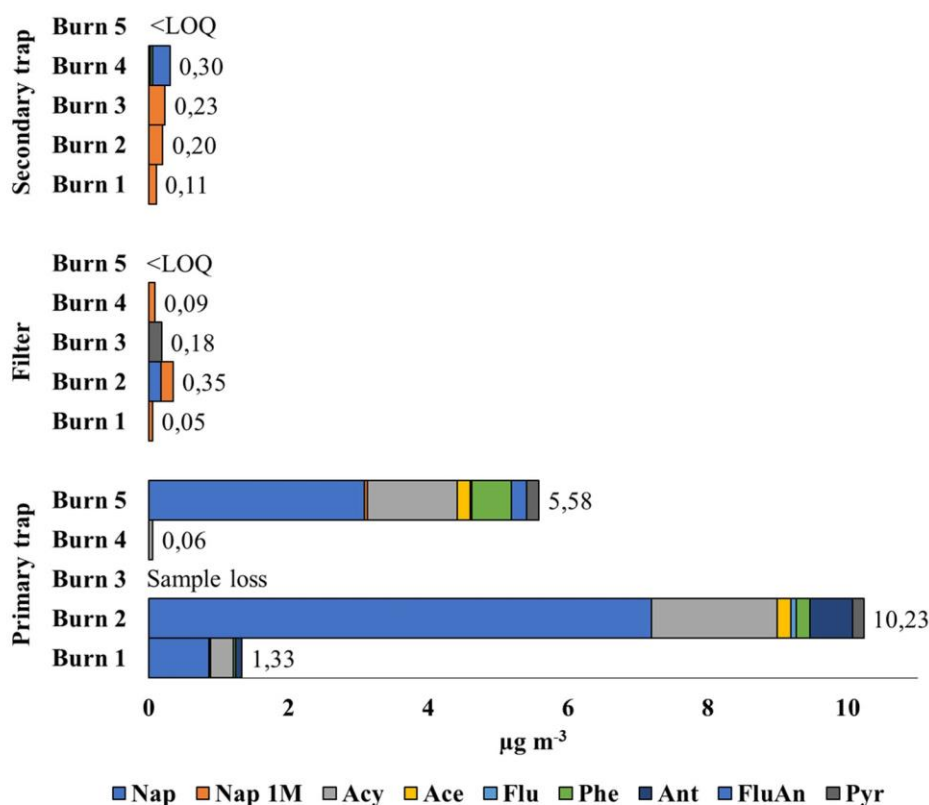


FIGURE 5: Individual polycyclic aromatic hydrocarbon (PAH) concentrations detected during each burn event on the primary trap, filter, and secondary trap of the denuder sampling device. LOQ = limit of quantitation. For other abbreviations, see Table 2.

significantly between each burn event. The concentration as well as number of PAHs also differed markedly between the primary trap and filter samples, indicating the complexity of the partitioning of PAHs with prevailing weather and burn conditions. The lower molecular weight PAHs such as naphthalene and 1-methyl naphthalene that were detected on the filter samples, which are normally partitioned in the gas phase, were likely in a condensed form due to the humidity before or during sampling. Kural et al. (2018) investigated the relationship between PAH concentrations and meteorological conditions in Istanbul, Turkey and reported that due to precipitation, high relative humidity, and high dust concentration, naphthalene was found in the condensed phase associated with particles. This complexity would be expected to increase even more with time due to additional atmospheric aging processes and reactions that occur resulting in the formation of secondary organic aerosols and harmful oxygenated and nitrated PAH derivatives (Keyte et al., 2016; Vione et al., 2004).

From Figure 5, it can be seen that the primary trap samples had the highest concentrations of PAHs, with Burn 2 and Burn 5 having the highest total PAH concentrations, of 10.23 and 5.58 $\mu\text{g m}^{-3}$ respectively. The numbers of PAHs detected were also the most during these two burn events, ranging from two-ring naphthalene to four-ring pyrene. As discussed in the *Total PAH emissions* section, Burns 2 and 5 were conducive to higher incomplete combustion emissions based on the conditions of the burn, the crop variety, and meteorological parameters that

consequently resulted in the formation of more PAHs including the higher molecular weight pyrene and fluoranthene. The slow burns associated with these two events produced more of a smolder than a high flame burn, which would result in incomplete combustion and overall lower temperature burns; they are also accompanied by higher amounts of PM, which act as nuclei for PAH particle associations. The overall gas-to-particle partitioning for these burn events favored the gas phase, which is influenced largely by the ambient temperature, relative humidity, and physical properties of the PAH.

The lowest total PAH concentrations of 0.06, 0.09, and 0.30 $\mu\text{g m}^{-3}$ for the primary trap, filter, and secondary trap, respectively, are associated with Burn 4 (Figure 5). The lower total PAH emissions in this burn event can be mainly attributed to the fast and contained burn with more complete combustion. This burn event reflects the lowest number of PAHs in the gas phase, with 1-methyl naphthalene and acenaphthylene being the only PAHs detected on the primary trap. Interestingly, the secondary trap sample for Burn 4 showed the largest range of PAHs compared with the other secondary trap samples, with the detection of 1-methyl naphthalene, phenanthrene, and fluoranthene. The heavier PAHs have larger breakthrough volumes than naphthalene, so it is not likely due to breakthrough, and blow-off is expected to be minimal due to the sampling methodology; thus the presence of these PAHs on the secondary trap may be attributed to transient particle association. This can be explained by the substantially higher

humidity and lower ambient temperatures during Burn 4 compared with other burn events, which favored particle phase association.

The findings from our study were consistent with what was reported in a study by Li et al. (2016); these authors found that atmospheric PAH emissions due to biomass burning were dominated by the light PAHs: naphthalene, phenanthrene, pyrene, fluorene, acenaphthylene, anthracene, and acenaphthene (Chen et al., 2017; Li et al., 2016).

The presence of the heavier PAHs such as benzo[a]pyrene, benzo[b]fluoranthene, benzo[ghi]perylene, dibenz[a,h]anthracene, and indeno[1,2,3-cd]pyrene was not detected in any of the samples, which can be attributed to limits below quantification as well as the small sample volumes and amount of PM collected, because these analytes are expected to be predominantly particle associated; however, heavier PAHs have been detected and quantified with this analytical method previously (Geldenhuys et al., 2015). Desorption of SVOCs from PM on filters was optimized and demonstrated with TD-GC×GC-MS analysis in various other studies (Dragan et al., 2020; Schnelle-Kreis, Sklorz, et al., 2005; Schnelle-Kreis, Welthagen, et al., 2005); in the present study, the LODs for PAHs on the QFF ranged from 0.04 to 6.41 ng m⁻³ with the heavier four- to six-ring PAHs having the higher LODs. The LODs for PAHs on the traps ranged from 0.06 to 9.12 ng m⁻³ (refer to Table 3). Heavier four- to six-ring PAHs were detected in low concentrations in PM in other studies, with Sevimoglu and Rogge (2016) finding that 55%–70% of the total particulate PAH mass was associated with particle diameters smaller than 0.49 μm. These authors reported total particulate PAH levels of 7.36 ng m⁻³ in rural regions and 3.00 ng m⁻³ in urban regions during the sugar cane harvest season (Sevimoglu & Rogge, 2016).

Determination of PAH toxic equivalence

The toxic equivalency factor (TEF) method is employed to evaluate structurally related compounds sharing a common mechanism of action (Delistraty, 1997). Toxicity of a specific PAH is often expressed relative to benzo[a]pyrene. The potential carcinogenicity of the PAH exposure is estimated based on the calculation of toxic equivalent quotient (TEQ), whereby benzo[a]pyrene-like toxicity or toxic equivalents are determined using the following equation:

$$TEQ = \sum(PAH_i \times TEF_i),$$

where PAH_i and TEF_i are the concentration and TEF, respectively, for individual PAHs.

The TEFs were proposed by Nisbet and Lagoy (1992) based on the toxicity and carcinogenic potential of individual PAHs relative to benzo[a]pyrene. Table 4 shows the TEQ values that were calculated based on the determined concentrations of the total (gas and particle) PAHs (μg m⁻³).

The highest risk potential of exposure was associated with Burn 2, which resulted in the largest TEQ. There are currently no exposure limits for PAHs in many countries, including South Africa; however, it is vital to understand the toxic equivalence concentration levels and potential health risks of exposure to PAHs to ensure that suitable risk assessment and risk management plans can be implemented. Several regulatory agencies such as the US Occupational Safety and Health Administration, the US National Institute for Occupational Safety and Health, and the German Committee on Hazardous Substances have imposed regulatory limits for coal tar pitch volatiles (benzene-soluble fraction) including anthracene, benzo[a]pyrene, phenanthrene, chrysene, and pyrene of 0.20 mg m⁻³ (Breuer, 2010; Rezaei et al., 2015). Although the Σbenzo[a]pyrene_{TEQ} for each burn event is well below the referenced regulatory limit for coal tar pitch volatiles, these findings suggest that at levels encountered in the air during the sugarcane burning season, exposure to individual and complex mixtures of PAHs may pose an increased health risk that varies between burn events. It should be noted that the risk estimates presented are not definitive but should rather be seen only as a crude estimation of potential cancer risk from the PAH inhalation.

Principal component analysis

Principal component analysis is a statistical technique employed to create uncorrelated variables in large data sets to successively maximize variance. This tool aids in increasing interpretability of data while minimizing loss of vital information. Figure 6 shows the loading and scores plot for total PAH concentrations.

The loading and scores plots are depicted for total PAH concentrations between the five burn events and how they

TABLE 4: Toxic equivalency factor values for polycyclic aromatic hydrocarbons (PAHs) and the calculated toxic equivalent quotient values for total gas and particle PAHs (μg m⁻³)

| PAH | TEF | Burn 1 | Burn 2 | Burn 3 | Burn 4 | Burn 5 |
|-------|----------------------|----------|----------|----------|----------|----------|
| Nap | 0.001 | 4.04E-04 | 6.00E-04 | 2.34E-04 | 3.59E-04 | 4.84E-04 |
| Acy | 0.001 | 3.18E-04 | 1.80E-03 | | 5.65E-05 | 1.29E-03 |
| Ace | 0.001 | | 2.02E-04 | | | 1.89E-04 |
| Flu | 0.001 | | 7.58E-05 | | | 2.52E-05 |
| Phe | 0.001 | 4.00E-05 | 1.99E-04 | | 1.83E-05 | 5.59E-04 |
| Ant | 0.01 | 8.56E-04 | 3.02E-03 | | | |
| FluAn | 0.001 | | | | 1.22E-04 | 2.21E-04 |
| Pyr | 0.001 | | 8.05E-05 | 1.82E-04 | | 1.76E-04 |
| | Σ BaP _{TEQ} | 1.62E-03 | 5.97E-03 | 4.16E-04 | 5.56E-04 | 2.94E-03 |

PAH = polycyclic aromatic hydrocarbon; TEF = toxic equivalency factor. For other abbreviations, see Table 2.

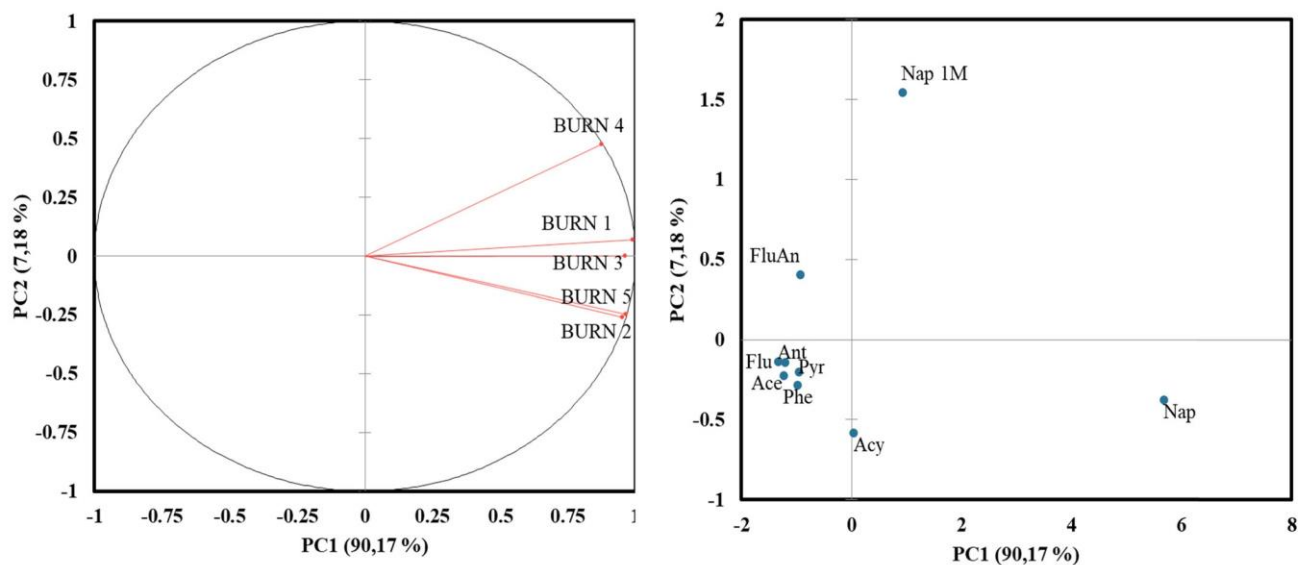


FIGURE 6: Loading plot (left) and scores plot (right) for total polycyclic aromatic hydrocarbon (PAH) concentrations (downwind [DW] gas + particle phase) between the different burn events. PC = principal component. For other abbreviations, see Table 2.

correlate to one another. The sum of components PC1 and PC2 accounted for 97.35% of variability from the initial data set. The first PC dimension represents 90.17% of the data, and the second PC dimension accounts for 7.18%. The angles between the vectors are all acute, indicating linked variables, and the vector lengths indicate the representativeness quality in the investigated PCA dimensions PC1 and PC2, which is very good. The loading plot validates previous discussion and shows the positive correlation between Burn 2 and Burn 5. Burn 4 shows the least correlation to the burn events in terms of PAH emissions. The scores plot relates individual PAHs to variables and to one another. The individual PAHs show that the lighter two- to three-ring PAHs, specifically naphthalene, 1-methyl

naphthalene, and acenaphthylene, are the most significant contributors toward variance between burn sites. The variance between the burn events cannot only be attributed to the emissions and therefore Figure 7 also includes meteorological data to see the bigger picture and how numerous factors contribute to emissions.

To identify the influence that meteorological parameters may have had on the PAH concentrations at the different burn events, a second PCA was conducted. Although the sample set is limited, the analysis provides valuable preliminary information on the correlation of certain meteorological parameters with PAH concentration, as well as their impact on atmospheric partitioning. It is hypothesized that temperature will influence the partitioning, with higher temperatures favoring the gas phase, which was evident from the results (Figure 7) with a close correlation evident between temperature and the primary trap PAH concentration (which samples gas phase analytes). Humidity was expected to have a positive correlation to condensed particle phase PAH concentrations. The results showed some correlation with respect to PC1 between humidity and the secondary trap PAH concentration, which may relate to the repartitioning of particle phase analytes into the gas phase on re-equilibration during sampling. Higher wind speeds may result in lower total PAH concentrations due to dispersion and dilution effects, but in the case of biomass burning, wind speed also impacts combustion efficiencies and thereby PAH emissions. In Figure 7 a strong correlation between wind speed and primary trap PAH concentrations is evident.

The biplot showing the loading and scores plots is depicted for total PAH partitioning at each burn event as well as the inclusion of meteorological data as variables between the five sites (Figure 7). Axes PC1 and PC2 account for 79.02% of variability from the initial data set. The horizontal axis is the first PC dimension and represents 58.57% of the data, and the second

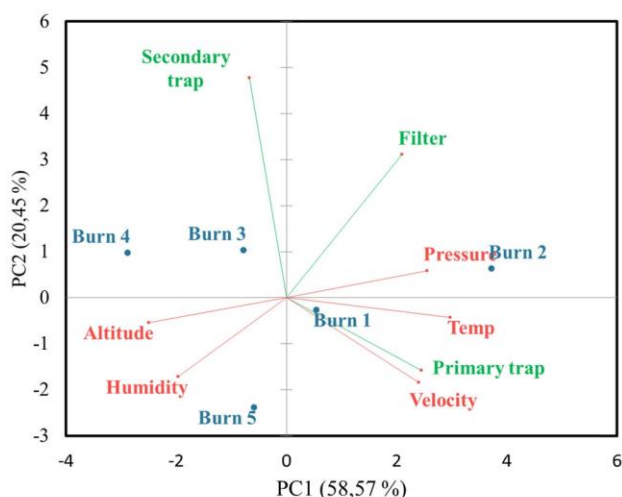


FIGURE 7: Biplot for sampling and meteorological variables relating to individual burn events. Total downwind (DW) polycyclic aromatic hydrocarbons (PAHs) on primary trap, filter, and secondary trap per burn event were used for the plot. PC = principal component.

dimension accounts for 20.45%. The investigated variables are represented by the red vectors for the meteorological variables and green vectors for the primary trap, filter, and secondary trap samples. The vector lengths indicate the representativeness quality in the investigated PC dimensions PC1 and PC2. The acute angles between the filter and secondary trap samples indicate positively linked variables, which confirms the occurrences of transient particle association and the relationship among the primary trap, filter, and secondary trap samples and points to efficient denudation by the samplers. The biplot relating individual burn events to the discussed variables clearly indicates that there is significant variance between each burn event, with the PAH partitioning and atmospheric conditions being key contributors to the observed variance. The wind velocity was less of an influence than expected with Burn 2 and Burn 5 showing the highest gas phase PAH concentrations but also being the two events with the highest recorded wind speeds. The crop variety played more of an influential role in the number and type of PAHs emitted as well as the partitioning thereof. The expanded ChromaTOF Tile PCA score and loading plot with other significant chemical features associated with biomass burning within the primary trap, filter, and secondary trap can be found in the Supporting Information, Figure S1 and Table S3. The key chemical feature contributing to the variance from the filter samples was found to be phthalic anhydride, whereas 1,3-dioxolane and benzene 1-ethyl-4-methyl were the dominant features on the secondary traps. The loading plot was dominated by chemical features found on the primary traps, with benzaldehyde, tridecane, azulene, 1-methyl naphthalene, and furfural being the main markers influencing the principal components. Benzaldehyde is an intermediate in the atmospheric oxidation of aromatic compounds, and the presence of this compound, as well as other organic features identified, may contribute to the formation of ozone and secondary organic aerosols in the atmosphere air and further contribute to poor air quality.

Correlation of black carbon measurements to PAH concentrations

The portable aethalometers used during sampling provided measurements of equivalent black carbon originating from emitted biomass particles. Table 5 shows the mean equivalent black carbon concentrations, which were background-corrected using the upwind samples.

The highest values for black carbon were reported for Burn 2, with a mean value equating to $430.91 \mu\text{g m}^{-3}$ for the stationary sample and the highest mean of $402.08 \mu\text{g m}^{-3}$ for a personal sample that was positioned on the collar of the researcher standing close to the stationary sample. Burn 5 showed the second highest black carbon value of $218.58 \mu\text{g m}^{-3}$ for the personal sampler that was fitted to the researcher walking around the field during the burn. This value was significantly higher than those reported for the other samples, which indicates that personal exposure can be minimized by the position of the worker during the burn event. The black carbon values correlated well with total PAHs (correlation coefficient $[r] = 0.91$ as per Supporting Information, Figure S2), with Burns 2 and 5 showing significantly higher concentrations of both PAHs and black carbon. The higher black carbon values are also indicative of more smoke during the burn and thus more incomplete combustion; therefore monitoring of black carbon provides a complementary tool to the monitoring of PAHs.

CONCLUSIONS

The sugar cane industry represents a vital portion of the South African economy, but the adverse environmental implications of preharvest practices need to be well understood, due to the atmospheric air pollutants emitted during biomass burning. These raise health concerns not only for the workers who are on site during the burn but also to rural and urban populations in the vicinity. In our study, gas and particulate PAHs were simultaneously determined, for the first time in South Africa, for different preharvest burn events at five different sites in the Kwa-Zulu Natal Province. Small portable denuder devices were successfully employed for sampling; these offer advantages over conventional methods in that they minimize sampling artifacts and avoid time-consuming and environmentally unfriendly sample preparation techniques. They are also readily portable and give additional insight into atmospheric partitioning. During preharvest sugar cane burns, the individual and total PAH concentrations, ranging from two-ring naphthalene to four-ring pyrene, increased up to 10 times compared with upwind samples, and over 90% of the overall total PAHs, equating to $17.20 \mu\text{g m}^{-3}$, were found to exist in the gas phase and $1.68 \mu\text{g m}^{-3}$ in the particulate phase. This is a significant finding because the smaller, gas phase PAHs, which have higher vapor pressures, undergo atmospheric oxidative

TABLE 5: Mean and median equivalent black carbon concentrations determined via aethalometer readings during different sugar cane burn events

| Burn no. | Stationary samples | | Personal sampler 1 | | Personal sampler 2 | | Personal sampler 3 | |
|----------|-------------------------------|---------------------------------|-------------------------------|---------------------------------|-------------------------------|---------------------------------|-------------------------------|---------------------------------|
| | Mean ($\mu\text{g m}^{-3}$) | Median ($\mu\text{g m}^{-3}$) | Mean ($\mu\text{g m}^{-3}$) | Median ($\mu\text{g m}^{-3}$) | Mean ($\mu\text{g m}^{-3}$) | Median ($\mu\text{g m}^{-3}$) | Mean ($\mu\text{g m}^{-3}$) | Median ($\mu\text{g m}^{-3}$) |
| Burn 1 | 18.06 | 4.04 | 41.01 | 22.26 | 21.96 | 7.37 | 6.34 | 2.98 |
| Burn 2 | 430.91 | 125.53 | 269.30 | 154.95 | 166.31 | 26.68 | 402.08 | 282.19 |
| Burn 3 | 40.41 | 3.78 | 23.33 | 2.36 | 18.58 | 2.07 | 22.58 | 2.71 |
| Burn 4 | 0.91 | 1.07 | 8.01 | 1.22 | 2.48 | 2.42 | <LOQ | <LOQ |
| Burn 5 | 1.90 | 1.45 | 1.77 | 1.59 | 3.03 | 3.06 | 218.58 | 8.58 |

Conditional formatting color scales were employed for visual effect, with red indicating the highest and green indicating the lowest concentrations. eBC = equivalent black carbon; LOQ = limit of quantitation.

gas-to-particle conversions and multiphase aging reactions and contribute to the toxicity of generated secondary organic aerosols (Offer et al., 2022). The PAH fingerprints were significantly different between each burn event, indicating the vital role that prevailing weather conditions as well as the nature of the burn and the crop play in emissions and the gas-particle partitioning thereof. The lowest total and individual PAH emissions were found for the burn event that was the most contained and rapid where there was no recorded wind.

It is recommended that the method employed be further optimized, specifically the method for desorption of PAHs from the QFF for the accurate quantification of heavier PAHs, which have higher toxicity. Further investigations should be conducted to better elucidate PAH phase partitioning, with an emphasis on transient phase associations in the fresh emissions to gain a better understanding of the role that atmospheric conditions such as ambient temperature and relative humidity may play. In this regard, a large sample set would be needed to demonstrate statistically significant correlations between a large number of variables, to form definitive conclusions. Atmospheric aging can result in the formation of toxic PAH derivatives due to chemical oxidation of primary gaseous PAHs, and because low-molecular-weight gas phase PAHs were found to be more abundant in our study, it would be valuable to characterize and quantify these derivatives as well as secondary organic aerosols resulting from the condensation of gas phase PAHs onto particles.

The findings of our study suggest that the determination of PM alone would lead to a gross underestimation of potential environmental and human health impacts and therefore gas phase PAH pollutants should be included when conducting risk assessments and considering control strategies. Although the burn events described in our study are performed in accordance with industry regulations, the present study may aid in further optimizing the burn conditions to ensure complete combustion and thus fewer PAH emissions, as seen during still conditions with a more contained and fast burn. Our study can aid in the determination of best practice in sugar cane harvesting toward enhancing greater sustainability. One consideration in this respect is the exploration of a combustion alternative and the conversion of biomass waste into biofuels, while simultaneously minimizing the emission of harmful air pollutants.

Supporting Information—The Supporting Information is available on the Wiley Online Library at <https://doi.org/10.1002/etc.5579>.

Acknowledgments—The Department of Chemistry at the University of Pretoria as well as Impala Platinum are acknowledged for their support and resources. The Helmholtz Zentrum, Helmholtz International Lab aeroHEALTH and the Federal Ministry of Education and Research (BMBF) in Germany are also duly acknowledged, with special thanks to the Comprehensive Molecular Analytics (CMA) group at Helmholtz Zentrum München. LECO is acknowledged for the use of ChromaTOF Tile software. Funding provided by the University of Pretoria,

Impala Platinum, and the National Research Foundation of South Africa (grant 105877) is acknowledged. Our research was supported by the Helmholtz Association/Berlin and the BMBF, research contract 01DG17023.

Disclaimer—The authors declare no conflict of interest.

Author Contributions Statement—**G. Geldenhuys**: Methodology; Validation; Formal analysis; Data curation; Writing—original draft and review & editing. **J. Orasche**: Methodology; Formal analysis; Writing—review & editing. **G. Jakobi**: Methodology; Formal analysis; Writing—review & editing. **Ralf Zimmermann**: Conceptualization; Writing—review & editing; Funding acquisition. **P.B.C. Forbes**: Conceptualization; Visualization; Project administration; Methodology; Formal analysis; Writing—review & editing; Funding acquisition.

Data Availability Statement—All associated data and calculation tools are available in the Supporting Information or directly from the corresponding author (patricia.forbes@up.ac.za).

REFERENCES

- Amarillo, A. C., & Carreras, H. (2016). Quantifying the influence of meteorological variables on particle-bound PAHs in urban environments. *Atmospheric Pollution Research*, 7(4), 597–602.
- Breuer, D. (2010). Analytical performance issues: GESTIS database: International limit values for chemical agents—A readily accessible source of Occupational Exposure Limits (OELs). *Journal of Occupational and Environmental Hygiene*, 7(7), D37–D42.
- Chen, J., Li, C., Ristovski, Z., Milic, A., Gu, Y., Islam, M. S., & He, C. (2017). A review of biomass burning: Emissions and impacts on air quality, health and climate in China. *Science of the Total Environment*, 579, 1000–1034.
- Climate-Data.org. (nd). Climate: Kwazulu-Natal. <https://en.climate-data.org/africa/south-africa/kwazulu-natal>
- Dat, N.-D., & Chang, M. B. (2017). Review on characteristics of PAHs in atmosphere, anthropogenic sources and control technologies. *Science of the Total Environment*, 609, 682–693.
- de Andrade, S. J., Cristale, J., Silva, F. S., Zocolo, G. J., & Marchi, M. R. (2010). Contribution of sugar-cane harvesting season to atmospheric contamination by polycyclic aromatic hydrocarbons (PAHs) in Araraquara city, Southeast Brazil. *Atmospheric Environment*, 44(24), 2913–2919.
- Delistraty, D. (1997). Toxic equivalency factor approach for risk assessment of polycyclic aromatic hydrocarbons. *Toxicological & Environmental Chemistry*, 64(1–4), 81–108.
- Dragan, G. C., Kohlmeier, V., Orasche, J., Schnelle-Kreis, J., Forbes, P. B., Breuer, D., & Zimmermann, R. (2020). Development of a personal aerosol sampler for monitoring the particle–vapour fractionation of SVOCs in workplaces. *Annals of Work Exposures and Health*, 64(8), 903–908.
- Elorduy, I., Elcoroaristizabal, S., Durana, N., García, J. A., & Alonso, L. (2016). Diurnal variation of particle-bound PAHs in an urban area of Spain using TD-GC/MS: Influence of meteorological parameters and emission sources. *Atmospheric Environment*, 138, 87–98.
- Flack-Prain, S., Shi, L., Zhu, P., da Rocha, H. R., Cabral, O., Hu, S., & Williams, M. (2021). The impact of climate change and climate extremes on sugarcane production. *GCB Bioenergy*, 13(3), 408–424.
- Forbes, P. (2015). *Monitoring of air pollutants: Sampling, sample preparation and analytical techniques* (Vol. 70). Elsevier.
- Forbes, P. B., Karg, E. W., Zimmermann, R., & Rohwer, E. R. (2012). The use of multi-channel silicone rubber traps as denuders for polycyclic aromatic hydrocarbons. *Analytica Chimica Acta*, 730, 71–79.

- Forbes, P. B., & Rohwer, E. R. (2009). Investigations into a novel method for atmospheric polycyclic aromatic hydrocarbon monitoring. *Environmental Pollution*, 157(8-9), 2529–2535.
- Geldenhuis, G., Rohwer, E. R., Naudé, Y., & Forbes, P. B. (2015). Monitoring of atmospheric gaseous and particulate polycyclic aromatic hydrocarbons in South African platinum mines utilising portable denuder sampling with analysis by thermal desorption–comprehensive gas chromatography–mass spectrometry. *Journal of Chromatography A*, 1380, 17–28.
- Godoi, A. F., Ravindra, K., Godoi, R. H., Andrade, S. J., Santiago-Silva, M., Van Vaeck, L., & Van Grieken, R. (2004). Fast chromatographic determination of polycyclic aromatic hydrocarbons in aerosol samples from sugar cane burning. *Journal of Chromatography A*, 1027(1-2), 49–53.
- Hall, D., Wu, C.-Y., Hsu, Y.-M., Stormer, J., Engling, G., Capeto, K., Wang, J., Brown, S., Li, H.-W., & Yu, K.-M. (2012). PAHs, carbonyls, VOCs and PM_{2.5} emission factors for pre-harvest burning of Florida sugarcane. *Atmospheric Environment*, 55, 164–172.
- Keith, L. H. (2015). The source of U.S. EPA's sixteen PAH priority pollutants. *Polycyclic Aromatic Compounds*, 35(2-4), 147–160. <https://doi.org/10.1080/10406638.2014.892886>
- Keyte, I. J., Albinet, A., & Harrison, R. M. (2016). On-road traffic emissions of polycyclic aromatic hydrocarbons and their oxy-and nitro-derivative compounds measured in road tunnel environments. *Science of the Total Environment*, 566, 1131–1142.
- Kohlmeier, V., Dragan, G. C., Karg, E. W., Schnelle-Kreis, J., Breuer, D., Forbes, P. B., & Zimmermann, R. (2017). Multi-channel silicone rubber traps as denuders for gas–particle partitioning of aerosols from semi-volatile organic compounds. *Environmental Science: Processes & Impacts*, 19(5), 676–686.
- Kumari, K. M., & Lakhani, A. (2018). PAHs in gas and particulate phases: Measurement and control. In T. Gupta, A. K. Agarwal, R. A. Argarwal, & N. K. Labhsetwar (Eds.), *Environmental contaminants* (pp. 43–75). Springer.
- Kural, G., Balkis, N. C., & Abdullah, A. K. S. U. (2018). Source identification of polycyclic aromatic hydrocarbons (PAHs) in the urban environment of Istanbul. *International Journal of Environment and Geoinformatics*, 5(1), 53–67.
- Li, X., Yang, Y., Xu, X., Xu, C., & Hong, J. (2016). Air pollution from polycyclic aromatic hydrocarbons generated by human activities and their health effects in China. *Journal of Cleaner Production*, 112, 1360–1367.
- Masih, J., Singhvi, R., Taneja, A., Kumar, K., & Masih, H. (2012). Gaseous/particulate bound polycyclic aromatic hydrocarbons (PAHs), seasonal variation in North central part of rural India. *Sustainable Cities and Society*, 3, 30–36.
- Mugica-Álvarez, V., Hernández-Rosas, F., Magaña-Reyes, M., Herrera-Murillo, J., Santiago-De La Rosa, N., Gutiérrez-Arzaluz, M., & González-Cardoso, G. (2018). Sugarcane burning emissions: Characterization and emission factors. *Atmospheric Environment*, 193, 262–272.
- Mugica-Álvarez, V., Santiago-de la Rosa, N., Figueroa-Lara, J., Flores-Rodríguez, J., Torres-Rodríguez, M., & Magaña-Reyes, M. (2015). Emissions of PAHs derived from sugarcane burning and processing in Chiapas and Morelos México. *Science of the Total Environment*, 527, 474–482.
- Munyeza, C. F., Kohlmeier, V., Dragan, G. C., Karg, E. W., Rohwer, E. R., Zimmermann, R., & Forbes, P. B. (2019). Characterisation of particle collection and transmission in a polydimethylsiloxane based denuder sampler. *Journal of Aerosol Science*, 130, 22–31.
- Nadali, A., Leili, M., Bahrami, A., Karami, M., & Afkhami, A. (2021). Phase distribution and risk assessment of PAHs in ambient air of Hamadan, Iran. *Ecotoxicology and Environmental Safety*, 209, 111807.
- Nisbet, I. C., & Lagoy, P. K. (1992). Toxic equivalency factors (TEFs) for polycyclic aromatic hydrocarbons (PAHs). *Regulatory Toxicology and Pharmacology*, 16(3), 290–300.
- Offer, S., Hartner, E., Di Bucchianico, S., Bisig, C., Bauer, S., Pantzke, J., & Zimmermann, R. (2022). Effect of atmospheric aging on soot particle toxicity in lung cell models at the air–liquid interface: Differential toxicological impacts of biogenic and anthropogenic secondary organic aerosols (SOAs). *Environmental Health Perspectives*, 130(2), 027003.
- Pandey, S. K., Kim, K.-H., & Brown, R. J. (2011). A review of techniques for the determination of polycyclic aromatic hydrocarbons in air. *TrAC, Trends in Analytical Chemistry*, 30(11), 1716–1739.
- Poster, D. L., Schantz, M. M., Sander, L. C., & Wise, S. A. (2006). Analysis of polycyclic aromatic hydrocarbons (PAHs) in environmental samples: A critical review of gas chromatographic (GC) methods. *Analytical and Bioanalytical Chemistry*, 386(4), 859–881. <https://doi.org/10.1007/s00216-006-0771-0>
- Pryor, S. W., Smithers, J., Lyne, P., & van Antwerpen, R. (2017). Impact of agricultural practices on energy use and greenhouse gas emissions for South African sugarcane production. *Journal of Cleaner Production*, 141, 137–145.
- PubChem. (2021). PubChem Database. <https://pubchem.ncbi.nlm.nih.gov/compound>
- Rengarajan, T., Rajendran, P., Nandakumar, N., Lokeshkumar, B., Rajendran, P., & Nishigaki, I. (2015). Exposure to polycyclic aromatic hydrocarbons with special focus on cancer. *Asian Pacific Journal of Tropical Biomedicine*, 5(3), 182–189.
- Rezaei, F., Kakooei, H., Ahmadvani, R., Azam, K., Omid, L., & Shahtaheri, S. J. (2015). Personal exposure to polycyclic aromatic hydrocarbons in newsagents in Tehran, Iran. *Iranian Journal of Public Health*, 44(5), 665.
- Samae, H., Tekasakul, S., Tekasakul, P., & Furuuchi, M. (2021). Emission factors of ultrafine particulate matter (PM < 0.1 μm) and particle-bound polycyclic aromatic hydrocarbons from biomass combustion for source apportionment. *Chemosphere*, 262, 127846.
- Sevimoglu, O., & Rogge, W. F. (2016). Seasonal size-segregated PM₁₀ and PAH concentrations in a rural area of sugarcane agriculture versus a coastal urban area in Southeastern Florida, USA. *Particuology*, 28, 52–59.
- Sevimoglu, O., & Rogge, W. F. (2019). Seasonal variations of PM₁₀—Trace elements, PAHs and Levoglucosan: Rural sugarcane growing area versus coastal urban area in Southeastern Florida, USA. Part II: Elemental concentrations. *Particuology*, 46, 99–108.
- Schnelle-Kreis, J., Sklorz, M., Peters, A., Cyrus, J., & Zimmermann, R. (2005). Analysis of particle-associated semi-volatile aromatic and aliphatic hydrocarbons in urban particulate matter on a daily basis. *Atmospheric Environment*, 39(40), 7702–7714.
- Schnelle-Kreis, J., Welthagen, W., Sklorz, M., & Zimmermann, R. (2005). Application of direct thermal desorption gas chromatography and comprehensive two-dimensional gas chromatography coupled to time of flight mass spectrometry for analysis of organic compounds in ambient aerosol particles. *Journal of Separation Science*, 28(14), 1648–1657.
- Sharma, H., Jain, V., & Khan, Z. H. (2007). Characterization and source identification of polycyclic aromatic hydrocarbons (PAHs) in the urban environment of Delhi. *Chemosphere*, 66(2), 302–310.
- Solomon, S. (2011). Sugarcane by-products based industries in India. *Sugar Tech: An International Journal of Sugar Crops and Related Industries*, 13(4), 408–416. <https://doi.org/10.1007/s12355-011-0114-0>
- South African Sugar Association (SASA). (2012). S.A. Sugar Association, Mount Edgecombe.
- South African Sugar Association. (2019). The South African Sugar Industry Directory 2019/2020 Report. https://sasa.org.za/custom_content/downloads/SASA-ID-2019-20.pdf
- South African Sugarcane Research Institute. (2022). Farms located throughout SA sugar belt. <https://sasri.org.za/variety-improvement/>
- Tan, J.-H., Bi, X.-H., Duan, J.-C., Rahn, K. A., Sheng, G.-Y., & Fu, J.-M. (2006). Seasonal variation of particulate polycyclic aromatic hydrocarbons associated with PM₁₀ in Guangzhou, China. *Atmospheric Research*, 80(4), 250–262.
- Tan, J., Guo, S., Ma, Y., Duan, J., Cheng, Y., He, K., & Yang, F. (2011). Characteristics of particulate PAHs during a typical haze episode in Guangzhou, China. *Atmospheric Research*, 102(1-2), 91–98.
- Vione, D., Barra, S., de Gennaro, G., de Rienzo, M., Gilardoni, S., Perrone, M. G., & Pozzoli, L. (2004). Polycyclic aromatic hydrocarbons in the atmosphere: Monitoring, sources, sinks and fate. II: Sinks and fate. *Annali di Chimica*, 94(4), 257–268. <https://doi.org/10.1002/adic.200490031>
- Zamperlini, G., Silva, M., & Vilegas, W. (1997). Identification of polycyclic aromatic hydrocarbons in sugar cane soot by gas chromatography–mass spectrometry. *Chromatographia*, 46(11-12), 655–663.

Paper 2: Supplementary Information

Table S1 Quantified PAHs ($\mu\text{g m}^{-3}$) as the sum of the primary trap (PT), filter (F) and secondary trap (ST) for each burn event.

| | Field Blank | | | | | | | | | | | |
|-----------|-------------|--------|----------|--------|------|------|------|------|------|-------|------|-------|
| | Nap | Nap 1M | | | | | | | | | | |
| FB PT | 0.27 | 0.38 | | | | | | | | | | |
| FB F | 0.78 | | | | | | | | | | | |
| FB ST | 1.25 | | | | | | | | | | | |
| | Upwind | | Downwind | | | | | | | | | |
| | Nap | Nap 1M | Nap | Nap 1M | Acy | Ace | Flu | Phe | Ant | FluAn | Pyr | Total |
| Burn 1 PT | <LOQ | <LOQ | 0.86 | 0.40 | 0.32 | <LOQ | <LOQ | 0.04 | 0.09 | <LOQ | <LOQ | 1.71 |
| Burn 2 PT | <LOQ | <LOQ | 7.19 | <LOQ | 1.80 | 0.20 | 0.08 | 0.20 | 0.60 | <LOQ | 0.16 | 10.23 |
| Burn 3 PT | <LOQ | <LOQ | Loss | | | | | | | | | |
| Burn 4 PT | <LOQ | <LOQ | <LOQ | <LOQ | 0.06 | <LOQ | <LOQ | <LOQ | <LOQ | <LOQ | <LOQ | 0.06 |
| Burn 5 PT | <LOQ | <LOQ | 3.09 | 0.05 | 1.29 | 0.19 | 0.03 | 0.56 | <LOQ | 0.22 | 0.18 | 5.58 |
| Burn 1 F | Loss | Loss | <LOQ | 0.05 | <LOQ | <LOQ | <LOQ | <LOQ | <LOQ | <LOQ | <LOQ | 0.05 |
| Burn 2 F | <LOQ | 0.06 | 0.18 | 0.23 | <LOQ | <LOQ | <LOQ | <LOQ | <LOQ | <LOQ | <LOQ | 0.46 |
| Burn 3 F | <LOQ | <LOQ | <LOQ | <LOQ | <LOQ | <LOQ | <LOQ | <LOQ | <LOQ | <LOQ | 0.18 | 0.18 |
| Burn 4 F | <LOQ | <LOQ | <LOQ | 0.09 | <LOQ | <LOQ | <LOQ | <LOQ | <LOQ | <LOQ | <LOQ | 0.09 |
| Burn 5 F | <LOQ | <LOQ | <LOQ | <LOQ | <LOQ | <LOQ | <LOQ | <LOQ | <LOQ | <LOQ | <LOQ | <LOQ |
| Burn 1 ST | Loss | Loss | <LOQ | 0.11 | <LOQ | <LOQ | <LOQ | <LOQ | <LOQ | <LOQ | <LOQ | 0.11 |
| Burn 2 ST | <LOQ | 0.10 | <LOQ | 0.30 | <LOQ | <LOQ | <LOQ | <LOQ | <LOQ | <LOQ | <LOQ | 0.40 |
| Burn 3 ST | <LOQ | <LOQ | <LOQ | 0.23 | <LOQ | <LOQ | <LOQ | <LOQ | <LOQ | <LOQ | <LOQ | 0.23 |
| Burn 4 ST | <LOQ | 0.08 | <LOQ | 0.10 | <LOQ | <LOQ | <LOQ | 0.04 | <LOQ | 0.24 | <LOQ | 0.47 |
| Burn 5 ST | <LOQ | 0.08 | <LOQ | 0.07 | <LOQ | <LOQ | <LOQ | <LOQ | <LOQ | <LOQ | <LOQ | 0.15 |

Table S2: Data processing parameters for ChromaTOF Tile (Version v1.01.00.0, Leco, USA)

| Parameter | Detail |
|--|---------------|
| Tile size D1 (modulations) | 5 |
| Tile size D2 (spectra) | 12 |
| S/N threshold | 200 |
| Samples that must exceed S/N threshold | 3 |
| Mass F-ratios to average | 1 |
| Threshold type to apply | p-value |
| p-value threshold | 0.05 |
| Minimum masses per tile | 3 |
| Minimum mass | 29 |
| Maximum mass | 650 |

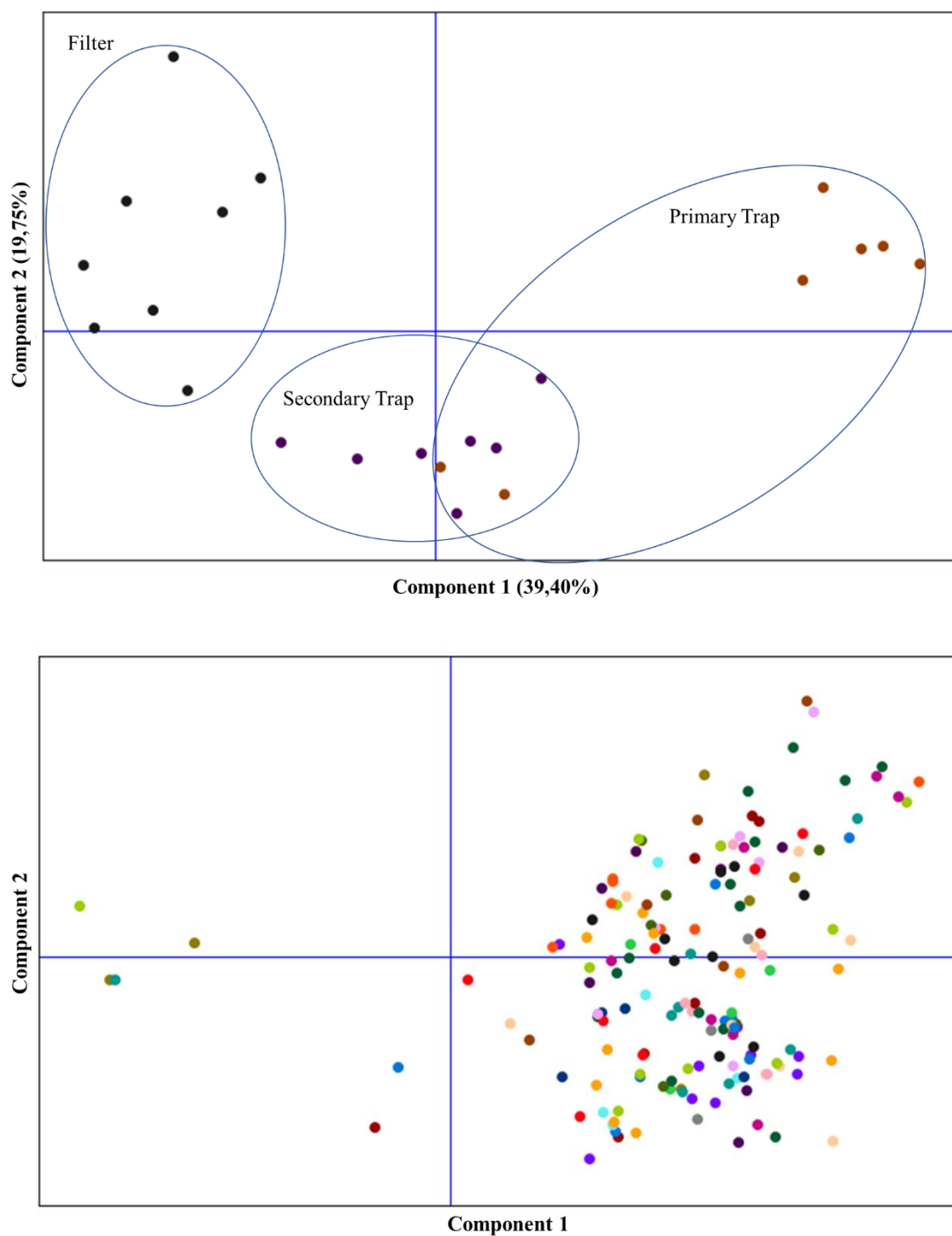


Figure S1. shows the PCA scores (top) and loading (bottom) plot for the primary trap, filter and secondary traps that take all other chemical compounds responsible for variance into account. The chemical compounds that had the highest loading are represented in Table S3.

Table S3: Chemical components with highest loadings towards the three classes of samples namely the primary trap, filter and secondary trap. Identification and similarity calculations were based on NIST library hits with a similarity >700.

| Name | Similarity | Probability | CAS | Quant mass |
|--------------------------------------|------------|-------------|------------|------------|
| 1,2,3-Trimethoxybenzene | 719 | 6947 | 634-36-6 | 168 |
| 1,3-Dioxolane | 825 | 8841 | 646-06-0 | 66 |
| 1,3-Dioxolane, 2-heptyl- | 836 | 6247 | 4359-57-3 | 114 |
| 2H-Inden-2-one, 1,3-dihydro- | 767 | 7528 | 615-13-4 | 132 |
| Azulene | 886 | 6103 | 275-51-4 | 129 |
| Benzaldehyde | 863 | 8329 | 100-52-7 | 77 |
| Benzene, 1,2,4-trimethyl- | 895 | 3217 | 95-63-6 | 106 |
| Benzene, 1,3-dimethyl- | 947 | 5238 | 108-38-3 | 63 |
| Benzene, 1-ethyl-4-methyl- | 761 | 2144 | 622-96-8 | 134 |
| Benzene, 1-methyl-2-(1-methylethyl)- | 844 | 4520 | 527-84-4 | 114 |
| Benzonitrile | 825 | 5939 | 100-47-0 | 76 |
| Benzonitrile, 2-methyl- | 784 | 3751 | 529-19-1 | 116 |
| Biphenyl | 738 | 7498 | 92-52-4 | 152 |
| Biphenylene | 871 | 7015 | 259-79-0 | 150 |
| Decane | 805 | 3229 | 124-18-5 | 85 |
| Dibenzofuran | 831 | 9440 | 132-64-9 | 168 |
| Ethylbenzene | 952 | 8429 | 100-41-4 | 75 |
| Furfural | 960 | 8174 | 1998-01-01 | 97 |
| Heptane, 2,2,4,6,6-pentamethyl- | 862 | 4877 | 13475-82-6 | 99 |
| Indene | 871 | 5686 | 95-13-6 | 116 |
| Indole | 821 | 6331 | 120-72-9 | 90 |
| Naphthalene, 1-methyl- | 889 | 5371 | 90-12-0 | 115 |
| Nonane | 912 | 7584 | 111-84-2 | 128 |
| o-Xylene | 957 | 4282 | 95-47-6 | 62 |
| Phenol, 2-(1,1-dimethylethyl)- | 764 | 3771 | 88-18-6 | 90 |
| Phenol, 2-methoxy- | 883 | 6643 | 1990-05-01 | 124 |
| Phenol, 2-methoxy-4-(1-propenyl)- | 883 | 6663 | 97-54-1 | 78 |
| Phenol, 2-methoxy-4-methyl- | 875 | 5034 | 93-51-6 | 63 |
| Phenol, 2-methoxy-4-propyl- | 710 | 7113 | 2785-87-7 | 137 |
| Phenol, 3-methyl- | 869 | 4984 | 108-39-4 | 90 |
| Phenol, 4-ethyl- | 897 | 6718 | 123-07-9 | 122 |
| Phenol, p-tert-butyl- | 766 | 5015 | 98-54-4 | 107 |
| Phthalan | 764 | 6456 | 496-14-0 | 92 |
| Phthalic anhydride | 905 | 6771 | 85-44-9 | 50 |

| | | | | |
|-----------|-----|------|----------|-----|
| Styrene | 927 | 6075 | 100-42-5 | 104 |
| Tridecane | 862 | 3512 | 629-50-5 | 99 |

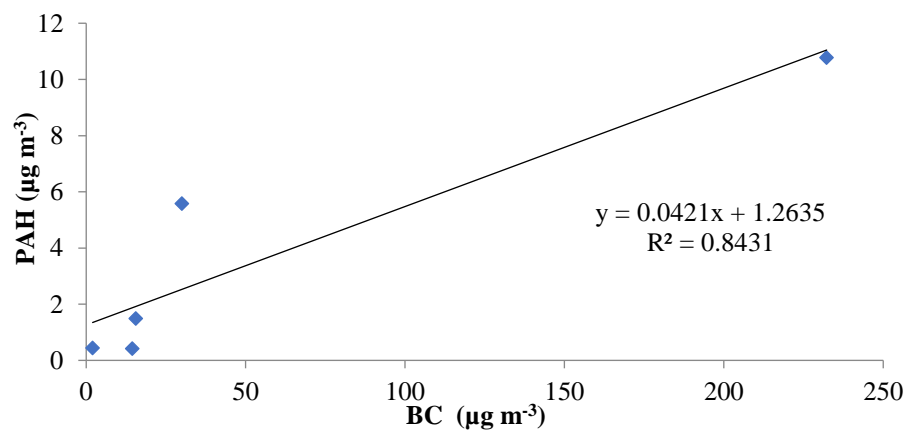


Figure S2. Correlation between total PAH and black carbon (BC) emissions at each of the five burn events.

Chapter 4: Feasibility study: Platinum mine industry (Paper 3)

A transition to sustainable alternative fuels in an underground platinum mining environment was investigated and the feasibility thereof in terms of efficiency, emissions, safety and cost considerations is presented in this chapter.

An abbreviated version of this chapter was submitted to Energy for Sustainable Development.

Geldenhuis, G., Wattrus, M., Fox, M. and Forbes. P.B.C. 2023. Transition to sustainable alternative fuels in an underground platinum mining environment: Efficiency, emissions, safety and cost considerations. *Energy for Sustainable Development*, Submitted.

Author Contributions

G Geldenhuis: Methodology, Validation, Formal analysis, Data curation, Writing- Original draft preparation, Writing - Review & Editing; **M Wattrus:** Methodology, Writing – Review and Editing; **M Fox:** Funding acquisition, Writing - Review & Editing; **P.B.C Forbes:** Conceptualization, Visualization, Project administration, Supervision, Methodology, Formal analysis, Writing - Review & Editing, Funding acquisition.

Transition to sustainable alternative fuels in an underground platinum mining environment: Efficiency, emissions, safety and cost considerations

G Geldenhuys^{1,2}, M Wattrus³, M Fox² and PBC Forbes^{1*}

¹ *Department of Chemistry, Faculty of Natural and Agricultural Sciences, University of Pretoria, Pretoria 0002, South Africa.*

² *Impala Platinum Ltd, 2 Fricker Road, Illovo, 2196, South Africa.*

³ *Energy Business, Sasol, Cape Town, South Africa*

Abstract

Adverse environmental impacts associated with the use of fossil fuels and the over-dependence on oil and natural gas have made energy security and sustainability a critical issue worldwide. The present work focuses on the feasibility of a transition to alternative fuels with focus on biodiesel and biomass-to-liquid fuel in the energy intensive platinum mining industry in South Africa. Biomass residues are an increasingly popular resource for sustainable bioenergy production, as there is no competition for food sources and its use also offers numerous environmental and socio-economic benefits for the country. The evaluation of this transition was carried out according to four indicators namely: potential reductions in air emissions of harmful substances, the functional performance of biofuel versus diesel, cost analysis as well as environmental and socio-economic factors. Results from an underground sampling campaign showed that total toxic polycyclic aromatic hydrocarbon (PAH) combustion emissions from a high idling load haul dump vehicle decreased dramatically when substituting the diesel fuel with gas-to-liquid or biodiesel fuels (total PAH gas phase concentrations of 34; 14 and 9 $\mu\text{g m}^{-3}$ for diesel, gas-to-liquid and rapeseed methyl ester respectively) and no substantial hinderance on engine performance or power was reported by mining staff. The economic analysis revealed that the average production cost estimate for second generation biofuel production was lower than the current cost of diesel and revenue based on diesel replacement, which can be used for a biofuel production plant, are approximately 2 649 335 \$ and 139 604 238 \$ per year for hybrid and fully mechanised operation respectively. From an environmental and socio-economic standpoint, the production and use of biomass-to liquid and biodiesel is a feasible solution towards sustainable development in underground platinum mines and potentially for other sectors in South Africa.

1. Background

Environmental protection and the search for cleaner, more sustainable fuels are two of the most important concerns modern society is facing today. The over-dependence on oil and natural gas, the intensifying demand for energy, as well as fossil fuel shortages have made energy security a critical issue worldwide (Ambaye, Vaccari et al. 2021). Although the economic impact may be negative, the adverse environmental impacts associated with the use of fossil fuels are far more extensive and will influence the planet and all future generations to come.

The projected negative impacts of climate change as well as the volatility of oil supply are forcing governments to search for alternative options. Several countries have already developed regulatory frameworks to allow the approval of biofuels and biofuel blends to meet transportation requirements and thereby reduce the reliance on conventional petroleum imports to help mitigate the impacts of volatile oil prices and reduce carbon emissions. Brazil launched a biodiesel initiative in 2002 that set targets for use of biodiesel within the mix of transport fuel of 2 %, 5 %, and 20 % by 2007, 2013, and 2020, respectively, whereas India started a large-scale biodiesel program which, among other things, introduces a blend containing 5 % biodiesel with fixed prices (Balat 2009). China boasts more than 100 biodiesel production facilities as market incentives and increased government support have enabled biodiesel production projects to mushroom nationwide since late 2005 (Walter et al. 2008) and Germany markets 100 % pure biodiesel and has excluded biofuels from taxation altogether (Kojima and Johnson, 2005). The United States Department of Agriculture created the Bioenergy Program in 2000 that encouraged biodiesel production through cash payments to producers and as a result of this program, biodiesel production reached 75 million gallons in 2005 (Balat 2009, Ebadian et al. 2020). Ebadian et al. further summarised biofuel mandates and their effectiveness on biofuels markets in numerous countries in their comprehensive study (Ebadian et al. 2020).

In addition to the extensive list of advantages listed in literature, biofuel generation and integration will encourage new entrepreneurs and boost the South African (SA) economy whilst simultaneously increasing economic activity internationally (Khan et al. 2021). One of the biggest industries contributing to the South African economy, contributing to 7.53 % to the GDP (Mineral Council SA, 2022), is the platinum mining industry, which is currently heavily dependent on fossil fuels.

Critical mining operations include the extensive use of trackless mobile diesel machinery (TMM) including: load haul dump vehicles (LHDs), utility vehicles (UVs), dump trucks,

cherry pickers and drill rigs. Combustion emissions from all of the above-mentioned sources contribute to gas and particulate air pollutant levels, including those of polycyclic aromatic hydrocarbons (PAHs) which are semi-volatile organic compounds (SVOCs). These compounds are not only a cause for concern from an environmental standpoint, as they are ubiquitous environmental contaminants, but also from a human health perspective, especially due to the confined working environments underground which results in an increased risk of occupational exposure to harmful and carcinogenic pollutants (Dat and Chang 2017).

A transition to alternative fuels, in these critical mining operations, can lead to a reduction in emissions of harmful pollutants and greenhouse gases but the transition must be accompanied by a comprehensive risk management strategy as there are many other aspects that need to be considered on a national level such as the type, source and availability of an alternative fuel, as well as the extent and cost of implementation.

Other clean energy solutions such as solar, hydro and nuclear energy are limited as they do not produce liquid fuel that is needed in transportation (Alalwan et al. 2019). Fuel cell technology offers many advantages that can assist in solving health, safety, productivity and operational efficiency in the mining industry, as well as zero environmental emissions. However currently the growth of hydrogen use is limited by the lack of hydrogen infrastructure, perceptions around hydrogen safety and sustainable development of a hydrogen economy (Guerra et al. 2020). One of the biggest contributing factors is also the initial capital expenditure required, as diesel engines would have to be entirely replaced which may provide a long-term solution but cannot be implemented immediately.

This research aims to determine the broad feasibility of a transition from fossil fuels to the use of biofuels in the South African underground platinum mining industry. Impacts which may arise on a short- or a long-term basis are explored in order to assess whether this could potentially serve as a sector-based solution to the energy crisis in developing countries. The evaluation of this transition was carried out according to three indicators namely; the functional performance of biofuel versus diesel in a heavy duty LHD, potential reductions in air emissions of potentially harmful substances, as well as cost implications of implementation. The study was conducted with consideration of the present and prospective energy sector in South Africa and the growing demand for healthier, more sustainable development. It also highlights the social, economic, and environmental aspects of such a transition, and provides information on long-term sustainability.

The viability of the transition to alternate fuel in the platinum mining sector was investigated according to the following four indicators:

- Criterion analysis of the project implementation efficiency in terms of reduction in air emissions as assessed by a sampling campaign and literature studies
- Changes in the physical values of functional performance indicators of the Trackless Mobile machinery
- Production costs of biofuels and sensitivity analysis
- Environmental and socio-economic factors such as air and soil quality, water availability and biodiversity for the former and food security, effect on income, employment, community health and safety as well as rural development for the latter.

In this study, a rapeseed methyl ester biodiesel (RME) and a synthetic gas-to-liquid (GTL) fuel are evaluated according to their potential use in current internal combustion engines in an underground platinum mine. RME is generated by transesterification of rapeseed oil and is primarily composed of fatty acid methyl esters (FAMES) with different length alkyl chains. This type of fuel does not contain aromatic compounds therefore no PAHs will result from unburned fuel, thus lower emissions of PAHs compared to diesel is expected and this was what was reported in numerous other studies (Prokopowicz, et al. 2015, McCaffery, Tsai, Chen et al. 2019, Zhu et al. 2022). PAH emissions cannot be completely abated as they are still generated during combustion through pyrosynthesis irrespective of PAH content in the fuel. GTL is primarily composed of long-chain alkanes and is expected to emit lower amounts of particulate matter (PM) and lower amounts of PAHs compared to fossil fuel combustion. Although GTL uses natural gas as a feedstock, an alternative to the synthetic GTL offers a more carbon neutral pathway namely biomass-to-liquid (BTL) fuel, which is produced in the same way as the GTL but from organic waste sources. The Fischer-Tropsch process is used to produce GTL from natural gas that results in a purely paraffinic liquid fuel that contains no aromatic compounds and can be used in conventional diesel engines without any engine hardware modifications (Moon et al. 2010).

During the sampling campaign, pollutants emitted from an LHD engine exhaust were compared when operated on pure diesel, RME or GTL and the influence of emissions on air quality in the mines and on human health was investigated as one feasibility indicator in this study. These

selected test fuels have the potential of being generated locally with sustainable feedstocks for first or second generation biofuel such as sugar cane, sunflower oil ester or waste biomass.

The findings of this study may thus aid in the determination of a strategy that could be implemented relatively quickly and cost efficiently and also paves the way to biofuel industrialisation.

2. Introduction

2.1 Generation of biofuels

Biofuels include biodiesel, biobutanol, bioethanol and biomethane with production involving the chemical and thermal decomposition or fermentation of organic biomass by microorganisms to produce liquid or gaseous fuels (Papakonstantinou et al. 2021). General categorisation of biofuels is based on the feedstocks utilised, as well as the method of production and are broadly referred to as first, second, third and fourth generation technologies as depicted in Figure 1 (Ambaye et al. 2021).

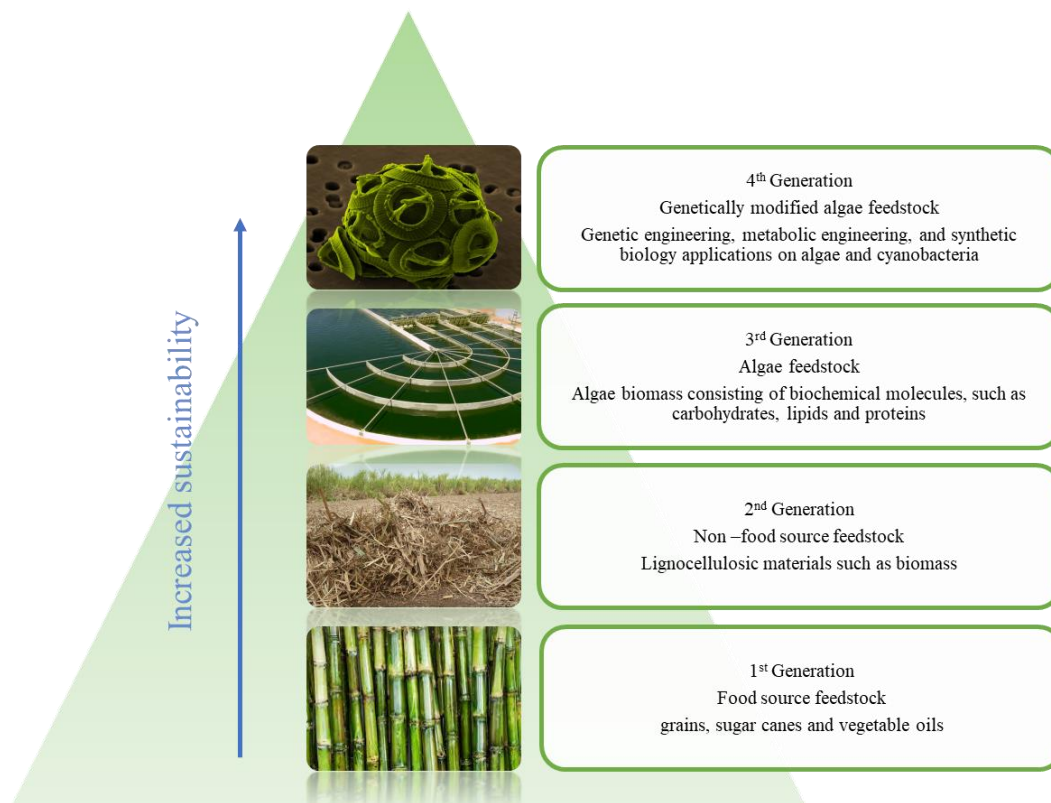


Figure 1 Biofuel generation based on different feedstocks (adapted from Ambaye et al. 2021).

First-generation biofuels include biodiesel, bioethanol, and biogas which can be used commercially and utilise feedstocks that are comprised primarily of edible biomass such as grains, starch, sugar canes and vegetable oils (Papakonstantinou, Mitsis et al. 2021). Transesterification, fermentation and anaerobic digestion are some of the comparatively well-established processes for producing these type of fuels (Khan et al. 2021). Although a step in the right direction in terms of cleaner energy, first generation biofuels compete with food security and thus inflict negative impacts on ecological, social, financial and political aspects due to the fact that mass production requires fertile, arable land and water use that would result in less of these critical resources being available for human and animal consumption. Other studies have found that changing to first-generation biofuels may result in an increase in greenhouse gas emissions, as increased agricultural activity will increase emissions, which with the concomitant increase in fertilizer and pesticide application may result in ecosystem loss rather than the anticipated reduction in greenhouse gas emissions from reduced fossil fuel use (Senauer 2008, Chaudhary and Brooks 2018, Khan et al. 2021). A possible exception to the aforementioned disadvantages is biofuel produced from sugar cane since it meets sustainability criteria in terms of the resultant greenhouse gas balance and net emission reductions, land and raw material use, as well as crop and cost efficiencies (Goldemberg et al. 2008).

Second generation biofuels overcome the fuel versus food dilemma and are based on more sustainable alternatives by utilizing inedible lignocellulosic biomass as feedstocks. These can include dedicated energy crops such as grass, straw and rotational forestry as well as sawdust, low-priced woods, crop wastes and even low value municipal and industrial solid waste (Papakonstantinou et al. 2021). While this generation overcomes the drawbacks of the first generation, more steps are required to produce adequate biofuels at a competitive cost and thus the principal disadvantage of this type of biofuel is the substantially higher capital cost associated with production infrastructure when compared to first generation biofuels. Furthermore, there are currently technical obstacles that prevent 2nd generation biofuels from reaching mass production and feasibility, specifically difficulties during pre-treatment processes and the inefficient conversion of lignocellulosic materials to biofuel due to the complex raw material structure (Neto et al. 2019, Papakonstantinou et al. 2021). Production processes generally include thermal and biological routes with the former having the advantage of higher versatility of feedstock. The biological process includes the pre-treatment of lignocellulosic biomass material, enzymatic hydrolysis, and the fermentation of resultant sugars by specific strains of microorganisms. The thermal route involves heat processing of

biomass under decreased oxidizing agent concentrations at temperatures ranging from 300 to 600 °C to produce biochar (solid biofuel) at the lower temperature ranges, whereas pyrolytic oil and syngas are produced at elevated temperatures, of up to 1000 °C, as the most energy concentrated substances. Different biodiesel yields from different feedstocks are summarised and discussed by Khan, Sudhakar and Mamat in a review of the role of biofuels in energy transition, green economy and carbon neutrality. The authors showed that bioethanol efficiency is higher than other biofuels with a second generation bioethanol yield of 165.0 g kg⁻¹ for sugarcane bagasse as the feedstock which was comparable to the 189.6 g kg⁻¹ for the first generation soybean biodiesel (Khan, Sudhakar et al. 2021).

Although an advancement on 1st generation biofuel production, 2nd generation biofuels still have an impact on sustainability and the balance of the life cycle of greenhouse gas emissions remains an obstacle. The extent of each obstacle is dependent on numerous considerations such as the location of the biofuel production site, modes of transportation, methods of processing, extent of deforestation, water consumption and increased crop prices. Climate regulation and ecosystem preservation are also environmental considerations that could be influenced by biomass feedstocks and land use (Havlík et al. 2011, Ambaye et al. 2021, Khan et al. 2021). Further research is required in order for 2nd generation biofuels to become commercially viable.

Aquatic feedstocks such as algae biomass are used in third-generation biofuels and overcome 2nd generation biofuel drawbacks. Algae biomass presents numerous advantages as a feedstock as it can grow throughout the year with high growth rates and can flourish under variable conditions and climate extremes, additionally, this type of feedstock would also not take up valuable agricultural land mass and may even inhibit evaporation of scarce water sources. Additional advantages include economically viable by-products of processing algae biomass such as ingredients for functional foods, medical chemicals, cosmetics, toiletries, and fragrance products (Papakonstantinou et al. 2021). Algae comprise a diverse group of species that are unicellular or multicellular organisms that are photosynthetic and have the ability produce oxygen and trap high concentrations of CO₂ so in terms of feedstock they are a promising and green solution. However, the high cost of production and decreased stability of the resulting biofuel are among the disadvantages. The manufacture of biofuels through algae is highly dependent upon lipid content thus specific microalgal strain selection and optimisation is required for greater efficiencies (Alalwan et al. 2019, Papakonstantinou et al. 2021).

Genetic manipulation or engineering can provide innovative routes to lipid and algal biomass production and paves the way to the last generation of biofuels, namely 4th generation biofuels, which are still in an early developmental stage. The feedstocks of the 4th generation biofuels are microorganisms including: microbes, microalgae, yeast, and cyanobacteria that are genetically engineered to boost productivity and lipid accumulation (Khan et al. 2021). Genetically modified algae biomasses are used to produce different fuels including ethanol, butanol, hydrogen, methane, vegetable oil, biodiesel, isoprene, gasoline, and jet fuel (Alalwan et al. 2019).

2.2 The South African energy sector: present status and perspectives

SA is a developing country and remains strongly oriented towards resource-based sectors whilst investment levels in productive capacity and infrastructure have remained low for the past two decades (Roberts 2022). The mining sector is one of the key industries contributing to the economy but at the same time is one of the most energy intensive sectors that needs more sustainable solutions. This is further accentuated as SA faces an energy crisis due to an aging fleet of coal-fired power plants, lack of maintenance, corruption, theft and vandalism (du Venage 2020, Masondo 2022).

The SA energy supply is dominated by coal which made up 65 % of the primary energy supply in 2018, followed by crude oil with 18 % and renewables with 11 %. Natural gas contributed 3 % while nuclear contributed 2 % to the total primary supply during the same period (SA DME 2021). Primary energy supply is sourced from both local and imported coal sources. Higher grade coking coal sources are preferentially exported (Dworzanowski 2013). Due to the lack of reserves, SA imports almost 90 % of its crude oil from Saudi Arabia, Nigeria and Angola. During the post-apartheid economic transformation stage, the country produced approximately 3.2 % of its fuel requirements from gas (GTL), 42.3 % from coal (coal-to-liquids (CTL)), and 54.4 % from crude oil (SA DME 2021). The closure of some of the local refineries has resulted in the logistically-constraining import of fully refined fuel with > 60 % of all fuels currently being imported into SA and the balance being refined in country (SAPIA 2021).

SA has the second largest oil refining capacity in Africa (Egypt is first) amounting to 718 000 barrels per day. There are six refineries in the country; four of which are on the coast and two are inland. Two of the refineries are synthetic fuels production facilities that produce liquid fuels from coal and gas, which are owned by Sasol and PetroSA respectively. Sasol uses both the CTL and GTL technologies. The Petroleum Oil and Gas Corporation of South Africa

(PetroSA) produces synthetic products using GTL technology. Major refineries include Sapref and Enref in Durban, Chevron in Cape Town, and Natref at Sasolburg.

As previously mentioned, the mining sector is one of the main consumers of energy in the country consuming 10 % (183 435 TJ/annum) of the total energy supply (The South African Energy Sector Report, 2021). Electricity accounted for 58 % of all the energy available to the sector in 2018, followed by petroleum products at 38 % (approximately 1 billion litres of diesel per annum (GlobalData. Mining nd.) and coal at 4 %. The sector also uses various heating fuels for processing minerals (fuel oil, paraffin, natural gas, hydrogen and low-pressure gas (LPG)).

The use of biofuels will not only reduce SA's energy dependence on imported fuels but it can lead to substantial reductions in air emissions of potentially harmful substances and greenhouse gases (GHGs), and thus to healthier, sustainable development. This potential has been acknowledged by government and in 2005, the then Department of Minerals and Energy (DME) and now Department of Minerals, Resources and Energy (DRME) proposed the development of a biofuels industry to Cabinet who went on to appoint and approve an inter-departmental Biofuels Task Team (BTT) (SA DME 2006). The BTT drafted the Biofuels Industrial Strategy (BIS) which provided a five-year pilot phase from 2008 to 2013 to initially introduce a 2 % penetration level of biofuels in the national transport fuels pool (petrol and diesel), whilst monitoring the resultant socio-economic benefits and adverse consequences. The Green Transport Strategy of South Africa (Department of Transport, n.d.), identifies biofuels as one of the clean transport fuels for the transition towards a lower carbon transport future of the country. With the gradual introduction of electric vehicles, a new biofuels industry is still relevant and sustainable in SA as it will:

- Reduce air pollutants and GHG emissions in the transport sector by reducing petrol or diesel use
- Reduce imports of transport fuels
- Create and preserve jobs in the agricultural industry.

The extreme volatility of oil prices has had a dramatic effect on the global economy and the country requires a new vision and fast-tracked protocol for re-industrialisation under a political settlement which prioritises long-term investment in more sustainable energy and productive capacity. The draft Regulatory Framework for the Biofuels Industry (DRME, 2020) was accepted by Cabinet in 2019 and it is recommended that a sector-based roll out be considered

for effective and regulated biofuel penetration which can then pave the way to national and commercial introduction of biofuels. The blending of biofuel, as laid out in the Biofuels Regulatory Framework, will reduce fossil fuel dependency but the advances in biofuel technology can allow for a complete transition from diesel to more sustainable and greener fuels without major engine modifications and without hampering engine performance.

3. Materials and Methods

To determine the feasibility of a transition from fossil fuel to the use of greener fuel in the platinum mining industry, four indicators were assessed namely:

- Reduction in air pollutant emissions as assessed by a sampling campaign
- Functional performance of the trackless mobile machinery
- Economic analysis of project implementation
- Environmental and socio-economic factors

The methods adopted to evaluate each indicator are described in this section.

3.1 Reduction in air emissions as assessed by a sampling campaign

3.1.1 Sampling Site

The sampling campaign took place in the underground workings of a platinum mine in the North West Province of South Africa, which is one of approximately 17 platiniferous reef mines in the Bushveld Igneous Complex. The depth of the mine, where the field studies were carried out, is between 620 and 1290 m below surface.

The samples were taken inside the parking bay of a trackless underground workshop such that there was fresh ventilation upwind, which was sourced from one of two ventilation shafts drawing air at flow rates above 10 m s^{-1} . The test LHD vehicle was positioned upwind from any mining activity to prevent other sources of emissions affecting the measurements. Details of the samples taken during the sampling campaign are presented in Table S1.

3.1.2 Tested fuels

Three different fuels were used for emissions sampling namely:

1) Petroleum-based diesel containing 50ppm sulfur with no biofuel content (pure diesel (PD)), representing the reference diesel used in the workplace,

2) Paraffinic fuel (GTL, ORYX, Qatar) compliant to EN15940 and

3) Biofuel (RME, SBE BioEnergie, Germany) compliant to EN14214 stabilized with oxidation stabilizer.

Properties of the diesel, RME and GTL fuel used in the underground sampling campaign are given in Table 1.

Table 1 Properties of the diesel, RME and GTL fuel used in the underground sampling campaign.

| Property | Units | Pure Diesel | RME | GTL |
|---|---------------------------------|--------------------|--------------------|---------------|
| Density | kg L ⁻¹ | 0.822 @ 20 °C | 0.860-0.900@ 15 °C | 0.765 @ 20 °C |
| Viscosity [cSt] at 40 °C | mm ² s ⁻¹ | 2.2 / 5.3 | 3.5-5.0 | 2.2 |
| Flash point | °C | > 55 | > 101 | 57 |
| Sulfur content | mg kg ⁻¹ | < 50 | < 10 | <1 |
| Cetane-number | | > 45 | > 51 | 80 |
| Water content | mg kg ⁻¹ | < 30 | < 500 | 50 |
| Total contamination (unsolved foreign substances in the fuel) | mg kg ⁻¹ | < 24 | < 24 | < 24 |

3.1.3 Test engine specifications and operating procedure

One designated LHD (see Table 2 for engine specifications and Figure S1 for a photograph of an LHD) was used throughout the sampling campaign. The LHD was mid-service interval and a good representative of the average fleet underground. The working LHD was pulled from routine production each day and parked in the workshop where the fuel was drained, the air and fuel filters were replaced and the system was flushed with test fuel after which it was filled with the test fuel for sampling. The LHD would then return to high intensity work in production, clearing blasted ore for approximately 30-60 min and then returned to the test site which was the underground workshop parking bay.

Table 2 LHD engine specifications.

| Engine parameter | Specification |
|------------------------|--|
| Model | Deutz BF 6L 914C |
| Emission Certification | Tier 2 |
| Rated Power | 141 kW (herein de-rated to 118 kW) |
| Maximum Torque | 700 Nm at 1600 rpm |
| No. of cylinders | 6 |
| Fuel Consumption rate | 210 g (kWh) ⁻¹ |
| Bore/Stroke | 102/132 mm |
| Displacement | 6.5 L |
| Compression Ratio | 18 |
| Induction | Charged air cooled |
| Fuel Injection | Five-hole nozzle injection; High pressure in-line injector pump with mechanical centrifugal governor |

3.1.4 Sampling Methodology

PAH air samples were collected with Gilair Plus personal sampling pumps (Sensidyne) attached to portable denuder devices via Tygon® thermoplastic tubing. The GilAir pumps were operated at a low flow rate of 0.5 L min⁻¹ to prevent breakthrough of the more volatile PAHs from the denuder traps. The denuder sampler consisted of two multi-channel silicone rubber traps (each trap: 178 mm long glass tube, 4.0 mm i.d., 6.0 mm o.d.) each containing 22 parallel polydimethylsiloxane (PDMS) tubes (55 mm long, 0.3 mm i.d., 0.6 o.d.) separated by a 6 mm diameter quartz fibre filter (QFF), held in position by a Teflon connector. This configuration allows for both gas and particulate phase sampling and has been validated in numerous studies (Forbes and Rohwer 2009, Forbes et al. 2012, Geldenhuys et al. 2015, Rohwer et al. 2015, Kohlmeier et al. 2017, Munyeza et al. 2019). The gas phase SVOCs were trapped by the first (primary) trap as the PDMS served as a solvent for these compounds; the particles were then trapped downstream on the QFF. The post filter trap (secondary trap) served to sample any blow-off from the QFF. Figure 2 graphically illustrates the sampling setup whereby each sample taken resulted in three individual samples, namely the primary trap (PT), filter (F) and secondary trap (ST) samples. A total of 25 samples were taken as summarised in Table S1. A field blank sample was taken and treated in the same manner as other samples but was not

connected to the sampling pump. This sample was used to determine if any contamination had been introduced during handling and transport of samplers prior to analysis

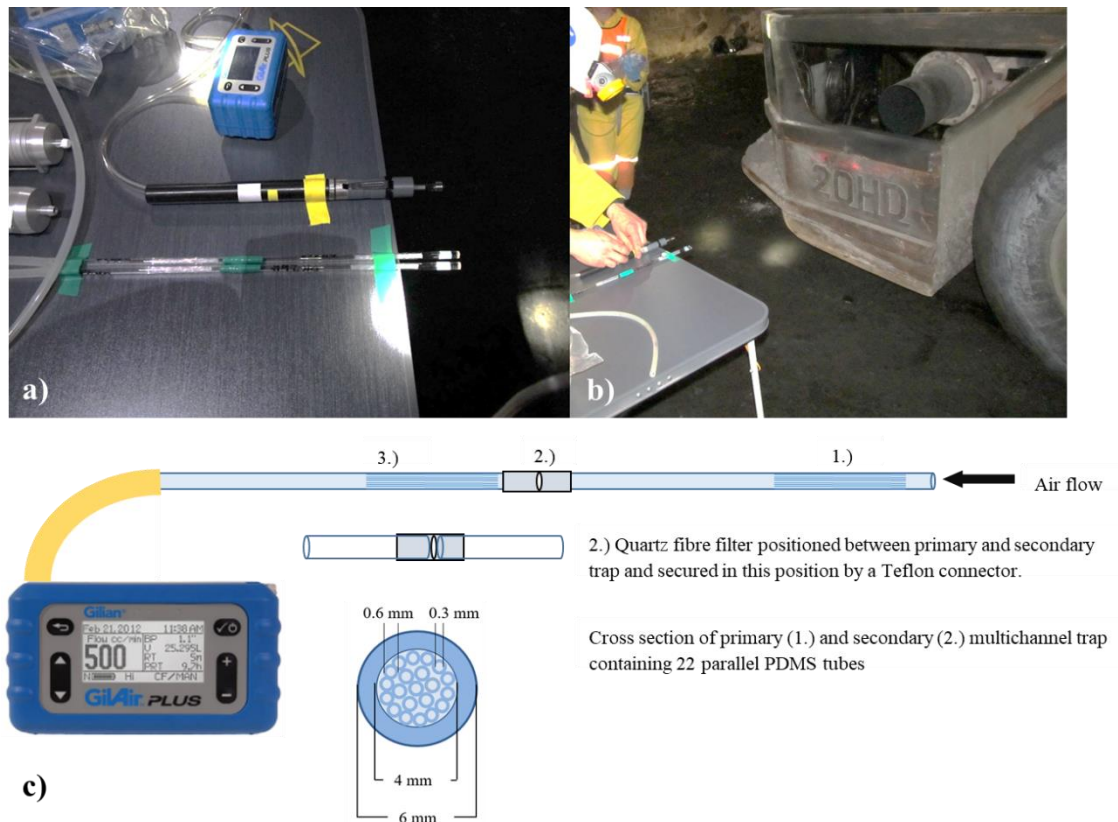


Figure 2 (a) Multi-channel trap denuder sampling devices secured on sampling table underground (b) Position of the multi-channel trap denuder sampling devices relative to the LHD exhaust (c) Schematic of multi-channel trap denuder sampling devices used for PAH sampling (Geldenhuys, Wattrus et al. 2022)

3.1.5 Test procedure

The LHD was operated in two modes namely high idle mode (HI) and a test cycle mode (TC). HI mode was characterised by full acceleration with no throttle and TC was a load test whereby the LHD bucket (capacity ranging from 0.8 to 10 m³) lifted a fixed mass (one LHD tyre of approximately 1 tonne) to mimic the LHD in operation. More information on underground LHD operation can be found in Wattrus et al. (Wattrus et al. 2016)

A 10 min HI pre-conditioning cycle was performed prior to sampling to ensure temperature stabilisation. Sampling was conducted at a fixed height (1 m) and distance (1.5 m) from the LHD exhaust. Upwind (UW) and downwind (DW) samples were also taken simultaneously to assess the impacted ambient conditions where the UW samples served as indicators of

background concentrations. After sampling, the LHD was returned to production and consumed the remaining fuel.

3.1.6 Analytical Method

Offline analysis of each individual denuder component was performed using a LECO Pegasus 4D instrument (LECO, St. Joseph, MI, USA) that was equipped with an Agilent Technologies 7890 GC (Palo Alto, CA, USA), a quad jet dual-stage modulator and a secondary oven. Data acquisition and processing was executed by ChromaTOF version 4.0 and ChromaTOF Tile software (LECO Corp., St. Joseph). A Gerstel 3 TDS was employed for sample introduction whereby the PDMS traps were directly thermally desorbed and the filter samples were inserted into the heating zone of an empty pre-cleaned glass tube for desorption. Synthetic air was used for the hot jets and liquid nitrogen was used to cool nitrogen gas for the cold jets with an AMI Model 186 liquid level controller to maintain sufficient levels. The GC column set consisted of a Restek Rxi-1MS nonpolar phase 100 % dimethyl polysiloxane; (30 m, 0.25 mm i.d., 0.25 μm df) as the first dimension (1D) and a Rxi-17Sil MS, midpolar 50 % phenyl 50 %-dimethyl polysiloxane (0.79 m, 0.25 mm i.d., 0.25 μm df) as the second dimension (2D). Thermal desorption occurred from 30 °C to 280 °C at a rate of 60 °C min^{-1} and was held for 5 min during which the analytes were cryogenically focused via a cooled injection system (CIS) at -50 °C using liquid nitrogen. The temperature was ramped at 12 °C s^{-1} to 280 °C and the inlet purge time was 3 min. The desorption flow rate was 100 mL min^{-1} and the TDS transfer line was set at 300 °C. The primary oven was ramped at 5 °C min^{-1} from 40 °C to 315°C which was held for 15 min. The secondary oven was offset by +5 °C and the modulator temperature was offset by 30 °C. The modulation period was 3 s with a hot pulse time of 1 s. The MS transfer line temperature was set to 280 °C and mass acquisition ranged from 50 to 500 Daltons (Da) at 100 spectra s^{-1} . The electron energy was 70 eV and the ion source temperature was 200 °C.

3.1.7 Matrix matched calibration standards

Calibration was performed using a certified standard PAH mix solution (Supelco, St Louis, MO), containing 15 priority PAHs. The nominal concentration of each compound in the mixture dissolved in methylene chloride was 2000 $\mu\text{g mL}^{-1}$. The names and abbreviations of the PAHs included are given in Table 3. A stock solution at a concentration of 100 $\mu\text{g mL}^{-1}$ was prepared in toluene and working solutions were prepared by appropriate dilutions of the stock solutions in n-hexane before use. All solvents used for dilutions and cleaning procedures

were of analytical grade (99 % purity) including toluene, methanol, dichloromethane (DCM) and n-hexane which were purchased from Sigma Aldrich (Sigma Aldrich, Bellefonte, USA) and acetone which was obtained from Associated Chemical Enterprises, (ACE, South Africa). Deuterated internal standards (I_{Std}): d_8 -naphthalene, d_{10} -phenanthrene, d_{10} -pyrene and d_{12} -chrysene were obtained from Isotec Inc (Sigma Aldrich, Bellefonte, USA) and were used in all standards and samples.

Table 3 Analytes investigated in this study including fifteen of the sixteen US EPA priority PAHs and their corresponding abbreviations, molar masses and boiling points (PubChem 2021).

| Formula | PAH Name | Abbreviation | Molar Mass (g mol ⁻¹) | Boiling point (°C) |
|---------------------------------|------------------------|--------------|--------------------------------------|-----------------------|
| C ₁₀ H ₈ | Naphthalene | Nap | 128 | 218 |
| C ₁₁ H ₁₀ | 1-Methyl naphthalene | Nap 1M | 142 | 240 |
| C ₁₂ H ₈ | Acenaphthylene | Acy | 152 | 265 |
| C ₁₂ H ₁₀ | Acenaphthene | Ace | 154 | 278 |
| C ₁₃ H ₁₀ | Fluorene | Flu | 166 | 295 |
| C ₁₄ H ₁₀ | Phenanthrene | Phe | 178 | 339 |
| C ₁₄ H ₁₀ | Anthracene | Ant | 178 | 340 |
| C ₁₆ H ₁₀ | Fluoranthene | FluAn | 202 | 375 |
| C ₁₆ H ₁₀ | Pyrene | Pyr | 202 | 360 |
| C ₁₈ H ₁₂ | Benz[a]anthracene | BaA | 228 | 435 |
| C ₁₈ H ₁₂ | Chrysene | Chy | 228 | 448 |
| C ₂₀ H ₁₂ | Benzo[b]fluoranthene | BbF | 252 | 481 |
| C ₂₀ H ₁₂ | Benzo[a]pyrene | BaP | 252 | 495 |
| C ₂₂ H ₁₂ | Benzo[g,h,i]perylene | BghiP | 276 | 536 |
| C ₂₂ H ₁₂ | Indeno[1,2,3-cd]pyrene | I123P | 276 | 536 |
| C ₂₂ H ₁₄ | Dibenz[a,h]anthracene | DbahA | 278 | 524 |

For gas phase PAHs, quantification was achieved by analysing individual conditioned PDMS traps that were spiked with 1 μ L of the following concentrations of mixed PAH standard in toluene: 0.1, 0.5, 1.0, 2.0, 5.0, 10.0 and 20.0 ng μ L⁻¹. Similarly, to quantify particle bound PAHs, pre-cleaned 6 mm QFF punches were spiked with 1 μ L of 0.1, 0.5, 1.0, 2.0, 5.0 and 10 ng μ L⁻¹ mixed PAH standards in toluene. One μ L of the I_{Std} mixture, containing d_8 -naphthalene, d_{10} -phenanthrene, d_{10} -pyrene and d_{12} -chrysene (1 ng μ L⁻¹) was spiked onto all samples and standards prior to analysis and calibration curves were derived using the area ratio of target analyte: I_{Std} . The I_{Std} correction accounted for any instrument variability or matrix effects. Linear regression analyses were performed using the Data Analysis Toolkit in Excel. The limit

of detection (LOD) of each target compound was calculated as three times the signal to noise (S/N) ratio and the limit of quantitation (LOQ) as ten times the S/N ratio using the lowest concentration calibration standard.

3.1.8 Quality Assurance

Empty traps were sonicated for 5 min in DCM and then 5 min in ethanol after which they were baked overnight in an oven at approximately 100 °C before use. Quartz fibre filter punches (Whatman) were rinsed twice with DCM and methanol after which they were dried in an oven at 200 °C for 2 h. The clean, dry punches were stored in an amber vial in a desiccator prior to use. Teflon connectors and end caps were repeatedly rinsed with DCM and methanol and left to air dry before use.

The PDMS traps were conditioned prior to use at 280 °C for 16 h under hydrogen ($\geq 99.999\%$ purity, AFROX, SA) with a gas flow of 100 mL min⁻¹ using a Gerstel TC 2 Tube Conditioner (Gerstel, Germany).

PDMS traps were wrapped in aluminium foil after the sampling period to prevent light assisted reactions or transformations and were stored in a freezer at -18 °C to prevent heat-assisted reactions or transformations. The loaded filters from the denuder samples were stored with their corresponding Teflon connectors still intact in amber quartz vials to prevent any sample loss and placed in the freezer. When analyzing the filter, the Teflon connector was placed on the end of a clean, empty glass tube with the loaded face of the filter facing towards the tube. The filter was then carefully positioned into the heating zone of the glass tube for thermal desorption. Procedural blanks were analysed in conjunction with the samples to ensure no carry-over.

3.1.9 Statistical evaluation

Statistical evaluation was performed using ChromaTOF Tile (LECO Corp. St. Joseph). A p-value of 0.05 was used for data comparison and F-ratios were evaluated for the significant compounds (F-ratio > 1000).

3.2 Functional performance of the trackless mobile machinery

Evaluation of this indicator was performed by conducting a literature review pertaining to the effects that biofuels can have on engine performance which could not be experimentally measured due to lack of resources. Physical observations were, however, made during the

sampling campaign by the LHD operator, researchers and selected mine staff regarding engine performance, smoke opacity and volume, and visible particulate matter (soot) when the LHD was operated on pure diesel, RME and GTL, respectively. The literature findings as well as feedback obtained from experimental observations were discussed and used to draw conclusions on the engine functional performance indicator.

3.3 Economic analysis of project implementation

This indicator was assessed by reviewing the literature regarding biofuel production costs and methods of financial analysis. The mine specific method adopted by Guerra et al. (2020) was then used to conduct an economic analysis. Here fully mechanised mining operations were compared to hybrid mining operations to evaluate the extent of the benefit of transition to alternate fuels. This method entails summarising all the costs that the underground mining company currently incurs for diesel fuel usage which can then be considered as revenue.

The following aspects were considered when estimating revenue:

- Individual mining vehicle consumption
- Total annual diesel consumption
- Cost of the diesel fuel to be replaced by alternative fuel
- Estimation of biofuel production plant revenue based on diesel replacement value
- Land leasing costs
- Gross water costs
- Weighted average US\$-based cost of capital (WACC)
- US\$-based inflation rate

3.4 Environmental and socio-economic factors

Environmental, economic, and social impacts pertaining to the use of diesel, biodiesel and GTL/BTL, respectively were reviewed and defined followed by the evaluation of this indicator by comparing and tabulating these factors for three scenarios namely, the current use of diesel, prospective use of greener alternative BTL and prospective use of greener alternative biodiesel.

4. Results and Discussion

The four indicators used for evaluation are reviewed and discussed in this section and results of the sampling campaign are reported.

4.1 Reduction in air pollutant emissions as assessed by a sampling campaign

The advantages of substituting petroleum-based fuels with alternative, greener fuels have been widely discussed in the literature with the main benefits being reported as the reduction in emissions of carbon monoxide (CO), carbon dioxide (CO₂), nitrogen oxide (NO_x), particulate matter (PM) and hydrocarbons (HCs) under various operating conditions and an overall lowered environmental burden (Karavlakakis et al. 2017, Altarazi et al. 2022). Additionally, biofuels are biodegradable, non-toxic and sulfur free, and consequently, at heavy loads and high gas temperatures, no sulphates are formed and the PM emissions have been reported to be reduced by up to 24 % (Labeckas and Slavinskas 2006).

In a study where emission characteristics of diesel, gas to liquid, and biodiesel-blended fuels in a diesel engine were compared, the authors found noticeable decreases in total hydrocarbons (THC) (22–56 %) and CO (16–52 %) emissions for GTL–biodiesel blends whereas NO_x emissions for GTL–biodiesel blends increased by a maximum of 12 % compared to diesel due to increased oxygen content and higher temperatures in the combustion chamber (Moon et al. 2010). The higher oxygen content for biofuel improves combustion quality but the increased temperatures favour the formation of NO_x through the Zel'dovich mechanism (Wright and Lewis 2022). The emissions of NO_x from combustion can be mitigated by internal measures, such as exhaust gas recirculation (EGR), fuel lean conditions and water injection, combined with exhaust after-treatment employing techniques such as selective catalytic reduction (SCR) and lean NO_x traps (LNT), which have shown to be efficient in dual-fuel applications (Wright and Lewis 2022).

Another important advantage of using biofuels, specifically biodiesel, in conventional diesel engines is the higher oxygen content due to the fatty acids that result in more complete combustion and thus lower emissions of harmful species, such PAHs (Labeckas and Slavinskas 2006, Prokopowicz, et al. 2015, McCaffery, Tsai, Chen et al. 2019, Zhu et al. 2022).

PAHs can generally originate from three different sources including pyrosynthesis during combustion, from the original unburned fuel or the lubrication oil respectively, and lastly formation by the hydrogen abstraction-C₂H₂ addition (HACA) mechanism (Czech et al. 2017). In combustion engines, unsubstituted PAHs are noticeably formed by the HACA mechanism. The number of rings formed in this process depends on the combustion temperature and conditions (Gawlitta et al. 2022).

This study was carried out with the aim of assessing the impacted environment underground due to combustion emissions from LHD vehicles operating on various fuels. PAHs were the target analytes due to their human and environmental toxicity as well as the paucity of information on gas and particle phase characterisation of these compounds in the underground environment (Geldenhuis et al. 2015).

In a collaborative effort, personal samples were also taken to assess the resultant exposure to mine workers (Gawlitta et al. 2022). Methylated PAHs and parent PAHs were highly abundant in the pure diesel combustion aerosol compared to that from GTL and RME. Gas phase analysis of emissions from the different fuels showed highest concentrations for the targeted aromatic species released from pure diesel followed by GTL and RME. GTL and RME combustion thus released lower amounts of chemical compounds connected to adverse health effects, therefore the substitution of petroleum-based fuels could benefit employees working in confined areas. When considering noxious emissions underground, advanced combustion due to higher octane of biodiesel and GTL, as well as the increased concentration of oxygenated species in biodiesel, typically result in slightly increased NO_x emissions resulting from the higher temperatures. This can be overcome through engine recalibration to retard injection timing with the net effect being the same NO_x emissions as with diesel but with PM emissions reduced substantially.

An earlier study by Geldenhuis et al. saw the characterisation of PAHs in various underground locations. In this earlier study, the authors found that PAHs were predominantly present in the gas phase with naphthalene and mono-methylated naphthalene being the most abundant at concentrations ranging from 0.01 to 18 µg m⁻³. Particle bound PAHs were found in the highest concentrations at the idling load haul dump vehicle exhausts with a dominance of fluoranthene and pyrene with total particle associated PAH concentrations ranging from 0.47 to 260 ng m⁻³. Heavier PAHs detected in the filter samples included benzo[*k*]fluoranthene, benzo[*a*]pyrene, indeno[1,2,3-*cd*]pyrene and benzo[*ghi*]perylene (Geldenhuis et al. 2015).

The sampling campaign results presented in Figure 3 revealed a clear difference in total PAH concentrations arising from exhaust emissions between the different fuels in both high idle and test cycle mode. It is evident that the concentrations from the combusted diesel fuel are substantially higher than the emissions from the other fuels. Diesel fuel produced the highest concentration of PAHs on the primary trap with a value of $19 \mu\text{g m}^{-3}$ followed by the GTL fuel at $6 \mu\text{g m}^{-3}$ and then the RME, which showed the lowest PAH concentrations which were almost 10-fold lower than that of the diesel fuel.

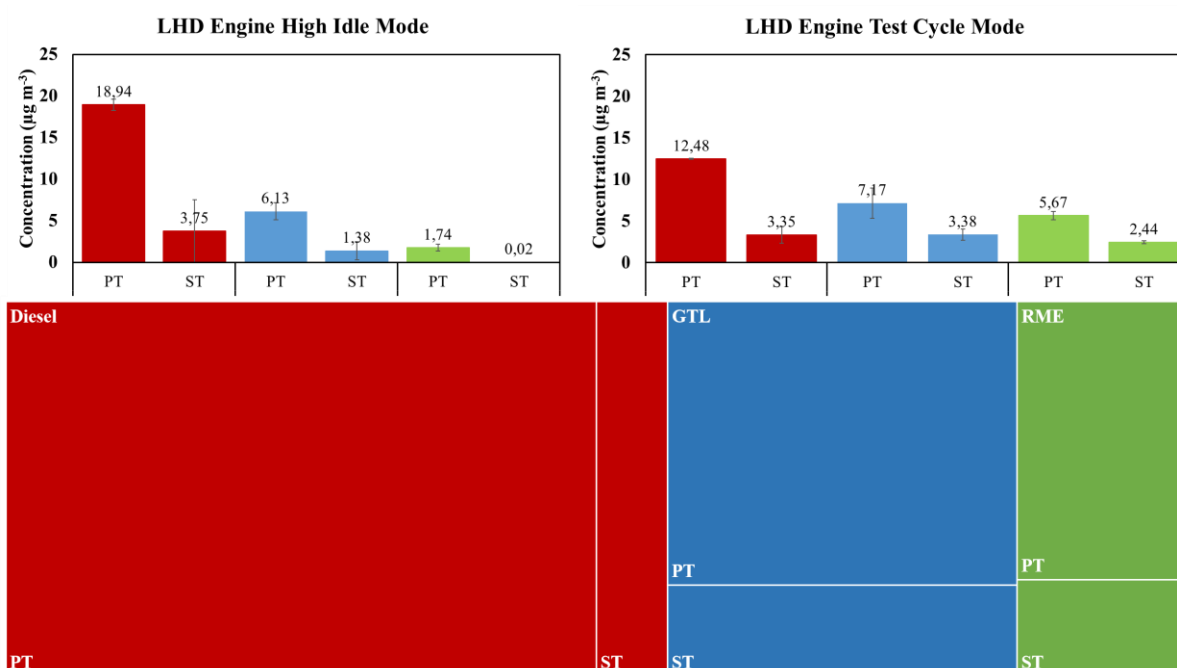


Figure 3 (Top left) Total PAH concentrations on the primary and secondary trap for the LHD engine exhaust samples during high idle mode using diesel, RME and GTL fuels (Top right) Total PAH concentrations on the primary and secondary trap for the LHD engine exhaust samples during test cycle mode using diesel, RME and GTL fuels and (bottom) hierarchical tree map chart of total PAH concentrations for different tested fuels during both cycles.

The lower PAH concentrations from the use of GTL and RME fuels were expected as the biofuel does not contain aromatic hydrocarbons and the GTL aromatic content is greatly reduced when compared to crude derived diesel. Additionally, the lower PM concentrations during combustion of these fuels would also result in lower PAH concentrations as these parameters have been positively correlated in other studies (He et al. 2010, Jin et al. 2014). The PAHs that were detected can therefore be attributed to the pyrolysis products formed during combustion. The test cycle PAH concentrations followed the same trend, however the most noticeable difference was the higher values for the RME samples when the engine was under load, resulting in a lower ratio between the diesel and RME PAH concentrations.

The downwind samples reveal that the total PAH concentrations (sum of PT and ST) for the diesel, GTL and RME fuels during high idle mode were 23, 8 and 2 $\mu\text{g m}^{-3}$ respectively. The downwind samples are representative of the fresh exhaust emissions implying that the PAHs remained in the gas phase and no particle association occurred during the sampling period. The tree map in Figure 3 displays the PAH concentration data for the different fuels in a hierarchical structure and it is evident that the PAH concentrations from the combusted diesel fuel are substantially higher than the PAH concentrations from the other fuels with the green section representing the RME biodiesel.

Based on these results it can be concluded that in addition to the reduction in known and regulated pollutants, such as PM, HCs, CO, and NO_x (Hassaneen et al. 2012), the substitution to biofuels will also lead to a substantial reduction in toxic PAH emissions.

To evaluate the other chemical compounds contributing to the distinct differences between PD, RME and GTL, analysis of variances was performed using principal component analysis of the PDMS samples from the LHD exhaust whilst operated utilising these three fuels (Figure 4 & 5).

Figure 4 showed that PC1 accounted for 98.68 % of variability in the initial dataset, whilst the second-dimension accounted for 0.62 % which indicated good representation. The greatest loadings towards the RME samples in Figure 5 included fatty acid methyl esters (FAMES) of various length of alkane side chains with 9-octadecenoic acid methyl ester being the most significant component. It must be noted that this type of statistical analysis does not reflect quantitative differences between the samples. The full list of the chemical features in Table S2 showed that the highest variances are for the straight chain alkanes from PD PDMS LHD samples and fatty acid methyl esters from equivalent RME samples. Cis-9-tetradecene-1-ol was the distinctive compound contributing to the highest variance between GTL and the other fuels.

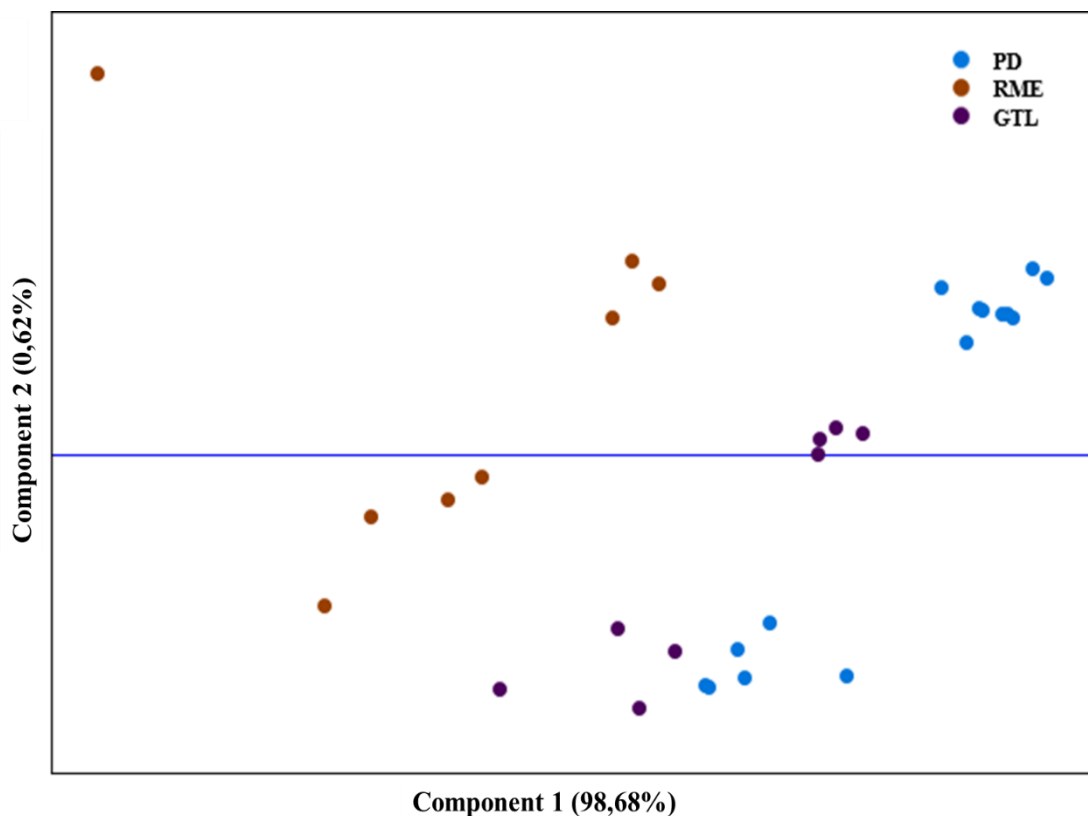


Figure 4 PCA Loading Plot of the PDMS trap samples for LHD operated on pure diesel, rapeseed methyl ester and gas-to-liquid fuels.

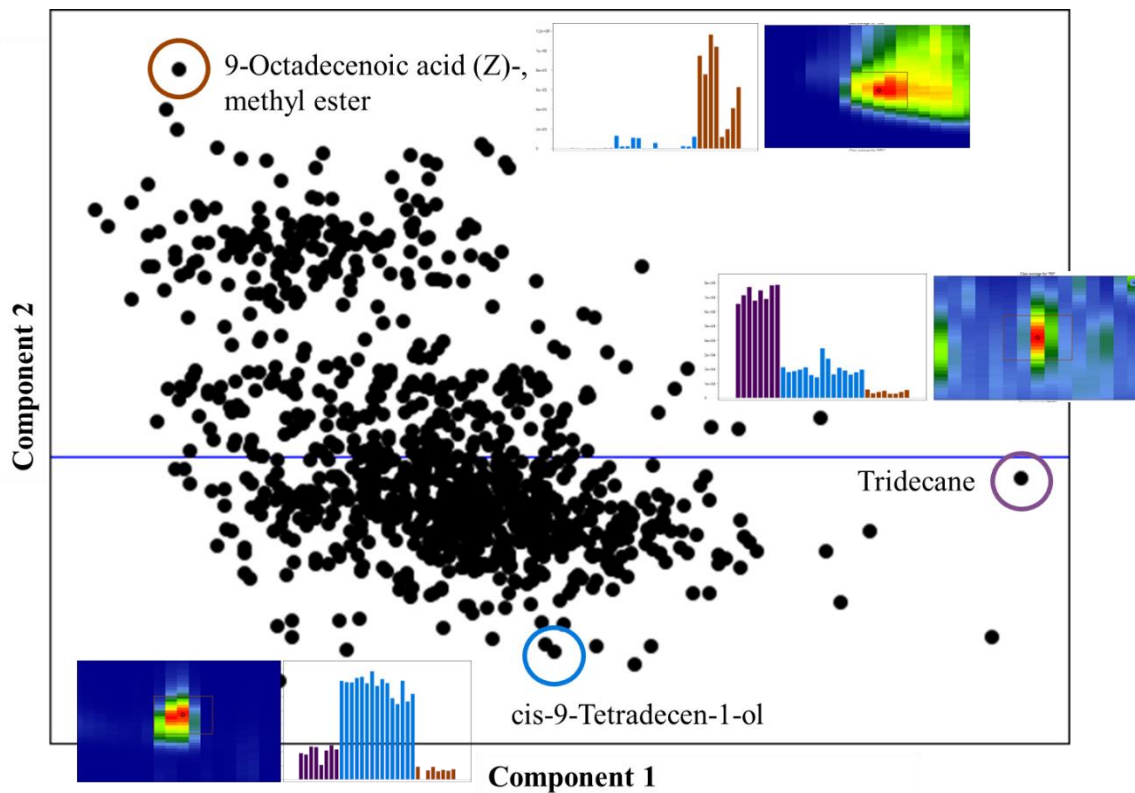


Figure 5 PCA Loading Plot of the PDMS trap samples for LHD operated on pure diesel, rapeseed methyl ester and gas-to-liquid fuels.

4.2 Functional performance of the trackless mobile machinery

The well-established advantage of using biodiesel is the reduction in the pollutant component of the exhaust which is why in the last few years, a double-digit annual growth rate of biodiesel production capacities has been reported (Karavalakis et al. 2017, Altarazi et al. 2022).

In a study by Labeckas and Slavinskas, the effect of rapeseed oil methyl ester on direct injection diesel engine performance and exhaust emissions was investigated. Comparative bench testing of a four stroke, four-cylinder, direct injection, unmodified, and naturally aspirated diesel engines were investigated when operating on neat RME and its 5 %, 10 %, 20 % and 35 % blends with diesel. The authors concluded that the brake specific fuel consumption at maximum torque (273.5 g/kW h) and rated power (281 g/kW h) for RME is higher by 18.7 % and 23.2 % relative to diesel. The maximum brake thermal efficiency values vary between 0.356–0.398 for RME and 0.373–0.383 for diesel and at all speeds and loads, the highest fuel energy content (9.36–9.61 MJ/kW h) is achieved during operation on a 10 % blend with diesel (B10), whereas the lowest fuel energy content belongs to the 35 % blend (B35) and neat RME (9.20–10.40 MJ/kW h). The authors noted that the fuel energy conversion efficiency depends on both the RME inclusion percent in the diesel and the engine performance conditions. When considering the emissions, the maximum NO_x emissions were found to increase proportionally with the mass percent of oxygen in the biofuel and engine speed, at 2000 min⁻¹ reaching the highest concentration of 2132 ppm for the B35 blend and 2107 ppm for neat RME. At the rated speed of 2200 min⁻¹, the total NO_x emissions for all fuels were slightly lower, ranging from 1885 ppm for diesel to 2051 ppm for B35, correlating with the lower brake thermal efficiency at this particular speed. The CO emissions and visible smoke emerging from the biodiesel (at constant air-to-fuel equivalence ratio of $k = 1.6$) over all loads and speeds are lowered by up to 51.6 % and 60.3 %, respectively. The CO₂ emissions, the fuel consumption and gas temperature, were slightly higher for the B20 and B35 blends and neat RME. The emission of unburned hydrocarbons for all fuels was found at ranges from 5–21 ppm with lower values obtained for RME and its blends with diesel (Labeckas and Slavinskas 2006).

Biodiesel and GTL can be used directly in diesel engines without any modification and in the context of implementation in the mining industry, this is key as it will allow for the continuous operation of the current LHD fleet and prevent costly and time intensive replacement. However, the use of alternative fuels with different chemical compositions and local conditions

leads to the distinctive performance of the diesel engine. Studies on the performance of a diesel engine with blends of biodiesel have reported higher brake specific fuel consumption and exhaust gas temperatures when using biodiesel but a decrease in brake thermal efficiency and authors concluded that the fuel energy conversion efficiency depends on both the biodiesel inclusion percent in the diesel and the engine performance conditions (Labeckas and Slavinskas 2006, Raheman et al. 2013).

The power and performance indicators of a diesel engine were investigated during the experimental study when a LHD was operated on pure diesel, RME and GTL as detailed in Section 2. The experimental observations of the LHD operated with different fuels is summarised in Table 4.

Table 4 Comparative qualitative observations of LHD engine performance parameters when operated on neat diesel, GTL and RME fuels.

| | Diesel | GTL | RME |
|------------------------------------|---|---|--|
| Engine performance | Status quo – no observed change | No change at low engine speeds. Reduction in power at higher engine speeds. | No change in power was observed. |
| Smoke opacity and volume | Lots of black smoke observed with characteristic pungent diesel fume odour. | Decreased amount of smoke and increased transparency of smoke. Slight odour. | Decreased amount of smoke and increased transparency of smoke. Slight odour. |
| Particulate matter and soot | Substantial PM and black smoke affecting visibility. | Less observed PM and soot. | Less observed PM and soot. |

The cetane number of RME is slightly higher than that of diesel but it is less volatile therefore is characterised by higher flash point, water content and up to 25 times higher contamination therefore it may reduce the auto-ignition delay and increase the amount of fuel premixed for rapid combustion and resultantly boosts the cylinder gas temperature, creating favourable preconditions for NO_x formation. The engine performance on neat RME and its blends with diesel, as well as its emission characteristics, depends largely on the injector nozzle design, the combustion chamber, needle valve opening pressure, air–fuel mixture quality, actual start of combustion and heat release peculiarities (Labeckas and Slavinskas 2006). Therefore, it must be noted that different engines may vary substantially and the results are not always directly comparative. There are, however, commonly reported advantages of biodiesel over diesel

which are summarised in Table 5 with the reported disadvantages, most of which can be mitigated with internal measures and exhaust after-treatment techniques (Alalwan et al. 2019).

Table 5 Advantages and disadvantages of the use of biodiesel over diesel (Alalwan et al 2019).

| Advantages of using biodiesel | Disadvantages of using biodiesel |
|--|--|
| Generates fewer regulated pollutant emissions of CO _x , SO ₂ , PM and HC compared to diesel | Its combustion generates higher NO ₂ and NO than diesel (can be mitigated) |
| It is non-flammable, non-toxic, and it reduces tailpipe emissions, visible smoke and odours | It has a higher pour point and cloud point which may cause fuel freezing and difficulty starting in cold weather |
| It has high combustion efficiency, portability, availability, and renewability | Degradation of lubricant will lead to shorter engine life with biodiesel |
| It is safer to handle and less toxic than diesel fuel | Power and volumetric fuel consumption is reduced with biodiesel |
| Lower sulfur and aromatic content, higher flashpoint and it is biodegradable | Dependent on the amount of waste (feedstock) available and refining is required. Biodiesel distillation is preferable to improve quality |
| Does not require any drilling or transportation or refinement | Leads to increased oil dilution by fuel causing accelerated oil degradation (due to lower volatility of biodiesel) |
| Higher cost efficiency than diesel | Lack of aromatics causes fuel system seal failure unless standard nitrile seals are replaced viton seals. |
| Its production is easier and faster than diesel | Resistance to change |
| It can be produced domestically and from renewable sources | |
| Lower PM emissions may result in a potential reduction of required underground airflow and thereby a reduction in associated ventilation costs | |

A recent comprehensive review on the effects of biofuel on engine performance and emissions verifies that all biodiesels and their blends have demonstrated the ability to reduce emissions such as carbon oxide (CO), carbon dioxide (CO₂), particulate matter (PM), hydrocarbons (HCs) and even nitrogen oxide (NO_x) under various operating conditions, as well as the ability to improve the engine performance, but it is vital to understand the combustion properties of fuels for their use in an engine (Altarazi et al. 2022). The use of biodiesel underground can thus provide numerous potential benefits to the mining industry pertaining to sustainability and improvements to human and environmental health. One of the holistic bigger benefits to a fuel

emitting lower PM is that potentially underground airflow can be reduced saving significantly on power and in a greenfield application on ventilation capital expenditure (capex). In some areas where the cross-sectional area of a tunnel is the constraining factor for air velocity, the tunnels could also be made potentially smaller with numerous benefits.

4.3 Economic analysis of project implementation

Low-carbon biofuels are considered vital for long term decarbonization of the transportation sector, due to incompatibilities that other fuel alternatives, such as electricity or hydrogen, have with heavy-duty fleets (Witcover and Williams 2019).

The oil price is crucial to the feasibility of biofuel production because it constitutes the benchmark for economic competitiveness and it determines the costs of many of the inputs used in growing, harvesting, processing and transporting crops (Brent et al. 2009). The price for diesel ranged from \$4.89 to \$5.81 per gallon over the past 6 months of 2022, which is substantially higher than the reported biofuel production prices which does make the transition to these greener fuels seem attractive and feasible. However, it must be noted that the production costs reported were excluding taxes or delivery costs and the recent surge in oil and natural gas prices will result in higher costs.

A comparison of biofuel cost estimates was published in 2019 whereby the trends during rollout of low carbon fuel policies were discussed and the paper comprehensively reviewed literature on production costs of biofuels using a levelized cost of fuel approach, applying common financing assumptions for capital amortization and converting all values to year 2016 dollars. To calculate the levelized cost of fuel (LCOF), capital amortization schedules (i.e., financing terms) were harmonized across all studies. Specifically, a debt-to-equity ratio of 60:40, 5 % annual interest on debt amortized over twenty years, a required rate of return (ROR) of 15 % for equity (this is profit), and a thirty-year life of project were used. The formula that was applied is as follows:

$$\text{LCOF}(\$/\text{gge}) = \frac{(\text{CapEx [amortized]} + \text{OpEx Feedstock Cost}) [\$/\text{y}]}{\text{Nameplate Fuel Production in 1 Year [as gge/y]}}$$

The average production cost estimate for cellulosic ethanol was \$4 per gallon-gasoline equivalent (gge), \$3.25/gge for pyrolysis-biocrude hydro treatment pathway, \$3.80/gge for

biomass to liquid (BTL) while hydrotreated esters and fatty acids (HEFA) averaged about \$3.70/gge (Witcover and Williams 2019).

A viability analysis of generalised underground mining machinery using green hydrogen as a fuel was conducted in Spain in 2020 and it was found that the total investment, including vehicles with hydrogen range extender, the hydrogen production plant and the hydrogen refuelling station would be in the range of 21.46 million \$ (Guerra et al. 2020). Although this transition would result in a reduction in toxic diesel emissions, decrease the mining ventilation burden and improve safety and overall working conditions, the price and timeframe for implementation may hinder immediate progress. Also noteworthy is that hydrogen storage does raise safety concerns and requires extra precautions as it is highly combustible and can be easily oxidized in containers and pipelines, although electrochemical hydrogen storage is relatively safer to handle than forms of liquid or gas storage (Singla et al. 2021). There are also other emerging technologies such as the storage of hydrogen in liquid organic hydrogen carriers and its direct use in engines, but this is still in the early stages of development (Modisha, Ouma et al. 2019, Niermann, Timmerberg et al. 2021).

The mine specific method adopted by Guerra et al. (2020) has been used whereby all the costs that the underground mining company is currently incurring for diesel fuel have been considered as revenue. Here fully mechanised mining operation were compared to hybrid mining operations to evaluate the extent of the benefit of transition to alternate fuels. The details of the revenue are detailed in Table 6 and are accordingly summarised:

- Mining vehicles have a consumption ranging from 5-188 L Day⁻¹ of diesel per unit depending on the type of machine and rated power.
- Given the total number of operating machines and their daily consumption, the total diesel consumption would equate to 1 639 440 and 86 388 761 L year⁻¹ for hybrid and fully mechanised operation respectively.
- Cost of the diesel fuel replaced by green biofuel: 1.616 \$ L⁻¹.
- Estimating the diesel price at 1.616 \$ L⁻¹ (which is the diesel price as on 25 July 2022)
- Based on diesel replacement, the biofuel production plant would produce revenues of about 2 649 335 \$ and 139 604 238 \$ per year for hybrid and fully mechanised operation respectively.
- Land leasing costs if own land to be used for biomass feedstock: 100 000 \$ per year
- Gross water costs: 2.5 \$ m⁻³

- Weighted average US\$-based cost of capital (WACC): 8 %.
- US\$-based inflation rate: 1.5 % per year

Table 6 Diesel consumption and power usage in hybrid and fully mechanised mining operations.

| | Units | Hybrid mining operations | Fully mechanised mining operations |
|---|-------|---|---|
| Mining Vehicle type | n/a | LHD | LHD Drillrig Bolter Utility vehicle Supervisory vehicle People carrier Water bowser |
| Installed power | kW | Cummings engine: 191 Kiloskar engine: 134 | LHD: 240-450 Drillrig: 58 - 74.9 Bolter: 58 - 74.9 Utility vehicle: 79.0 Supervisory vehicle: 110 People carrier: 54.0 - 79.0 Water Bowser: |
| Consumption per day per unit | L | LHD: 135 | LHD: 137 Dump Trucks 188 Drillrig: 5 Bolter: 8 Utility vehicle: 21 Supervisory vehicle: 35 People carrier: 16 Water bowser: 15 |
| Total Number of machines at mining site | n/a | LHD: 44 | All machines: 326 |
| Average annual operation | Hours | 2235.6 hrs/unit per annum (Average 8.1 hours per unit per working day) | 2526.42 hrs/unit per annum (Based on logged hours per machine type) |
| Annual diesel consumption | L | 37 260 L per unit per annum | LHD 86 995 Dump trucks: 119 380 Drillrig 2 896 |

| | | | |
|---|----------|--|---|
| | | Total for entire fleet: 1639440 L per annum | Bolter 4 801 Utility vehicle 13 335 Supervisory vehicle 22 225 People carrier 5840 Water Bowser 9525 Total for entire fleet: 86 388 761 L |
| CO ₂ Equivalent (Based on 0,0047 CO ₂ tonne generated per litre of diesel) | Tonnes | 175 tonnes CO ₂ per unit per annum Total for entire fleet: 7705 tonnes CO₂ | 1245 tonnes CO ₂ per unit per annum Total for entire fleet: 406 027 tonnes CO₂ |
| Ventilation cost | \$/annum | \$ 3 839 805 million per annum (high level estimate cost based on estimated kwh consumption of installed Main Fans and small ventilation fans underground) | \$ 9 826 650 million per annum (based on total power costs FY 2023) |

Diesel consumption and power usage in hybrid and fully mechanised mining operations were used for cost analysis. If a consumption of 1 639 440 and 86 388 761 l of diesel per year (for hybrid and fully mechanised operations respectively) can be avoided, up to 413 732 tonnes of CO₂ per year can be appreciably reduced and with technological advances potentially be completely avoided and assist mines in reaching their lower GHG commitments (Guerra et al. 2020). The high ventilation costs reported in Table 6 can be reduced as a result of the decreased PM concentrations when transitioning to greener fuels. However, the contribution that PM removal makes in the total ventilation requirement is complex and would require an additional study to be quantified.

Processing of feedstock into usable energy forms usually requires large-scale centralised facilities to take advantage of economies of scale. Therefore, transportation and logistics play an important role in the production of bioenergy. To overcome this logistical expense of transporting bulky biomasses, small decentralised plants can be built in various locations whereby the biomass can be converted into an energy dense biosyncrude or biochar. This two-stage process was successfully demonstrated by Karlsruhe Institute of Technology (KIT) with

the Bioliq biomass-to-liquid (BTL) process which was developed to overcome logistical, technical, and other biofuel production related hurdles (Dahmen et al. 2017, Niebel et al. 2021). This process is a very promising zero waste solution for SA.

Furthermore, sensitivity analyses would need to be performed for the most important parameters, such as the volatile fossil fuel and electricity prices. These two parameters are the only ones that will change in the future as a specific fleet in a specific mine have been considered.

4.4 Environmental and socio-economic factors

Sustainability is multidimensional and it acknowledges that there are inherent relations between economic, social, and environmental well-being as shown in Table 7 where the current use of diesel is compared to the prospective use of greener alternatives, BTL and biodiesel. These fuels offer more sustainable solutions that can be realised relatively quickly with the current infrastructure and expertise in SA. To add to this, research by Brent et al reviewed the viability of the SA biofuels strategy in the short term with respect to the environmental, social and economic conditions of sustainability and specifically the uncertainties pertaining to the three conditions that are identified from the feasibility study of the National Biofuels Task Team (Brent et al. 2009).

Table 7 Comparison of environmental, economic and social impacts pertaining to the use of alternate fuels. The plus symbols indicate the extent of the positive impact and the minus symbols represent the negative impact.

| | Diesel | BTL | Biodiesel |
|----------------------|--------|--|---|
| Environmental Impact | | <p style="text-align: center;">++</p> <p>Reduction of harmful atmospheric emissions.</p> <p>Reduction in GHG emissions.</p> <p>Sustainable feedstock.</p> <p>Low indirect land-use change impact.</p> <p>Positive environmental impact if sugarcane trash used as there will be a reduction in pre-harvest burn emissions.</p> | <p style="text-align: center;">+++</p> <p>Reduction of harmful atmospheric emissions.</p> <p>Reduction in GHG emissions.</p> <p>Sustainable feedstock for 2nd generation biodiesel.</p> <p>Positive environmental impact if sugarcane trash used as there will be a reduction in pre-harvest burn emissions.</p> <p>Land-use change impact.</p> <p>Saving of fossil fuels.</p> |

| | | | |
|-----------------|---|---|---|
| | -- | | |
| | <p>Unstainable fossil fuel dependence.</p> <p>Diesel exhaust emissions toxic to environment.</p> | | |
| Economic Impact | + | +++ | +++ |
| | <p>Technology and methods are established and no additional expenditure required.</p> | <p>Energy sufficiency and self-sufficiency.</p> <p>Refining power available in SA.</p> <p>Infrastructure: filling stations and routes of distribution can continue to be used.</p> <p>Fuels can be tailored to the needs of different types of engines.</p> <p>Farmers can benefit by selling biomass for refining.</p> <p>Job creation will contribute to SA GDP.</p> <p>CAPEX for required de-centralised plants.</p> <p>Increased fuel cost.</p> <p>Increased production cost and additional R&D required.</p> | <p>Energy sufficiency and self-sufficiency.</p> <p>Refining power available in SA.</p> <p>Independence of energy imports and rising oil prices.</p> <p>Infrastructure: filling stations and routes of distribution can continue to be used.</p> <p>Fuels can be tailored to the needs of different types of engines.</p> <p>Farmers can benefit by selling biomass for refining.</p> <p>Job creation will contribute to SA GDP.</p> <p>Increased fuel cost.</p> <p>Increased production cost and additional R&D required.</p> |
| | -- | - | - |
| | <p>Oil price dependant.</p> <p>Prices likely to continuously increase due to unsustainable reserves.</p> <p>Taxes and penalties may be implemented in future.</p> | <p>Cost of expansion and development of infrastructure and logistics for energy crop cultivation, processing and exports.</p> <p>Given the low volume production of biofuels they are often linked to crude-oil derived fuels in price and offer little saving to the end user unless the end user backward</p> | <p>Cost of expansion and development of infrastructure and logistics for energy crop cultivation, processing and exports.</p> |

| | | | |
|----------------|----|---|--|
| | | integrates into biofuel production. | |
| Social Impacts | | <p style="text-align: center;">+++</p> <p>Strengthening of regional agriculture. Job creation. Wide range of raw materials can be used. No competition for land with food production.</p> | <p style="text-align: center;">++</p> <p>Strengthening of regional agriculture. Job creation. Wide range of raw materials can be used. No competition for land with food production.</p> |
| | -- | Adverse health impacts from carcinogenic diesel exhaust emissions. | |

A sector-based approach could ease the rollout of the biofuel penetration: as an example, two major industries in South Africa could collaborate for mutual benefit. The sugar cane industry in South Africa is one of the world's leading producers of high-quality sugar with an estimated average production of 2.2 million tons per season (SASA 2012). The burning of sugar cane prior to harvest is common practice in South Africa where over 90 % of the sugar cane is burnt to improve harvest, handling and milling efficiencies (Pryor et al. 2017). These burn events result in atmospheric emissions, including semi-volatile organic compounds (Geldenhuys et al. 2022b), that have adverse impacts on air quality and human health on a local, regional and even a global scale. An alternative to pre-harvest burning is “green harvesting” which involves the cutting of the adult cane stalk and the removal of leaves and unwanted matter which is not typically done as it increases harvest time and costs. The increase in cost for labour could be offset by remuneration for the sugarcane trash as biomass feedstock for BTL fuel. Not only will this have positive socio-economic impacts by additional job creation in the sugarcane industry, it will also result in the reduction of biomass burn emissions and lead to healthier more sustainable development in the sugar industry, whilst at the same time providing a sustainable feedstock for alternative fuel in the mining industry for sustainable development. Another promising avenue that would promote a circular economy would be a collaborative effort with the forestry industry and synthetic fuel production industry, such as Sasol, which would close the loop between feedstock producers, refining industry and fuel user. The mining

industry is currently a large off taker of poor-quality timber for mine support beams used underground so integration with a forestry company would not only be feasible but also beneficial as waste foliage is potentially a good second-generation waste source. In this sense, the major sectors of the country can lead by example in finding greener solutions and striving for carbon neutrality and pave the way for the establishment of a biofuel industry.

5. Conclusion

Environmental protection and the search for cleaner, more sustainable fuels are two of the most important concerns modern society is facing today. The projected negative impacts of climate change and human health as well as the volatility of oil supply are forcing governments to search for alternative options. The mining sector is one of the key industries contributing to the economy but at the same time is one of the most energy intensive sectors that needs more sustainable solutions. The present work focuses on the feasibility of a transition to alternative greener fuels with focus on biodiesel and biomass-to-liquid fuel in the platinum mining industry. These selected test fuels have the potential of being generated locally with sustainable feedstocks for first or second generation of biofuel such as from sugar cane, sunflower oil or waste biomass. For biofuels to be a viable alternative, these types of liquid fuels should; be technical compatible with existing engine technology at varying fuel blends with diesel, provide a net energy gain, have environmental benefits, be economically competitive and be producible in large quantities without reducing food supplies. It is for this reason that biomass residues are an increasingly popular resource for sustainable bioenergy production and they also have numerous environmental and socio-economic benefits for the country.

The evaluation of the transition from diesel to alternative fuels was carried out according to four indicators namely; potential reductions in air emissions of harmful substances, the functional performance of biofuel versus diesel noted in practice when utilising these fuels in a LHD underground, the economic analysis of the transition from diesel to biofuel, as well as the cost and socio-economic implications of implementation.

During the underground test and sampling campaign, pollutants emitted from LHD engine exhaust were compared when operated on pure diesel, RME and GTL and the influence of emissions on air quality in the mines and thereby on human health was investigated as one aspect of this study. Here PAHs were the target analytes due to their adverse environmental and human health effects and they were sampled using portable denuder devices that simultaneously trap gas and particle phase compounds. Results showed PAHs existed primarily

in the gas phase and total PAH emissions from a high-idling load haul dump vehicle decreased considerably when substituting the diesel fuel with gas-to-liquid or biodiesel with total PAH concentrations of 34; 14 and 9 $\mu\text{g m}^{-3}$ for emissions from the diesel, GTL and RME fuelled engine respectively.

Literature findings state that biodiesel and GTL can be used directly in diesel engines without any modification, which in the mining industry implies that the current LHD fleet can be used which prevents costly and time intensive replacements. However, understanding the combustion properties of a fuel is vital to optimise the engine. Experimental observations pertaining to engine performance, changes in smoke volume and opacity as well as visual particulate matter, that were made during sampling revealed no appreciable hinderance on engine performance between the three fuels but a noticeable reduction in smoke and PM when the diesel fuel was substituted with GTL and biodiesel.

Cost analysis revealed that the production of second generation biofuels was below \$4 per gallon-gasoline for various feedstocks which was lower than the current price of diesel. Considering potential revenue based on diesel replacement, the biofuel production plant would produce revenues of about 2 649 335 \$ and 139 604 238 \$ per year for hybrid and fully mechanised operation respectively. From this study it can be concluded that the use of BTL and/or biodiesel are feasible solutions to sustainable development in South African underground platinum mines and could be implemented without excessive capital expenditure or government support.

A comparison of the environmental and socio-economic factors pertaining to the current use of diesel versus the use of biofuels clearly favours the use of biofuels with a wealth of positive impacts especially relevant in a developing country context. Positive impacts include job creation and strengthening of regional agriculture whilst the main negative impact is the cost of implementation.

From this study, and evaluation of the four indicators, it can be concluded that the use of BTL and/or biodiesel are feasible solutions to sustainable development in South Africa underground platinum mines and could be implemented without excessive capital expenditure or government support.

6. Author Information

Corresponding Author

*Patricia B.C. Forbes, patricia.forbes@up.ac.za, +27 12 420 5426 (P. Forbes),

Present Addresses

† Genna-Leigh Geldenhuys, currently at: Skin Rejuvenation Technologies, Irene, South Africa.

7. Author Contributions

G Geldenhuys: Methodology, Validation, Formal analysis, Data curation, Writing- Original draft preparation, Writing - Review & Editing; Mark Wattrus: Methodology, Writing – Review and Editing; Martyn Fox: Funding acquisition, Writing - Review & Editing; PBC Forbes: Conceptualization, Visualization, Project administration, Methodology, Formal analysis, Writing - Review & Editing, Funding acquisition.

All authors have given approval to the final version of the manuscript.

8. Funding Sources

Funding provided by the University of Pretoria, Impala Platinum Ltd. and the National Research Foundation of South Africa (NRF, grant number 105877) is acknowledged.

9. Acknowledgements

The Department of Chemistry at the University of Pretoria as well as Impala Platinum Ltd are acknowledged for their support and resources. LECO is acknowledged for the use of ChromaTOF Tile software.

10. References

- Alalwan, H.A., Alminshid, A.H. and Aljaafari, H.A. 2019. Promising evolution of biofuel generations. Subject review. *Renewable Energy Focus* 28: 127-139. DOI: <https://doi.org/10.1016/j.ref.2018.12.006>.
- Altarazi, Y.S., Yu, J., Gires, E., Ghafir, M.F.A. Lucas, J. and Yusaf, T. 2022. Effects of biofuel on engines performance and emission characteristics: A review. *Energy* 238: 121910. DOI: <https://doi.org/10.1016/j.energy.2021.121910>.
- Ambaye, T.G., Vaccari, M., Bonilla-Petriciolet, A., Prasad, S., van Hullebusch, E.D and Rtimi, S. 2021. Emerging technologies for biofuel production: a critical review on recent

- progress, challenges and perspectives. *Journal of Environmental Management* 290: 112627. DOI: <https://doi.org/10.1016/j.jenvman.2021.112627>.
- Balat, M. 2009. Prospects for worldwide biodiesel market development. *Energy Sources, Part B* 4(1): 48-58. DOI: <https://doi.org/10.1080/15567240701423951>.
- Brent, A., Wise C.R and Fortuin, H. 2009. The viability of the South African biofuels industrial strategy. *International Journal of Environment and Pollution* 39(1-2): 74-91.
- Chaudhary, A. and Brooks, T.M. 2018. Land use intensity-specific global characterization factors to assess product biodiversity footprints. *Environmental Science & Technology* 52(9): 5094-5104. DOI: <https://doi.org/10.1021/acs.est.7b05570>.
- Czech, H., Stengel, B., Adam, T., Sklorz, M., Streibel, T. and Zimmermann, R. 2017. A chemometric investigation of aromatic emission profiles from a marine engine in comparison with residential wood combustion and road traffic: Implications for source apportionment inside and outside sulphur emission control areas. *Atmospheric Environment* 167: 212-222. DOI: <https://doi.org/10.1016/j.atmosenv.2017.08.022>.
- Dahmen, N., Abeln, J., Eberhard, M., Kolb, T., Leibold, H., Sauer, J., Stapf, D. and Zimmerlin, B. 2017. The bioliq process for producing synthetic transportation fuels. *Wiley Interdisciplinary Reviews: Energy and Environment* 6(3): e236. DOI: <https://doi.org/10.1002/wene.236>.
- Dat, N.D. and Chang, M.B. 2017. Review on characteristics of PAHs in atmosphere, anthropogenic sources and control technologies. *Science of the Total Environment* 609: 682-693. DOI: <https://doi.org/10.1016/j.scitotenv.2017.07.204>.
- Department of Mineral Resources and Energy (DRME). 2020. South African Biofuels Regulatory Framework. Available online at: https://www.gov.za/sites/default/files/gcis_document/202002/43003gon116.pdf
- Department of Transport. n.d. Green Transport Strategy for South Africa (2018-2050). Available online at: https://www.transport.gov.za/documents/11623/89294/Green_Transport_Strategy_2018_2050_onlineversion.pdf/71e19f1d-259e-4c55-9b27-30db418f105a.
- du Venage, G. 2020. South Africa comes to standstill with Eskom's load shedding. *Engineering and Mining Journal* 221(1): 18-18
- Dworzanowski, M. 2013. Coal-balance between supplies to Eskom and exports. *Journal of the Southern African Institute of Mining and Metallurgy* 113(11): 01.

- Ebadian, M., van Dyk, S., McMillan, J.D. and Saddler, J. 2020. Biofuels policies that have encouraged their production and use: An international perspective. *Energy Policy* 147: 111906. DOI: <https://doi.org/10.1016/j.enpol.2020.111906>.
- Forbes, P.B.C. 2015. *Monitoring of Air Pollutants: Sampling, Sample Preparation and Analytical Techniques*. Elsevier.
- Forbes, P.B.C., Karg, E.W., Zimmermann, R. and Rohwer, E.R. 2012. The use of multi-channel silicone rubber traps as denuders for polycyclic aromatic hydrocarbons. *Analytica Chimica Acta* 730: 71-79. DOI: <https://doi.org/10.1016/j.aca.2011.11.013>.
- Forbes, P.B.C and Rohwer, E.R. 2009. Investigations into a novel method for atmospheric polycyclic aromatic hydrocarbon monitoring. *Environmental Pollution* 157(8-9): 2529-2535. DOI: <https://doi.org/10.1016/j.envpol.2009.03.004>.
- Gawlitta, N., Orasche, J., Geldenhuys, G., Jakobi, G., Wattrus, M., Jennerwein, M., Michalke, B., Gröger, T., Forbes, P.B.C. and Zimmermann, R. 2022. Comparison of the Chemical Profile of Heavy-Duty Machinery Aerosol in an Occupational Exposure Scenario with a Focus on the Impact of Alternative Fuels. *Environmental Science and Pollution Research*, Manuscript submitted.
- Geldenhuys, G., Rohwer, E.R., Naudé, Y and Forbes, P.B.C. 2015. Monitoring of atmospheric gaseous and particulate polycyclic aromatic hydrocarbons in South African platinum mines utilising portable denuder sampling with analysis by thermal desorption–comprehensive gas chromatography–mass spectrometry. *Journal of Chromatography A* 1380: 17-28. DOI: <https://doi.org/10.1016/j.chroma.2014.12.062>.
- Geldenhuys, G., Wattrus, M. and Forbes, P.B.C. 2022a. Gas and particle phase polycyclic aromatic hydrocarbon emission factors from a diesel vehicle engine: Effect of operating modes in a developing country context. *Atmospheric Environment: X* 13: 100158. DOI: <https://doi.org/10.1016/j.aeoa.2022.100158>.
- Geldenhuys, G., Orasche, J., Jakobi, G., Zimmermann, R. and Forbes, P.B.C. 2022b. Characterization of gaseous and particulate phase polycyclic aromatic hydrocarbons emitted during pre-harvest burning of sugar cane in different regions of Kwa-Zulu Natal, South Africa. *Environmental Toxicology and Chemistry* - submitted manuscript.
- GlobalData. Mining. nd. Available online at: <https://www.globaldata.com/industries-we-cover/mining/>
- Goldemberg, J., Coelho, S.T. and Guardabassi, P. 2008. The sustainability of ethanol production from sugarcane. *Energy Policy*, 36(6): 2086-2097. DOI: <https://doi.org/10.1016/j.enpol.2008.02.028>.

- Guerra, C.F., Reyes-Bozo, L., Vyhmeister, E., Caparrós, M.J., Salazar, J., Godoy-Faúndez, A., Clemente-Jul, C. and Verastegui-Rayó, D. 2020. Viability analysis of underground mining machinery using green hydrogen as a fuel. *International Journal of Hydrogen Energy* 45(8): 5112-5121. DOI: <https://doi.org/10.1016/j.ijhydene.2019.07.250>.
- Hassaneen, A., Munack, A., Ruschel, Y., Schroeder, O. and Krahl, J. 2012. Fuel economy and emission characteristics of Gas-to-Liquid (GTL) and Rapeseed Methyl Ester (RME) as alternative fuels for diesel engines. *Fuel*, 97: 125-130. DOI: <https://doi.org/10.1016/j.fuel.2012.01.077>.
- Havlík, P., Schneider, U.A., Schmid, E., Böttcher, H., Fritz, S., Skalský, R., Aoki, L., De Cara, S., Kindermann, G. and Kraxner, F. 2011. Global land-use implications of first and second generation biofuel targets. *Energy Policy* 39(10): 5690-5702. DOI: <https://doi.org/10.1016/j.enpol.2010.03.030>.
- He, C., Ge, Y., Tan, J., You, K., Han, X. and Wang, J. 2010. Characteristics of polycyclic aromatic hydrocarbons emissions of diesel engine fueled with biodiesel and diesel. *Fuel* 89(8): 2040-2046. DOI: <https://doi.org/10.1016/j.fuel.2010.03.014>.
- Jin, T., Qu, L., Liu, S., Gao, J., Wang, J., Wang, F., Zhang, P., Bai Z., and Xu, X. 2014. Chemical characteristics of particulate matter emitted from a heavy duty diesel engine and correlation among inorganic and PAH components. *Fuel* 116: 655-661. DOI: <https://doi.org/10.1016/j.fuel.2013.08.074>.
- Karavalakis, G., Gysel, N., Schmitz, D.A., Cho, A.K., Sioutas, C., Schauer, J.J., Cocker, D.R. and Durbin, T.D. 2017. Impact of biodiesel on regulated and unregulated emissions, and redox and proinflammatory properties of PM emitted from heavy-duty vehicles. *Science of the Total Environment* 584: 1230-1238. DOI: <https://doi.org/10.1016/j.scitotenv.2017.01.187>
- Khan, N., Sudhakar, K. and Mamat, R. 2021. Role of Biofuels in Energy Transition, Green Economy and Carbon Neutrality. *Sustainability* 13(22): 12374. DOI: <https://doi.org/10.3390/su132212374>.
- Kohlmeier, V., Dragan, G.C., Karg, E.W., Schnelle-Kreis, J., Breuer, D., Forbes, P.B.C., Rohwer E.R. and Zimmermann, R. 2017. Multi-channel silicone rubber traps as denuders for gas-particle partitioning of aerosols from semi-volatile organic compounds. *Environmental Science: Processes & Impacts* 19(5): 676-686. DOI: DOI <https://doi.org/10.1039/C7EM00044H>.
- Kojima, M. and Johnson, T. 2005. Potential for Biofuels for Transport in Developing Countries. Washington, D.C.: Energy Sector Management Assistance Programme

- (ESMAP), Energy and Water Department, The World Bank Group. URI: <http://hdl.handle.net/10986/18007>.
- Labeckas, G. and Slavinskas, S. 2006. The effect of rapeseed oil methyl ester on direct injection diesel engine performance and exhaust emissions. *Energy Conversion and Management* 47(13-14): 1954-1967. DOI: <https://doi.org/10.1016/j.enconman.2005.09.003>.
- Masondo, H. 2022. Energy crisis and the economy. *Without Prejudice* 22(1): 44-45. URI: https://hdl.handle.net/10520/ejc-jb_prej_v22_n1_a24.
- McCaffery, C., Zhu, H., Ahmed, C.S., Canchola, A., Chen, J.Y., Li, C., Johnson, K.C., Durbin, T.D., Lin, Y.H. and Karavalakis, G. 2022. Effects of hydrogenated vegetable oil (HVO) and HVO/biodiesel blends on the physicochemical and toxicological properties of emissions from an off-road heavy-duty diesel engine. *Fuel* 323: 124283. DOI: <https://doi.org/10.1016/j.fuel.2022.124283>.
- Modisha, P.M., Ouma, C.N., Garidzirai, R., Wasserscheid, P. and Bessarabov, D. 2019. The prospect of hydrogen storage using liquid organic hydrogen carriers. *Energy & Fuels* 33(4): 2778-2796. DOI: <https://doi.org/10.1021/acs.energyfuels.9b00296>.
- Moon, G., Lee, Y., Choi, K. and Jeong, D. 2010. Emission characteristics of diesel, gas to liquid, and biodiesel-blended fuels in a diesel engine for passenger cars. *Fuel* 89(12): 3840-3846. DOI: <https://doi.org/10.1016/j.fuel.2010.07.009>.
- Munyeza, C.F., Kohlmeier, V., Dragan, G.C., Karg, E.W., Rohwer, E.R., Zimmermann, R. and Forbes, P.B.C. 2019. Characterisation of particle collection and transmission in a polydimethylsiloxane based denuder sampler. *Journal of Aerosol Science* 130: 22-31. DOI: <https://doi.org/10.1016/j.jaerosci.2019.01.001>.
- Neto, J.M., Komesu, A., Martins, L.H.D.S., Gonçalves, V.O., De Oliveira, J.A.R. and Rai, M. 2019. Third-generation biofuels: An overview. *Sustainable Biofuel and Biomass*: 261-280. eBook ISBN9780429265099.
- Niebel, A., Funke, A., Pfitzer, C., Dahmen, N., Weih, N., Richter, D. and Zimmerlin, B. 2021. Fast pyrolysis of wheat straw—improvements of operational stability in 10 years of Bioliq pilot plant operation. *Energy & Fuels* 35(14): 11333-11345. DOI: <https://doi.org/10.1021/acs.energyfuels.1c00851>.
- Niermann, M., Timmerberg, S., Drünert, S. and Kaltschmitt, M. 2021. Liquid Organic Hydrogen Carriers and alternatives for international transport of renewable hydrogen. *Renewable and Sustainable Energy Reviews* 135: 110171. DOI: <https://doi.org/10.1016/j.rser.2020.110171>.

- Papakonstantinou, E., Mitsis, T., Dragoumani, K., Efthimiadou, A., Bacopoulou, F., Chrousos, G.P., Eliopoulos, E. and Vlachakis, D. 2021. Materials of biological origin and biofuels: Small environmental footprint and epigenetic impact. *International Journal of Epigenetics* 1(3): 1-8. DOI: <https://doi.org/10.3892/ije.2021.6>.
- Prokopowicz, A., Zaciera, M., Sobczak, A., Bielaczyc, P. and Woodburn, J. 2015). The effects of neat biodiesel and biodiesel and HVO blends in diesel fuel on exhaust emissions from a light duty vehicle with a diesel engine. *Environmental Science & Technology* 49(12): 7473-7482. DOI: <https://doi.org/10.1021/acs.est.5b00648>.
- Pryor, S.W., Smithers, J., Lyne, P. and van Antwerpen, R. 2017. Impact of agricultural practices on energy use and greenhouse gas emissions for South African sugarcane production. *Journal of Cleaner Production* 141: 137-145. DOI: <https://doi.org/10.1016/j.jclepro.2016.09.069>.
- PubChem 2021. PubChem Database, Available online at: <https://pubchem.ncbi.nlm.nih.gov/compound> [Accessed on 19/06/2022].
- Raheman, H., Jena, P.C. and Jadav, S.S. 2013. Performance of a diesel engine with blends of biodiesel (from a mixture of oils) and high-speed diesel. *International Journal of Energy and Environmental Engineering*, 4(1), 1-9. DOI: <https://doi.org/10.1186/2251-6832-4-6>.
- Roberts, S. 2022. Structural Transformation in South Africa: Moving Towards a Smart, Open Economy for All. *Open Economy for All* (May 8, 2022). DOI: <http://dx.doi.org/10.2139/ssrn.4103733>.
- SAPIA. South African Petroleum Industry Association. 2021. The economic contribution of the downstream oil industry to South Africa in 2019. Available online at: https://www.sapia.org.za/wp-content/uploads/2022/04/SAPIA_Economic-Impact-Assessment.pdf
- SA DME. South African Department of Minerals and Energy 2003. White paper on renewable energy. Available online at: <http://www.dme.gov.za/energy/documents.stm>
- SA DME. South African Department of Minerals and Energy. 2006. Draft biofuels industrial strategy of the Republic of South Africa, Directorate of Clean Energy and Energy Planning. Available online at: <http://www.dme.gov.za/energy/documents.stm>
- SA DME. South African Department of Minerals and Energy. 2021. The South African energy sector report. Available online at:

- <http://www.energy.gov.za/files/media/explained/2021-South-African-Energy-Sector-Report.pdf>.
- Senauer, B. 2008. Food market effects of a global resource shift toward bioenergy. *American Journal of Agricultural Economics* 90(5): 1226-1232. DOI: 10.1111/j.1467-8276.2008.01208.x.
- Singla, M.K., Nijhawan, P. and Oberoi, A.S. 2021. Hydrogen fuel and fuel cell technology for cleaner future: a review. *Environmental Science and Pollution Research* 28(13): 15607-15626. DOI: <http://doi.org/10.1007/s11356-020-12231-8>.
- The Minerals Council South Africa. 2023. Facts and Figures 2022 Pocketbook. Available online at: <https://www.mineralscouncil.org.za/industry-news/publications/facts-and-figures>.
- Tsai, J.H., Chen, S.J., Lin, S.L., Huang, K.L., Hsueh, C.K., Lin, C.C. and Li, P.M. 2019. Emissions of PM_{2.5}-bound polycyclic aromatic hydrocarbons and metals from a diesel generator fueled with biodiesel converted from used cooking oil. *Aerosol and Air Quality Research* 19(7): 1555-1565. DOI: <https://doi.org/10.4209/aaqr.2019.04.0204>.
- Van Zyl, W. and Prior, B.A. 2009. South Africa biofuels. *IEA Task Group 39*: 1-5.
- Walter, A., Rosillo-Calle, F., Dolzan, P., Piacente, E. and da Cunha, K.B. 2008. Perspectives on fuel ethanol consumption and trade. *Biomass and Bioenergy* 32(8): 730-748. DOI: <https://doi.org/10.1016/j.biombioe.2008.01.026>.
- Watson, H., Garland, G., Purchase, B., Dercas, N., Griffee, P. and Johnson, F. 2008. Bioenergy for sustainable development and global competitiveness: The case of sugar cane in Southern Africa. *Thematic Report 1*. Stockholm: SEI. CARENSA/SEI special report series.
- Wattrus, M.C., Biffi, M., Pretorius, C.J. and Jacobs, D. 2016. Assessing stationary laboratory test methods for underground mining vehicles to determine their suitability in replicating real-world emissions. *CSIR Research Space*. URI: <http://hdl.handle.net/10204/9309>.
- Witcover, J. and Williams, R. 2019. Comparison of 'Advanced' biofuel cost estimates: trends during rollout of low carbon fuel policies. *Transport and Environment* 79:102211. DOI: <https://doi.org/10.1016/j.trd.2019.102211>.
- Wright, M.L. and Lewis, A.C. 2022. Decarbonisation of heavy-duty diesel engines using hydrogen fuel: a review of the potential impact on NO_x emissions. *Environmental Science: Atmospheres* 2: 852-866. DOI: 10.1039/D2EA00029F.

Paper 3: Supplementary Information

Table S1 Sample details for underground platinum mine campaign

| Sample name | Sample abbreviation | Location | Number of denuders | Sample point description | Sampling duration (min) | Sampling Volume (L) | Air velocity at sampling positions ($m\ s^{-1}$) |
|--|---------------------|----------------------|--------------------|---|-------------------------|---------------------|--|
| Field Blank | FBLK | Workshop parking bay | 1 | n/a | n/a | n/a | n/a |
| Upwind (Uw) LHD High Idle (HI) Pure diesel (PD) (Dw LHD-HI-PD) | Uw-LHD-PD | Workshop parking bay | 1 | 16 m upwind from LHD tailpipe in line | 10 | 5.012 | 1.1 |
| LHD High Idle (HI) Pure diesel (PD) (LHD-HI-PD) | LHD-HI-PD A,B | Workshop parking bay | 2 | 1 m from tailpipe | 11, 10 | 5.025 | 0.9 |
| Downwind (Dw) LHD High Idle (HI) Pure diesel (PD) (Dw LHD-HI-PD) | Dw-LHD-HI-PD | Workshop parking bay | 1 | 16 m downwind from LHD tailpipe in line | 10 | 5.054 | 0.5 |
| Upwind (Uw) LHD Test cycle (TC) Pure diesel (PD) (Uw LHD-TC-PD) | Uw LHD-TC-PD | Workshop parking bay | 1 | 16 m upwind from LHD tailpipe in line | 10 | 5.028 | 1.1 |
| LHD Test Cycle(TC) Pure diesel (PD) (LHD TC-PD) | LHD TC-PD A, B | Workshop parking bay | 2 | 1 m from tailpipe | 10 | 5.399, 5.353 | 0.9 |
| Downwind (Dw) LHD Test cycle (TC) Pure diesel (PD) (Dw LHD-TC-PD) | Dw LHD-TC-PD | Workshop parking bay | 1 | 16 m downwind from LHD tailpipe in line | 10 | 5.198 | 0.5 |
| Upwind (Uw) LHD High Idle (HI) Gas to liquid (GTL) (Uw LHD-HI-GTL) | Uw-LHD-GTL | Workshop parking bay | 1 | 16 m upwind from LHD tailpipe in line | 10 | 5.135 | 1.2 |
| LHD High Idle (HI) Gas to liquid (GTL) (LHD-HI-GTL) | LHD-HI-GTL A, B | Workshop parking bay | 2 | 1 m from tailpipe | 10 | 5.122, 5.112 | 0.8 |
| Downwind (Dw) LHD High Idle (HI) Gas to liquid (GTL) (Dw LHD-HI-GTL) | Dw-LHD-HI-GTL | Workshop parking bay | 1 | 16 m downwind from LHD tailpipe in line | 10 | 4.994 | 0.7 |
| Upwind (Uw) LHD Test cycle (TC) Gas to liquid (GTL) (Uw LHD-TC-GTL) | Uw LHD-TC-GTL | Workshop parking bay | 1 | 16 m upwind from LHD tailpipe in line | 10 | 4.868 | 1.2 |
| LHD Test Cycle(TC) Gas to liquid (GTL) (LHD TC-GTL) | LHD TC-GTL A, B | Workshop parking bay | 2 | 1 m from tailpipe | 10 | 4.360, 3.748 | 0.8 |
| Downwind (Dw) LHD Test cycle (TC) Gas to liquid (GTL) (Dw LHD-TC-GTL) | Dw LHD-TC-GTL | Workshop parking bay | 1 | 16 m downwind from LHD tailpipe in line | 10 | 4.999 | 0.7 |
| Upwind (Uw) LHD High Idle (HI) Rapeseed methyl ester (RME) (Dw LHD-HI-RME) | Uw-LHD-PD | Workshop parking bay | 1 | 16 m upwind from LHD tailpipe in line | 10 | 5.203 | 1.4 |
| LHD High Idle (HI) Rapeseed methyl ester (RME) (LHD-HI-RME) | LHD-HI-PD A, B | Workshop parking bay | 2 | 1 m from tailpipe | 10 | 5.247, 5.028 | 0.8 |
| Downwind (Dw) LHD High Idle (HI) Rapeseed methyl ester (RME) (Dw LHD-HI-RME) | Dw-LHD-HI-PD | Workshop parking bay | 1 | 16 m downwind from LHD tailpipe in line | 10 | 5.224 | 0.6 |
| Upwind (Uw) LHD Test cycle (TC) Rapeseed methyl ester (RME) (Uw LHD-TC-RME) | Uw LHD-TC-RME | Workshop parking bay | 1 | 16 m upwind from LHD tailpipe in line | 10 | 5.103 | 1.4 |
| LHD Test Cycle(TC) Rapeseed methyl ester (RME) (LHD TC-RME) | LHD TC-PD A, B | Workshop parking bay | 2 | 1 m from tailpipe | 10 | 5.146, 5.210 | 0.8 |

| | | | | | | | |
|---|-----------------|----------------------|---|---|----|--------------|------|
| Downwind (Dw) LHD Test cycle (TC) Rapeseed methyl ester (RME) (Dw LHD-TC-RME) | Dw LHD-TC-RME | Workshop parking bay | 1 | 16 m downwind from LHD tailpipe in line | 10 | 5.071 | 0.6 |
| Upwind (Uw) LHD High Idle (HI) Pure diesel bracket (PDB) (Dw LHD-HI-PDB) | Uw-LHD-PDB | Workshop parking bay | 1 | 16 m upwind from LHD tailpipe in line | 10 | 5.026 | 1.2 |
| LHD High Idle (HI) Pure diesel bracket (PDB) (LHD-HI-PDB) | LHD-HI-PDB A, B | Workshop parking bay | 2 | 1 m from tailpipe | 10 | 4.885, 4.898 | 0.8 |
| Downwind (Dw) LHD High Idle (HI) Pure diesel bracket (PDB) (Dw LHD-HI-PDB) | Dw-LHD-HI-PDB | Workshop parking bay | 1 | 16 m downwind from LHD tailpipe in line | 10 | 4.943 | 0.65 |
| Upwind (Uw) LHD Test cycle (TC) Pure diesel bracket (PDB) (Uw LHD-TC-PDB) | Uw LHD-TC-PDB | Workshop parking bay | 1 | 16 m upwind from LHD tailpipe in line | 10 | 5.028 | 1.2 |
| LHD Test Cycle(TC) Pure diesel bracket (PDB) (LHD TC-PDB) | LHD TC-PDB A, B | Workshop parking bay | 2 | 1 m from tailpipe | 10 | 5.027, 5.035 | 0.8 |
| Downwind (Dw) LHD Test cycle (TC) Pure diesel bracket (PDB) (Dw LHD-TC-PDB) | Dw LHD-TC-PDB | Workshop parking bay | 1 | 16 m downwind from LHD tailpipe in line | 10 | 4.981 | 0.65 |

Table S2 ChromaTOF File list of chemical features contributing to variances between gas phase LHD PDMS samples for PD, RME and GTL fuel.

| Name | Formula | Similarity | CAS | Quant mass | F-ratio |
|---|----------|------------|------------|------------|---------|
| Undecane | C11H24 | 883 | 1120-21-4 | 157 | 482 |
| cis-9-Tetradecen-1-ol | C14H28O | 749 | 35153-15-2 | 91 | 397 |
| 9-Tetradecen-1-ol, (E)- | C14H28O | 754 | 52957-16-1 | 93 | 326 |
| Tridecane | C13H28 | 791 | 629-50-5 | 155 | 298 |
| Nonane | C9H20 | 815 | 111-84-2 | 170 | 292 |
| Decane | C10H22 | 818 | 124-18-5 | 170 | 280 |
| 7-Phenyl-1-heptyl chloride | C13H19Cl | 765 | 71434-47-4 | 104 | 279 |
| Benzene, 1-methyl-2-(1-methylethyl)- | C10H14 | 889 | 527-84-4 | 102 | 268 |
| 3-Hexanone, 2,2-dimethyl- | C8H16O | 804 | 5405-79-8 | 157 | 225 |
| Benzene, 1,3-diethyl- | C10H14 | 776 | 141-93-5 | 118 | 220 |
| p-Xylene | C8H10 | 820 | 106-42-3 | 103 | 215 |
| Phenol, 2-methyl-6-(2-propenyl)- | C10H12O | 715 | 3354-58-3 | 131 | 193 |
| Benzene, 2-ethyl-1,4-dimethyl- | C10H14 | 740 | 1758-88-9 | 131 | 189 |
| Cyclohexane, pentyl- | C11H22 | 757 | 4292-92-6 | 67 | 184 |
| 1-Undecanol | C11H24O | 851 | 112-42-5 | 68 | 173 |
| Benzene, 1,2,3,4-tetramethyl- | C10H14 | 937 | 488-23-3 | 63 | 169 |
| Octane, 3,5-dimethyl- | C10H22 | 790 | 15869-93-9 | 170 | 160 |
| Pentadecane | C15H32 | 770 | 629-62-9 | 140 | 141 |
| n-Tridecan-1-ol | C13H28O | 758 | 112-70-9 | 153 | 139 |
| 2,2-Dimethyl-3-heptene trans | C9H18 | 781 | 19550-75-5 | 153 | 129 |
| Indane | C9H10 | 806 | 496-11-7 | 74 | 116 |
| 11-Hexadecen-1-ol, (Z)- | C16H32O | 794 | 56683-54-6 | 168 | 93 |
| 1-Undecanol | C11H24O | 746 | 112-42-5 | 166 | 68 |
| 9-Octadecenoic acid (Z)-, methyl ester | C19H36O2 | 872 | 112-62-9 | 264 | 50 |
| Benzene, 1-ethyl-2-methyl- | C9H12 | 833 | 611-14-3 | 62 | 48 |
| Cyclohexene, 1-methyl-4-(1-methylethylidene)- | C10H16 | 761 | 586-62-9 | 93 | 47 |
| Dodecanal | C12H24O | 764 | 112-54-9 | 155 | 46 |
| Isooctanol | C8H18O | 759 | 26952-21-6 | 155 | 41 |
| Hexadecane | C16H34 | 791 | 544-76-3 | 184 | 38 |
| Cyclohexane, ethyl- | C8H16 | 831 | 1678-91-7 | 168 | 38 |
| 2(3H)-Furanone, dihydro-5-propyl- | C7H12O2 | 755 | 105-21-5 | 85 | 34 |
| Benzofuran | C8H6O | 853 | 271-89-6 | 89 | 34 |
| Phthalan | C8H8O | 890 | 496-14-0 | 92 | 32 |
| Cyclohexane, (2-methylpropyl)- | C10H20 | 864 | 1678-98-4 | 54 | 31 |
| 1-Dodecene | C12H24 | 758 | 112-41-4 | 153 | 28 |
| Benzene, 1,2,3-trimethyl- | C9H12 | 964 | 526-73-8 | 134 | 23 |
| Indene | C9H8 | 941 | 95-13-6 | 63 | 21 |
| Benzene, 1-(1,1-dimethylethyl)-3,5-dimethyl- | C12H18 | 807 | 98-19-1 | 146 | 21 |
| Azulene | C10H8 | 915 | 275-51-4 | 135 | 21 |
| Cyclopentadecanol | C15H30O | 774 | 4727-17-7 | 124 | 20 |
| 1-Tridecene | C13H26 | 769 | 2437-56-1 | 139 | 19 |

| | | | | | |
|---|----------|-----|------------|-----|----|
| 2-Naphthaleneethanol | C12H12O | 765 | 1485-07-0 | 154 | 19 |
| Oxirane, [[(2-ethylhexyl)oxy]methyl]- | C11H22O2 | 707 | 2461-15-6 | 167 | 18 |
| Phenol, 2,6-dimethyl- | C8H10O | 731 | 576-26-1 | 104 | 17 |
| Benzaldehyde, 2-hydroxy- | C7H6O2 | 860 | 1990/02/08 | 94 | 17 |
| Acetophenone | C8H8O | 829 | 98-86-2 | 76 | 15 |
| Oleyl Alcohol | C18H36O | 703 | 143-28-2 | 79 | 15 |
| Phenol, 3-methyl- | C7H8O | 876 | 108-39-4 | 90 | 14 |
| Î ³ Dodecalactone | C12H22O2 | 713 | 2305/05/07 | 141 | 14 |
| 1,2-Naphthalenedione | C10H6O2 | 826 | 524-42-5 | 129 | 13 |
| 1-Pentanol, 3-methyl- | C6H14O | 774 | 589-35-5 | 56 | 13 |
| Naphthalene, 1-methyl- | C11H10 | 945 | 90-12-0 | 70 | 13 |
| 1,1'-Biphenyl, 2-methyl- | C13H12 | 922 | 643-58-3 | 170 | 13 |
| Vitamin A aldehyde | C20H28O | 762 | 116-31-4 | 164 | 13 |
| Benzene, propyl- | C9H12 | 880 | 103-65-1 | 105 | 11 |
| 1(2H)-Naphthalenone, 3,4-dihydro-5,7-dimethyl- | C12H14O | 710 | 13621-25-5 | 187 | 11 |
| Hexane, 2,4-dimethyl- | C8H18 | 838 | 589-43-5 | 142 | 11 |
| Octadecanoic acid, methyl ester | C19H38O2 | 839 | 112-61-8 | 255 | 10 |
| Naphthalene, 1-(1-methylethyl)- | C13H14 | 846 | 6158-45-8 | 156 | 10 |
| 1-Pentadecene | C15H30 | 726 | 13360-61-7 | 111 | 10 |
| Tetracosane | C24H50 | 772 | 646-31-1 | 74 | 10 |
| 4-Isopropylcyclohexanone | C9H16O | 719 | 5432-85-9 | 139 | 10 |
| Hexadecanoic acid, methyl ester | C17H34O2 | 847 | 112-39-0 | 241 | 9 |
| 9-Hexadecen-1-ol, (Z)- | C16H32O | 705 | 10378-01-5 | 220 | 9 |
| Eicosane | C20H42 | 856 | 112-95-8 | 226 | 9 |
| Tridecanoic acid, methyl ester | C14H28O2 | 862 | 1731-88-0 | 326 | 9 |
| Gibberellic acid | C19H22O6 | 785 | 1977/06/05 | 271 | 9 |
| n-Hexadecanoic acid | C16H32O2 | 725 | 1957/10/03 | 303 | 9 |
| Heptadecanoic acid, methyl ester | C18H36O2 | 761 | 1731-92-6 | 284 | 9 |
| Dodecanoic acid, methyl ester | C13H26O2 | 807 | 111-82-0 | 87 | 9 |
| Î ² Carotene | C40H56 | 765 | 7235-40-7 | 292 | 9 |
| 1-Decanol | C10H22O | 830 | 112-30-1 | 54 | 9 |
| Naphthalene, 1,6,7-trimethyl- | C13H14 | 873 | 2245-38-7 | 142 | 9 |
| Cholest-5-en-3-ol (3Î ²)-, tetradecanoate | C41H72O2 | 713 | 1989-52-2 | 258 | 9 |
| Retinal, 9-cis- | C20H28O | 755 | 514-85-2 | 257 | 9 |
| n-Pentadecanol | C15H32O | 722 | 629-76-5 | 294 | 9 |
| Biphenyl | C12H10 | 968 | 92-52-4 | 76 | 9 |



Figure S1 Photograph of load haul dump vehicle used for underground mining operations

Chapter 5: Development of a novel sampler based on graphene wool (Paper 4)

This chapter consists of three papers that were published in the Journal of Materials Science, ACS Omega & Environmental Technology & Innovation, respectively

Firstly, the synthesis and optimisation of a novel graphene wool material is presented in Paper 4 which was published in the *Journal of Materials Science*.

Schoonraad, G., Madito J.M., Manyala N. and Forbes P.B.C. 2020. Synthesis and optimisation of a novel graphene wool material by atmospheric pressure chemical vapour deposition, *Journal of Materials Science*, 55, 545-564. DOI: <https://doi.org/10.1007/s10853-019-03948-0>.

Author contributions

G Schoonraad: Conceptualization, Investigation, Methodology, Formal analysis, Writing - original draft. **J.M Madito:** Conceptualization, Investigation, Methodology, Formal analysis, Writing - review & editing. **N Manyala:** Resources, Writing - review & editing. **P.B.C Forbes:** Conceptualization, Methodology, Investigation, Formal analysis, Writing - review & editing, Supervision, Project administration, Resources, Funding acquisition.



Synthesis and optimisation of a novel graphene wool material by atmospheric pressure chemical vapour deposition

Genna-Leigh Schoonraad^{1,2}, Moshawe Jack Madito³, Ncholu Manyala³, and Patricia Forbes^{1,*}

¹Department of Chemistry, University of Pretoria, Lynnwood Road, Hatfield, Pretoria 0001, South Africa

²Processing Laboratory, Impala Platinum Ltd, 123 Bethlehem Drive, Rustenburg 0299, South Africa

³Department of Physics, Institute of Applied Materials, University of Pretoria, Lynnwood Road, Hatfield, Pretoria 0001, South Africa

Received: 29 April 2019

Accepted: 20 August 2019

© Springer Science+Business Media, LLC, part of Springer Nature 2019

ABSTRACT

A novel graphene wool material was synthesised by non-catalytic chemical vapour deposition using a high-purity quartz wool substrate. The in situ synthesis method avoids post-growth transfer and isolation steps and allows the graphene to be directly synthesised into graphene wool. In the absence of a catalyst during graphene growth, the cracking of methane and nucleation is not as efficient, resulting in graphene defects which can be minimised by optimising the growth conditions. The roles of the methane and hydrogen flow rates in the synthesis of the graphene wool were investigated, as was the effect of growth temperature, growth time and cooling rates. The precursor flow rates and growth temperature were found to be the most vital parameters. The best quality graphene wool showed a minimum ratio of the disordered carbon relative to the graphitic carbon ($I_D/I_G \approx 0.8$) with a calculated crystallite grain size of 24 nm. The morphology of the optimised graphene wool was flake-like, and the X-ray photoelectron spectroscopy analysis revealed a surface composition of 94.05 at.% C 1s and 5.95 at.% O 1s. With this new material, the integrity of the synthesised graphene surface is preserved in use and it has the added advantage of structural support from the quartz substrate. Unlike many other forms of graphene, this fibrous graphene wool is flexible, malleable and compressible, allowing for a wealth of potential applications including in electronics, energy storage, catalysis, and gas sorption, storage, separation and sensing applications.

Address correspondence to E-mail: patricia.forbes@up.ac.za

<https://doi.org/10.1007/s10853-019-03948-0>

Published online: 27 August 2019

Springer

Introduction

Graphene is a crystalline allotrope of carbon nanomaterial that has received worldwide attention due to its unique physical, mechanical, electrical and optical properties, not to mention its high specific surface area and hydrophobic properties which also deems graphene a suitable candidate for sorbents [1–6]. Graphene can be visualised as an atomic-scale hexagonal arrangement of sp^2 -bonded carbon atoms which are densely packed in a two-dimensional plane. Each carbon atom is approximately 0.142 nm apart and has four bonds, three of which are σ bonds to carbon neighbours and one π -bond that is oriented out of the basal plane. The stability of graphene can be attributed to the sp^2 orbital hybridisation of each carbon atom that has a p_z orbital perpendicular to the molecular plane [7]. The overlap of adjacent p_z orbitals forms hybrid π -band and π^* -bands which permit free-moving electrons which constitute graphene's notable electronic properties [7].

The recognition of graphene's properties promulgated a number of graphene-related materials for potential applications in electronics, energy storage, catalysis, and gas sorption, storage, separation and sensing [8–18]. Over the last couple of years, various methodologies for the synthesis of graphene have been tried and tested including mechanical exfoliation and cleavage [19, 20], reduction from chemically exfoliated graphene oxide [21, 22], epitaxial growth on silicon carbide [23, 24] and chemical vapour deposition (CVD). Chemical vapour deposition includes thermal CVD, plasma-enhanced CVD and thermal decomposition on SiC and other substrates. CVD has proved to be the most popular method for graphene syntheses as it yields high-quality, large-area and grain-size graphene films with controlled thickness, and it is a reproducible technique. However, conventionally grown graphene on metal surfaces must be isolated from the metal or transferred to the desired substrate for desired applications. The isolation and transfer procedures tend to induce mechanical damage, metal etching residues and chemical contamination which is why it is exceedingly desirable to produce graphene directly through CVD without a metallic catalyst [5]. In spite of the complexity of CVD graphene synthesis and transfer from different metal catalysts, the physical principles underlying the synthesis mainly rely on carbon precursor decomposition due to the metal catalytic

reaction and graphene nucleation on the catalyst surface [25–30].

With metal-catalyst-free CVD methods, e.g. on SiO_2/Si [1], Al_2O_3 [31], silicon [32], gallium [33] and boron nitride [34], carbon precursor decomposition and graphene nucleation mainly rely on the reaction parameters used during CVD synthesis. The main parameters include carbon precursor concentration, growth temperature and time, H_2 concentration (H_2 effect on graphene nucleation and growth) and chemical surface modification of the substrate. In addition, these parameters have received much attention in the optimisation of CVD graphene synthesis using the metal-catalyst CVD method for which various metal catalysts have been investigated [27, 28, 35–39]. In this work, similar reaction parameters were investigated for metal-catalyst-free CVD graphene synthesis using a high-purity quartz wool substrate. Other quartz substrates, such as z-cut single crystals (0001) and commercially available polished quartz discs and plates, have been used for graphene growth [5, 40]; however, these substrates are very rigid by nature which can limit the application of the resulting graphene material. To date, no study has reported on graphene synthesised on quartz wool by CVD to produce flexible graphene wool.

Herein, we report on atmospheric pressure CVD synthesis of graphene on a high-purity quartz wool substrate [41]. The roles of the methane and hydrogen flow rates, as well as the effect of growth temperature, growth time and cooling rates on the quality of graphene wool were investigated. The quality and number of graphene layers were analysed using confocal Raman spectroscopy imaging. Scanning electron microscopy (SEM) images were used to investigate the graphene wool morphology and surface homogeneity. The chemical composition of the best quality graphene wool according to Raman analysis was subsequently examined by X-ray photoelectron spectroscopy (XPS). Based on the characterisation of as-synthesised graphene wool, we present the reaction details for each experiment (synthesis process) and propose optimal growth parameters to produce the best quality graphene wool, which has a wide range of potential uses, including in electronics, energy storage, catalysis, and gas sorption, storage, separation and sensing applications [42].

Materials and method

Chemicals and synthesis of graphene wool

Commercially available 9–30- μm coarse quartz wool (Arcos Organics, New Jersey, USA) was used as a substrate for the growth of graphene by atmospheric pressure chemical vapour deposition (APCVD). The quartz wool was placed in the middle of the horizontal quartz tube (50 mm o.d., 44 mm i.d., \times 1000 mm length) of the OTF 1200X-50-5L high-temperature furnace (MTI Corporation, California, USA). A mixture of 500 sccm argon (99.999%, Afrox, South Africa) and hydrogen (99.999%, Afrox, South Africa) was introduced into the system after which the temperature was ramped at $20\text{ }^\circ\text{C min}^{-1}$ to the desired growth temperature (Fig. 1a). The substrate was annealed under these conditions for 10 min after which methane (99.95%, Afrox, South Africa) was introduced for graphene growth. After the growth period had elapsed, the system was cooled under Ar and H_2 by shifting the furnace chamber off centre for rapid cooling at a rate of $-14.5\text{ }^\circ\text{C s}^{-1}$ and for slow cooling the furnace was switched off and cooled under ambient conditions at a rate of $-0.4\text{ }^\circ\text{C s}^{-1}$. The deposited graphitic carbon takes the shape of the quartz wool substrate by covering the surface of each fibre, and it was not necessary to remove the substrate; thus, the term 'graphene wool (GW)' in this study infers graphene coated on quartz wool. In order to optimise the growth conditions to achieve the highest quality graphene, the following parameters were varied: methane gas flow (20, 50, 100, 150, 200 sccm), hydrogen gas flow (500, 250, 0 sccm),

grow time (30, 60, 90 min), growth temperature (800, 1200, 1300 $^\circ\text{C}$) and cooling rate (slow, rapid).

Characterisation techniques

The as-grown graphene on quartz wool was characterised by a combination of techniques including Raman spectroscopy and scanning electron microscopy (SEM) where high-resolution X-ray photoelectron spectroscopy (XPS) and high-resolution transmission electron microscopy were also performed on the optimised sample.

The quality and thickness of the graphene were evaluated using confocal Raman imaging which was carried out using a WITec alpha300 RAS+ confocal Raman microscope (WiTec, Germany) and a 532 nm excitation laser at low power of 5 mW. The image scans were acquired using a $50\times/0.75$ Zeiss objective with diffraction limited lateral resolution of 433 nm, and the scans were acquired over $50\times 50\text{ }\mu\text{m}^2$ area with 150 points per line and 150 lines per image using an integration time of 0.5 s. To acquire the confocal Raman imaging along each quartz wool fibre with the true surface held in constant focus during the entire measurement procedure, the true surface imaging mode was used.

XPS (K-Alpha, Thermo Fisher Scientific Inc., USA) was used to characterise the sample composition, and the binding energies were referenced to the C 1s line at 284.8 eV. The analysis was carried out under ultra-high vacuum chamber using an Al $\text{K}\alpha$ X-rays at 1486.66 eV, and a take-off angle of 20° was selected for higher surface sensitivity.

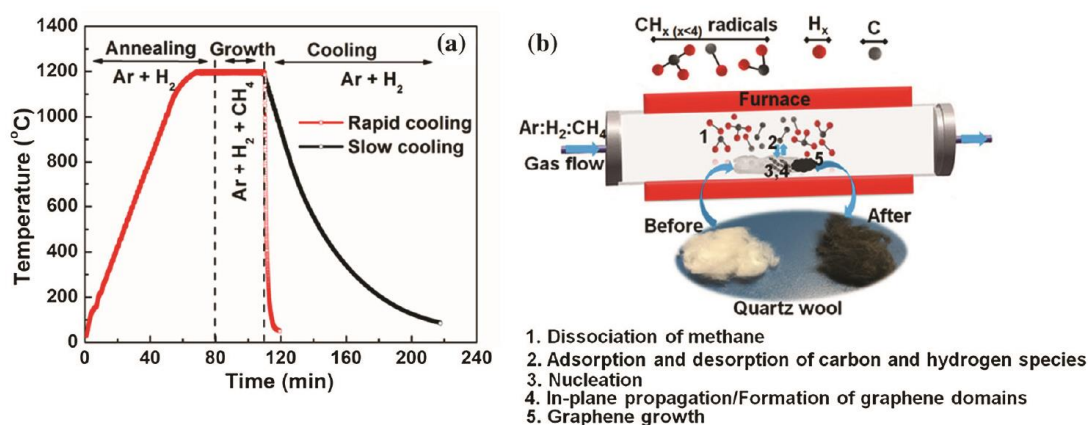


Figure 1 a Temperature profile of the CVD process as measured by a series of thermocouples and b schematic of the non-catalytic direct growth mechanism of CVD graphene on quartz wool substrate.

The surface morphologies of the graphene wool samples were characterised by Zeiss Ultra Plus 55 field emission scanning electron microscope (FE-SEM), operated at 2.0 kV (Zeiss, Germany). The graphene wool was mounted with carbon tape onto a stainless steel stub and sputtered with gold prior to SEM analysis. Transmission electron microscopy (TEM) images were taken using a JEOL JEM 2100F (JOEL Ltd, Tokyo, Japan) operated at 200 kV.

Results and discussion

The non-catalytic direct growth mechanism of CVD graphene

The mechanisms applicable to CVD growth of graphene are dependent on the substrate, with metal surfaces commonly found to follow carbon precipitation processes or metal-catalysed processes to yield high-quality graphene films. In the literature, the numerous proposed mechanisms for graphene growth on SiO₂ are not in full agreement with a vapour–solid–solid growth mechanism and the van der Waals growth model both successfully being applied, whilst most other authors do not revert to a single model [1, 4, 32]. Figure 1a graphically represents the temperature profile in the CVD system, illustrating the three stages of the process, and our proposed growth mechanism is presented. During the annealing stage, the hydrogen gas flow cleans the surface of the quartz wool substrate with the additional role of roughening of the surface to facilitate nucleation for graphene growth. During the growth stage at high temperatures (> 1000 °C), methane gas is introduced into the system and the main processes involved include:

1. Dissociation of methane to form reactive carbon and hydrogen species (Fig. 1b) that possess sufficient activation energy to reach the surface of the quartz wool ($\text{CH}_4 = \text{C} + 2\text{H}_2$ ($\Delta H = 75.6 \text{ kJ mol}^{-1}$)) [43].
2. Adsorption and desorption of carbon and hydrogen species at the surface.
3. Nucleation which occurs as active carbon atoms are anchored onto the quartz surface, mainly through van der Waal C–O and H–O bonding arising from electrostatic interactions between electronic charge density fluctuations [44].

4. In-plane propagation as more carbon atoms are adsorbed at the edges of the stable nuclei in such a way that small, flat monolayer or bilayer graphene domains are primarily formed [32]. In-plane propagation is plausible as the cohesion energy between the polar quartz surface and graphene is higher than between two carbon atoms suggesting that subsequent carbon species favourably land on the clean quartz substrate instead of stacking on top of existing domains [5].
5. Graphene growth: As more methane gas enters the system, the number of active carbonaceous radicals increases and the deposition of the carbon atoms by physisorption becomes more sporadic resulting in further in-plane propagation of existing domains, edge-stacking and ultimately C–C coupling and stacking of graphene sheets [1]. Due to the resultant number of irregular domains of varying thickness and orientation, it is also possible that vertical stacking occurs. The overall graphene formation is thus bi- and multi-layered sheets on the surface of the quartz wool.

During the cooling stage, the above-mentioned processes are terminated by rapid cooling of the substrate/furnace centre by shifting the furnace chamber off centre.

The effect of growth temperature on the quality of graphene wool

The effect of the growth temperature was the first parameter that was optimised as preliminary tests as well as other literature studies [1, 32, 40] confirmed that temperature was the most critical parameter in the synthesis in that it would ultimately either yield or not produce graphene. Experiments were carried out by growing graphene on three separate quartz wool samples under the same conditions (500:500:100 sccm, Ar/H₂/CH₄, 30 min growth) with varied growth temperature from 800 to 1300 °C.

In this study, confocal Raman spectroscopy was adopted to identify the quality of graphene and the number of layers formed. Typically, the Raman characteristic features of high-quality graphene are the G-band mode at $\sim 1590 \text{ cm}^{-1}$ and the 2D band mode at $\sim 2690 \text{ cm}^{-1}$ which originate from the normal first-order Raman scattering process (the tangential vibration of the sp^2 carbon atoms) and the

second-order process (double resonance Raman process) that involves two in-plane transverse optical mode (iTO) phonons near the *K*-point [5, 32], respectively. In defective graphene, an additional band, namely disorder-induced D band at $\sim 1350 \text{ cm}^{-1}$ is observed which originates from a double resonance Raman process involving intervalley scattering of iTO phonon and defect near the *K*-point [7]. The electronic band structure of graphene is sensitive to interlayer interactions (influenced by the number of layers) and stacking orders which can be shown using Raman spectroscopy due to the double resonance nature of the D band and 2D band. To determine the number of layers in high-quality graphene, the 2D-to-G peak intensity ratio (I_{2D}/I_G), 2D band line-shape and peak width are analysed [7]. In defective graphene, a high disorder (high D peak intensity) could influence the broadening of the 2D peak since the 2D band is the overtone of the D band [31]. Nonetheless, it is accepted that for monolayer graphene, the D and 2D bands are composed of a symmetric Lorentzian peak [35].

Figure 2 shows the Raman data of the graphene wool obtained at different growth temperatures. Figure 2a, d, g shows the optical microscope image with an overlay mapping of the G peak intensities which confirm that the quartz wool substrate was coated with carbon at higher temperatures with the most intense bright yellow surface for 1200 °C. To confirm this finding the Raman spectra (Fig. 2j) revealed that the signature defective graphene D, G and 2D bands were not observed at the lower temperature growth of 800 °C but were clearly seen for samples at higher temperatures. When considering the growth at higher temperatures at 1200 and 1300 °C, the calculated I_D/I_G ratio (the area under the D peak) increases with increasing growth temperature from an average value of 0.85 at 1200 °C to 1.60 at 1300 °C (Fig. 2k) suggesting lower-quality (or more highly disordered) graphene at higher temperatures (> 1200 °C). The calculated 2D-to-G peak intensity ratios (I_{2D}/I_G) decrease with increasing growth temperature from an average value of 0.95 at 1200 °C to 0.60 at 1300 °C which demonstrates the characteristics of a bilayer at 1200 °C and multi-layered graphene at 1300 °C. From the literature, the typical Raman spectra of high-quality monolayer, bilayer and multilayer graphene show I_{2D}/I_G ratios of > 2, ~ 1 and < 0.7, respectively [45]. The optimum temperature for graphene growth in this study was thus

found to be 1200 °C which yields uniform bilayer graphene coating of the quartz wool.

The SEM images in Fig. 3 correlate with the Raman data and show that the nucleation density is the highest at 1200 °C as is the visual surface area of graphene. This sample is dominated by a high density of graphene islands that are flaky in appearance. The increase in nucleation density with increasing temperature was also found in a study by Tai et al. [32] who further demonstrated that the average grain number and the maximum grain size vary as a function of growth temperature indicating that temperature is a key factor in controlling graphene nucleation and growth. However, the authors who used single-crystal silicon substrates also noted that if the temperature is too high it can destroy the quartz surface. In this study, it appears that the substrate surface was modified at the higher temperature of 1300 °C (Fig. 3d) resulting in a more bulging graphene surface which was significantly different to that seen at 1200 °C in Fig. 3c. As aforementioned, the Raman spectra confirmed the presence of graphene at a higher temperature but with a higher level of disorder.

The results of the temperature based experiments can be explained by considering the fundamental growth and nucleation processes. At 800 °C, graphene was not able to be synthesised as a direct result of the inefficient decomposition of the methane precursor [40]. The lower temperature also results in lower activation energies for the carbon species that are then consequently not able to form stable bonds with the substrate surface and are unable to form stable nuclei. This is the opposite of what was found at the highest growth temperature of 1300 °C. Here, the methane can be efficiently broken down resulting in large numbers of carbon species, including fragments (CH_x ($x < 4$)) as well as various dimers and monomers [4, 5]. At elevated temperatures, these carbon species have very high activation energies and easily come into contact with the quartz surface and are then adsorbed by dispersive C–O and H–O binding, but it must also be noted that thermal vibrational energy also increases with increasing temperature [5], disrupting the weak intermolecular bonds resulting in the higher rate of desorption compared to adsorption of the carbon species from the substrate and thus lower-quality graphene. The growth at 1200 °C can be viewed as an ideal balance between the activation and thermal vibrational

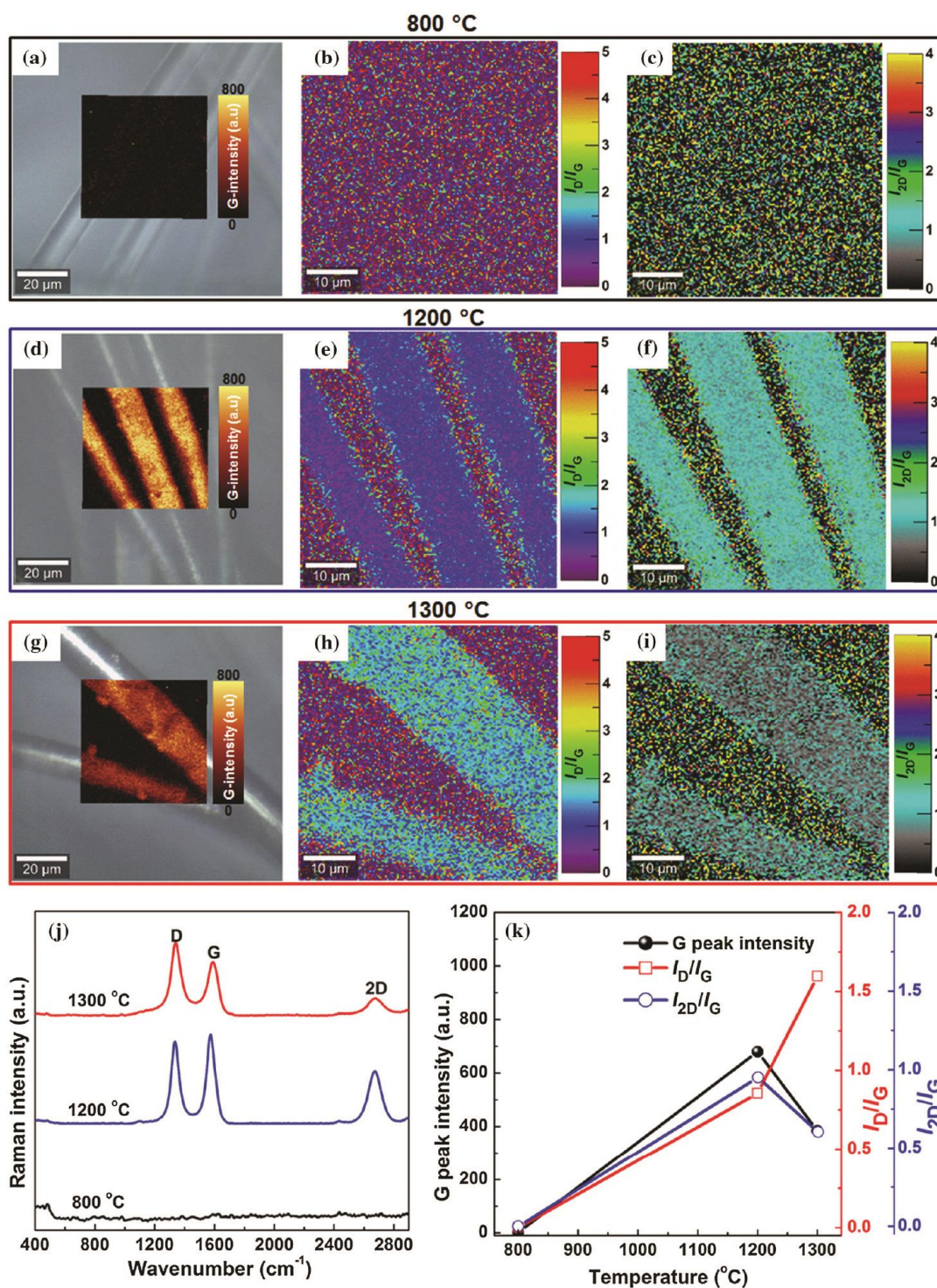
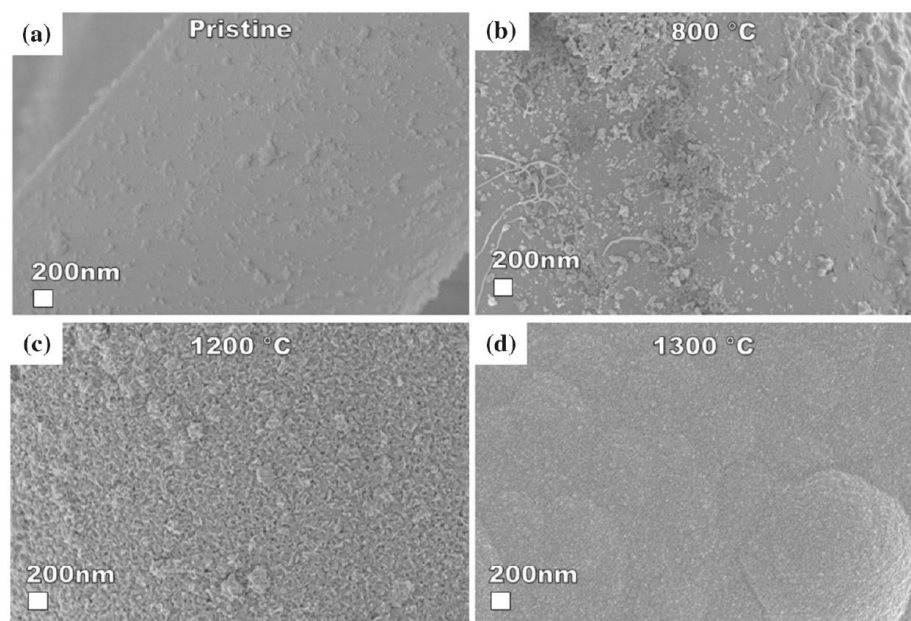


Figure 2 G intensity map (a), I_D/I_G ratio map (b) and I_{2D}/I_G ratio map (c) for GW grown at 800 °C. G intensity map (d), I_D/I_G ratio map (e) and I_{2D}/I_G ratio map (f) for GW grown at 1200 °C. G intensity map (g), I_D/I_G ratio map (h) and I_{2D}/I_G ratio map (i) for

GW grown at 1300 °C. Comparison of the D, G and 2D peaks in the Raman spectra (j) and graph representing G intensity and I_D/I_G and I_{2D}/I_G ratios (k).

Figure 3 SEM images for pristine quartz wool (a), GW grown at 800 °C (b), 1200 °C (c) and 1300 °C (d).



energy, and as a result, the highest quality graphene wool was obtained with a minimum ratio of the disordered carbon relative to the graphitic carbon (I_D/I_G).

The effect of cooling rate on the quality of graphene

To investigate the effect of the cooling rate on the quality of synthesised graphene, two options were considered with two separate samples, each sample grown with the following parameters 500:500:50 sccm (Ar/H₂/CH₄) for 30 min. The growth was carried out at 1200 °C which was established to be the optimum temperature in the previous experiment. Slow cooling occurred by simply switching the furnace off after the growth period and leaving the CVD system to cool under ambient conditions at an average rate of -0.4 °C s^{-1} . Rapid cooling occurred by switching off the furnace and shifting the tube horizontally so that the sample was completely removed from the heating zone where additional cooling was facilitated by a built-in fan, resulting in a rapid cooling rate of approximately -14.5 °C s^{-1} . Figure 4a–h shows the Raman data of individual graphene wool fibres obtained at slow and rapid cooling rates. When comparing the G peak intensity mapping for the slowly cooled sample in Fig. 4a with the fast cooled sample in Fig. 4d, it is

evident that the rapidly cooled sample yielded a much better and more uniform carbon surface coverage. This finding correlated to a significantly lower I_D/I_G peak ratio of ~ 1.7 for the rapidly cooled sample (Fig. 4e) as opposed to the value of ~ 2.7 (Fig. 4b) for the slowly cooled sample. The average Raman spectra depicted in Fig. 4g confirmed higher-quality graphene in the rapidly cooled sample with more intense characteristic G and 2D bands at ~ 1590 and $\sim 2700\text{ cm}^{-1}$, respectively, with a lower D band contribution at $\sim 1350\text{ cm}^{-1}$. Based on the findings of these experiments, all of the subsequent samples in this study were grown at 1200 °C and rapidly cooled.

The SEM images for the synthesised graphene wool under different cooling rates are shown in Fig. 5b, c for slow and rapid cooling, respectively, and compared to the pristine quartz surface in Fig. 5a. The rapidly cooled sample showed a higher density of graphene domains suggesting that the cooling rate affected nucleation. This notion is supported by the G map images showing that the rapidly cooled surface had higher G intensities, thus more surface coverage with carbon. To explain this, the rapid drop in temperature coincides with lower vibrational energies on the surface, thereby reducing desorption of anchored carbon nuclei that are bound to the surface by weak van der Waals forces [44].

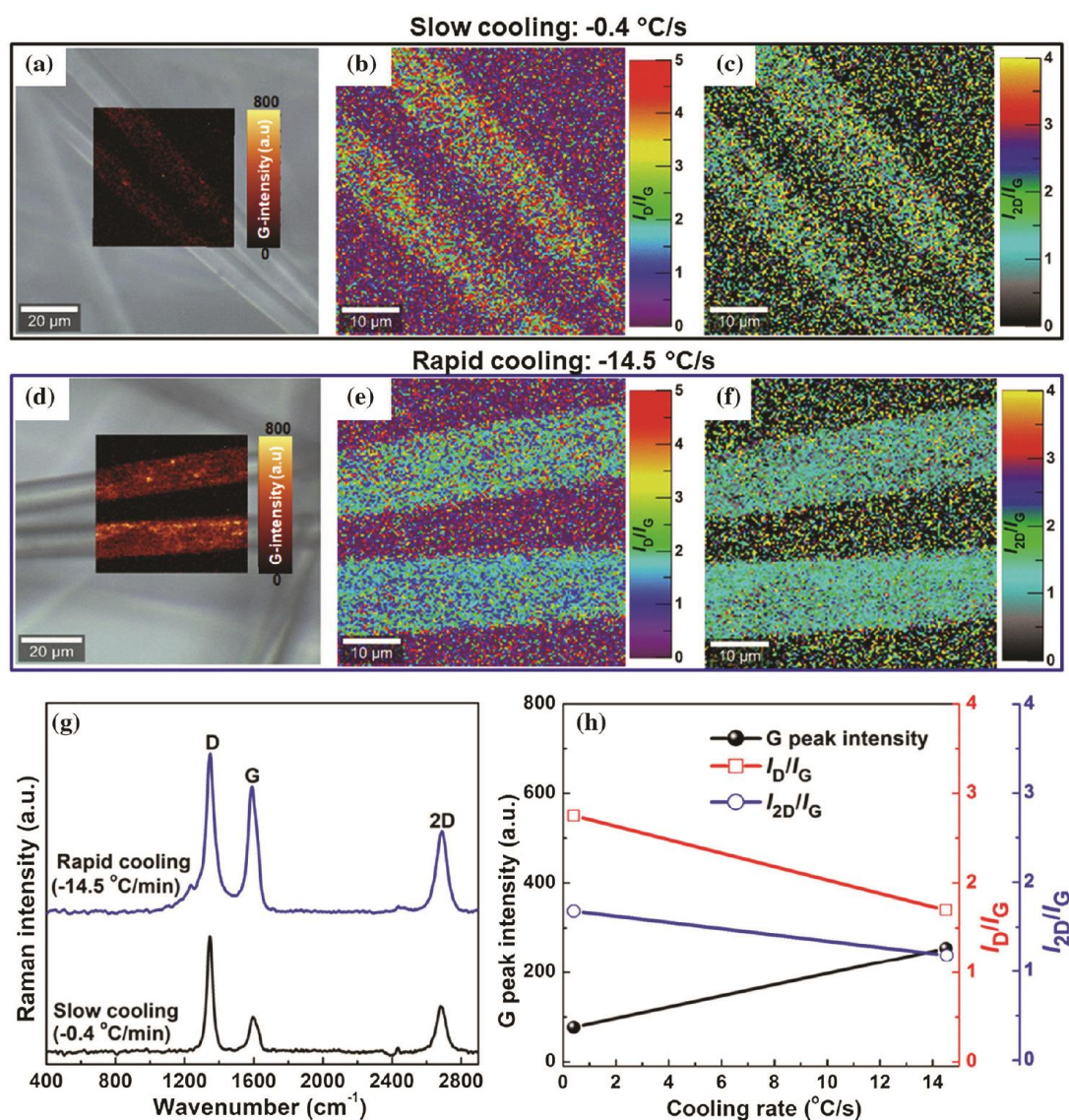


Figure 4 G intensity map (a), I_D/I_G ratio map (b) and I_{2D}/I_G ratio map (c) for GW that was cooled slowly at $-0.4\text{ }^\circ\text{C s}^{-1}$. G intensity map (d), I_D/I_G ratio map (e) and I_{2D}/I_G ratio map (f) for

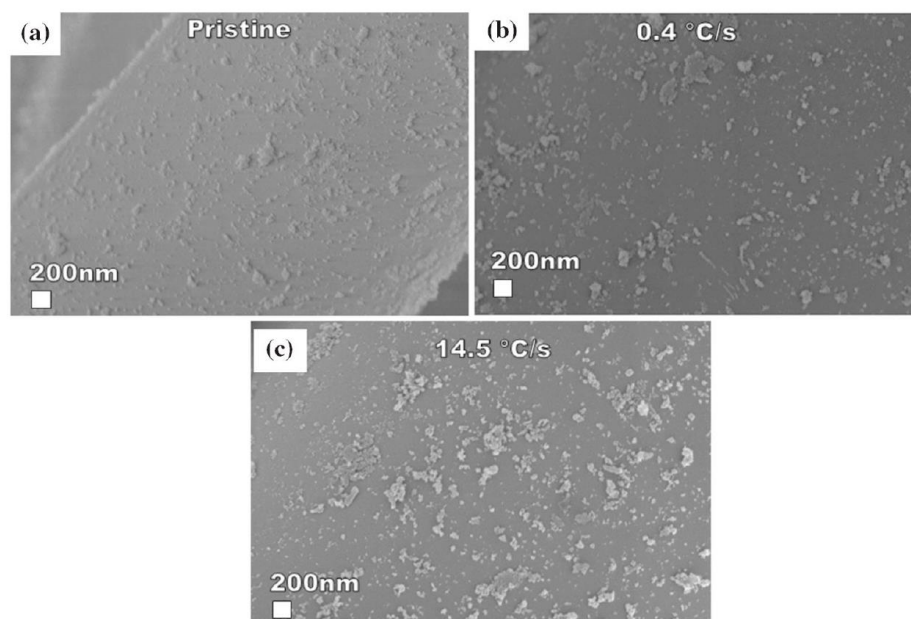
GW that was cooled rapidly at $-14.5\text{ }^\circ\text{C s}^{-1}$. **g** Comparison of the D, G and 2D peaks in the Raman spectra (**g**) and graph representing G intensity and I_D/I_G and I_{2D}/I_G ratios (**h**).

The effect of methane flow rate on the quality of graphene

The effect of methane flow rate was investigated by growing graphene on five separate quartz wool samples under the conditions (500:500:20–200 sccm, Ar/H₂/CH₄, 30 min growth at 1200 °C and cooled at $-14.5\text{ }^\circ\text{C s}^{-1}$) where the methane flow rate was varied from 20 to 200 sccm during the growth period. Figures 6 and 7 show the Raman data relating to the graphene wool obtained at different methane flow

rates. Based on the G, I_D/I_G and I_{2D}/I_G mapping in Fig. 6a–o, the methane flow rate of 100 sccm (Fig. 6g–i) could be clearly identified as the optimum flow rate when considering the bright intensity of the G mapping and lower I_D/I_G ratio of < 1 (Fig. 7b). At higher methane flow rates > 100 sccm, the ratio of the disordered carbon relative to the graphitic carbon increases due to more defective graphene deposition on the quartz wool. The decrease in I_{2D}/I_G ratio with increasing methane flow rate confirms multi-layered graphene growth. Figure 6a–c relating to a low flow

Figure 5 SEM images for pristine quartz wool (a), GW grown and cooled slowly at a rate of $-0.4\text{ }^{\circ}\text{C s}^{-1}$ (b) and GW grown and cooled rapidly at a rate of $-14.5\text{ }^{\circ}\text{C s}^{-1}$ (c) at 200 nm range.



rate (20 sccm) shows little/no graphitic carbon present on the quartz surface, and the absence of the characteristic 2D peak in Fig. 7a further suggests that graphene was not formed at lower methane flow rates (≤ 20 sccm). This finding was consistent with the study by Xu et al. [5] in which the authors used methane flow rates ranging from 8 to 400 sccm to control the number of graphene layers formed on polished quartz discs. In other studies, lower methane flow rates ranging from 1 to 20 sccm were successfully applied in the growth of graphene; however, this was demonstrated on a catalytic copper surface [46]. Placing a substrate vertically in the CVD tube, as in the study by Chen et al. [4], can significantly increase the probability of collisions between the reactive carbon fragments and the quartz surface and result in lower required methane flow rates and shorter growth times however, the less rigid nature of the quartz wool substrate used in this study limited the orientation options in the CVD tube. The number of layers appears to be different at various methane flow rates suggesting that the kinetic rate-limiting step is in the transport of gas molecules to the surface of the substrate and not the surface reaction [46]. Consequently, the growth is not self-limiting and the formation of bi- and multi-layered graphene is possible.

The SEM images for the samples grown at different methane flow rates are shown in Fig. 8a–f. It can be

clearly seen that the nucleation densities increase with increasing methane flow rates with the most significant increase observed when doubling the flow rate from 50 sccm (Fig. 8c) to 100 sccm (Fig. 8d). The optimum flow rate of 100 sccm showed a very densely covered surface with a relatively uniform flaky appearance. When the flow rate was increased to 150 and 200 sccm, respectively, the morphology changed to being more clustered and irregular in nature as a result of the non-uniform number of layers associated with an excess of methane, and the increase in spherical shapes is likely due to the presence of amorphous carbon.

The effect of hydrogen flow rate on the quality of graphene

The effect of hydrogen flow rate was investigated by growing graphene on three separate quartz wool samples under the exact same conditions except for the hydrogen flow rate that differed during the growth period (500:0–500:100 sccm, Ar/H₂/CH₄ 30 min growth time at 1200 °C and cooled at $-14.5\text{ }^{\circ}\text{C s}^{-1}$). When comparing the G intensity mapping in Fig. 9a, d, g, it is evident that 500 sccm was the optimum flow rate as confirmed by the most intense and uniform carbon coverage of the fibrous quartz surface. The I_D/I_G ratio maps in Fig. 9b, e, h and the lowest average I_D/I_G ratio of ~ 0.7 as seen in

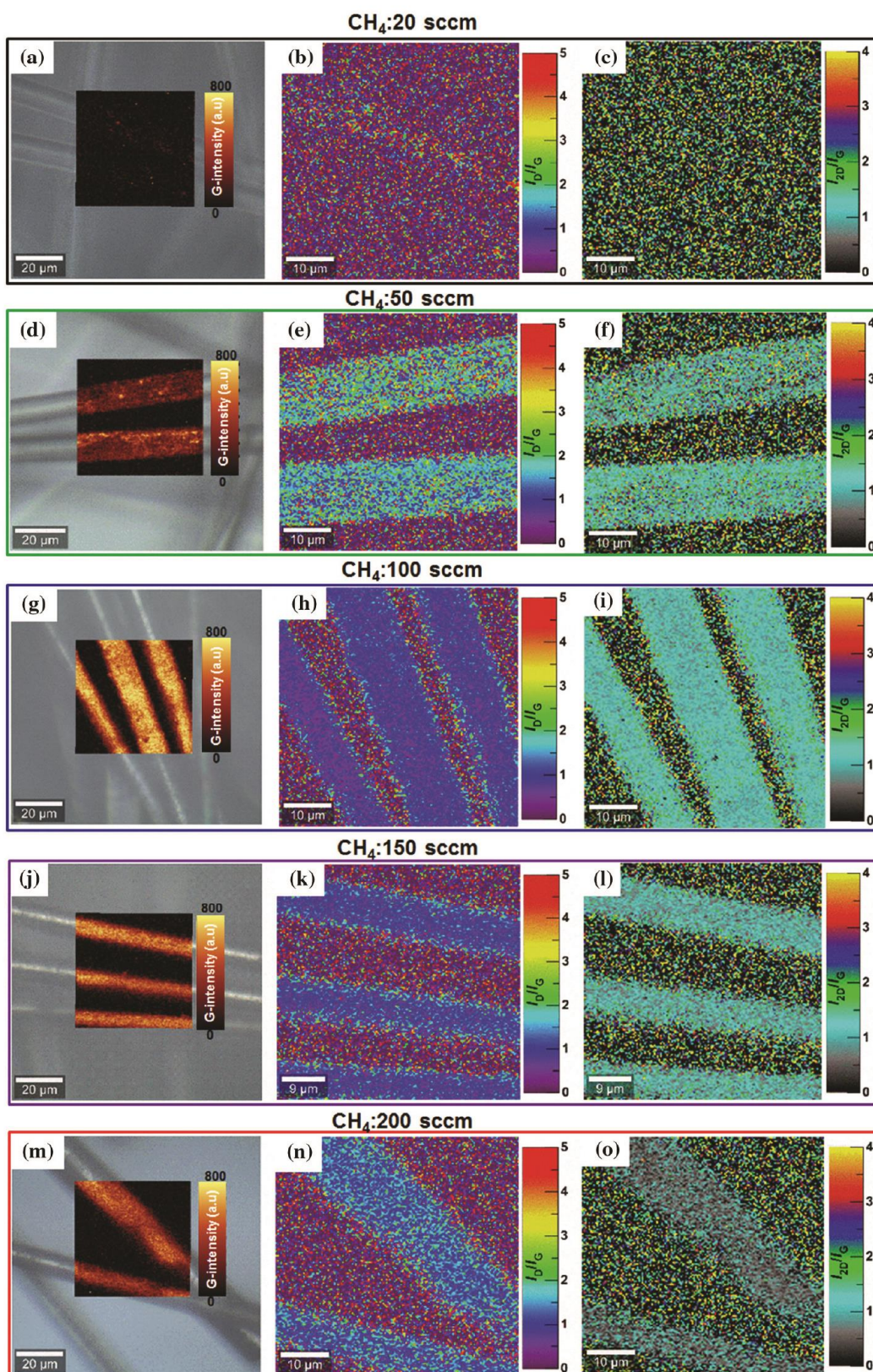


Figure 6 G intensity map (a), I_D/I_G ratio map (b) and I_{2D}/I_G ratio map (c) for GW grown with 20 sccm CH_4 . G intensity map (d), I_D/I_G ratio map (e) and I_{2D}/I_G ratio map (f) for GW grown with 50 sccm CH_4 . G intensity map (g), I_D/I_G ratio map (h) and I_{2D}/I_G ratio map (i) for GW grown with 100 sccm CH_4 . G intensity map (j), I_D/I_G ratio map (k) and I_{2D}/I_G ratio map (l) for GW grown with 150 sccm CH_4 . G intensity map (m), I_D/I_G ratio map (n) and I_{2D}/I_G ratio map (o) for GW grown with 200 sccm CH_4 .

Fig. 9k further revealed the obvious optimum H_2 flow rate. The I_{2D}/I_G ratio maps in Fig. 9c, f, i visually demonstrate the vital role that H_2 plays during the growth of graphene as the I_{2D}/I_G ratio approaches zero if the H_2 flow is too low due to the absence of the characteristic 2D peak. This is supported by the Raman spectra in Fig. 9j that shows that when the growth was carried out in the absence of hydrogen, there was no graphene present on the quartz wool as there was no 2D band. The spectra resembled that of amorphous carbon in that there were signature broad bands enveloping the G and D bands [5]. Similar amorphous carbon signatures were found when the hydrogen was introduced at a lower flow rate of 250 sccm. These findings strongly demonstrate the vital role of hydrogen in non-catalytic growth of graphene on a quartz wool substrate. The H_2 aids in the efficient cracking of methane and substrate surface roughening, thereby increasing the number of nucleation sites for graphene growth, and it has been found that hydrogen saturation can stabilise the graphene edges by reducing the desorption rates of carbon-containing species [47]. In terms of the actual

growth, the H_2 also plays a role in governing the number of graphene layers and thickness of surface coverage as it facilitates the H-termination of graphene domains which influences the growth mechanism. This is in agreement with other findings relating to the growth mechanism of a hydrogen-excluded CVD process, which suggests that hydrogen plays a critical role in determining the rate-limiting step and whether or not monolayer graphene is obtainable irrespective of the surface roughness [46].

Based on the SEM images shown in Fig. 10 for samples grown with and without the addition of H_2 , it is evident that the samples in which the hydrogen flow was either not present (0 sccm, Fig. 10b) or too low (250 sccm, Fig. 10c) showed a significant difference in surface morphology when compared to the optimum flow rate of 500 sccm in Fig. 10d. The optimum H_2 flow rate showed a uniform flake-like morphology, whereas the samples grown without sufficient H_2 flow showed a very different bulging morphology.

The effect of growth time on the quality of graphene

The growth time investigation was carried out under the exact same conditions (500:500:100 sccm, Ar/ H_2 / CH_4 at 1200 °C and cooled at -14.5 °C s^{-1}) where only the growth period was varied from 30 to 90 min. It can be seen from the Raman data in Fig. 11 that the growth time had less of an effect on the quality of graphene than the other parameters with the I_D/I_G ratios of ~ 0.80 , 0.75 and 0.70 for 30, 60 and 90 min

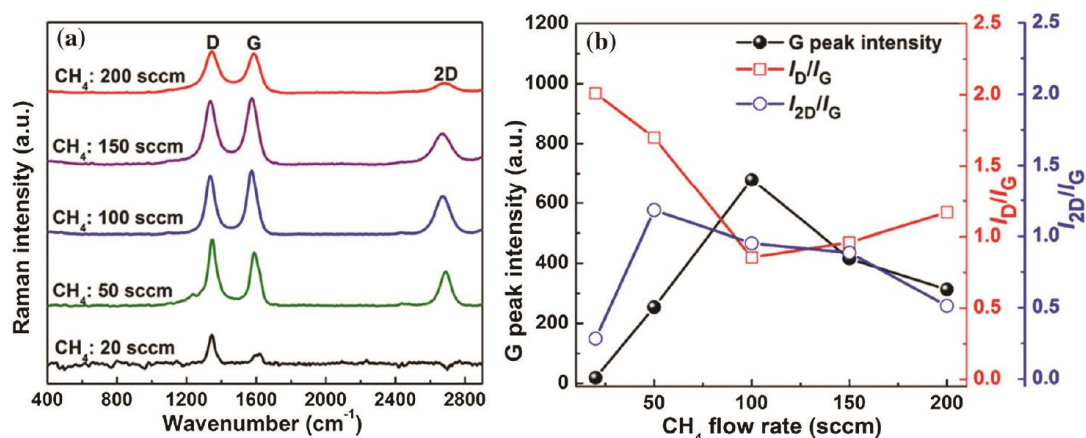
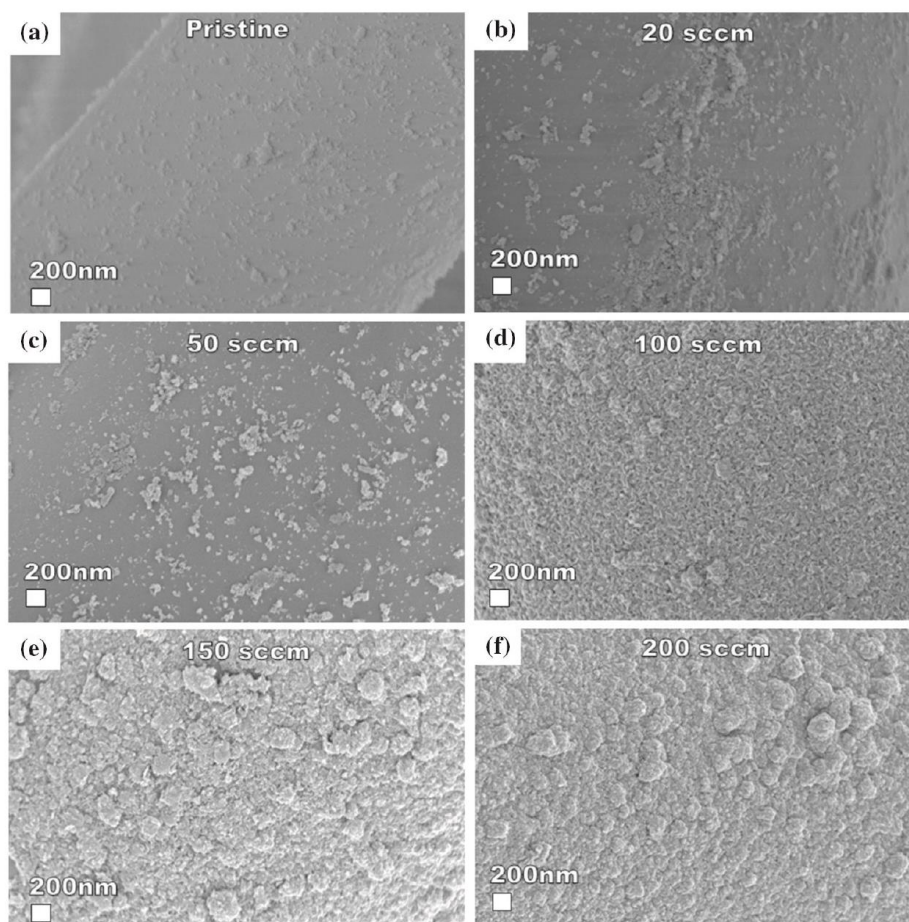


Figure 7 Comparison of the D, G and 2D peaks in the Raman spectra (a) and graph representing G intensity and I_D/I_G and I_{2D}/I_G ratios (b) for GW grown at different methane flow rates.

Figure 8 SEM images for pristine quartz wool (a) and GW grown with methane flow rates of 20 sccm (b), 50 sccm (c), 100 sccm (d), 150 sccm (e) and 200 sccm (f).



growth, respectively. The I_{2D}/I_G ratio was relatively consistent between the three growth temperatures as seen in the ratio maps (Fig. 11c, f, i) as well as the average intensities in Fig. 11k implying that the number of layers did not change significantly.

Having considered the increased cost and time involved with 90 min growth, it was not selected as an optimum parameter especially since it was very comparable to the 30 min growth time.

The surface morphologies of the graphene wool samples grown for different time periods are evident from the SEM images in Fig. 12b–d. At first glance, the image for the sample grown for 30 min (Fig. 12b) appears to have the highest nucleation density and the most uniform surface coverage. Figure 12c, d for 60 and 90 min growth times, respectively, showed very similar morphologies to that of the sample grown for 30 min in terms of the flaky appearance with few clustered arrangements; however, they appear to be much less uniform with more flat

surfaces visible in between the graphene domains and a higher density of larger carbon clusters.

Characterisation of graphene wool synthesised under optimised conditions

Raman

The Raman images of the graphene wool grown under optimised conditions are presented in Fig. 13 (500:500:100 sccm, Ar/H₂/CH₄ for 30 min at 1200 °C and cooled at -14.5 °C s⁻¹). The G intensity mapping (Fig. 13a) exhibited relatively uniform carbon coverage across the sample with an average I_D/I_G ratio of 0.85, as depicted in Fig. 13b. The I_{2D}/I_G mapping (Fig. 13c) displayed an average value of 0.93, and the 2D peaks full width at half maximum (FWHM) mapping (Fig. 13d) showed values in the range of 25–80 cm⁻¹ which demonstrated the characteristics of bilayer graphene, indicating the formation of mostly bilayer graphene wool.

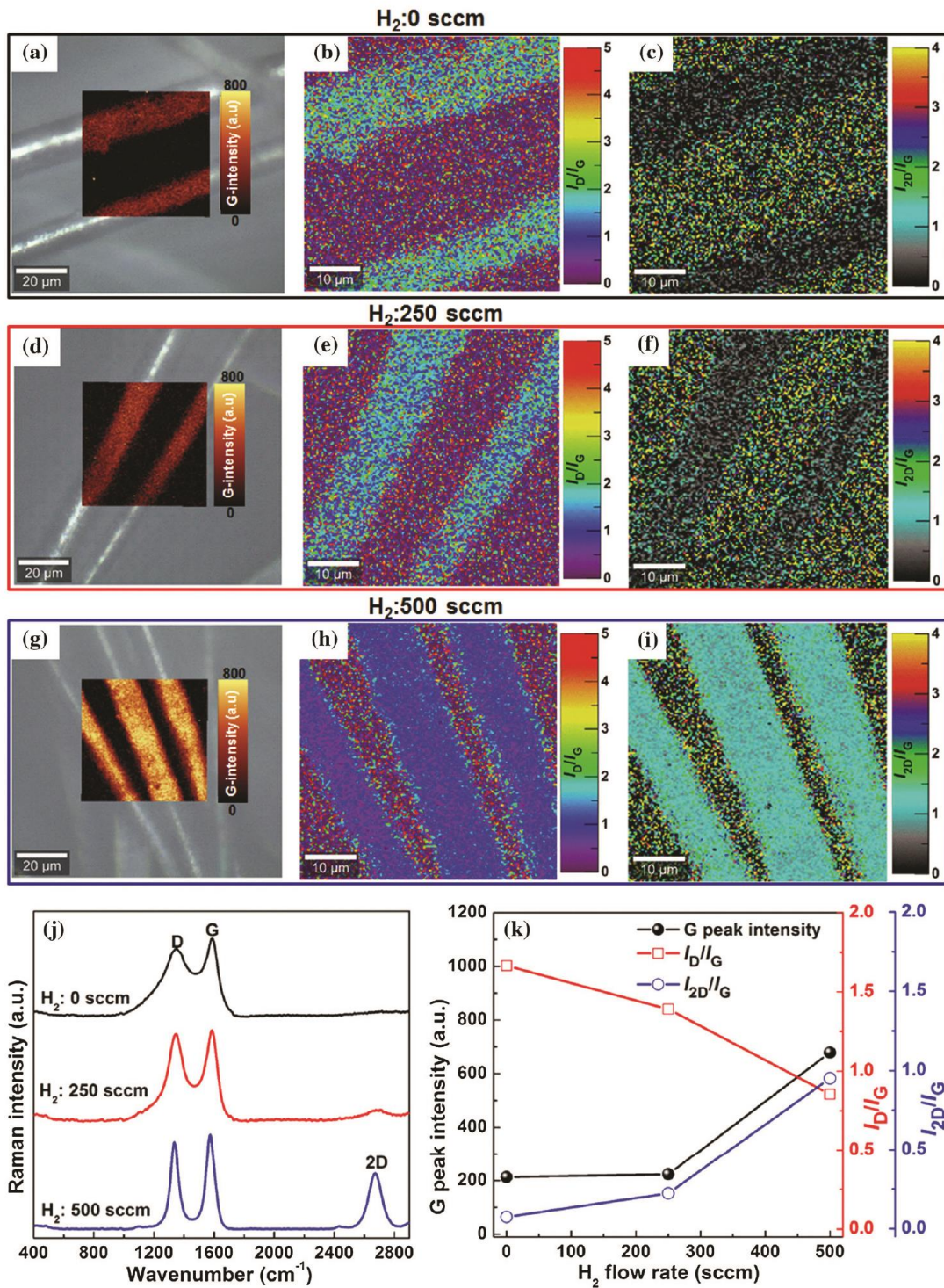
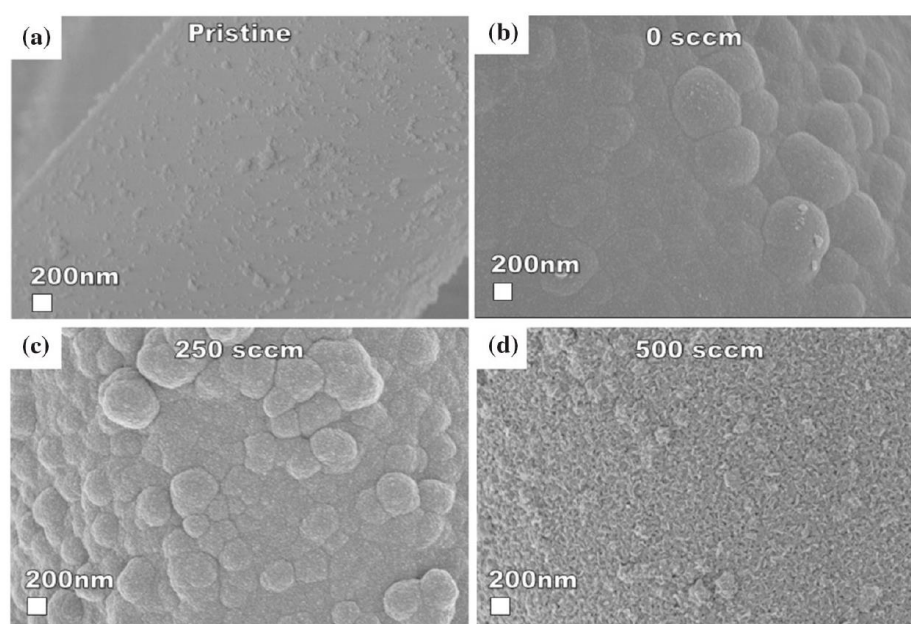


Figure 9 G intensity map (a), I_D/I_G ratio map (b) and I_{2D}/I_G ratio map (c) for GW grown with 0 sccm H_2 . G intensity map (d), I_D/I_G ratio map (e) and I_{2D}/I_G ratio map (f) for GW grown at 250 sccm H_2 . G intensity map (g), I_D/I_G ratio map (h) and I_{2D}/I_G ratio map

(i) for GW grown with 500 sccm H_2 . Comparison of the D, G and 2D peaks in the Raman spectra (j) and graph representing G peak intensity and I_D/I_G and I_{2D}/I_G ratios (k).

Figure 10 SEM images for pristine quartz wool (a) and GW grown with hydrogen flow rates of 0 sccm (b), 250 sccm (c) and 500 sccm (d).



The I_D/I_G ratio is inversely proportional to the crystallite grain size (L_a) and has been widely used to estimate the quality of graphene or the size of the graphene domain. The grain size of graphene grown at 1200 °C was calculated using the following formula [48] L_a (nm) = $2.4 \times 10^{-10} \times \lambda^4 \times (I_D/I_G)^{-1}$ where the wavelength of excitation laser, λ , is 532 nm and the I_D/I_G is as shown in Fig. 13b. Figure 13e displays a crystallite grain size mapping which shows an average value of 24 nm which is comparable to the grain size of graphene grown on other commercially available substrates such as z-cut single quartz crystals and quartz discs that ranged from 17 to 100 nm [5, 40].

TEM

Graphene on the quartz wool was investigated using TEM by transferring suspended GW fibres onto a copper grid.

Figure 14a shows that the coverage of the quartz wool by graphene is continuous with a varying number of layers and thickness which confirms the proposed mechanism. The irregular, flaky appearance of the graphene can clearly be seen to be as a result of vertical staking (Fig. 14b). Figure 14c, d further illustrates multiple-layered in-plane and out-

of-plane staking of the graphene flake-like sheets depicted by the varying translucence. Vertical and in-plane staking of graphene was also reported by other authors who found that domains in the range of ~ 0.7 nm signifies a monolayer of graphene and an increase in the thickness signifies an increase in graphene layers which ranges from 1.9 to 2.9 nm corresponding to 3–5 multi-layered graphene [32, 49, 50].

XPS

Figure 15a shows a wide scan XPS spectrum of the optimised graphene wool, which displays the surface composition (94.05 at.% C 1s and 5.95 at.% O 1s) of the sample. The core level spectrum of C 1s (Fig. 15b) shows the strongest peak of sp^2 C = C at 284.4 eV (graphene component) and low-intensity oxide constituent peaks, namely, C–OH (285.2 eV), C–O–C (286.5 eV), C=O (287.7 eV) and COOH (289.7 eV) [51–53]. In addition, the core-level spectrum of O 1s further confirms the oxide constituents present in the surface of the graphene wool. Based on the XPS data, it can be mentioned that the observed D peak in the Raman spectra of the samples is due to the broken sp^2 carbon network into nanoscale oxidised domains which occurred during CVD synthesis [1].

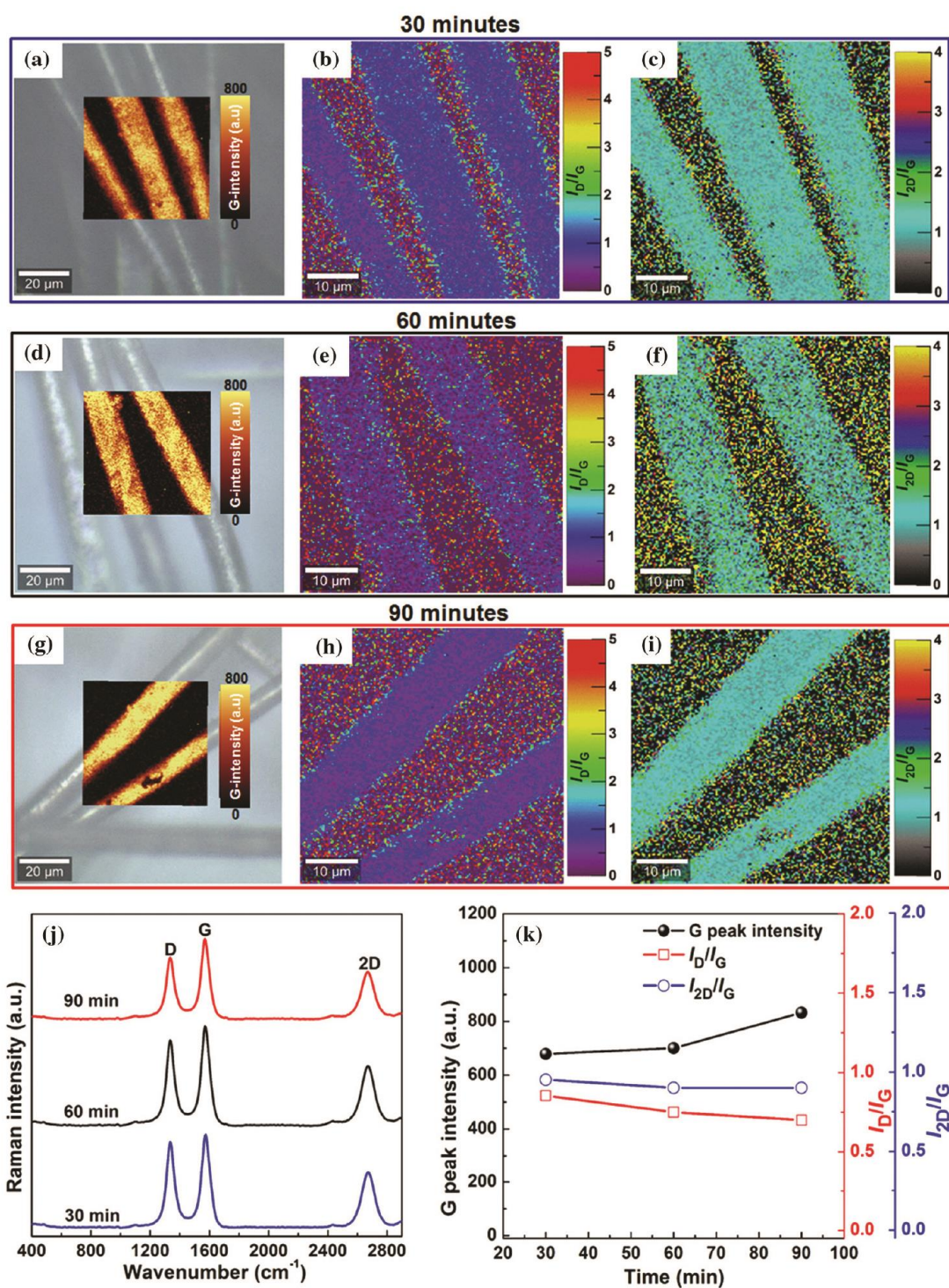


Figure 11 G intensity map (a), I_D/I_G ratio map (b) and I_{2D}/I_G ratio map (c) for GW grown for 30 min. G intensity map (d), I_D/I_G ratio map (e) and I_{2D}/I_G ratio map (f) for GW grown for 60 min. G intensity map (g), I_D/I_G ratio map (h) and I_{2D}/I_G ratio map (i) for

GW grown for 90 min. Comparison of the D, G and 2D peaks in the Raman spectra (j) and graph representing G intensity and I_D/I_G and I_{2D}/I_G ratios (k).

Figure 12 SEM images for pristine quartz wool (a) and GW grown for 30 min (b), 60 min (c) and 90 min (d).

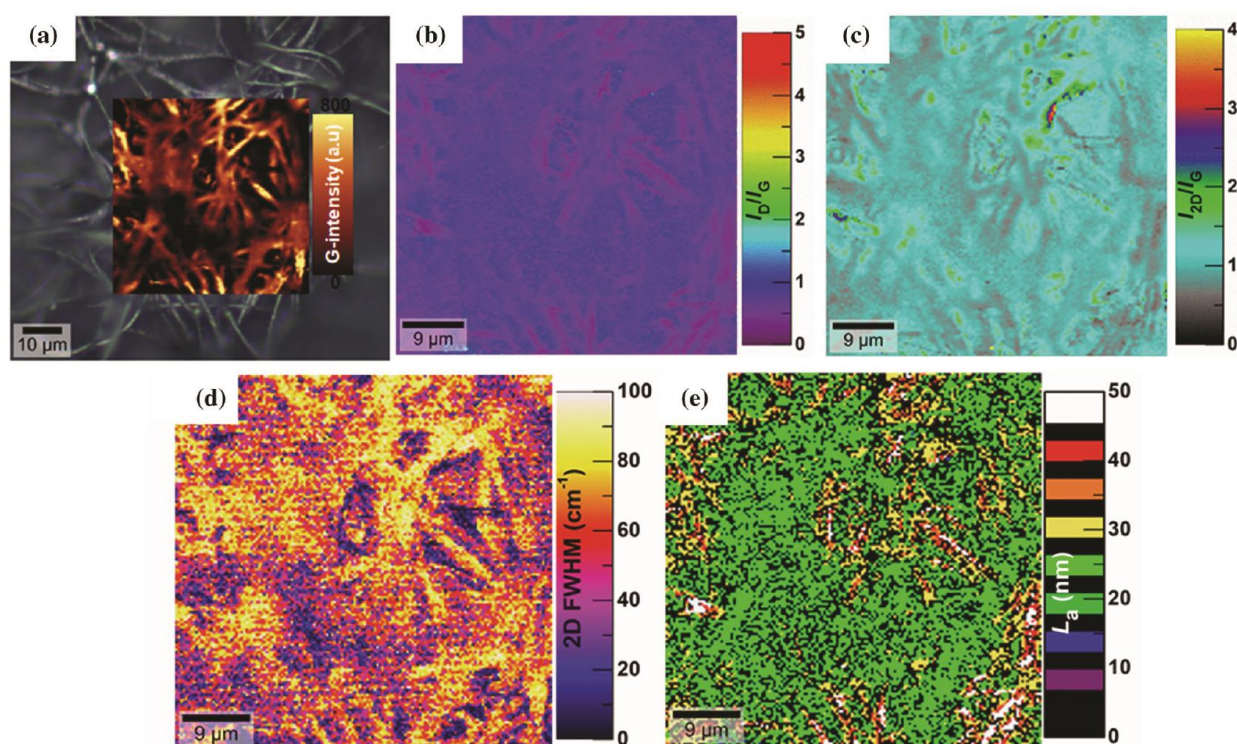
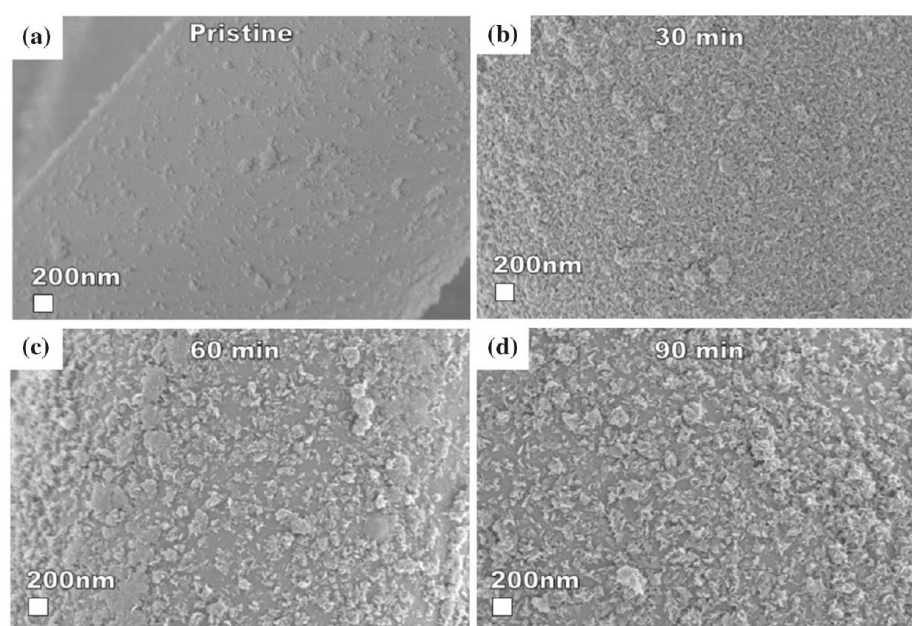
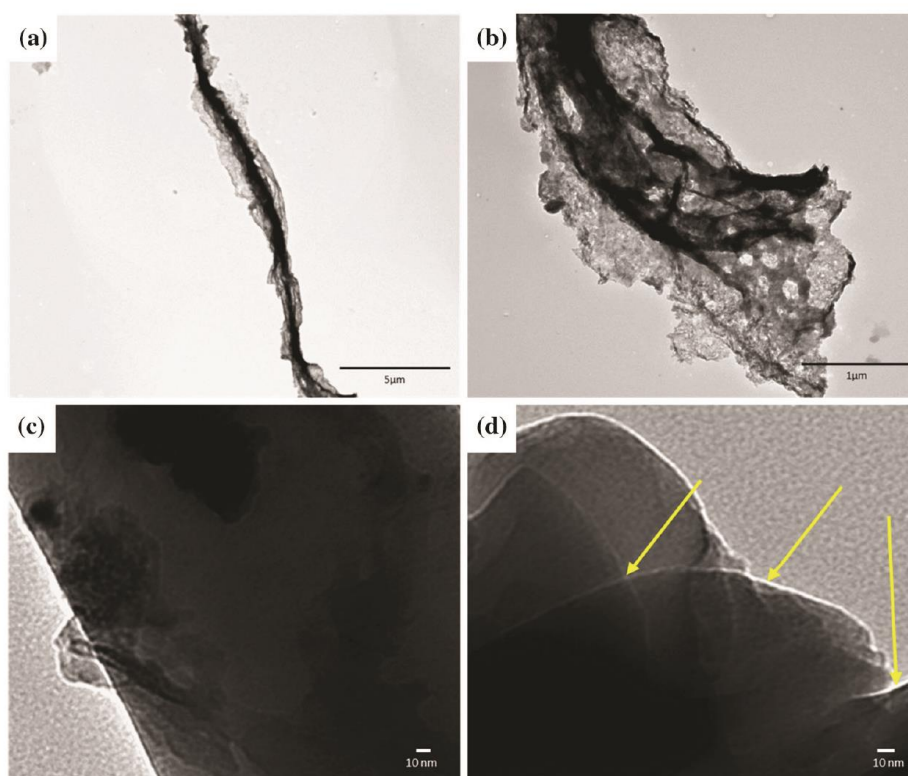


Figure 13 G intensity map (a), I_D/I_G ratio map (b) and I_{2D}/I_G ratio map (c), full width half maximum (FWHM) of 2D peak (d) and grain size (L_a) (e) for GW that was grown using optimised experimental conditions.

Figure 14 TEM images for the graphene wool grown under optimised experimental conditions (500:500:100 sccm, Ar/H₂/CH₄ at 1200 °C and cooled at -14.5 °C s^{-1}).



Conclusions

We have developed a simple and efficient non-catalysed atmospheric pressure CVD process for synthesising novel high-quality graphene wool on a large scale avoiding time-consuming and complex synthesis transfer steps, not to mention the accompanying risk of contamination and damage. The key parameters for the growth of high-quality graphene wool were found to be growth temperature and precursor gas flows (H₂ and CH₄). Other parameters such as cooling rate and growth time can be tweaked to improve the quality of the graphene wool but are not detrimental to the growth mechanism. The kinetic rate-limiting step was found to be in the transport of gas molecules to the surface of the substrate and was not self-limiting. The optimised graphene wool was grown for 30 min at 1200 °C with Ar/H₂/CH₄ 500:500:100 sccm gas flow rates, resulting in bi- and multi-layered graphene which showed a minimum ratio of the disordered carbon relative to the graphitic

carbon ($I_D/I_G \approx 0.8$) and crystallite grain size of 24 nm. The morphology of the graphene was flake-like, and XPS analysis of the optimised graphene revealed a surface composition of 94.05 at.% C 1s and 5.95 at.% O 1s. Oxygen-aided synthesis may prove useful in producing higher-quality graphene, if required, as this will increase the collision frequency of the carbon precursor on the quartz wool substrate during nucleation. However, defective graphene is desirable for specific applications such as gas adsorption whereby defects act as additional adsorption sites as well as sites for possible covalent functionalisation to improve specificity. This novel fibrous graphene wool has the integrity of a crystalline graphene surface with the advantage of structural support from the quartz substrate, making it very easy to manipulate and less rigid than many other forms of graphene, lending itself to a wide range of potential uses, including in electronics, energy storage, catalysis, and gas sorption, storage, separation and sensing applications.

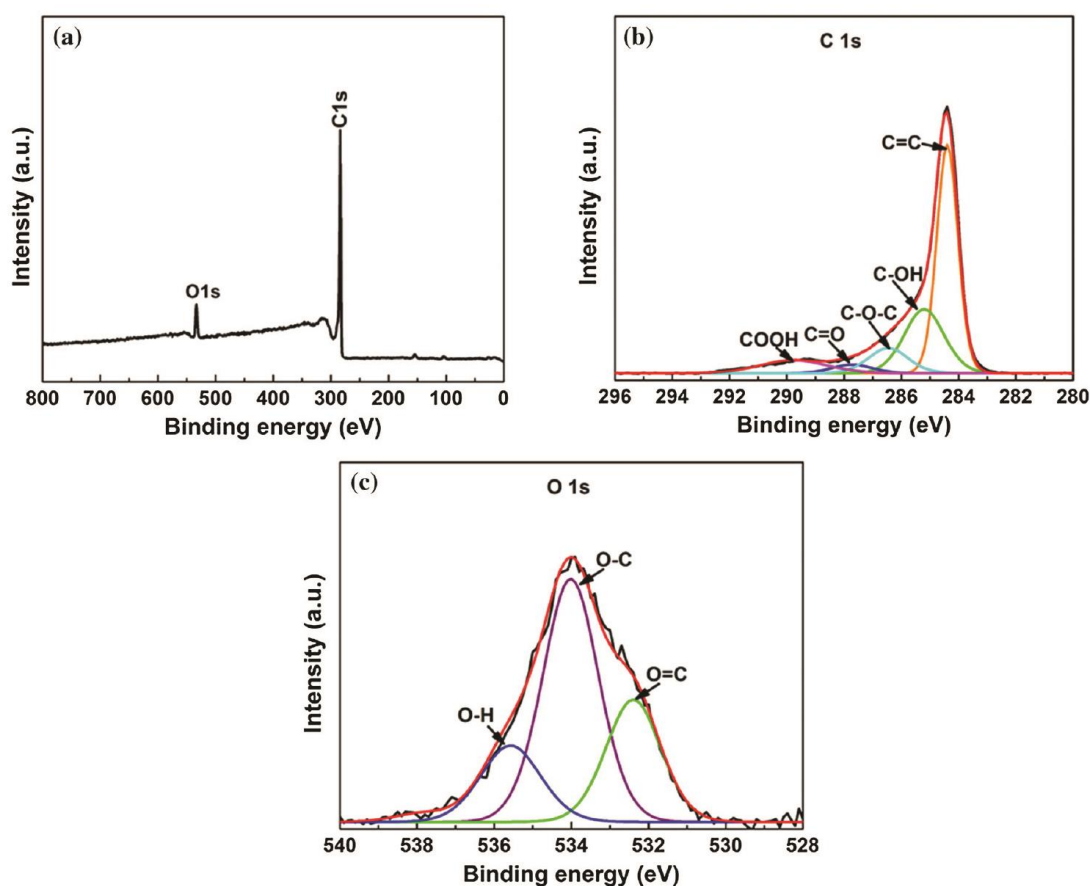


Figure 15 The XPS spectra: **a** wide scan spectrum, **b** C 1s and **c** O 1s core-level spectra obtained from the optimised graphene wool.

Acknowledgements

The Departments of Chemistry and Physics at the University of Pretoria as well as Impala Platinum Ltd are duly acknowledged for their support and resources as well as the South African Research Chairs Initiative (SARChI) of the Department of Science and Technology and the National Research Foundation (NRF) of South Africa (Grant No. 61056).

Compliance with ethical standards

Conflict of interest The authors declare that there are no conflicts of interest.

References

- [1] Chen J, Wen Y, Guo Y, Wu B, Huang L, Xue Y, Geng D, Wang D, Yu G, Liu Y (2011) Oxygen-aided synthesis of polycrystalline graphene on silicon dioxide substrates. *J Am Chem Soc* 133(44):17548–17551
- [2] Singh V, Joung D, Zhai L, Das S, Khondaker SI, Seal S (2011) Graphene based materials: past, present and future. *Prog Mater Sci* 56(8):1178–1271
- [3] Zhang G, Guo X, Wang S, Wang X, Zhou Y, Xu H (2014) New graphene fiber coating for volatile organic compounds analysis. *J Chromatogr B* 969:128–131
- [4] Chen Z, Guo X, Zhu L, Li L, Liu Y, Zhao L, Zhang W, Chen J, Zhang Y, Zhao Y (2018) Direct growth of graphene on vertically standing glass by a metal-free chemical vapor deposition method. *J Mater Sci Technol* 34(10):1919–1924
- [5] Xu S, Man B, Jiang S, Yue W, Yang C, Liu M, Chen C, Zhang C (2014) Direct growth of graphene on quartz substrates for label-free detection of adenosine triphosphate. *Nanotechnology* 25(16):165702
- [6] Xu Z, Zhu H, Xu Z, Xie D, Fang Y (eds) (2018) Fundamental properties of graphene. In: *Graphene*. Academic Press, Cambridge, pp 73–102
- [7] Aoki H, Dresselhaus MS (2014) *Physics of graphene*, 1st edn. Springer, Basel
- [8] Stankovich S, Dikin DA, Dommett GH, Kohlhaas KM, Zimney EJ, Stach EA, Piner RD, Nguyen ST, Ruoff RS

- (2006) Graphene-based composite materials. *Nature* 442(7100):282–286
- [9] Eda G, Fanchini G, Chhowalla M (2008) Large-area ultrathin films of reduced graphene oxide as a transparent and flexible electronic material. *Nat Nanotechnol* 3(5):270–274
- [10] Ramanathan T, Abdala AA, Stankovich S, Dikin DA, Herrera-Alonso M, Piner RD, Adamson DH, Schniepp HC, Chen X, Ruoff RS, Nguyen ST, Aksay IA, Prud'Homme RK, Brinson LC (2008) Functionalized graphene sheets for polymer nanocomposites. *Nat Nanotechnol* 3(6):327–331
- [11] He Y, Liu Y, Wu T, Ma J, Wang X, Gong Q, Kong W, Xing F, Gao J (2013) An environmentally friendly method for the fabrication of reduced graphene oxide foam with a super oil absorption capacity. *J Hazard Mater* 260:796–805
- [12] Wu S, Kong L, Liu J (2016) Removal of mercury and fluoride from aqueous solutions by three-dimensional reduced-graphene oxide aerogel. *Res Chem Intermed* 42(5):4513–4530
- [13] Yousefi N, Lu X, Elimelech M, Tufenkji N (2019) Environmental performance of graphene-based 3D macrostructures. *Nat Nanotechnol* 14(2):107–119
- [14] Shi J, Wang Y, Du W, Hou Z (2016) Synthesis of graphene encapsulated Fe₃C in carbon nanotubes from biomass and its catalysis application. *Carbon* 99:330–337
- [15] Vaziri S, Lupina G, Henkel C, Smith AD, Ostling M, Dabrowski J, Lippert G, Mehr W, Lemme MC (2013) A graphene-based hot electron transistor. *Nano Lett* 13(4):1435–1439
- [16] Ganesan A, Shaijumon MM (2016) Activated graphene-derived porous carbon with exceptional gas adsorption properties. *Microporous Mesoporous Mater* 220:21–27
- [17] Kumar R, Suresh VM, Maji TK, Rao CN (2014) Porous graphene frameworks pillared by organic linkers with tunable surface area and gas storage properties. *Chem Commun (Camb)* 50(16):2015–2017
- [18] Nidheesh PV (2017) Graphene-based materials supported advanced oxidation processes for water and wastewater treatment: a review. *Environ Sci Pollut Res* 24(35):27047–27069
- [19] Pang S, Englert JM, Tsao HN, Hernandez Y, Hirsch A, Feng X, Müllen K (2010) Extrinsic corrugation-assisted mechanical exfoliation of monolayer graphene. *Adv Mater* 22(47):5374–5377
- [20] Yi M, Shen Z (2015) A review on mechanical exfoliation for the scalable production of graphene. *J Mater Chem A* 3(22):11700–11715
- [21] Pei S, Cheng H-M (2012) The reduction of graphene oxide. *Carbon* 50(9):3210–3228
- [22] Saleem H, Haneef M, Abbasi HY (2018) Synthesis route of reduced graphene oxide via thermal reduction of chemically exfoliated graphene oxide. *Mater Chem Phys* 204:1–7
- [23] Poon SW, Chen W, Tok ES, Wee ATS (2008) Probing epitaxial growth of graphene on silicon carbide by metal decoration. *Appl Phys Lett* 92(10):104102
- [24] Mishra N, Boeckl J, Motta N, Iacopi F (2016) Graphene growth on silicon carbide: a review graphene growth on silicon carbide. *Physica Status Solidi (a)* 213(9):2277–2289
- [25] Gao L, Guest JR, Guisinger NP (2010) Epitaxial graphene on Cu(111). *Nano Lett* 10(9):3512–3516
- [26] Chen H, Zhu W, Zhang Z (2010) Contrasting behavior of carbon nucleation in the initial stages of graphene epitaxial growth on stepped metal surfaces. *Phys Rev Lett* 104(18):186101
- [27] Li X, Cai W, An J, Yang D, Piner R, Velamakanni A, Jung I, Ruoff RS, Kim S, Nah J, Tutuc E, Banerjee SK, Colombo L (2009) Large-area synthesis of high-quality and uniform graphene films on copper foils. *Science* 324(5932):1312–1314
- [28] Xue Y, Wu B, Guo Y, Huang L, Jiang L, Chen J, Geng D, Liu Y, Hu W, Yu G (2011) Synthesis of large-area, few-layer graphene on iron foil by chemical vapor deposition. *Nano Res* 4(12):1208–1214
- [29] Jung DH, Kang C, Kim M, Cheong H, Lee H, Lee JS (2014) Effects of hydrogen partial pressure in the annealing process on graphene growth. *J Phys Chem C* 118(7):3574–3580
- [30] Vlassioux I, Smirnov S, Regmi M, Surwade SP, Srivastava N, Feenstra R, Eres G, Parish C, Lavrik N, Datskos P, Dai S, Fulvio P (2013) Graphene nucleation density on copper: fundamental role of background pressure. *J Phys Chem C* 117(37):18919–18926
- [31] Cole MT, Lindvall N, Yurgens A (2012) Noncatalytic chemical vapor deposition of graphene on high-temperature substrates for transparent electrodes. *Appl Phys Lett* 100(2):022102
- [32] Tai L, Zhu D, Liu X, Yang T, Wang L, Wang R, Jiang S, Chen Z, Xu Z, Li X (2018) Direct growth of graphene on silicon by metal-free chemical vapor deposition. *Nano-Micro Lett* 10(2):1–9
- [33] Han W, Zettl A (2002) An efficient route to graphitic carbon-layer-coated gallium nitride nanorods. *Adv Mater* 14(21):1560–1562
- [34] Ding X, Ding G, Xie X, Huang F, Jiang M (2011) Direct growth of few layer graphene on hexagonal boron nitride by chemical vapor deposition. *Carbon* 49(7):2522–2525
- [35] Guermoune A, Chari T, Popescu F, Sabri SS, Guillemette J, Skulason HS, Szkopek T, Siaj M (2011) Chemical vapor deposition synthesis of graphene on copper with methanol, ethanol, and propanol precursors. *Carbon* 49(13):4204–4210
- [36] Reina A, Thiele S, Jia X, Bhaviripudi S, Dresselhaus MS, Schaefer JA, Kong J (2009) Growth of large-area single- and bi-layer graphene by controlled carbon precipitation on polycrystalline Ni surfaces. *Nano Res* 2(6):509–516

- [37] Kwon SY, Ciobanu CV, Petrova V, Shenoy VB, Bareño J, Gambin V, Petrov I, Kodambaka S (2009) Growth of semiconducting graphene on palladium. *Nano Lett* 9(12):3985–3990
- [38] Imamura G, Saiki K (2011) Synthesis of nitrogen-doped graphene on Pt(111) by chemical vapor deposition. *J Phys Chem C* 115(20):10000–10005
- [39] Chen S, Cai W, Piner RD, Suk JW, Wu Y, Ren Y, Kang J, Ruoff RS (2011) Synthesis and characterization of large-area graphene and graphite films on commercial Cu–Ni alloy foils. *Nano Lett* 11(9):3519–3525
- [40] Hwang J, Kim M, Cha H-Y, Spencer M, Lee J-W (2014) Metal free growth of graphene on quartz substrate using chemical vapor deposition (CVD). *J Nanosci Nanotechnol* 14(4):2979–2983
- [41] Schoonraad G, Forbes PBC (2019) System and method for manufacturing graphene wool, South Africa. Patent no: 2019/00675
- [42] Schoonraad G, Forbes PBC (2019) Air pollutant trap. Patent no: 2019/00674
- [43] Kozlov GI, Knorre VG (1962) Single-pulse shock tube studies on the kinetics of the thermal decomposition of methane. *Combust Flame* 6:253–263
- [44] Hermann J, DiStasio RA Jr, Tkatchenko A (2017) First-principles models for van der Waals interactions in molecules and materials: concepts, theory, and applications. *Chem Rev* 117(6):4714–4758
- [45] Ndiaye NM, Ngom BD, Sylla NF, Masikhwa TM, Madito MJ, Momodu D, Ntsoane T, Manyala N (2018) Three dimensional vanadium pentoxide/graphene foam composite as positive electrode for high performance asymmetric electrochemical supercapacitor. *J Colloid Interface Sci* 532:395–406
- [46] Shin YC, Kong J (2013) Hydrogen-excluded graphene synthesis via atmospheric pressure chemical vapor deposition. *Carbon* 59:439–447
- [47] Chen J, Li C, Ristovski Z, Milic A, Gu Y, Islam MS, Wang S, Hao J, Zhang H, He C (2017) A review of biomass burning: emissions and impacts on air quality, health and climate in China. *Sci Total Environ* 579:1000–1034
- [48] Cançado LG, Takai K, Enoki T, Endo M, Kim YA, Mizusaki H, Jorio A, Coelho LN, Magalhães-Paniago R, Pimenta MA (2006) General equation for the determination of the crystallite size of nanographite by Raman spectroscopy. *Appl Phys Lett* 88(16):163106
- [49] Chen J, Guo Y, Wen Y, Huang L, Xue Y, Geng D, Wu B, Luo B, Yu G, Liu Y (2013) Two-stage metal-catalyst-free growth of high-quality polycrystalline graphene films on silicon nitride substrates. *Adv Mater* 25(7):992–997
- [50] Sun J, Gao T, Song X, Zhao Y, Lin Y, Wang H, Ma D, Chen Y, Xiang W, Wang J, Zhang Y, Liu Z (2014) Direct growth of high-quality graphene on high- κ dielectric SrTiO₃ substrates. *J Am Chem Soc* 136(18):6574–6577
- [51] Butenko YV, Krishnamurthy S, Chakraborty AK, Kuznetsov VL, Dhanak VR, Hunt MRC, Šiller L (2005) Photoemission study of onionlike carbons produced by annealing nanodiamonds. *Phys Rev B* 71(7):075420
- [52] Hsiao M-C, Liao S-H, Yen M-Y, Teng C-C, Lee S-H, Pu N-W, Wang C-A, Sung Y, Ger M-D, Ma C-CM, Hsiao M-H (2010) Preparation and properties of a graphene reinforced nanocomposite conducting plate. *J Mater Chem* 20(39):8496–8505
- [53] Ogawa S, Yamada T, Ishidzuka S, Yoshigoe A, Hasegawa M, Teraoka Y, Takakuwa Y (2013) Graphene growth and carbon diffusion process during vacuum heating on Cu(111)/Al₂O₃ substrates. *Jpn J Appl Phys* 52(11R):110122

Publisher's Note Springer Nature remains neutral with regard to jurisdictional claims in published maps and institutional affiliations.

Secondly, investigations into graphene wool material as an adsorbent material are presented in Paper 5 which was published in *ACS Omega*.

Geldenhuis, G., Mason, Y., Dragan, G.C., Zimmermann, R. and Forbes, P.B.C. 2021. Novel graphene wool gas adsorbent for volatile and semi-volatile organic compounds. *ACS Omega*, 6(38):24765-76. DOI: <https://doi.org/10.1021/acsomega.1c03595>.

Author contributions

G Geldenhuis: Conceptualization, Methodology, Investigation, Formal analysis, Writing - original draft. **Y Mason:** Methodology, Investigation, Formal analysis, Writing - review & editing. **G.C Dragan:** Methodology, Investigation, Formal analysis, Project administration, Writing - review & editing. **R Zimmermann:** Conceptualization, Resources, Funding acquisition. **P.B.C Forbes:** Conceptualization, Methodology, Investigation, Formal analysis, Writing - review & editing, Supervision, Project administration, Resources, Funding acquisition

Novel Graphene Wool Gas Adsorbent for Volatile and Semivolatile Organic Compounds

Genna-Leigh Geldenhuys, Yvonne Mason, George C. Dragan, Ralf Zimmermann, and Patricia Forbes*

Cite This: *ACS Omega* 2021, 6, 24765–24776

Read Online

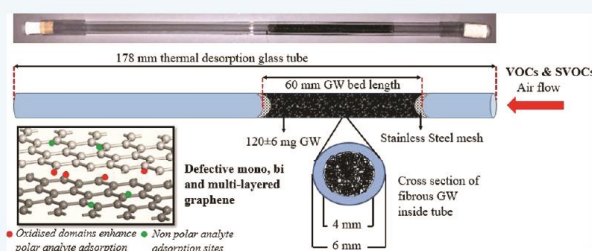
ACCESS |

Metrics & More

Article Recommendations

Supporting Information

ABSTRACT: Volatile and semivolatile organic compounds in ambient air and occupational settings are of great concern due to their associated adverse human health and environmental impacts. Novel graphene wool samplers have been developed and tested to overcome limitations of commercially available sorbents that can only be used once and typically require solvent extraction. Graphene wool (GW) was synthesized by non-catalytic chemical vapor deposition with optimized conditions, resulting in a novel fibrous graphene wool that is very easy to manage and less rigid than other forms of graphene, lending itself to a wide range of potential applications. Here, the air pollutant sampling capabilities of the GW were of interest. The optimal packing weight of GW inside a glass tube (length 178 mm, i.d. 4 mm, o.d. 6 mm) was investigated by the adsorption of vaporized alkane standards on the GW, using a condensation aerosol generator in a temperature-controlled chamber and subsequent detection using a flame ionization detector. The optimized GW packing density was found to be 0.19 mg mm^{-3} at a flow rate of 500 mL min^{-1} , which provided a gas collection efficiency of $>90\%$ for octane, decane, and hexadecane. The humidity uptake of the sampler is less than 1% (m/m) for ambient humidities $<70\%$. Breakthrough studies showed the favorable adsorption of polar molecules, which is attributed to the defective nature of the graphene and the inhomogeneous coating of the graphene layers on the quartz wool, suggesting that the polar versus non-polar uptake potential of the GW can be tuned by varying the graphene layering on the quartz wool substrate during synthesis. Oxidized domains at the irregular edges of the graphene layers, due to a broken, non-pristine sp^2 carbon network, allow for adsorption of polar molecules. The GW was applied and used in a combustion sampling campaign where the samplers proved to be comparable to frequently used polydimethylsiloxane sorbents in terms of sampling and thermal desorption of non-polar semivolatile organic compounds. The total alkane concentrations detected after thermal desorption of GW and PDMS samplers were found to be 17.96 ± 13.27 and $18.30 \pm 16.42 \mu\text{g m}^{-3}$, respectively; thus, the difference in the alkane sampling concentration between the two sorbent systems was negligible. GW provides a new, exciting possibility for the monitoring of organic air pollutants with numerous advantages, including high sampling efficiencies, simple and cost-effective synthesis of the thermally stable GW, solvent-free and environmentally friendly analysis, and, importantly, the reusability of samplers.

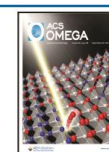


1. INTRODUCTION

Air quality is of global concern, and efficient means to monitor air pollutants is critical, particularly those which require monitoring by law due to the environmental and human health impacts they may incur. Volatile and semivolatile organic compounds (VOCs and SVOCs, respectively) are emitted to the atmosphere from numerous sources, such as the petrochemical, agricultural, paint, and mining industries. Current commercially available carbon-based sorbents, including activated charcoal, Anasorb 747, Carboxen, and carbon molecular sieves, used to sample VOCs and SVOCs in air typically require solvent extraction prior to analysis, which is costly, time-consuming, and environmentally unfriendly, and they cannot be reused, which increases operational costs.

Graphene is a crystalline allotrope of carbon nanomaterials that has received worldwide attention due to its unique two-dimensional planar monolayer structure, outstanding chemical and thermal stability, high specific surface area, and hydro-

phobic properties which deem graphene to be a suitable sorbent candidate.^{1–6} The recognition of graphene's properties resulted in a number of potential applications in electronics, energy storage, catalysis, and gas sorption, storage, separation, and sensing.^{2,7–10} The majority of graphene materials in environmental applications see their use in sensing and storage; however, to the best of our knowledge, graphene has not been used as a sorbent material for organic gas-phase pollutants for environmental sampling to date. The aim of our research was to develop a novel graphene wool (GW) trap and

Received: July 8, 2021
Published: September 13, 2021

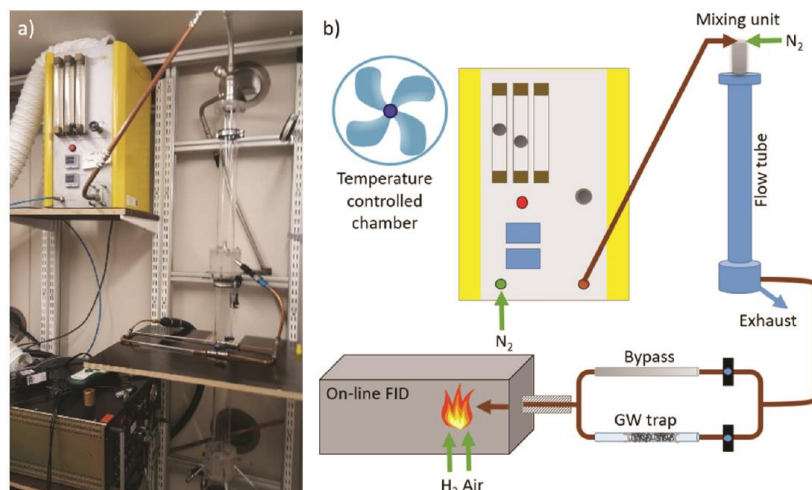


Figure 1. Experimental setup for the determination of gas collection efficiency on the GW trap (a) and schematic of the experimental setup (b).

evaluate its application as a sorbent material for ambient and occupational air pollution sampling of SVOCs and VOCs.^{11,12}

The GW trap samplers which we have developed can be thermally desorbed for analysis (which does not use solvents and is thus more environmentally friendly and cost-effective), and importantly, they can be conditioned and reused multiple times. The low back pressure of the GW sampler also enables the use of a small portable battery-operated personal sampling pump, whereby the GW trap can be used as a standalone sorbent or in a sampling train with other sampling media. In this paper, the GW adsorbents were evaluated in terms of gas-phase collection efficiencies, breakthrough volumes, and humidity uptake. Following this, their real-life application was demonstrated in a fuel emission sampling campaign.

2. MATERIALS AND METHODS

2.1. Chemicals and Synthesis of GW. Commercially available 9–30 μm coarse quartz wool (Arcos Organics, New Jersey, USA) was used as a substrate for the growth of graphene by atmospheric pressure chemical vapor deposition (APCVD), as reported in Schoonraad.¹³ The quartz wool was placed in the center of a horizontal quartz tube (50 mm o.d., 44 mm i.d., \times 1000 mm length) of a OTF 1200X-50-5L high-temperature furnace (MTI Corporation, California, USA). A 500:500 sccm argon (99.999%, Afrox, South Africa): hydrogen (99.999%, Afrox, South Africa) mix was introduced into the system after which the temperature was ramped to 1200 °C. After a 10 min annealing period, 100 sccm methane (99.95%, Afrox, South Africa) was introduced for 30 min for graphene growth. The system was rapidly cooled under Ar and H₂ after the growth period had elapsed. The deposited graphitic carbon takes the form of the quartz wool substrate by covering the surface of each fiber, and for the purpose of its application, the substrate was not removed; thus, the term “graphene wool (GW)” in this work infers graphene coated on quartz wool. The synthesis steps, optimization, and full characterization of GW (Raman spectroscopy, scanning electron microscopy (SEM), high-resolution X-ray photoelectron spectroscopy (XPS), and high-resolution transmission electron microscopy (TEM)) are detailed in Schoonraad et al.^{12,13}

2.2. Assembly and Optimization of the GW Trap. To assemble the final, optimized GW traps (Figure S1), 120 \pm 6

mg of synthesized GW was weighed out using a calibrated Sartorius Entris analytical balance. The GW was gently packed into 178 mm-long glass tubes (i.d. 4 mm, o.d. 6 mm, Listco, SA) using tweezers and an in-house manufactured wire tool consisting of a 10 cm straight wire (o.d 2 mm) with one side bent into a hook. The GW was packed into a bed length of 50 mm and was held securely in place using stainless-steel screens (Merck, SA). The GW samplers were conditioned for 8 h at 300 °C with hydrogen (\geq 99.999% purity, AFROX, SA) with a gas flow of 100 mL min⁻¹ using a Gerstel TC 2 tube conditioner (Chemetrix, SA). The open ends of the conditioned traps were then capped with endcaps consisting of 1 cm quartz glass rods secured with Teflon sleeves.

In order to determine the final parameters of the GW trap (120 g of GW packed into 50 mm bed length), the assembly of the GW trap was first optimized by determining the maximum gas-phase collection efficiency with varying masses (50, 99, 110, and 120 mg) of the sorbent material at different bed lengths (20, 35, 50, and 55 mm) using the experimental setup as described in Section 2.3.

2.3. Gas-Phase Collection Efficiency of the GW Trap.

The substance-specific gas-phase collection efficiency of the GW trap was investigated using vaporized octane (C₈), dodecane (C₁₂) (99%, Merck, Hohenbrunn, Germany), and hexadecane (C₁₆) (99%, Alfa Aesar, Karlsruhe, Germany) in an experimental setup as depicted in Figure 1, which was a similar setup used by Kohlmeier et al. who validated multichannel silicone rubber traps as denuders for gas–particle partitioning of aerosols from semivolatile organic compounds.¹⁴ Each substance was individually vaporized using a Sinclair-La-Mer 270 condensation aerosol generator at flow rates of 2.5 L min⁻¹ for octane and 5 L min⁻¹ for dodecane and hexadecane, followed by dilution with nitrogen to a total flow of 50 L min⁻¹. The generated vapor was then passed through a 150 cm-long flow tube to ensure that the generated vapor was below the saturation concentration of each substance and avoid droplet formation. The resultant gas was redirected through either a bypass line or a GW trap via copper tubing. The alternate switching between the bypass line and the graphene trap was made possible using two-way valves, and the subsequent concentration of gas molecules was measured with a 109A-type flame ionization detector (FID) (J. U. M.

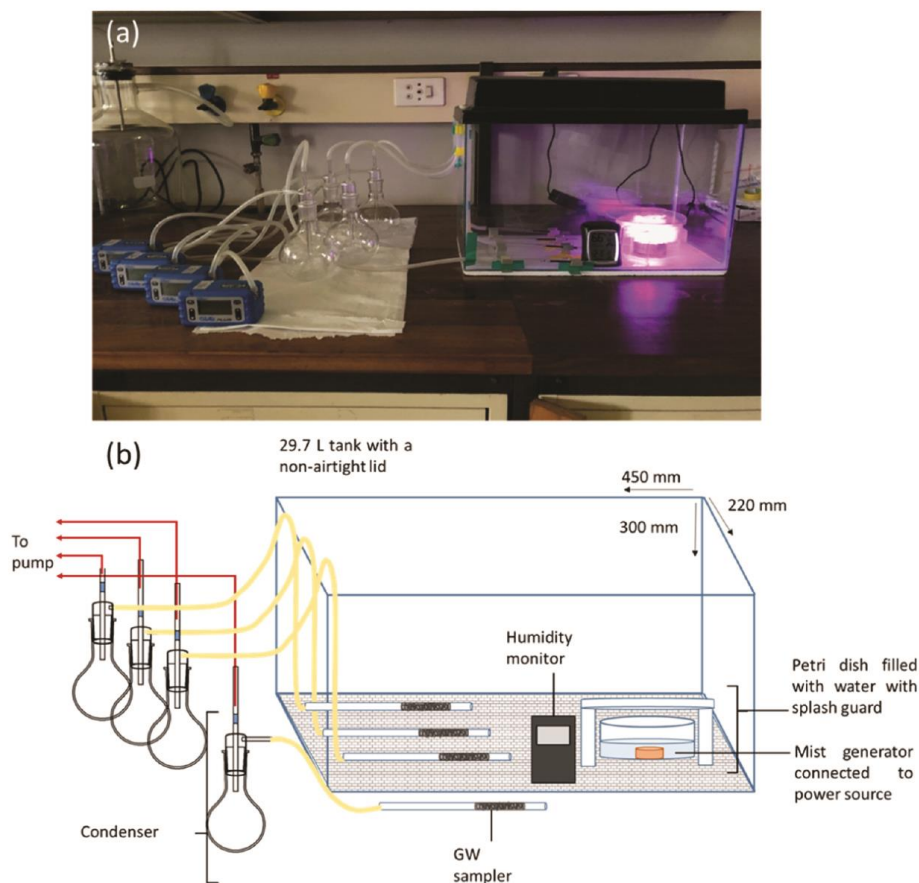


Figure 2. Experimental setup for the determination of humidity uptake on GW traps (a) and schematic of the experimental setup (b).

Engineering, Karlsfeld, Germany), which was operated at a flow rate of 0.5 L min^{-1} . The FID was calibrated daily with propane (Linde, Germany), and the instrument zero was validated using pure nitrogen (Linde, Germany). The concentration ratio measured between the GW trap and bypass line was used to obtain the time-dependent gas-phase collection efficiency (%) as in eq 1

$$\text{Collection efficiency} = \left(1 - \left(\frac{C_{\text{Trap}}}{C_{\text{Bypass}}} \right) \right) \times 100 \quad (1)$$

To ensure that the detected concentration was not biased from the adsorption of gases onto the copper tubing surface, the lines were saturated prior to the experiment by inserting an empty liner in place of the GW trap and verifying a constant FID signal. All experiments were performed in triplicate inside a temperature-controlled chamber at $24.7 \pm 0.2 \text{ }^\circ\text{C}$.

Three different GW traps were used in each experiment, and the traps were conditioned with nitrogen gas (Linde, Germany) for 5 h at $230 \text{ }^\circ\text{C}$ in between subsequent experiments to successfully demonstrate the reusability and reproducibility of the novel adsorbent. In order to determine the strength of adsorption and thus storage capabilities of GW, nitrogen gas was passed through a loaded trap to check if any FID signal was observed, which would indicate that the analytes were desorbing from the GW and breakthrough had occurred.

2.3.1. Comparative Traps Used in Gas Collection Efficiency Experiments. The PDMS samplers were prepared based on the method described by Ortner and Rohwer.¹⁵ Each trap consisted of 22 parallel PDMS tubes, with a total mass of 385 mg, (55 mm long, 0.3 mm i.d., 0.6 mm o.d., Sil-Tec, Technical Products, Georgia, US) in a 178 mm-long glass tube (6 mm o.d., 4 mm i.d., Listco, SA). The PDMS traps were conditioned prior to use at $280 \text{ }^\circ\text{C}$ for 16 h using hydrogen ($\geq 99.999\%$ purity, AFROX, SA) with a gas flow of 100 mL min^{-1} using a Gerstel TC 2 tube conditioner. The PDMS samplers were capped identically to the GW traps in Section 2.2. Commercially available activated charcoal adsorbent tubes (Dräger, type BIA, Lübeck, Germany) were also used to compare gas-phase collection efficiencies of VOCs.

2.4. Moisture Uptake by the GW. The humidity uptake on GW traps was tested gravimetrically using the setup illustrated Figure 2. A fish tank (450 mm \times 220 mm \times 300 mm, Lifestyle Pet Hyper, SA) was used as the humidity chamber, and an aquarium mist maker (M-12L, Sobo, China), submerged in water inside a Petri-dish (110 mm i.d., 115 mm o.d., 64 mm height), was used to generate aerosols that simulated set ambient humidity ranges $>75\%$. A makeshift splash guard was placed above the Petri-dish to allow only a fine mist to flow from the dish and to prevent larger water droplets from splashing out and compromising the study. Aluminum stands held the samplers in place at the same height as the ambient air humidity monitor (Monitor de la Humedad,

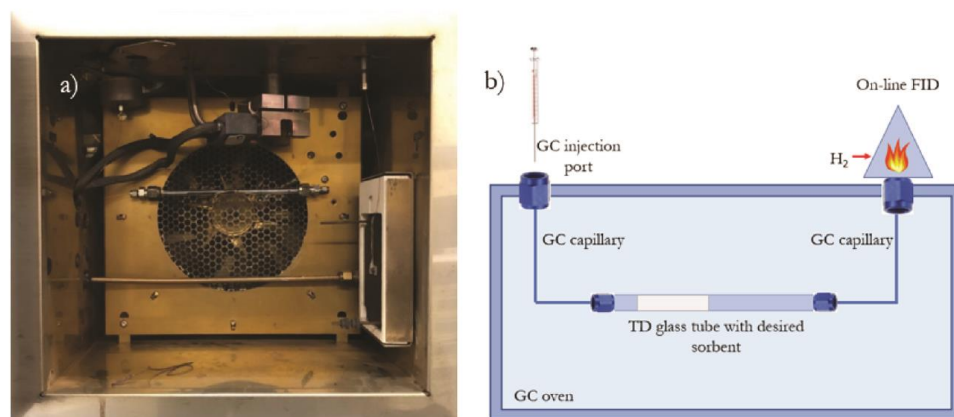


Figure 3. Experimental setup within the GC oven for the determination of breakthrough volume (a) and schematic of the experimental setup (b).

AcuRite, US). Teflon tubing was used to connect the samplers to Gilian GilAir Plus air sampling pumps (Sensidyne, US) via a condenser to prevent water from entering the pumps. GW samplers were conditioned, using a Gerstel TC 2 tube conditioner (Chemetrix, SA), with H₂ at 250 °C for 5 h prior to use and were weighed before and after the hygroscopicity experiment to determine the gross uptake of humidity by mass on the GW traps.

Triplicate GW samplers were placed inside the chamber to sample the air for a period of 10 min at a flow rate of 500 mL min⁻¹ at three set humidities (50, 60, and 70%). The mist generator was switched off, and the lid was removed during this study to obtain a constant humidity with no undesired variations due to air flow effects. A GW sampler was also connected outside the chamber as a control, which was sampled in parallel to other samples. For humidity ranges >75%, the mist generator was switched on, and the lid was placed on the tank to simulate a more humid environment than what was typically experienced under ambient conditions. A GW trap was then compared to a quartz wool (QW) control trap for humidity ranges >75% to accurately assess the effect the graphene layers have on the moisture uptake. The entrained moisture was investigated by weighing the GW trap after sampling and then flicking the trap 10 times consecutively and reweighing the trap in order to determine how much of the moisture was absorbed versus that physically entrained in the fibers of the sorbent.

2.5. Experimental Determination of Breakthrough Volumes. Breakthrough volumes as a function of temperature were determined using the setup depicted in Figure 3. An uncoated capillary column (15 cm, 0.25 mm i.d., 0.363 mm d.f., SGE Analytical Science) was connected to each end of the GW trap using relevant nuts and ferrules with one of the uncoated capillaries connected directly to the injection port of a Varian 6890 gas chromatograph (GC) (Agilent, US), and the second capillary connected the other end of the GW trap to a FID such that the GW trap took the place of the GC column. The inlet pressure of the GC injection port was held at 8 kPa, and H₂ was used as the carrier gas at a flow rate of 10 mL min⁻¹. The FID H₂ gas flow was set at 40 mL min⁻¹ with the air and N₂ make-up flow rates at 400 and 10 mL min⁻¹, respectively. N₂ was generated using a Peak Scientific nitrogen generator (Peak Scientific, Scotland), while hydrogen, dry air, and helium (≥99.999% purity) were supplied by AFROX (SA). Once the sampler was connected to the uncoated

capillaries and was securely positioned in the GC oven, the setup was leak-tested using a gas leak detector (LD-223, GL Sciences Inc., Japan).

The chosen sorbents to which the breakthrough volumes of the GW sampler were compared were the PDMS trap as it has historically been used in a wide range of air-monitoring studies and a sampler made of quartz wool to the same specifications of the GW sampler as a control. The GC oven was operated isothermally at set temperatures for each experimental run, which was done in duplicate; thereafter, the temperature was increased in suitable increments until a satisfactory Gaussian peak was observed on the FID chromatogram. The set temperatures were between 25 and 190 °C, 25 and 200 °C, and 25 and 340 °C for the GW, QW, and PDMS samplers, respectively.

The breakthrough volume for the samplers was calculated using the retention times from the experimentally acquired FID chromatograms for the GW, PDMS, and QW samplers using eq 2.¹⁶ As this research aimed to develop a new sampler, the mass of the sorbent to be used in the sampler was not fixed, as this aspect was to be optimized; therefore, BV is reported in units of volume per g of sorbent

$$BV = \frac{(RT \times \text{flow})}{W_a \times 1000 \text{ mL/L}} \quad (2)$$

where BV = breakthrough volume (L g⁻¹), RT = retention time of the analyte (min), flow = carrier gas flow (mL min⁻¹), W_a = specific sorbent mass (g), and 1000 mL/L = conversion factor to convert data from mL g⁻¹ to L g⁻¹.

In the case of the QW, GW, and PDMS, these masses were found to be 0.141, 0.120, and 0.366 g, respectively.

The FID chromatograms were produced by injecting 1 μL of each of the following nine analytes into the GC injection port—methanol (bp 64.7 °C), hexane (bp 68 °C), propanol-2-ol (82.5 °C), toluene (bp 110.6 °C), butan-1-ol (bp 117.7 °C), octane (bp 125.6 °C), cyclohexanone (bp 155.6 °C), dodecane (216.2 °C), and hexadecane (286.8 °C). These analytes were chosen due to their range of boiling points and their differing polarities in order to investigate the effect that both parameters have on the interaction between an analyte and the selected sorbents. Methanol (≥99% purity) and *n*-hexane (≥97% purity) were purchased from Sigma-Aldrich (SA). Propanol-2 (≥99% purity), butan-1-ol, (≥99% purity), and dodecane (≥99% purity) were purchased from Merck. Cyclohexanone

($\geq 98.5\%$ purity) was purchased from UNILAB (Philippines); octane ($\geq 99.5\%$ purity) and hexadecane ($\geq 99.5\%$ purity) were purchased from BDH laboratory reagents (SA). Acetone ($\geq 97\%$ purity) and toluene ($\geq 99.5\%$ purity) were obtained from Associated Chemical Enterprises (ACE, SA).

The temperature increments of the breakthrough experiments differed as the temperature increments were dependent on the sorbent and the tested analyte. A minimum of four temperature increments were used. The duplicate chromatographic FID data for each sampler were then averaged for each analyte at the specific isothermal temperature run, and the retention time of the selected analyte for the point corresponding to where the maximum signal occurred was taken from the averaged results. Thereafter, eq 2 was used to calculate the temperature-dependent breakthrough volume for a range of VOCs on GW, PDMS, and QW.

2.6. Application of the GW Sampler. **2.6.1. CAST Experimental Setup.** A combustion aerosol standard (CAST, Jing mini-CAST 5201D, Switzerland) generator was operated with propane (99.95%, Linde AG, Germany) according to settings described by Mason et al.¹⁷ Rapeseed oil methyl ester (RME) fuel was one of the fuels tested and was purchased from ASG Analytik-Service GmbH, Augsburg, Germany. The fuel was introduced to the CAST generator using a high-performance liquid chromatography (HPLC) pump (Kontron, type 420, Germany), which generated 22 L min^{-1} undiluted combustion exhaust, which then passed through a series of online analytical instrumentation (a FID (SK-Electronic, GMBH) and a Fourier transform infrared spectroscopy (FT-IR) gas analyzer (Gasmet, Model: DX4000, Finland)). After online analysis, 0.3 L min^{-1} undiluted CAST exhaust was introduced to a porous tube dilutor (Mikro-Glasfaser Filterelement, Type GF-12-57-80E) to which dry air was added to make up a total diluted flow of 3 L min^{-1} . An ejector dilutor drew 3 L min^{-1} from the porous dilutor and diluted the flow with synthetic air at 27 mL min^{-1} , after which a custom-built three-way Y-piece stainless-steel splitter was fitted to allow for the diluted flow to be directed to selected samplers, which included PDMS and GW traps that sampled at a flow rate of 500 mL min^{-1} for 10 min with GilAir Plus air-sampling pumps. A full description of the CAST setup is described by Mason et al., where this system was used to sample gas-phase volatile and semivolatile organic fuel emissions from three different fuels.¹⁷

2.6.2. GC-MS Analysis. Samplers were thermally desorbed using helium at 60 mL min^{-1} from $80 \text{ }^\circ\text{C}$ to 250 and $280 \text{ }^\circ\text{C}$ for PDMS and GW samplers, respectively, with a hold time of 30 min using a thermal desorption system (TD-20, Shimadzu, Japan). The cooled injection system (CIS) method was ramped from 5 to $330 \text{ }^\circ\text{C}$ and held for 30 min. For analysis, a GC-2010 Plus was coupled to a MS-QP2010 Ultra (both Shimadzu, Japan), and the helium carrier gas was set at a flow rate of 1.6 mL min^{-1} with a split ratio of 10:1 using a VF-XMS $30 \text{ m} \times 0.25 \text{ mm i.d.} \times 0.25 \text{ } \mu\text{m d.f.}$ column (Agilent, Netherlands). The GC oven was initially held at $60 \text{ }^\circ\text{C}$ for 6 min and then ramped at $5 \text{ }^\circ\text{C min}^{-1}$ to $250 \text{ }^\circ\text{C}$. The transfer line temperature was set to $250 \text{ }^\circ\text{C}$. The mass spectrometry method scanned mass ranges of m/z 35–500 with an electron ionization energy of 70 eV and an ion source temperature of $230 \text{ }^\circ\text{C}$. Calibration of the GW and PDMS was performed using individually prepared standards of alkanes in hexane (2 – $200 \text{ ng } \mu\text{L}^{-1}$ made from alkane standard solution C_8 – C_{20} , Sigma-Aldrich, Supelco, US) that were spiked onto traps with $1 \text{ } \mu\text{L}$ of internal standard mix (*n*-heptane d_{16} , *n*-dodecane d_{26} ,

and *n*-hexadecane d_{34} , Sigma-Aldrich, Supelco, US). The concentrations of the internal standards can be found in Table S1.

3. RESULTS AND DISCUSSION

3.1. Optimization of the GW Trap Assembly in Terms of GW Mass, Volume, and Density. In order to determine the final parameters of the GW trap, the assembly of the GW trap was first optimized by determining the maximum gas-phase collection efficiency at varying masses of the sorbent material at different bed lengths, resulting in varying densities that are depicted in Table 1.

Table 1. Density, Mass, and Volume of GW Packed Into a Glass Tube for the Optimization Study

| mass of GW (mg) | bed length (mm) | volume of GW (mm^3) | density of GW packing (mg mm^{-3}) |
|-----------------|-----------------|--------------------------------|---|
| 50 | 70 | 879.645 | 0.0568 |
| 50 | 35 | 439.823 | 0.1137 |
| 50 | 20 | 251.327 | 0.1989 |
| 99 | 50 | 628.318 | 0.1576 |
| 110 | 55 | 691.150 | 0.1592 |
| 120 | 50 | 628.318 | 0.1910 |

In order to achieve the optimal packing of the sorbent material in a glass tube, where the tube dimensions were chosen to be compatible with a commercial thermal desorber, the gas-phase collection efficiency for octane was investigated at varying masses of the GW sorbent material. The gas-phase collection efficiency of the GW was then compared to that of two other gas-phase samplers—a PDMS trap and a commercially available activated charcoal adsorbent tube. Figure 4a reveals that the GW gas-phase collection efficiency increased from 42 to 94% when increasing the GW mass from 0.01 to 0.11 g in the glass tube, which was then comparable to the collection efficiency of activated charcoal. However, it must be noted that the GW mass in the trap was significantly less than the mass of charcoal required to achieve the same results. The charcoal has the advantage of excellent VOC adsorption but the tradeoff is more difficult desorption that requires time-consuming solvent extraction steps. The activated charcoal has a mass of 900 mg in a bed length of 69 mm, and due to its high surface area and high degree of microporosity, the gas molecules penetrate deep into the sorbent pores when compared to the GW, which is only a thin surface layer of graphene, as seen in TEM images of the material in Schoonraad et al., which is why thermal desorption is possible with GW and not charcoal.¹²

The PDMS adsorbent (with a mass of 365 mg) proved to be an ineffective medium for the collection of volatile organic species, such as octane, as the premature fall in the FID signal quickly increased to 50% of the bypass signal within a few seconds, indicating that breakthrough from the trap was occurring, and gas-phase collection efficiency was just above 40%. This was not a surprising finding, considering the fact that PDMS has been validated for trapping of SVOCs.^{18–20} This can be explained by the mechanism and kinetics, which are entirely different for PDMS in that absorption of analytes takes place instead of adsorption as in the case of charcoal and GW.

Another important practical aspect favoring the use of GW is the sampling back pressure (BP). The BP is the resistance

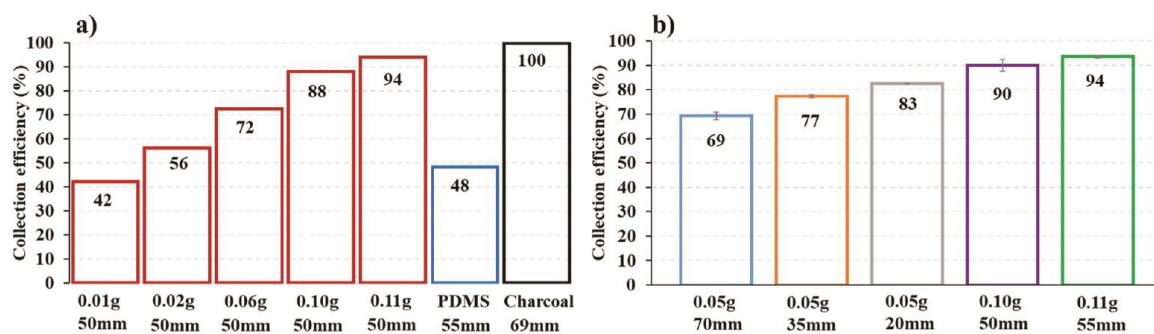


Figure 4. (a) Octane collection efficiency of GW traps as a function of increasing mass of GW but constant bed length, in comparison to PDMS and charcoal traps and (b) octane collection efficiency of GW traps as a function of packing density which was varied by altering the bed length (mm) of the GW inside the glass tube with the error bars showing standard deviation for $n = 3$.

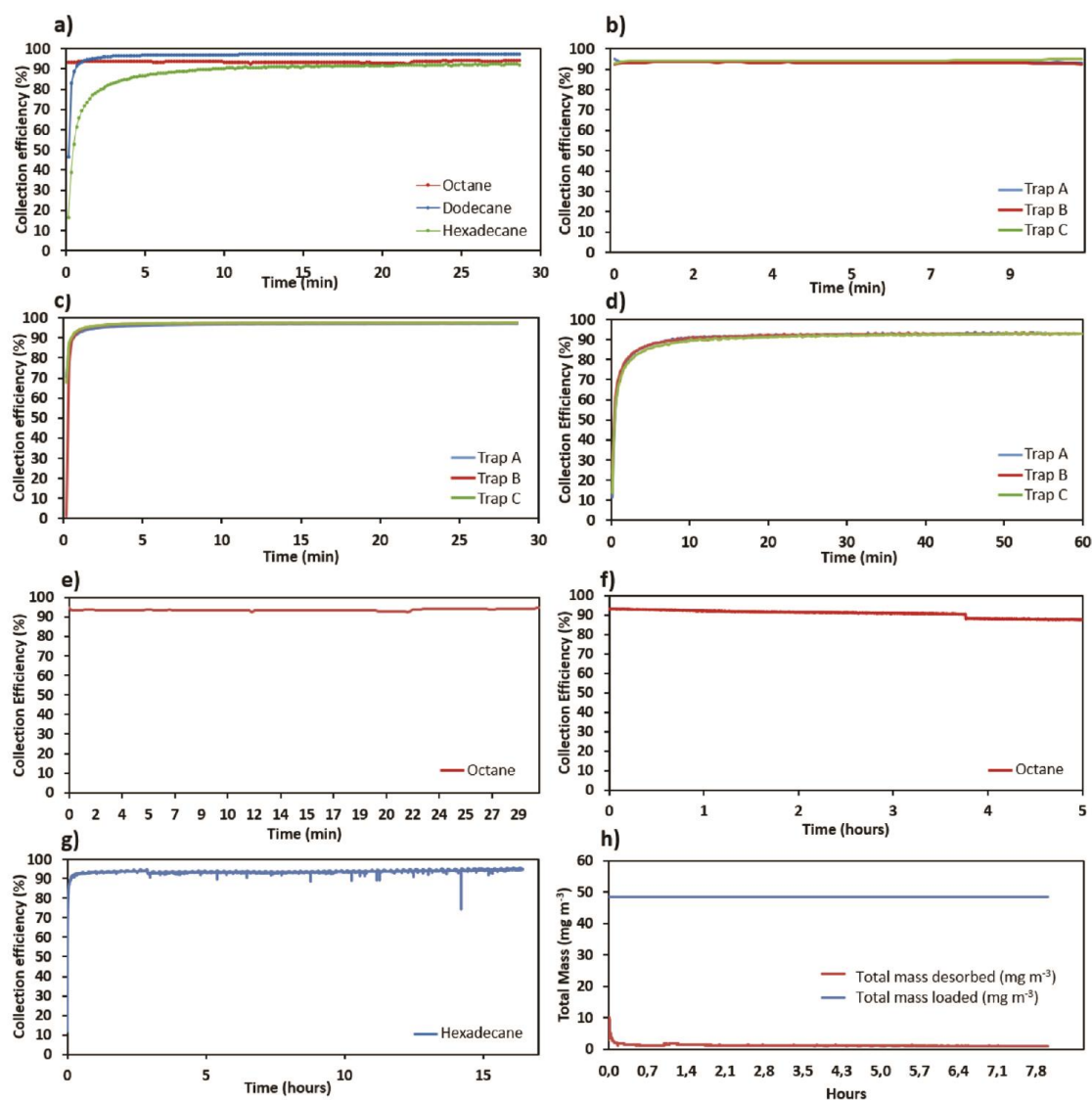


Figure 5. Average gas collection efficiency of C8, C12, and C16 alkanes on GW traps A–C (a). Individual collection efficiency of octane (b), dodecane (c), and hexadecane (d) on three different GW traps. Desorption of octane over a period of 30 min (e) and 5 h (f) and of hexadecane over 15 h (g). The total concentration desorbed versus the total concentration loaded of dodecane on the GW trap over a period of 8 h (h).

Table 2. Moisture Uptake of GW Traps at Various Levels of Humidity ($n = 3$)

| average humidity | average mass of the GW sampler before exp (g) | average mass of the GW sampler after exp (g) ^a | average mass difference (g) | % (m/m) H ₂ O on trap |
|------------------|---|---|-----------------------------|----------------------------------|
| 50% ^b | 6.3488 | 6.3489 | 0.0001 | 0.0817 |
| 60% | 6.3604 ± 0.0096 | 6.3607 ± 0.0094 | 0.0003 ± 0.0005 | 0.2180 ± 0.3775 |
| 70% | 6.3612 ± 0.0100 | 6.3616 ± 0.0099 | 0.0004 ± 0.0001 | 0.3321 ± 0.0861 |
| extreme | 6.3646 ± 0.0183 | 6.4272 ± 0.0047 | 0.0626 ± 0.0147 | 51.9439 ± 12.6622 |

^aMass recorded after removing entrained moisture. ^bBased on one GW trap, as no mass difference was found for the other two traps.

opposing the desired air flow through the sampler that may lead to unstable sampling flow rates at high BPs. The BP of the GW traps was found to be ±13" H₂O at a constant flow of 400 mL·min⁻¹, as measured and displayed using the GilAir portable sampling pumps. The low back pressure can be attributed to the low sorbent packing density of the GW and its fibrous nature, which adds to the versatility of samplers as it allows them to be used with a personal sampling pump (BP threshold of 40" H₂O) in a variety of sampling setups, including denuders.²⁰

The effect of the packing density of the GW trap was investigated by keeping the mass of the GW constant and varying the bed length. From Figure 4b, it is evident that the gas-phase collection efficiency is inversely proportional to the bed length, which is due to the mean free path of the analyte decreasing with a more compact bed, resulting in higher rates of gas collection. When maintaining a GW mass of 50 mg, the gas collection efficiency increased from 69 to 77% when decreasing the bed length by a factor of 2 and further improved to an average of 83% when the bed length was decreased to 20 mm. The GW mass was then doubled to improve the capacity of the GW trap further. Taking all the assembly parameters in this study into consideration, the optimal GW trap assembly consisted of 120 ± 20 mg of GW housed in a glass tube (5.0 mm o.d. × 4.0 mm i.d.) with a 50 mm bed length corresponding to a density of 0.19 mg mm⁻³. The collection efficiency of the octane was also determined to be 94 ± 0.5% for three different GW traps with the same packing density, which confirms repeatability of the experiments and reproducibility of the manmade trap assembly.

3.2. Gas Collection Efficiency of GW Traps. Three replicate traps (A–C) were made according to the optimized assembly as set out in Section 3.1 and were then used to determine the gas collection efficiency with three different alkanes ranging from the more volatile octane to the semivolatile hexadecane. Figure 5a shows the average collection efficiency of octane (C8), dodecane (C12), and hexadecane (C16) on three different GW traps A–C, and Figure 5b–d shows the individual gas-phase collection efficiencies for octane, dodecane, and hexadecane, respectively. The collection efficiency was very good at over 90% for all three alkanes over a period of 30 min. When switching from the bypass line, it can be clearly seen that the time taken to reach the maximum collection efficiency was significantly longer for hexadecane due to the slower adsorption kinetics;¹⁴ similarly, dodecane adsorption on the GW was slower than that of octane; this follows Fick's Law of diffusion, which is governed by the molecule size-dependent diffusion coefficient. The vapor pressure also leads to differences in the vapor saturation concentration of the tested substances, and since octane has the highest vapor pressure, saturation is reached faster due to the higher number of molecules available to be

adsorbed on the lines, which can only adsorb a finite number of molecules.

In order to determine the strength of adsorption and thus storage capabilities of GW, nitrogen gas was passed through a loaded trap to check if any FID signal was observed, which would indicate that the analytes were desorbing from the GW and breakthrough was occurring. Figure 5e reveals that the octane collection efficiency remained unchanged after a period of 30 min, but after a period of 4 h, a breakthrough of <5% was observed in Figure 5f. To confirm this finding, the experiment was repeated with the less-volatile hexadecane over an extended period of 15 h, and no significant breakthrough occurred (Figure 5g). This experiment will also be beneficial for the future investigation of displacement mechanisms if mixtures of gas-phase analytes are to be sampled. The breakthrough experiment of dodecane, illustrated in Figure 5h, showed that <2% of the total adsorbed concentration of 48.42 mg m⁻³ was desorbed after a period of 8 h.

The affinity of graphene for alkanes has been demonstrated theoretically,²¹ and it was found that the desorption energy increases as a function of the n-alkane chain length, which supported our experimental data as we found hexadecane to have the highest affinity for the GW. When optimizing the atomic positions during adsorption, the authors found that all calculations reached an energetic minimum when the alkane carbon skeletons were parallel to the graphene surface.²¹ However, the GW in this study is not pristine graphene, so it is likely that the adsorption of gas molecules on the defective GW is much stronger, and the orientation of the adsorbates may differ.¹⁰

This work proves the excellent affinity and capacity of the GW for non-polar analytes in the volatile and semivolatile ranges. These GW traps can also be used for extended periods of time without breakthrough, which renders them as potentially suitable samplers for full 8 h-shift occupational monitoring.

3.3. Humidity Study. Molecular adsorbates can act as either acceptor or donor molecules when interacting with graphene, and H₂O has been found to be an acceptor adsorbate, resulting in p-type doping of the graphene, whereby the water molecules adsorb only on the surface of the graphene, as the hydroxyl groups are too large to penetrate the graphene film.^{10,22–24}

As mentioned previously, a high sample humidity can have an influence on the type and extent of molecular adsorption of other analytes on the GW, and it can lead to a decrease in their breakthrough volume as a result of reduced availability of active sites on the GW surface; thus, hygroscopicity studies are vital to determine the feasibility of a novel sorbent. Table 2 represents the moisture uptake of GW traps as a function of humidity.

Samples were taken in triplicate in different humidity ranges from 50 to 70%, which are commonly experienced in ambient

and occupational environments. Samples were also taken in triplicate inside the controlled-humidity chamber under visibly humid conditions where extremely high-humidity environments were artificially produced using a mist generator. This experiment was conducted to investigate the extent of the H₂O adsorption on the GW surface versus water droplets that are entrained within the GW fiber layers and cavities in the trap. After sampling, the GW sampler was weighed and compared to the dry-conditioned trap to reveal that the mass of the sorbent had doubled, representing over 100% moisture uptake. After flicking the trap 10 times consecutively and reweighing the trap, it was found that over 40% of the moisture was not physically adsorbed. Based on this finding, the entrained moisture was removed from all traps after sampling in the same fashion. The specific mass of GW in each trap was used to calculate % (m/m) H₂O for each replicate (GW in sampler 1: 0.1223500 g, GW in sampler 2: 0.1198255 g, and GW in sampler 3: 0.1198255 g).

The results in Table 2 show that moisture uptake in the GW traps increased with increasing humidity with values of 0.08, 0.22, and 0.33% (m/m) H₂O for average humidity levels of 50, 60, and 70%, respectively. The moisture uptake is considered insignificant at these humidities, but caution must be taken at higher humidity where the H₂O molecules will compete with analyte molecules for active sites on the GW surface. It is recommended that the GW sampler is not to be used in extremely high-humidity environments unless coupled with an upstream moisture trap.

The interaction between water adsorbates and the graphene surface is largely dictated by the orientation of the water molecules with respect to the surface of the graphene and the structure of the graphene surface itself, whether it is defective, doped, or pristine.¹⁰ This was confirmed by Leenaerts et al., who used density functional theory (DFT) to demonstrate that the adsorption energy was primarily determined by the orientation of the molecule and to a lesser extent by the molecule position.²⁵ In our study, the defective SiO₂ substrate promotes adsorption from water molecules, as the defects in the GW result in oxygen-containing species at the surface, as confirmed by XPS,¹² which interact with the polar water molecules. It was even found that H₂O adsorbates can shift the SiO₂ substrate's impurity bands and change their hybridization with the graphene bands.²⁶ This is in contrast to pristine graphene that is non-polar in nature and thus more insensitive to H₂O adsorbates with the only mechanism of adsorption being physisorption by weaker dispersive forces.^{22,25,26}

3.4. Chromatographic Determination of the Breakthrough Volume of Selected Analytes. Breakthrough analysis is expedient to determine the maximum loading capacity of the sorbent before breakthrough and/or loss of the analyte occurs, which in turn will be used to determine suitable sampling volumes. The adsorption and desorption of analytes on the GW surface were investigated by breakthrough analysis at room temperature and at elevated temperatures.

In Section 3.2, the excellent gas collection of non-polar, planar alkanes in the volatile and semivolatile ranges was demonstrated; therefore, this section will extend to the more polar and volatile range. Here, the elution technique was utilized, whereby the Gaussian gas chromatographic peaks depicted in Figure 6 for each VOC and SVOC were used in conjunction with eq 2¹⁶ to determine the specific breakthrough volume. It should be noted that the methodology used is based on the literature; however, the injection of pure liquid samples

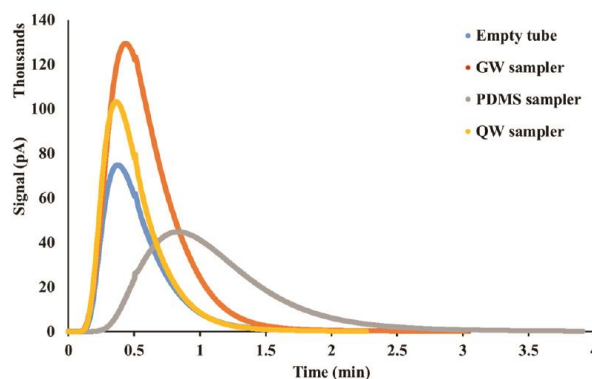


Figure 6. Overlaid chromatograms illustrating the differing retention of methanol at 25 °C for samplers used in the breakthrough study.

may lead to overloading of the sorbents. The results should thus be seen as providing comparative measurements between sorbents but may not reflect the true gas-phase breakthrough volumes. The average retention times used for the calculations at isothermal temperatures for each sorbent are reported in Tables S2–S4. The dead volume correction was not done, as this value required the injection of a non-retained analyte into the GC port, and typical non-retained analytes, such as methane, have been found to be adsorbed by graphene.⁶

The resultant breakthrough curves for each analyte on each sampler type are represented in Figure 7, and their corresponding exponential equations and correlation coefficients are shown in Table S6. The exponential equations derived from the curves were used to calculate the BV values for analytes, which could not be measured experimentally, due to retention by sorbents at this temperature, and these values are presented in Table 3. From the curves in Figure 7, it is immediately evident that all BVs decrease with increasing temperature, and GW showed significantly higher breakthrough volumes for polar analytes when compared to PDMS samplers.

The studied polar VOCs were selected to represent a range of boiling points from 64.7 to 155.6 °C. The correlation coefficients (R^2 values in Table S5) ranged from 0.7570 to 0.9902, which shows a good fit to experimental data, enabling extrapolation to 25 °C in order to determine the breakthrough volumes at ambient sampling temperatures. Calculated GW BVs predictably increased with decreasing volatility of the analyte, but the low BVs obtained, ranging from 0.029 to 0.202 L g⁻¹, demonstrated that in this experiment, non-polar VOCs did not have a very strong affinity for the GW surface. Other sorbent materials such as Tenax have specific breakthrough volumes (SBVs), an order of magnitude larger than for GW, but it must be noted that the polarity of this sorbent lends itself to polar adsorbates.

From Figure 7 and Table 3, it can be seen that at room temperature (25 °C), the GW breakthrough volume for the most volatile compound, methanol, is calculated to be 0.058 L g⁻¹. However, when targeting analytes with higher boiling points such as cyclohexanone, the breakthrough volume is calculated to be 0.563 L g⁻¹. When considering a more semivolatile, non-polar compound such as hexadecane, the BV decreases to 0.202 L g⁻¹.

The extrapolated breakthrough volume at a specific temperature should be considered when selecting the sampling

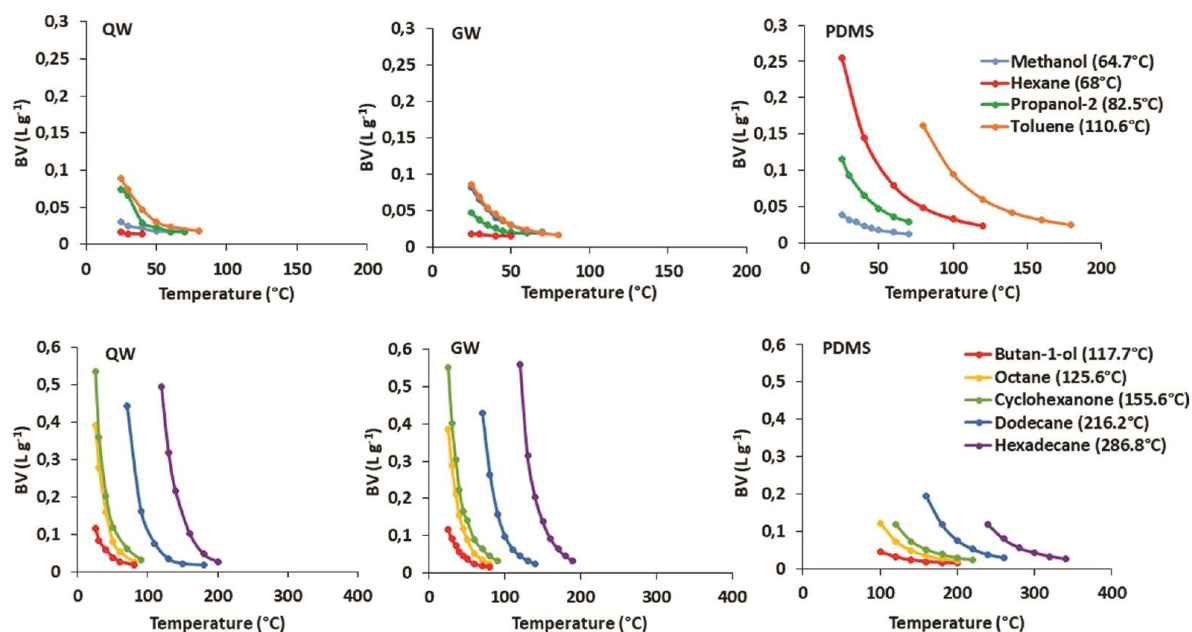


Figure 7. Breakthrough volume curves for the 0.120 g QW (left), 0.141 g GW (middle), and 0.365 g PDMS (right) samplers at various isothermal temperatures.

Table 3. BVs of QW, GW, and PDMS along with the Boiling Points, Molecular Masses, and Densities of the Compounds at the Inlet Temperature of 250 °C²⁷

| analyte with the corresponding BP | polarity expressed as Log P | MM of compounds (g mol ⁻¹) | density at 25 °C (g L ⁻¹) | QW BV at 25 °C (L g ⁻¹) | GW BV at 25 °C (L g ⁻¹) | PDMS BV at 25 °C (L g ⁻¹) |
|-----------------------------------|-----------------------------|--|---------------------------------------|-------------------------------------|-------------------------------------|---------------------------------------|
| Polar Compounds | | | | | | |
| methanol (64.7 °C) | -0.77 | 32.04 | 0.875 | 0.043 | 0.058 | 0.044 |
| propanol-2 (82.5 °C) | 0.05 | 60.10 | 0.79 | 0.086 | 0.093 | 0.120 |
| butan-1-ol (117.7 °C) | 0.88 | 74.12 | 0.81 | 0.405 | 0.397 | 0.168 ^a |
| cyclohexanone (155.6 °C) | 0.81 | 98.15 | 0.94 | 0.549 | 0.563 | 0.227 ^a |
| Non-polar Compounds | | | | | | |
| hexane (68 °C) | 3.90 | 86.18 | 0.66 | 0.029 | 0.029 | 0.259 |
| toluene (110.6 °C) | 2.73 | 92.14 | 0.86 | 0.102 | 0.097 | 0.185 ^a |
| octane (125.6 °C) | 5.18 | 114.23 | 0.70 | 0.128 | 0.129 | 0.194 ^a |
| dodecane (216.2 °C) | 6.10 | 170.33 | 0.75 | 0.170 ^a | 0.142 ^a | 0.266 ^a |
| hexadecane (286.8 °C) | 8.30 | 226.41 | 0.77 | 0.212 ^a | 0.202 ^a | 0.347 ^a |

^aCalculated values are distinguished from the experimentally determined values.

flow rate and sample volume and additional parameters such as sampling humidity, which also influences the breakthrough behavior of an analyte due to the adsorbed water molecules taking up active adsorption sites on the surface of the GW, which was discussed in Section 3.3.

From Table 3, it can be seen that PDMS has larger breakthrough volumes for all non-polar analytes, whereas GW showed higher breakthrough volumes for all polar analytes.

To establish the extent of adsorption of the GW surface, the BV volumes were directly compared to those of the parent QW substrate. GW shows higher BV at 25 °C than QW for almost every analyte; however, these differences are not considered significant. This can be explained by the non-uniform bi- and multilayered graphene surface on the QW. Regions of the QW are exposed on the GW, resulting in the same adsorption mechanisms of polar analytes and therefore similar retention and breakthrough. These findings suggest that the growth of graphene on the QW could be further optimized in terms of

the surface coverage and level of defects to enhance molecular interactions with both polar and non-polar analyte molecules.

When comparing the GW sorbent to the PDMS sorbent, which has already been validated for PAHs and more polar compounds,^{14,20} it can be seen from Table 3 and Figure 7 that GW had higher BVs for methanol, butan-1-ol, dodecane, and cyclohexadecane. The PDMS, on the other hand, showed better BVs for non-polar analytes only, which can be explained by the differences in the sorbent material. The PDMS is a non-polar medium that traps analytes by absorption rather than adsorption; therefore, only molecules with the same polarity will be absorbed. The GW sorbent showed an increase in BVs with an increase in the carbon chain length of the non-polar analytes, which was also seen in the gas collection efficiency study in Section 3.2, and it can be rationalized by the increase in desorption energy, as determined theoretically by Londero and colleagues.²¹ The affinity of the GW for polar molecules is due to the defective nature of the GW that contains polar

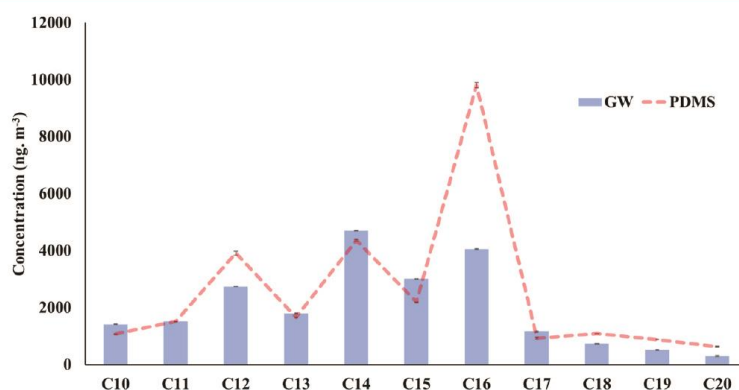


Figure 8. Concentration of C_{10} – C_{20} alkanes in RME biodiesel combustion emissions on GW and PDMS samplers that were thermally desorbed and analyzed by GC–MS.

regions with increased electrostatic potential and increased dispersive forces for polar analyte adsorption. Oxidized domains exist in the material as a result of a broken sp^2 carbon network, which occurred during CVD synthesis.¹³ These domains occur at the irregular edges of the graphene layers and are the main site of adsorption of polar molecules due to interactions with electronegative oxygen, resulting in dispersive forces, of which hydrogen bonding is the most predominant. A similar result was reported by Berashevich and Chakraborty, who found that adsorbed polar molecules formed a cluster along the oxidized zigzag edges of graphene. The oxidized edges tend to donate a charge to the adsorbates, and the extent of adsorption is governed by the intermolecular distance and by the location of the adsorbed molecules relative to the plane of graphene.²⁸

The BV for octane, dodecane, and hexadecane in this study was significantly lower than that determined in the gas collection efficiency study in Section 3.2, and it must be noted that the experimental setups were different, which plays a major role in the results obtained, specifically when the temperature is concerned. The temperature-controlled chamber was held at ambient temperature during all measurements, whereas this FID experimental setup had a heated inlet, resulting in an increase in the kinetic energy of analytes, leading to an increased rate of desorption and thus lower BVs. Another drawback of this study was that only one GW trap was used in the configuration, as it was not practicably feasible to change the sampler after each experiment. This can result in a deterioration of the GW coating with time and an increase in defects, which ultimately affect the polarity and retention capabilities of the sampler; therefore, the results must be interpreted with caution. It is suggested that further investigation is required in order to accurately determine the GW material interaction with polar versus non-polar analytes. In this study, the peak areas for methanol on GW were found to be significantly higher than for other samplers (Figure 6), and it was hypothesized that the graphene material is broken down when it is flushed with certain solvents, such as methanol, which resulted in the elevated FID signal in the experiment. This is another aspect to the novel material that requires further research in order to fully understand the uses and limitations of the sampler.

For future work in this regard, it is advised to further optimize the GW sampler to contain a higher mass of the GW sorbent per sampler to increase the BVs and then introduce a

second GW sampler downstream to potentially act as a gauge for breakthrough. This will allow for more accurate determination of the SBVs for target analytes under varying conditions, which are encountered in real-world sampling. Headspace gas sampling should be conducted where the breakthrough of analytes can be determined by means of permeation tubes, as in the experiments conducted here, overloading of the sorbents was likely resulting under non-linear chromatographic conditions. A good starting point would be the determination of breakthrough of naphthalene using headspace sampling, as this can directly be compared to the validation of PDMS sorbents, for which the breakthrough volume of naphthalene is 5 L at a sampling flow rate of 0.500 L min^{-1} .²⁹

3.5. Application of the GW Sampler in Fuel Combustion Emission Sampling. The GW sampler and various other samplers were used in conjunction with a controlled-combustion aerosol standard system, where duplicate air combustion emission measurements were taken from diesel, gas-to-liquid fuel, and rapeseed methyl ester biofuel, as described in detail by Mason et al.¹⁷ For the scope of this study, only one fuel, namely, RME biodiesel, was considered to demonstrate the practical use of the GW sampler.

From Figure S1, it can be clearly seen that the GW calibration curves for C_{10} – C_{20} alkanes had correlation coefficients >0.999 for every analyte, which depicts excellent linearity for the range of concentrations with LODs ranging from 424 to 4874 ng m^{-3} , as seen in Table S6 in the Supporting Information. The linear response also demonstrated the successful thermal desorption of analytes from the GW, therefore showing that no solvent extraction is required. The fact that TD quantitatively removes the non-polar C_{10} – C_{20} alkane analytes, with molecular weights and boiling points ranging from 114 to 282 g mol^{-1} and 125.6 to $343 \text{ }^\circ\text{C}$, respectively, from the sampler further confirms the sustainable reusability of the samplers with respect to these analytes.

The GW sampler was shown to be very effective in sampling alkanes in the volatile–semivolatile range, which were found to be in the low $\mu\text{g m}^{-3}$ range with tetradecane being the most abundant, as seen in Figure 8. The performance of the GW sampler was directly compared to that of a PDMS sampler, which has been tested, validated, and applied in numerous studies,^{14,17–20,30,31} and it was found to be very comparable in both emission profiles and concentrations of each analyte, excluding hexadecane, with an % difference of 1.9% between

the total alkane concentrations. The GW showed higher recoveries of the lower alkanes <C15 when compared to the PDMS but lower concentrations for the higher alkanes. The significantly large discrepancy between the two samplers for hexadecane (83% difference) and all alkanes >C15 was likely due to incomplete thermal desorption of heavier alkanes from the GW, as the TD method was optimized for PDMS. These findings were consistent with those found in Section 3.2, which demonstrated the high affinity of GW for non-polar analytes, but were contrary to those found in Section 3.4, which showed better retention of polar analytes on the GW. This can be explained by better coverage of graphene layers on the QW for the traps used in the CAST study and the fact that each GW sampler was only used once, ensuring the integrity of the graphene surface.

4. CONCLUSIONS

A novel GW trap was optimized in terms of sorbent mass, bed length, and packing density and was tested for use as a sampler for a range of volatile and semivolatile analytes. The GW sampler was compared to commercially available and validated PDMS and charcoal samplers to assess accuracy and efficacy. The gas-phase collection efficiency was found to be >94% for octane, dodecane, and hexadecane at ambient temperatures, which was comparable to that of activated charcoal. The humidity uptake onto GW was found to be insignificant where moisture was predominantly found to be entrained in the fibers and not physisorbed on the graphene surface. The experimental and theoretical breakthrough studies showed that GW had higher breakthrough volumes for polar analytes when compared to the PDMS sampler, however BVs of GW did not significantly increase when compared to QW, which demonstrated the high degree of defects of the GW and the non-uniform surface of bi- and multilayers. Subsequently, a more practical breakthrough experiment may be required, such as using headspace sampling, to aid in the validation of the retention volumes at set pressures and temperatures using numerous replicates of different GW traps.

The GW sampler efficacy was then demonstrated in a real-world application, where it was employed as an air sampler for volatile and semivolatile organic compounds arising from the combustion of a rapeseed methyl ester biofuel. The linear response of each analyte demonstrated the successful thermal desorption of the C₁₀–C₂₀ alkane analytes from the GW sampler, therefore, showing that no solvent extraction is required. The GW was found to be very comparable in both emission profiles and concentrations of each analyte to a PDMS sampler and can be used as a standalone sampler or as a secondary trap in a sampling train similar to that of a PDMS denuder setup.^{19,20}

GW is thus a novel adsorbent that has proven to be an effective sampling medium comparable to currently available technologies. It has numerous advantages including the fact that it is reusable, sustainable and cost-effective and, very importantly, does not require time-consuming and toxic solvent extraction techniques. Another significant advantage is the possibility to tune the surface chemistry of the GW for targeted polar or non-polar analytes by modifying the surface coverage of graphene on the QW. The presence of oxidized domains at the edges of the non-pristine graphene results in dispersive forces with polar analytes due to interactions with the electronegative oxygen and results in edge-type adsorption. The extent of polar adsorption is thus largely governed by the

intermolecular distance, the extent of oxidation of the graphene, and the location of the adsorbed molecules relative to the graphene layer plane.

This tunability can also provide additional capabilities regarding device design, for applications including filtration, microfluidics, chemical sensing, and, as in this study, chemical sampling.

■ ASSOCIATED CONTENT

Supporting Information

The Supporting Information is available free of charge at <https://pubs.acs.org/doi/10.1021/acsomega.1c03595>.

The Supporting Information provides a photograph of the optimized graphene wool sampler assembly; internal standards information; additional breakthrough volume data; and limits of detection and quantification and calibration curves for the target analytes which were thermally desorbed from the GW samplers (PDF)

■ AUTHOR INFORMATION

Corresponding Author

Patricia Forbes – Department of Chemistry, University of Pretoria, Pretoria 0001, South Africa; orcid.org/0000-0003-3453-9162; Phone: +27 12 420 5426; Email: patricia.forbes@up.ac.za

Authors

Genna-Leigh Geldenhuys – Department of Chemistry, University of Pretoria, Pretoria 0001, South Africa; Processing Laboratory, Impala Platinum Limited, Rustenburg 0299, South Africa; Present Address: Skin Rejuvenation Technologies, Irene, Pretoria, 0157, South Africa

Yvonne Mason – Department of Chemistry, University of Pretoria, Pretoria 0001, South Africa

George C. Dragan – Joint Mass Spectrometry Centre, Cooperation Group “Comprehensive Molecular Analytics”, Neuherberg D-85758, Germany; Present Address: Federal Institute for Occupational Safety and Health, D-44149 Dortmund, Germany.

Ralf Zimmermann – Joint Mass Spectrometry Centre, Cooperation Group “Comprehensive Molecular Analytics”, Neuherberg D-85758, Germany; Joint Mass Spectrometry Centre, Institute of Chemistry, University of Rostock, Rostock D-18051, Germany

Complete contact information is available at: <https://pubs.acs.org/doi/10.1021/acsomega.1c03595>

Author Contributions

The manuscript was written through contributions of all authors. All authors have given approval to the final version of the manuscript.

Funding

Funding provided by the University of Pretoria, Impala Platinum Ltd. and the National Research Foundation of South Africa (NRF, grant number 105807) is acknowledged. This work was supported by the German Federal Ministry of Education and Research (BMBF), research contract 01DG17023.

Notes

The authors declare no competing financial interest.

ACKNOWLEDGMENTS

The National Research Foundation (NRF, grant number 105807) and the Departments of Chemistry and Physics at the University of Pretoria and Impala Platinum Ltd are acknowledged for their support and resources. The Helmholtz Zentrum and Federal Ministry of Education and Research (BMBF) in Germany are also duly acknowledged with special thanks to the Comprehensive Molecular Analytics (CMA) group at Helmholtz Zentrum München.

REFERENCES

- (1) Zhang, G.; Guo, X.; Wang, S.; Wang, X.; Zhou, Y.; Xu, H. New graphene fiber coating for volatile organic compounds analysis. *J. Chromatogr. B: Anal. Technol. Biomed. Life Sci.* **2014**, *969*, 128–131.
- (2) Wang, T.; Huang, D.; Yang, Z.; Xu, S.; He, G.; Li, X.; Hu, N.; Yin, G.; He, D.; Zhang, L. A review on graphene-based gas/vapor sensors with unique properties and potential applications. *Nano-Micro Lett.* **2016**, *8*, 95–119.
- (3) Singh, V.; Joung, D.; Zhai, L.; Das, S.; Khondaker, S. I.; Seal, S. Graphene based materials: Past, present and future. *Prog. Mater. Sci.* **2011**, *56*, 1178–1271.
- (4) Yousefi, N.; Lu, X.; Elimelech, M.; Tufenkji, N. Environmental performance of graphene-based 3D macrostructures. *Nat. Nanotechnol.* **2019**, *14*, 107–119.
- (5) Chen, Z.; Guo, X.; Zhu, L.; Li, L.; Liu, Y.; Zhao, L.; Zhang, W.; Chen, J.; Zhang, Y.; Zhao, Y. Direct growth of graphene on vertically standing glass by a metal-free chemical vapor deposition method. *J. Mater. Sci. Technol.* **2018**, *34*, 1919–1924.
- (6) Zhu, Z. W.; Zheng, Q. R. Methane adsorption on the graphene sheets, activated carbon and carbon black. *Appl. Therm. Eng.* **2016**, *108*, 605–613.
- (7) Eda, G.; Fanchini, G.; Chhowalla, M. Large-area ultrathin films of reduced graphene oxide as a transparent and flexible electronic material. *Nat. Nanotechnol.* **2008**, *3*, 270–274.
- (8) Ramanathan, T.; Abdala, A. A.; Stankovich, S.; Dikin, D. A.; Herrera-Alonso, M.; Piner, R. D.; Adamson, D. H.; Schniepp, H. C.; Chen, X.; Ruoff, R. S.; et al. Functionalized graphene sheets for polymer nanocomposites. *Nat. Nanotechnol.* **2008**, *3*, 327–331.
- (9) Xu, S.; Man, B.; Jiang, S.; Yue, W.; Yang, C.; Liu, M.; Chen, C.; Zhang, C. Direct growth of graphene on quartz substrates for label-free detection of adenosine triphosphate. *Nanotechnology* **2014**, *25*, 165702.
- (10) Kong, L.; Enders, A.; Rahman, T. S.; Dowben, P. A. Molecular adsorption on graphene. *J. Phys.: Condens. Matter* **2014**, *26*, 443001.
- (11) Schoonraad, G.; Forbes, P. B. C. Air Pollutant Trap. SA provisional patent application 2019/00674. 2019. Filed 1 February 2019.
- (12) Schoonraad, G.-L.; Madito, M. J.; Manyala, N.; Forbes, P. Synthesis and optimisation of a novel graphene wool material by atmospheric pressure chemical vapour deposition. *J. Mater. Sci.* **2020**, *55*, 545–564.
- (13) Schoonraad, G.; Forbes, P. B. C. Graphene wool and manufacture thereof, PCT International Application PCT/ZA2020/050005. Filed 24 January 2020.
- (14) Kohlmeier, V.; Dragan, G. C.; Karg, E. W.; Schnelle-Kreis, J.; Breuer, D.; Forbes, P. B. C.; Rohwer, E. R.; Zimmermann, R. Multi-channel silicone rubber traps as denuders for gas-particle partitioning of aerosols from semi-volatile organic compounds. *Environ. Sci.: Processes Impacts.* **2017**, *19*, 676–686.
- (15) Ortner, E. K.; Rohwer, E. R. Trace analysis of semi-volatile organic air pollutants using thick film silicone rubber traps with capillary gas chromatography. *J. High Resolut. Chromatogr.* **1996**, *19*, 339–344.
- (16) Manura, J. J. Calculation and Use of Breakthrough Volume Data Scientific Instrument Services (SIS): Adaptas Solutions. 2019, [Available from: <https://www.sisweb.com/index/referenc/resin10.htm>]. (accessed on April, 17th 2021).
- (17) Mason, Y. C.; Schoonraad, G.-L.; Orasche, J.; Bisig, C.; Jakobi, G.; Zimmermann, R.; Forbes, P. B. C. Comparative sampling of gas phase volatile and semi-volatile organic fuel emissions from a combustion aerosol standard system. *Environ. Technol. Innovation* **2020**, *19*, 100945.
- (18) Forbes, P. B.; Rohwer, E. R. Investigations into a novel method for atmospheric polycyclic aromatic hydrocarbon monitoring. *Environ. Pollut.* **2009**, *157*, 2529–2535.
- (19) Geldenhuys, G.; Rohwer, E. R.; Naudé, Y.; Forbes, P. B. C. Monitoring of atmospheric gaseous and particulate polycyclic aromatic hydrocarbons in South African platinum mines utilising portable denuder sampling with analysis by thermal desorption-comprehensive gas chromatography-mass spectrometry. *J. Chromatogr. A* **2015**, *1380*, 17–28.
- (20) Forbes, P. B. C.; Karg, E. W.; Zimmermann, R.; Rohwer, E. R. The use of multi-channel silicone rubber traps as denuders for polycyclic aromatic hydrocarbons. *Anal. Chim. Acta* **2012**, *730*, 71–79.
- (21) Londero, E.; Karlson, E. K.; Landahl, M.; Ostrovskii, D.; Rydberg, J. D.; Schröder, E. Desorption of n-alkanes from graphene: a van der Waals density functional study. *J. Phys.: Condens. Matter* **2012**, *24*, 424212.
- (22) Wang, W. L.; Kaxiras, E. Graphene hydrate: theoretical prediction of a new insulating form of graphene. *New J. Phys.* **2010**, *12*, 125012.
- (23) Bunch, J. S.; Verbridge, S. S.; Alden, J. S.; Van Der Zande, A. M.; Parpia, J. M.; Craighead, H. G.; McEuen, P. L. Impermeable atomic membranes from graphene sheets. *Nano Lett.* **2008**, *8*, 2458–2462.
- (24) Romero, H. E.; Joshi, P.; Gupta, A. K.; Gutierrez, H. R.; Cole, M. W.; Tadigadapa, S. A.; Eklund, P. C. Adsorption of ammonia on graphene. *Nanotechnology* **2009**, *20*, 245501.
- (25) Leenaerts, O.; Partoens, B.; Peeters, F. M. Adsorption of H₂O, NH₃, CO, NO₂, and NO on graphene: A first-principles study. *Phys. Rev. B: Condens. Matter Mater. Phys.* **2008**, *77*, 125416.
- (26) Wehling, T. O.; Lichtenstein, A. I.; Katsnelson, M. I. First-principles studies of water adsorption on graphene: The role of the substrate. *Appl. Phys. Lett.* **2008**, *93*, 202110.
- (27) PubChem. 2021, [Available from: <https://pubchem.ncbi.nlm.nih.gov/>]. (accessed on May, 14th 2021).
- (28) Berashevich, J.; Chakraborty, T. Doping graphene by adsorption of polar molecules at the oxidized zigzag edges. *Phys. Rev. B: Condens. Matter Mater. Phys.* **2010**, *81*, 205431.
- (29) Forbes, P. B. Development of a Laser Induced Fluorescence Technique for the Analysis of Organic Air Pollutants, Doctoral dissertation, University of Pretoria, 2010.
- (30) Munyeza, C. F.; Kohlmeier, V.; Dragan, G. C.; Karg, E. W.; Rohwer, E. R.; Zimmermann, R.; Forbes, P. B. C. Characterisation of particle collection and transmission in a polydimethylsiloxane based denuder sampler. *J. Aerosol Sci.* **2019**, *130*, 22–31.
- (31) Dragan, G. C.; Kohlmeier, V.; Orasche, J.; Schnelle-Kreis, J.; Forbes, P. B. C.; Breuer, D.; Zimmermann, R. Development of a Personal Aerosol Sampler for Monitoring the Particle-Vapour Fractionation of SVOCs in Workplaces. *Ann. Work Exposures Health* **2020**, *64*, 903–908.

Thirdly, practical application of the graphene wool sampler is presented in Paper 6 whereby fuel emissions from a combustion aerosol standard system were measured and compared when using GW, PDMS traps and commercial activated charcoal. Paper 6 was published in *Environmental Technology & Innovation*.

Mason, Y.C., Schoonraad, G., Orasche, J., Bisig, C., Jakobi, G., Zimmermann, R., and Forbes, P.B.C. 2020. Comparative sampling of gas phase volatile and semi-volatile organic fuel emissions from a combustion aerosol standard system. *Environmental Technology & Innovation*, 19, 100945. DOI: <https://doi.org/10.1016/j.eti.2020.100945>.

Author contributions

Y.C Mason: Investigation, Formal analysis, Writing - original draft. **G Schoonraad:** Conceptualization, Investigation. **J Orasche:** Methodology, Investigation, Formal analysis, Project administration, Writing - review & editing. **C Bisig:** Methodology, Investigation, Writing - review & editing. **G Jakobi:** Methodology, Investigation. **R Zimmermann:** Conceptualization, Resources, Funding acquisition. **P.B.C Forbes:** Conceptualization, Methodology, Investigation, Formal analysis, Writing - review & editing, Supervision, Project administration, Resources, Funding acquisition.



Contents lists available at ScienceDirect

Environmental Technology & Innovation

journal homepage: www.elsevier.com/locate/eti

Comparative sampling of gas phase volatile and semi-volatile organic fuel emissions from a combustion aerosol standard system[☆]



Yvonne C. Mason^a, Genna-Leigh Schoonraad^a, Jürgen Orasche^b,
Christoph Bisig^b, Gert Jakobi^b, Ralf Zimmermann^{b,c}, Patricia B.C. Forbes^{a,*}

^a Department of Chemistry, Faculty of Natural and Agricultural Sciences, University of Pretoria, Lynnwood Road, 0002, South Africa

^b Comprehensive Molecular Analytics (CMA), Helmholtz Zentrum München, Gmunder Str. 37, 81379 München, Germany

^c Joint Mass Spectrometry Center, Chair of Analytical Chemistry, University of Rostock, Germany

ARTICLE INFO

Article history:

Received 26 March 2020

Received in revised form 28 May 2020

Accepted 30 May 2020

Available online 1 June 2020

Keywords:

CAST

Graphene wool sampler

PDMS sampler

Diesel combustion

Biodiesel

ABSTRACT

The incomplete combustion of fossil fuels generates hazardous gaseous compounds which have been linked to various adverse environmental and human health effects worldwide. Cleaner alternatives such as gas-to-liquid (GTL) and biofuels such as rapeseed oil methyl ester (RME) have therefore been investigated. In this study, a Combustion Aerosol Standard (CAST) was used to generate a diluted, consistent and relatively stable source of fuel emissions from the combustion of diesel, GTL and RME, respectively. Gas phase sampling was carried out by removing particulates using a filter upstream of three different samplers: i) a commercialised activated charcoal sampler; ii) a validated polydimethylsiloxane (PDMS) sampler; and iii) a novel graphene wool (GW) sampler. The latter two were thermally desorbed, whilst the charcoal sampler was solvent extracted. All three samplers were analysed for trace levels of selected volatile organic compounds (VOCs) and semi-volatile organic compounds (SVOCs) by means of gas chromatography–mass spectrometry (GC–MS).

The GW sampler outperformed the PDMS and activated charcoal samplers as the GW sampled the most compounds and had a lower variability in VOC and SVOC (selected polycyclic aromatic hydrocarbon and n-alkane) concentrations sampled, especially in the case of the n-alkanes (average %RSDs of the GW, PDMS and activated charcoal samplers were found to be 23.8%, 43.1% and 52.9%, respectively). The activated charcoal sampler was found to be unsuitable in this study due to the low number of detected compounds, as well as high benzene and toluene backgrounds of the sorbent. Combustion of diesel was found to emit a total VOC and SVOC concentration 4–5 times that of GTL and RME, respectively, based on GW sampler analyses. This study therefore further supports GTL and RME as cleaner fuel alternatives to petroleum derived diesel.

© 2020 Elsevier B.V. All rights reserved.

[☆] Capsule: A novel graphene wool sampler allowed for the detection of more gaseous VOCs and SVOCs with better reproducibility than other samplers, including standard activated charcoal.

* Corresponding author.

E-mail address: patricia.forbes@up.ac.za (P.B.C. Forbes).

1. Introduction

The detection of hazardous gaseous compounds has become ever more critical as an increasing number of studies link various adverse environmental and human health effects to increasing ambient air pollution (Landrigan et al., 2019; Goldemberg et al., 2018; Yan et al., 2018). Commonly known constituents of air pollution include compounds such as NO_x, SO_x, CO and particulate matter (PM) in addition to volatile organic compounds (VOCs) and semi-volatile organic compounds (SVOCs). Recent literature shows that vehicular emissions are generally reported in terms of the CO, CO₂, NO_x and PM produced (Dagaut et al., 2019; Borillo et al., 2018; He, 2016). There are multiple studies which have focused on the adverse side effects of PM (Bae and Hong, 2018; Gautam et al., 2018; Hime et al., 2018; Chen et al., 2017; Künzli et al., 2005; Peters et al., 1997), which thereby warrants combustion emissions being reported in terms of PM production, however, it is also crucial to be cognisant of gaseous emissions, such as VOCs and SVOCs, as these have also shown to be detrimental to human health (Points, 2019; Mirzaei et al., 2016; Yu and Kim, 2010; Jia et al., 2008; Kawamura et al., 2006). VOCs and SVOCs have been noted to be potentially carcinogenic and may cause the enhancement of respiratory, cardiovascular, infectious and allergic diseases through contact with the skin or through inhalation (Helen et al., 2019; Lerner et al., 2018; Raza et al., 2018; Bernstein et al., 2004; Finlayson-Pitts and Pitts Jr, 1999; Finlayson-Pitts and Pitts, 1997; Hemminki and Pershagen, 1994). It has been noted that a trend towards using biodiesel over petroleum-derived diesel has arisen due to lower reported PM emissions from biodiesel combustion, therefore it is generally considered a cleaner alternative fuel (Damanik et al., 2018; Knothe and Razon, 2017). However, little has been reported on the gaseous organic by-products released by the combustion of these biofuels.

As research into the effects of VOCs and SVOCs has progressed over the years, governing environmental bodies have made it ever more imperative to create a means by which to monitor even lower trace concentrations of these analytes. Currently, VOCs are typically sampled onto retaining media such as commercially available Carbotrap, Carbosieve™S-III and Tenax® which are either carbon- or polymer-based samplers. SVOCs are commonly sampled onto the same retaining media as the VOCs in addition to retaining media such as multi-channel polydimethylsiloxane (PDMS) traps (Munyeza et al., 2018; Forbes and Rohwer, 2009; Ortner and Rohwer, 1996).

The use of carbon-based air samplers is not a novel concept in the field of environmental analysis, however a novel class of carbon nanostructures, known as graphene, is gaining attention in analytical chemistry due to many of its innately attractive properties. Graphene has been calculated to have an impressive theoretical specific surface area of 2630 m² g⁻¹ (Züttel et al., 2004) which is far above the 1000 m² g⁻¹ required of a “strong” sorbent (United States Environmental Protection Agency, 1999). Due to the ultrahigh surface area graphene possesses in combination with its non-polar nature, Schoonraad and Forbes developed a means to synthesise graphene in a way which allows facile use thereof as an adsorbent in an active air sampler, called a graphene wool (GW) sampler, as shown in Figure S1 in the Supplementary Information (Schoonraad and Forbes, 2019a,b; Schoonraad et al., 2020).

A CAST generator, which is based on a laminar propane co-flow diffusion flame, is a useful way to produce stable trace level emissions that mimic the physical and chemical properties which are characteristic of real-world emissions from the combustion of selected fuel sources (Moore et al., 2014). To solve the difficulty of analysing combustion aerosols, which have a tendency to coagulate, particles need to be produced instantaneously in a continuous process with reliable reproducibility (Kasper, 2009) from a regulated aerosol generator. It is from this need that the CAST generator was developed, in which soot particles are formed when the combustion process is quenched with inert “quenching” gas, and its operation has been investigated by various authors (Mueller et al., 2015; Moore et al., 2014). In this study, trace level gas phase emissions which are simultaneously produced from a CAST generator were utilised to evaluate the performance of three different air samplers. Due to the various methods implemented to stabilise the exhaust emissions from the CAST generator, it has been viewed as a stable and repeatable source of PM of a certain size range (Mueller et al., 2015) and therefore the diluted exhaust stream may also be a source of trace levels of organic gas phase combustion emission products.

Here we describe the sampling of gas phase VOCs and SVOCs from a CAST generator utilising a filter upstream of each sampler to capture the PM and thereby only sample the gas phase analytes. The VOCs of interest included benzene, toluene, ethylbenzene and xylenes (BTEX), whilst SVOCs included n-alkane hydrocarbons and polycyclic aromatic hydrocarbons (PAHs). Emissions from each of three different fuel types were sampled from the CAST exhaust in parallel by three different samplers of interest, namely a multichannel PDMS sampler prepared in-house, a commercial activated charcoal sampler, and a novel GW sampler prepared in-house. The activated charcoal sampler was selected due to its use in VOC methods published by the International Organization for Standardization (ISO) and Methods for the Determination of Hazardous Substances (MDHS) (International Organization for Standardization ISO 9487:1991 (E); International Organization for Standardization ISO 16200-1:2001 (E); Methods for the Determination of Hazardous Substances MDHS 96 (2000)). Activated charcoal is also a cheaper alternative to graphitised materials such as Carbotrap®. The CAST system was utilised in this comparison of the performance of the chosen samplers due to the improved stability of emissions the system produces in comparison to real-world emissions, which typically would vary over time which in turn introduces sampling uncertainties. Other gas standard emission generators tend to produce only one compound at a time, and standard gas cylinder mixtures of VOCs cover a very limited range of analytes. The CAST system therefore provides a suitable means to evaluate the performance of the selected samplers, thereby allowing for the determination and evaluation of the strengths and weaknesses of each type of sampler in determining the concentrations of the target organic gas phase analytes at trace levels.

2. Materials and methods

2.1. Reagents and materials

The three fuels that were tested, namely petroleum derived diesel with no added biodiesel (B0), gas-to-liquid (GTL) and rapeseed oil methyl ester (RME) fuels were all purchased from ASG Analytik-Service GmbH, Neusäss, Germany. An ultrasonic bath was utilised to degas each fuel for 30 min prior to use.

Individual stock standards of 36 volatile organic compounds (VOCs) and semi-volatile organic compounds (SVOCs) along with 13 internal standards were purchased from the suppliers listed in Table S1 of the Supplementary Information. Working solutions were prepared by appropriate dilutions of the stock solutions prior to use. For the extraction of analytes from the activated charcoal sampler, anhydrous carbon disulphide (CS₂) (>99% purity) was purchased from Merck, Germany.

2.2. Sampler details

Each of the polydimethylsiloxane (PDMS) traps consisted of twenty-two 55 mm long parallel PDMS tubes (Technical Products, Inc., Georgia, USA) of 0.3 mm i.d. which were housed in a 89 mm long Supelco glass TD tube with an i.d. of 4 mm. Graphene wool (GW) was synthesised in-house as per the optimised conditions described by Schoonraad et al. (2020) using a quartz wool substrate (Acros, Industrial Analytical, South Africa). For the assembly of the GW samplers, approximately 120 mg of GW was weighed out using a calibrated Sartorius Entris analytical balance and then packed into the same glass tubing as the PDMS traps, whilst maintaining a bed length of 60 mm for the GW sampler. The sorbent was held in place by stainless steel screens (Sigma Aldrich, South Africa) which are designed for Gerstel TD tubes of the same i.d.. The traps were then conditioned using a multi-tube conditioner (TC-20 MARKES International, Germany) at 250 °C for 8 h under hydrogen gas flow and were then sealed using Shimadzu stainless steel tube caps. The activated charcoal type BIA tubes were purchased from Dräger, Germany.

2.3. CAST setup

A Combustion Aerosol Standard generator (diesel CAST, Jing mini-CAST 5201D, Switzerland) was operated with propane (99.95%, Linde AG, Germany). The settings were as follows: dilution air (10 L min⁻¹), oxidation air (2.2 L min⁻¹), quenching gas (10 L min⁻¹, fixed), propane fuel (30 mL min⁻¹, fixed) (refer to Mueller et al. (2016) for further details regarding the operation of the CAST). The fuel of choice was supplied to the CAST generator using an inlet from a high-performance liquid chromatography (HPLC) pump at 50 mL min⁻¹. In the viewing window, illustrated by number 4 of Fig. 1, it could be seen that the flame changed from blue to orange once the fuel of interest was added to the propane already combusting in the CAST generator. A photograph of the CAST setup is shown in Figure S2 in the Supplementary Information.

The fuel was introduced to the CAST generator using polytetrafluoroethylene (PTFE) tubing (50 cm) and polyurethane (PU) tubing (5 cm) using a HPLC pump (Kontron, type 420, Germany) and then subsequently, copper tubing was used to connect the HPLC pump to the CAST generator. Antistatic polyurethane hose of 12.0 mm o.d. × 8.0 mm i.d. (Riegler, Germany) was used for all the connections between the CAST and various dilutors, splitters and sampling instrumentation involved in this study. The CAST generated 22 L min⁻¹ of undiluted combustion exhaust. From the CAST generator, an exhaust outlet, shown by number 6 in Fig. 1, allowed for the undiluted excess exhaust emissions to be released whilst continuously sampling 0.3 L min⁻¹ of this exhaust over the course of the 10 min sampling period for analysis by a flame ionisation detector (FID) (SK-Electronik, GMBH), calibrated with propane (30 ppm) in nitrogen (Linde, Germany), and a Fourier-transform infrared spectroscopy (FT-IR) Gas Analyser (Gasmeter, Model: DX4000, Finland). The FID sampled the undiluted CAST exhaust using a 380 °C heated transfer line. Thereafter, 0.3 L min⁻¹ (1.5 L min⁻¹ for GTL and RME) of the undiluted CAST exhaust was introduced to a porous tube dilutor (Mikro-Glasfaser Filterelement, Type GF-12-57-80E) to which 2.7 L min⁻¹ (1.5 L min⁻¹ for GTL and RME) of dry air was added to make up a total diluted flow of 3 L min⁻¹. The ejector dilutor then drew the 3 L min⁻¹ from the porous dilutor and further diluted the CAST exhaust with laboratory air that was first cleaned by passing through Intersorb Plus (Intersurgical, Sankt Augustin, Germany) to remove CO₂, and then activated charcoal (Carl Roth, Karlsruhe, Germany) and finally through Silicagel (Azelis, Sankt Augustin, Germany) at 27 mL min⁻¹. Any overpressure which may have occurred in the ejector dilutor was released through the outlet shown as number 10 in Fig. 1.

From the ejector dilutor, a custom-built three-way Y-piece stainless steel splitter allowed for the diluted flow of the CAST exhaust to be directed to various sampling instrumentation as well as to the selected samplers. Two of the Y-piece exits lead directly to two sampling stations to which selected samplers were attached and diluted CAST exhaust was drawn through these at 500 mL min⁻¹ for 10 min by Gilian® GilAir® Plus Air Sampling Pumps (Sensidyne®, USA).

The second Y-piece was utilised for the measurement of the light absorption properties of the CAST aerosols measured online by means of an Aethalometer® (Magee Scientific, Model AE33-7, Slovenia), which had an optimised diluted flow using a PALAS® VKL 10E dilutor as the Aethalometer® typically required a dilution of 1:10 000 in order to not over saturate the instrument. From the same PALAS® VKL 10E dilutor, the diluted CAST exhaust was additionally measured by a Condensation Particle Counter (CPC, TSI, Model 3022A, USA) and an Electrostatic Classifier (TSI, Model 3082, USA)

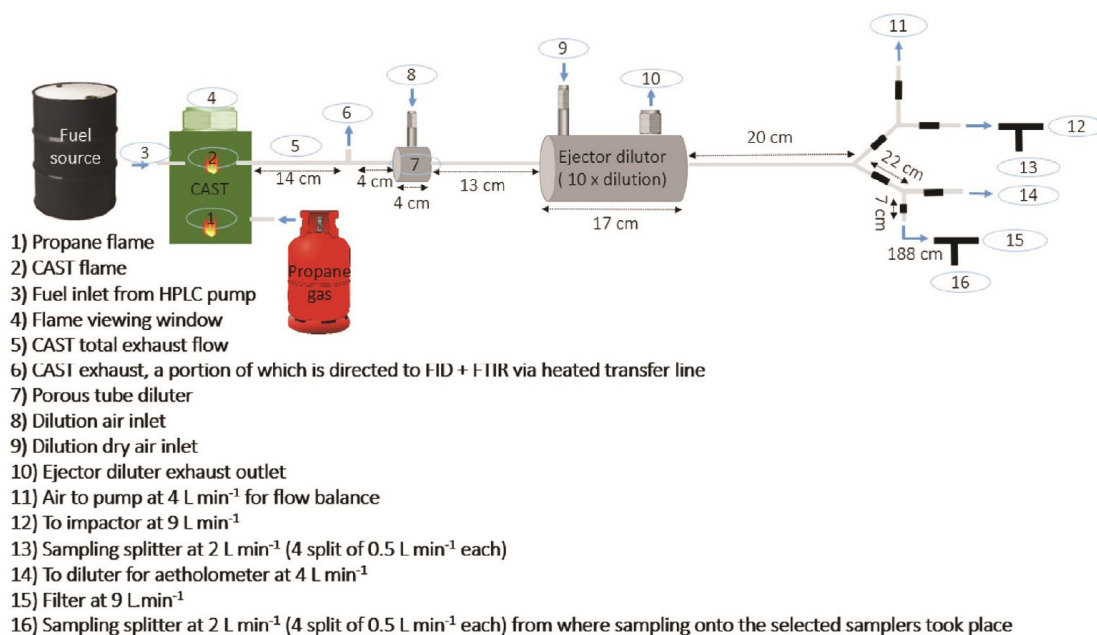


Fig. 1. Schematic diagram of the CAST generator sampling set-up.

connected to a CPC (TSI, Model 3750) in order to determine the stability of the particle number concentration produced from the CAST after changing fuel sources. The particulate matter (PM) measurements were conducted in order to check the stability of the emissions and suitability of the dilution ratios of the different fuels. The combustion of diesel (B0) resulted in higher PM emissions than the other fuels, therefore the emissions required different dilutions for gas phase sampling. The fuel of interest was thus combusted in the CAST generator and the exhaust thereof passed through a porous tube diluter and an ejector diluter, in which the dilution flows were adjusted to dilute diesel (B0) emissions by a factor of 100 and to dilute the GTL and RME emissions by a factor of 20.

2.4. Sample collection and extraction

Prior to introducing a new fuel into the CAST generator, the system was cleaned with cotton swabs, Kimtech wipes and a vacuum cleaner. Once cleaned, the selected degassed fuel was introduced into the CAST generator using the HPLC pump and the combustion emissions were monitored by the particle counter and the aethalometer to ensure that the CAST generator was stable and producing a consistent concentration of aerosols. A stainless-steel filter holder assembly was positioned between an empty glass tube upstream and the selected sorbent sampler downstream. The filter holder contained a 13 mm quartz-microfibre disc (Ahlstrom Munksjö, T 293) with a precipitation area diameter of 10 mm. Each sampler was connected to a Gilian® GilAir® Plus Air Sampling Pump (Sensidyne®, USA) using Teflon tubing (Fig. 2), which was operated at 500 mL min⁻¹ for 10 min. A photograph of the set-up is shown in Figure S3 in the Supplementary Information.

These sampling pumps were all calibrated for each specific sampler used prior to sampling by means of a Gilibrator 2® (Sensidyne®, USA). This accounted for the individual differing back pressures of the different sampler types. A Kestrel 4500 weather station (Envirocon, South Africa) was used to measure the ambient conditions at the time of the sampling event which are shown in Table S2 of the Supplementary Information. After sampling, PDMS and GW samplers were end-capped and were subsequently wrapped in aluminium foil, sealed in zip lock polyethylene bags and were stored in a freezer at -18 °C until analysis took place within 72 h.

The charcoal tubes were opened with an adjustable ORBO™ Tube Cutter after the sampling event, and the charcoal was emptied into 20 mL amber vials. 3 mL of CS₂ was added, the vials were then sealed and allowed to extract for 12 h in a fume hood at room temperature. Although accredited methods such as the ISO 9487: 1991 (E) state that 500 µL of solvent be used in the extraction of analytes from activated charcoal sorbents, it was found that 3 mL of solvent was required to completely submerge the activated charcoal. After overnight extraction, the extract, with the activated charcoal still in contact with the solvent, was sonicated (Allpax Palsonic, Germany) for 15 min. The supernatant extract was subsequently transferred into a 5 mL amber GC vial and stored in a freezer at -18 °C until batch-wise analysis was conducted within 72 h.

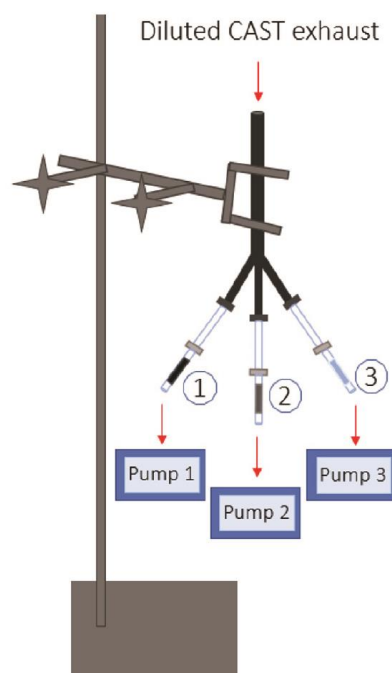


Fig. 2. Schematic of the sampler setup where numbers ①, ② and ③ illustrate the positions of the activated charcoal, GW and PDMS samplers, respectively, during CAST sampling events.

2.5. GC-MS analysis

The PDMS and GW samplers were thermally desorbed using a Thermal Desorption System (TD-20, Shimadzu, Japan) using 60 mL min^{-1} helium from $80 \text{ }^{\circ}\text{C}$ to $250 \text{ }^{\circ}\text{C}$ for the PDMS and to $280 \text{ }^{\circ}\text{C}$ for the GW sampler, both with a hold time of 30 min. The cooled injection system (CIS) method started at $5 \text{ }^{\circ}\text{C}$ and ended at $330 \text{ }^{\circ}\text{C}$ with a hold time of 30 min. A GC-2010 Plus was coupled to a MS-QP2010 Ultra (both Shimadzu, Japan) and helium was used as carrier gas at a flow rate of 1.6 mL min^{-1} . A split ratio of 10:1 was applied whilst the column used was a VF-XMS $30 \text{ m} \times 0.25 \text{ mm i.d.} \times 0.25 \text{ }\mu\text{m d.f.}$ column (Agilent, Netherlands). The GC oven method started with a hold time of 6 min at $60 \text{ }^{\circ}\text{C}$ and was ramped to $250 \text{ }^{\circ}\text{C}$ at $5 \text{ }^{\circ}\text{C min}^{-1}$. The transfer line temperature was set to $250 \text{ }^{\circ}\text{C}$. The mass spectrometry method was set to scan from m/z 35 to m/z 500 with an electron ionisation energy of 70 eV and an ion source temperature of $230 \text{ }^{\circ}\text{C}$.

The charcoal extracts were injected by a $1 \text{ }\mu\text{L}$ hot injection at $280 \text{ }^{\circ}\text{C}$. Helium was used as the carrier gas with a flow rate of 1.5 mL min^{-1} . A split ratio of 1:1 was applied and a SGE BX5 $25 \text{ m} \times 0.22 \text{ mm i.d.} \times 0.25 \text{ }\mu\text{m d.f.}$ column was used. The oven started with a hold time of 1 min at $40 \text{ }^{\circ}\text{C}$ and was ramped to $250 \text{ }^{\circ}\text{C}$ at $5 \text{ }^{\circ}\text{C min}^{-1}$ and then held for 2 min. The transfer line temperature was set to $270 \text{ }^{\circ}\text{C}$. The mass spectrometry method was the same as for the PDMS and GW sampler analysis.

3. Results and discussion

3.1. FID/FTIR analyses

Since this study occurred over a period of three days, it was of interest to investigate the inter-day CAST generator combustion and emission stability using the flame ionisation detector (FID) and Fourier-transform infrared spectroscopy (FTIR) over the sampling period to determine the reliability of the CAST system for organic gas phase emission sampling. In order to do this, the sampling of the emissions from the CAST generator started with the diesel (B0) fuel type, which was used as a basis for comparison of the other two fuels tested, as petroleum-derived diesel is widely used throughout the world. The experiments then continued onto the gas-to-liquid (GTL) and rapeseed oil methyl ester (RME) fuel types, respectively, and ended with sampling the B0 fuel type as a bracket test to gauge the reproducibility of the CAST emissions between the duplicate measurements sampled over the course of the days over which the sampling took place. In Table 1, each fuel type is allocated numbers 1–4, where 1 and 2 designate the duplicate measurements of the first round of sampling the emissions from each fuel, which were carried out directly after each other, whereas numbers 3 and 4 relate to the duplicate measurements of the second sampling event of the same fuel which were carried out sequentially on a different day.

Table 1
Mean FID results for the sampling events of the undiluted fuel emissions over each 10 min sampling period.

| Sampling event | FID (ppm) | | |
|----------------|-----------|------|------|
| | B0 | GTL | RME |
| 1 | 8.87 | 7.33 | 5.60 |
| 2 | 8.75 | 7.27 | 5.57 |
| 3 | 7.63 | 7.09 | 5.30 |
| 4 | 7.60 | 7.05 | 5.49 |
| Mean | 8.21 | 7.19 | 5.49 |
| SD | 0.69 | 0.14 | 0.13 |
| %RSD | 8.42 | 1.89 | 2.46 |

As can be seen from Table 1, the response of the FID showed higher gas phase organic emissions from each fuel type during the first sampling event as compared to the second sampling event. Although the duplicate sampling events for each fuel type were carried out on different days, no rinsing occurred for intra-fuel sampling events of the GTL and RME fuel types. This could have in turn contributed to the smaller FID measurement difference (i.e. lower %RSD) in the combustion fuel emissions of these fuel types, measured between the duplicate fuel measurements, as compared to B0 which was sampled as a bracket test. Nevertheless, the fuel combustion emissions recorded by the FID, for all of the fuel types, showed that the combustion emissions were significantly different between days, using a statistical t-test at a 95% confidence level. This implies that it is preferable to conduct all tests of a particular fuel type sequentially on one day when using the CAST system, in order to reduce these uncertainties. During the sampling events of each fuel type, additional measurements were taken of the H₂O, CO₂, O₂ percentage and amount of CO (ppm) contained within the combustion emissions from the CAST exhaust. These values were found to not differ significantly during the sampling period (Table S3 in the Supplementary Information).

In order to compare the performance of the samplers, the results from the second sampling events of the B0 and GTL combustion were used, i.e. B0 and GTL 3 and 4 in Table 1, as these results proved to be more reliable from the FID measurements; in that lower %RSDs were recorded. Additionally, it was found that the first round of sampling of the B0 and GTL yielded concentrations that were significantly larger with greater variation than in the second round of sampling as shown in Figure S4 of the Supplementary Information. Since the RME fuel did not contain additives i.e. stabilisers, polymerisation of the combustion products occurred around the flame tip during the second sampling event causing a partial blockage with related potential inconsistencies in results, therefore the duplicates from the first sampling event for that fuel type, i.e. RME 1 and 2 in Table 1, were used for the comparison of the samplers and fuel types.

3.2. Comparison of the compounds detected on each sampler type

The highest number of target analytes were detected from the emissions of diesel (B0), where thermal desorption of the PDMS sampler resulted in the detection of 33 target analytes, whilst 34 were detected upon analysis of the GW sampler. Analysis of the charcoal sampler extracts resulted in the detection of only two of the 36 target analytes in all fuel types sampled; namely benzene and toluene, of which only benzene was above the limit of quantification (LOQ). The low number of analytes detected was likely due to the dilution volume. After analysis of a blank extraction of the activated charcoal sorbent, it was evident that the detected analytes were from the sorbent itself, which contained particularly high levels of benzene. The blank analysis data of the three samplers is shown in Table S4 in the Supplementary Information. Therefore, the comparison of the concentrations of benzene and toluene emitted upon combustion of different fuels is based only on the analysis of the PDMS and GW samplers (as shown in Fig. 3 and detailed in Section 3.4).

There are a number of factors contributing to the lack of analytes detected upon analysis of the activated charcoal sampler extracts as compared to the number of compounds detected upon analysis of the PDMS and GW samplers, as shown in Fig. 3 (also refer to Tables S5 and S6). Firstly, the volume of solvent experimentally determined to be required (3 mL) for the extraction of the activated charcoal may have diluted the sampled analytes to below the limit of detection (LOD) of the analytical method. The charcoal sampler was preliminarily calibrated for only 8 of the 36 target analytes. Further calibration of the remaining 28 target analytes did not occur as no other target compounds other than benzene and toluene were detected upon analysis of the activated charcoal extracts. The LODs for the activated charcoal sampler were calculated to range from 0.48 $\mu\text{g m}^{-3}$ for naphthalene to 2.26 $\mu\text{g m}^{-3}$ for m-xylene (Tables S7a and S7b). Comparatively, the LODs for PDMS ranged from 0.0001 $\mu\text{g m}^{-3}$ for 1,2-dimethylnaphthalene to 0.80 $\mu\text{g m}^{-3}$ for n-octane, whilst the LODs for GW ranged from 0.002 $\mu\text{g m}^{-3}$ for toluene to 0.79 $\mu\text{g m}^{-3}$ for n-octane and n-nonane.

Another reason why the analysis of the activated charcoal extracts could have resulted in the detection of so few compounds is that the activated charcoal may have bound the analytes in an irreversible manner and this, in combination with the low gas phase analyte concentrations which the CAST system produces, could have resulted in the analytes not being detected. The lack of analytes detected occurred even though the activated charcoal was left in CS₂ for 10 h as compared to the recommended extraction time of 30 min (ISO 9487:1991 (E)).

Table 2

The relative advantages and disadvantages of GW, PDMS and charcoal samplers for the sampling of the selected VOCs, PAHs and n-alkanes at trace levels.

| | GW sampler | PDMS sampler | Activated charcoal sampler |
|---------------|--|--|--|
| Advantages | Low background noise | | |
| | Can be reused | Can be reused | Reasonable cost (€3.26 per sampler) |
| | On average, the lowest standard deviation in recorded duplicate measurements | | |
| | Largest number of compounds detected | A large number of compounds detected | |
| | Similar analysis time to PDMS | Similar analysis time to GW | |
| | Can be thermally desorbed therefore requires no solvents in preparation for analysis | Can be thermally desorbed therefore requires no solvents in preparation for analysis | Does not require a lab equipped with a TD system |
| Disadvantages | | Sorbent background (due to siloxanes) | Sorbent background (for toluene and benzene) |
| | Reasonably costly (€6.88 per sampler) | Most costly (€7.55 per sampler) | Single use |
| | Lower concentrations of several target analytes reported as compared to PDMS | Larger standard deviation in recorded duplicate measurements as compared to the GW sampler, especially for the n-alkanes | Largest standard deviation in recorded duplicate measurements of benzene |
| | Requires a lab equipped with thermal desorption system | Requires a lab equipped with a thermal desorption system | Lowest number of compounds detected |
| | | | Long extraction time |
| | | | Incomplete analyte recovery |
| | | | Toxicity of solvent used for extraction i.e. CS ₂ |

As can be seen from Fig. 3(c), the GW sampler was found to be more effective than PDMS in retaining the lighter n-alkanes such as n-octane and n-nonane. However, analysis of the GW sampler generally gave lower concentrations of each target analyte than the PDMS sampler (Fig. 3(a)–(c)). This may be indicative of the GW sampler having a lower breakthrough volume compared to the PDMS sampler however, the true cause is probably due to the thermal desorption parameters being optimised for the PDMS sampler and not for GW desorption. Therefore, the lower concentrations of analytes determined upon analysis of the GW samplers are most likely due to the incomplete thermal desorption of analytes from the GW sampler, which retains analytes more strongly by adsorption rather than by sorption as in the case of PDMS.

3.3. Comparison of the variability between the samplers

As previously stated, the analysis of the PDMS samplers reflected higher concentrations of the target compounds as compared to the GW samplers (Fig. 3). However, the reported concentrations from the analysis of the PDMS samplers showed larger standard deviations as compared to the GW samplers. This could be due to PDMS functioning as a sampler through the action of absorption as opposed to the GW sampler, which functions by adsorbing analytes. Additionally, the structure of the GW sorbent itself, which involves a 2D monolayered structure of one atom thickness, leads to a large number of active sites being open and available for adsorption.

The range of target analytes were dominated by non-polar compounds which would theoretically tend to interact better with the non-polar GW sorbent as compared to the less non-polar PDMS sorbent. The lower standard deviation in the concentrations reported through the analysis of the GW samplers as compared to the analysis of the PDMS samplers is particularly noticeable for the concentrations of the polycyclic aromatic hydrocarbons (PAHs) detected (Fig. 3b) but even more so for the concentrations of n-alkanes detected (Fig. 3c). Therefore, due to the lower degree of uncertainty in concentrations reported upon analysis of the GW sampler and the greater number of compounds detected by the GW sampler as compared to the other two samplers, the GW sampler proved to be the superior sampler as compared to the activated charcoal sampler and the PDMS sampler for the sampling of the selected trace level VOCs, PAHs and n-alkanes in this study. The strengths and weaknesses of the various samplers are summarised in Table 2.

3.4. Effect of the different fuels on the combustion emission profiles

Throughout the sampling period, the ambient temperature differed slightly from 26.8–27.7 °C with a standard deviation of 0.4 whilst the barometric pressure ranged from 955.5–956.2 hPa with a standard deviation of 0.2, as shown in Table S2.

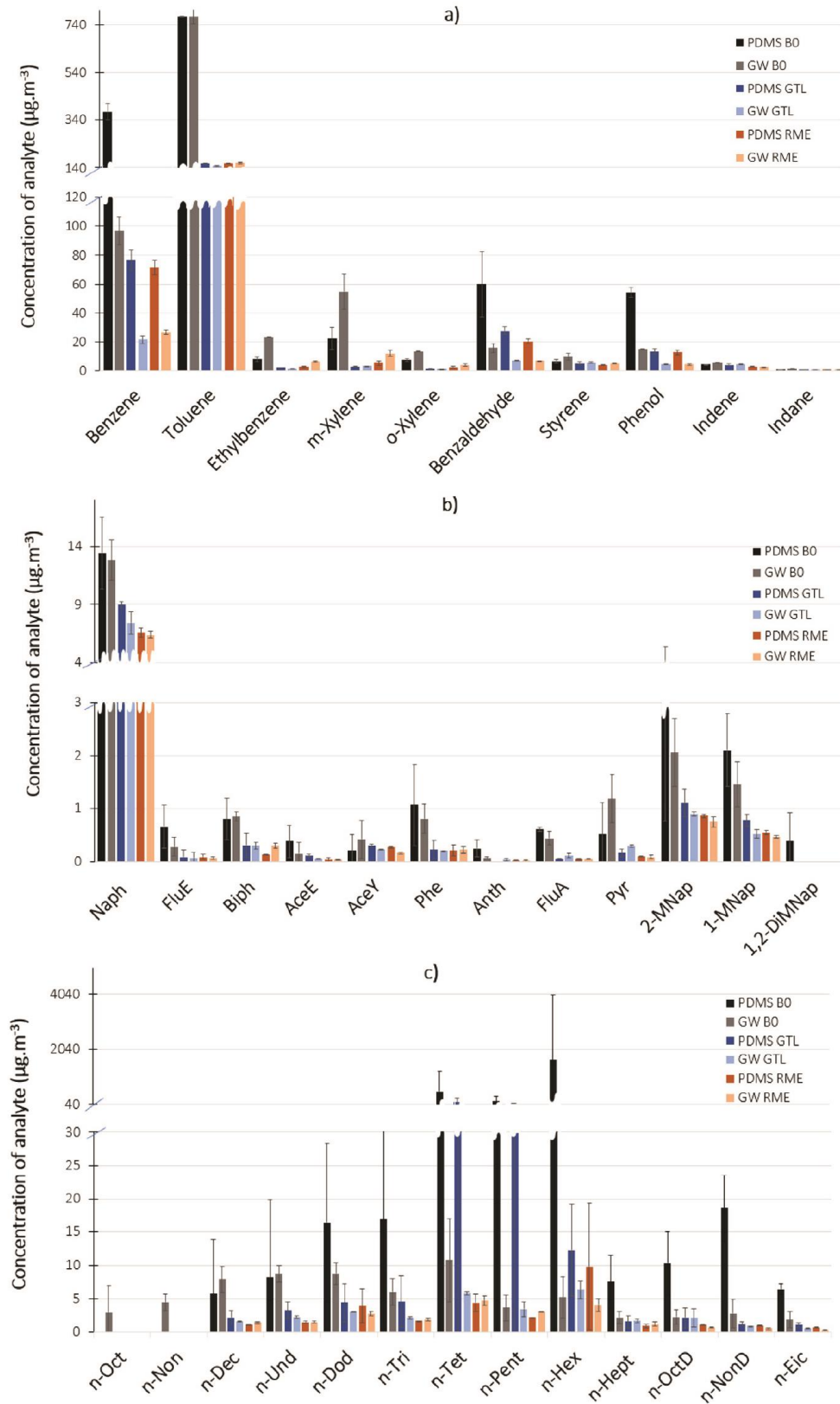


Fig. 3. Detected concentrations of (a) VOCs, (b) PAHs and (c) n-alkanes from the combustion of fuel types B0, GTL and RME sampled from the CAST generator exhaust using PDMS and GW samplers. The error bars are based on the standard deviation (SD) of duplicate measurements and abbreviations can be found listed in Tables S7a and S7b.

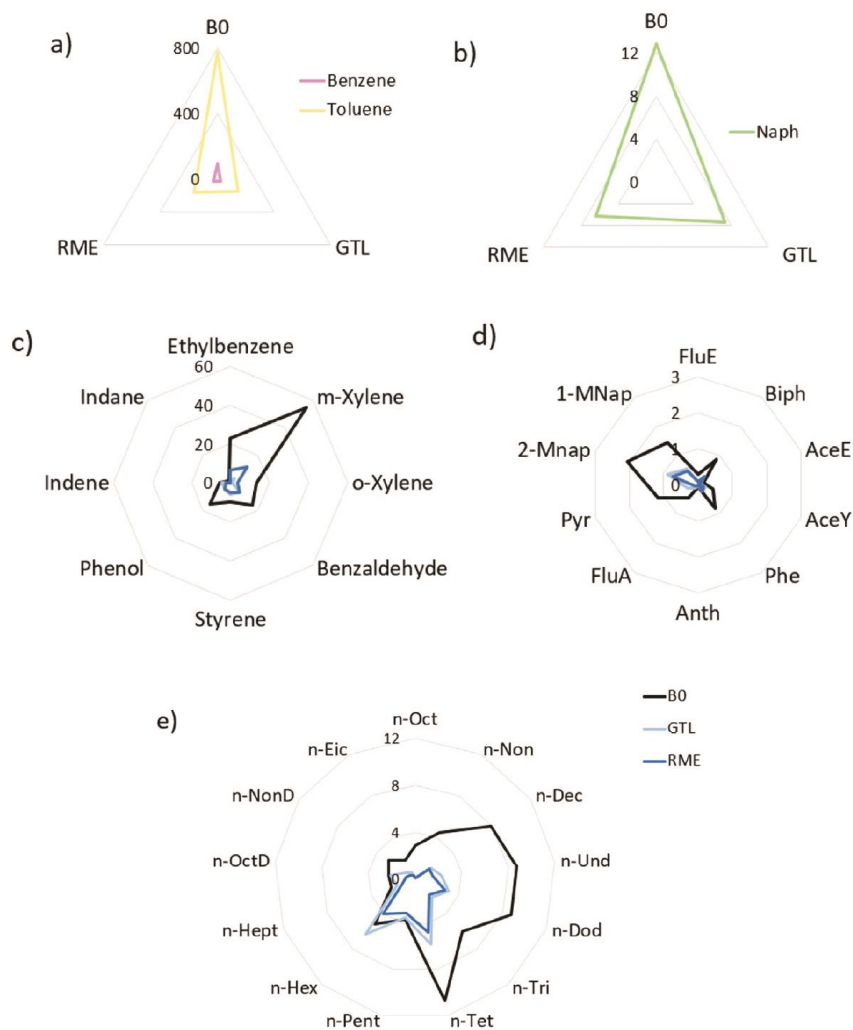


Fig. 4. Relative abundance ($\mu\text{g m}^{-3}$) of various compounds detected upon analysis of the GW sampler after sampling the gas phase emissions from B0, GTL and RME combustion: (a) benzene and toluene, (b) naphthalene, (c) VOCs, (d) PAHs and (e) n-alkanes.

This showed that the ambient conditions during sampling were fairly consistent and thereby allowed for the comparison of the fuel measurements and the CAST system over the sampling period.

Most of the CAST combustion emission compound profiles for the different fuels tested reflected a similar trend as seen in Fig. 3, when sampled by the PDMS and the GW sampler. Since it has been identified that the PDMS sampler had more variability in the resultant concentrations reported as compared to the GW sampler, the relative concentrations of target analytes within each fuel type emission profile will be discussed in terms of the results reported upon analysis of the GW samplers. Comparing the three fuel types sampled in this study, the combustion of diesel (B0) resulted in higher concentrations of target compounds in most cases, with the exception of the hexadecane in the combustion emissions of gas-to-liquid (GTL) (Fig. 4). As expected, the combustion emissions of rapeseed oil methyl ester (RME) reflected lower concentrations of targeted VOCs and SVOCs as compared to diesel and GTL, with the exception of ethylbenzene and the xylene isomers in the case of GTL (Fig. 4c).

These reported results align with the visual analysis of the filter papers which were placed upstream of the samplers. It can be seen in Fig. 5 that the PM filter from B0 combustion is considerably darker than the filters relating to GTL and RME combustion. The same trend was also observed in the duplicate sampling events conducted with B0 and GTL and RME.

The percent carbon content and total unburned hydrocarbons (THCs) are typically reported in the literature to be the largest in diesel whilst GTL tends to have less, and biodiesels, such as RME, have been reported to have the lowest concentrations (Dagaut et al., 2019; Soriano et al., 2018; Damanik et al., 2018). The measurements are done on %w/w of the fuel before combustion or the measurements of the target molecules are accomplished through the analysis of the PM phase formed after the combustion of the fuel. The compounds present in the different fuels and the relative



Fig. 5. PM filtered from (a) B0, (b) GTL and (c) RME CAST emissions prior to gas phase sampling.

abundancies in terms of engine emissions are also reported. It is important to note that the CAST generator pyrolyses the fuel by means of a diffusion flame therefore the combustion conditions and consequently the emissions, would differ to real-world engine emission scenarios making direct comparisons to other studies difficult.

Furthermore, compounds present in various fuel sources are often reported in terms of total carbon (TC); which is the summation of elemental carbon (EC) and organic carbon (OC) fractions with little detail regarding which specific compounds are present in the OC fraction (Zhou et al., 2019; Atiku et al., 2016; Nyström et al., 2016; Shen et al., 2013). In terms of bettering the fuel source for many forms of machinery in order to reduce emissions which are potentially hazardous to human health, it will be important to determine emission profiles of fuels not only in terms of the particulate matter generated, but also specifically which volatile and semi-volatile organic compounds are being released into the atmosphere, as these can also be detrimental to the environment and to human health, even though they may not be visible.

4. Conclusions

In this study it was found that the commercial activated charcoal sampler was not effective in sampling the trace levels of target analytes produced upon combustion of the fuels tested by the CAST. This could be due to the sample being too dilute and below the LOD due to the volume of the extraction solvent required, as well as the low levels of gas phase VOCs and SVOCs produced by the CAST system, and the small sample volume. In addition to the target analytes being below the LOD for the activated charcoal extracts, the activated charcoal sampler may have irreversibly adsorbed the target analytes. It is also noted that the extraction method for the activated charcoal sampler is time consuming and requires a toxic solvent, and high background concentrations were found for some target analytes. The activated charcoal sampler proved to be the cheapest however, with a once-off use, whilst the PDMS and GW have the advantage of being able to be reconditioned and reused.

The results of the PDMS sampler analysis reflected relatively higher concentrations of the VOC and SVOCs target analytes detected to that of the GW sampler. However, the results from the PDMS sampler analysis also showed a higher variability in the duplicate concentrations reported, particularly for the n-alkanes. The analysis of the GW sampler showed that target analytes were determined with lower uncertainties than with the PDMS sampler and lighter n-alkanes, such as octane and nonane, were detected with the GW sampler but not with the other two samplers. However, the analysis of the GW samplers did reflect lower concentrations of all target analytes sampled as compared to the concentrations reflected by the PDMS sampler. This could indicate that the GW has a lower breakthrough volume than the PDMS sampler or, most likely, that the TD parameters were optimal for the PDMS but resulted in incomplete desorption from the GW sorbent which therefore requires further optimisation such as a higher desorption temperature. Overall, the GW sampler has proven to be superior, as compared to the activated carbon as well as the PDMS sampler in the sampling of the selected trace levels of VOCs, PAHs and n-alkanes in this study. In terms of fuel comparisons, diesel (B0) produced the highest concentration of VOCs and SVOCs upon combustion in the CAST, as compared to rapeseed oil methyl ester (RME) and gas-to-liquid (GTL) fuels.

Regarding the CAST generator itself, it is suggested that one fuel type is used and sampled over a continuous period to definitively establish the reproducibility of the CAST, as significant variation was observed when sampling the fuel emissions on different days, although this variability was compounded by the low levels of target analytes produced by the CAST system. In future comparisons, the final extract volume for the charcoal sampler should be reduced to improve detection limits, especially in light of the low emission levels from the CAST system. It may also be of use to analyse the various fuel types before combustion to determine the aromatic content thereof and compare these to the combustion profiles reported in this study, as well as to compare the samplers using another combustion source which generates higher levels of target VOCs and SVOCs.

CRedit authorship contribution statement

Yvonne C. Mason: Investigation, Formal analysis, Writing - original draft. **Genna-Leigh Schoonraad:** Conceptualization, Investigation. **Jürgen Orasche:** Methodology, Investigation, Formal analysis, Project administration, Writing - review &

editing. **Christoph Bisig:** Methodology, Investigation, Writing - review & editing. **Gert Jakobi:** Methodology, Investigation. **Ralf Zimmermann:** Conceptualization, Resources, Funding acquisition. **Patricia B.C. Forbes:** Conceptualization, Methodology, Investigation, Formal analysis, Writing - review & editing, Supervision, Project administration, Resources, Funding acquisition.

Declaration of competing interest

The authors declare that they have no known competing financial interests or personal relationships that could have appeared to influence the work reported in this paper.

Acknowledgments

Thanks is extended to the Comprehensive Molecular Analytics (CMA) group at Helmholtz Zentrum München for assisting in the sampling campaign as well as the Department of Physics at the University of Pretoria for CVD use. Christoph Bisig would like to acknowledge the support of the Swiss National Science Foundation (grant number P2FRP3_178112). We also thank ASG Analytik-Service for providing the fuels for this campaign.

Funding

Funding provided by the University of Pretoria and the National Research Foundation of South Africa (NRF, grant number 105807) is acknowledged. This work was supported by the German Federal Ministry of Education and Research (BMBF), research contract 01DG17023.

Appendix A. Supplementary data

Supplementary material related to this article can be found online at <https://doi.org/10.1016/j.eti.2020.100945>.

References

- Atiku, F.A., Mitchell, E.J.S., Lea-Langton, A.R., Jones, J.M., Williams, A., Bartle, K.D., 2016. The impact of fuel properties on the composition of soot produced by the combustion of residential solid fuels in a domestic stove. *Fuel Process. Technol.* 151, 117–125. <http://dx.doi.org/10.1016/j.fuproc.2016.05.032>.
- Bae, S., Hong, Y.-C., 2018. Health effects of particulate matter. *J. Korean Med. Assoc.* 61 (12), 749–755. <http://dx.doi.org/10.5124/jkma.2018.61.12.749>.
- Bernstein, J.A., Alexis, N., Barnes, C., Bernstein, I.L., Nel, A., Peden, D., Diaz-Sanchez, D., Tarlo, S.M., Williams, P.B., 2004. Health effects of air pollution. *J. Allergy Clin. Immunol.* 114 (5), 1116–1123. <http://dx.doi.org/10.1016/j.jaci.2004.08.030>.
- Borillo, G.C., Tadano, Y.S., Godoi, A.F.L., Pauliquevis, T., Sarmiento, H., Rempel, D., Yamamoto, C.I., Marchi, M.R.R., Potgieter-Vermaak, s., Godoi, R.H.M., 2018. Polycyclic aromatic hydrocarbons (PAHs) and nitrated analogs associated to particulate matter emission from a Euro V-SCR engine fuelled with diesel/biodiesel blends. *Sci. Total Environ.* 644, 675–682. <http://dx.doi.org/10.1016/j.scitotenv.2018.07.007>.
- Chen, H., Kwong, J.C., Copes, R., Hystad, P., van Donkelaar, A., Tu, K., Brook, J.R., Goldberg, M.S., Martin, R.V., Murray, B.J., Wilton, A., Kopp, A., Burnett, R.T., 2017. Exposure to ambient air pollution and the incidence of dementia: a population-based cohort study. *Environ. Int.* 108, 271–277. <http://dx.doi.org/10.1016/j.envint.2017.08.020>.
- Dagaut, P., Bedjanian, Y., Dayma, G., Foucher, F., Gosselin, B., Romanias, M., Shahla, R., 2019. Emission of carbonyl and polyaromatic hydrocarbon pollutants from the combustion of liquid fuels: impact of biofuel blending. *J. Eng. Gas Turbines Power* 141 (3), 1–8. <http://dx.doi.org/10.1115/1.511136>.
- Damanik, N., Ong, H.C., Tong, C.W., Mahlia, T.M.I., Silitonga, A.S., 2018. A review on the engine performance and exhaust emission characteristics of diesel engines fueled with biodiesel blends. *Environ. Sci. Pollut. Res.* 25 (16), 15307–15325. <http://dx.doi.org/10.1007/s11356-018-2098-8>.
- Finlayson-Pitts, B.J., Pitts, J.N., 1997. Tropospheric air pollution: ozone, airborne toxics, polycyclic aromatic hydrocarbons, and particles. *Science* 276 (5315), 1045–1051. <http://dx.doi.org/10.1126/science.276.5315.1045>.
- Finlayson-Pitts, B.J., Pitts Jr, J.N., 1999. *Chemistry of the Upper and Lower Atmosphere: Theory, Experiments, and Applications*. Elsevier.
- Forbes, P.B.C., Rohwer, E.R., 2009. Investigations into a novel method for atmospheric polycyclic aromatic hydrocarbon monitoring. *Environ. Pollut.* 157 (8–9), 2529–2535. <http://dx.doi.org/10.1016/j.envpol.2009.03.004>.
- Gautam, S., Patra, A.K., Sahu, S.P., Hitch, M., 2018. Particulate matter pollution in opencast coal mining areas: a threat to human health and environment. *Int. J. Min. Reclam. Environ.* 32 (2), 75–92. <http://dx.doi.org/10.1080/17480930.2016.1218110>.
- Goldemberg, J., Martinez-Gomez, J., Sagar, A., Smith, K.R., 2018. Household air pollution, health, and climate change: cleaning the air. *Environ. Res. Lett.* 13 (3), 030201. <http://dx.doi.org/10.1088/1748-9326/aaa49d>.
- He, B.-Q., 2016. Advances in emission characteristics of diesel engines using different biodiesel fuels. *Renew. Sustain. Energy Rev.* 60, 570–586. <http://dx.doi.org/10.1016/j.rser.2016.01.093>.
- Helen, G.S., Liakoni, E., Nardone, N., Addo, N., Jacob, P., Benowitz, N.L., 2019. Comparison of systemic exposure to toxic and/or carcinogenic volatile organic compounds (VOCs) during vaping, smoking, and abstinence. *Cancer Prev. Res.* <http://dx.doi.org/10.1158/1940-6207.CAPR-19-0356>.
- Hemminki, K., Pershagen, G., 1994. Cancer risk of air pollution: epidemiological evidence. *Environ. Health Perspect.* 102 (4), 187–192. <http://dx.doi.org/10.1289/ehp.94102s4187>.
- Hime, N.J., Marks, G.B., Cowie, C.T., 2018. A comparison of the health effects of ambient particulate matter air pollution from five emission sources. *Int. J. Environ. Res. Public Health* 15 (6), 1206. <http://dx.doi.org/10.3390/ijerph15061206>.
- International Organization for Standardization, 1991. *Workplace air – determination of vaporous aromatic hydrocarbons – charcoal tube/solvent desorption/gas chromatographic method*. ISO 9487:1991 (E).
- International Organization for Standardization, 2001. *Workplace air quality – sampling and analysis of volatile organic compounds by solvent desorption/gas chromatography – Part 1: pumped sampling method*. ISO 16200-1:2001 (E).
- Jia, C., Batterman, S., Godwin, C., 2008. VOCs in industrial, urban and suburban neighborhoods—Part 2: Factors affecting indoor and outdoor concentrations. *Atmos. Environ.* 42 (9), 2101–2116. <http://dx.doi.org/10.1016/j.atmosenv.2007.11.047>.

- Kasper, M., 2009. CAST - Combustion aerosol standard: Principle and new applications. [Online] Available at: <http://www.sootgenerator.com/documents/Kasper.pdf>.
- Kawamura, K., Ishiyama, M., Nagatani, N., Hashiba, T., Tamiya, E., 2006. Development of a novel hand-held toluene gas sensor: Possible use in the prevention and control of sick building syndrome. *Measurement* 39 (6), 490–496. <http://dx.doi.org/10.1016/j.measurement.2005.12.014>.
- Knothe, G., Razon, L.F., 2017. Biodiesel fuels. *Prog. Energy Combust. Sci.* 58, 36–59. <http://dx.doi.org/10.1016/j.pecs.2016.08.001>.
- Künzli, N., Jerrett, M., Mack, W.J., Beckerman, B., LaBree, L., Gilliland, F., Thomas, D., Peters, J., Hodis, H.N., 2005. Ambient air pollution and atherosclerosis in Los Angeles. *Environ. Health Perspect.* 113 (2), 201–206. <http://dx.doi.org/10.1289/ehp.7523>.
- Landrigan, P.J., Fuller, R., Fisher, S., Suk, W.A., Sly, P., Chiles, T.C., Bose-O'Reilly, S., 2019. Pollution and children's health. *Sci. Total Environ.* 650, 2389–2394. <http://dx.doi.org/10.1016/j.scitotenv.2018.09.375>.
- Lerner, J.E.C., de los Angeles Gutierrez, M., Mellado, D., Giuliani, D., Massolo, L., Sanchez, E.Y., Porta, A., 2018. Characterization and cancer risk assessment of VOCs in home and school environments in gran La Plata, Argentina. *Environ. Sci. Pollut. Res.* 25 (10), 10039–10048. <http://dx.doi.org/10.1007/s11335>.
- Methods for the Determination of Hazardous Substances, 2000. *Volatile Organic Compounds in Air* (4). Laboratory method using pumped solid sorbent tubes, solvent desorption and gas chromatography. MDHS 96.
- Mirzaei, A., Leonardi, S.G., Neri, G., 2016. Detection of hazardous volatile organic compounds (VOCs) by metal oxide nanostructures-based gas sensors: A review. *Ceram. Int.* 42 (14), 15119–15141. <http://dx.doi.org/10.1016/j.ceramint.2016.06.145>.
- Moore, R.H., Ziemba, L.D., Dutcher, D., Beyersdorf, A.J., Chan, K., Crumeyrolle, S., Raymond, T.M., Thornhill, K.L., Winstead, E.L., Anderson, B.E., 2014. Mapping the operation of the miniature combustion aerosol standard (Mini-CAST) soot generator. *Aerosol Sci. Technol.* 48 (5), 467–479. <http://dx.doi.org/10.1080/02786826.2014.890694>.
- Mueller, L., Jakobi, G., Orasche, J., Karg, E., Sklorz, M., Abbaszade, G., Weggler, B., Jing, L., Schnelle-Kreis, J., Zimmermann, R., 2015. Online determination of polycyclic aromatic hydrocarbon formation from a flame soot generator. *Anal. Bioanal. Chem.* 407 (20), 5911–5922. <http://dx.doi.org/10.1007/s0021>.
- Mueller, L., Schnelle-Kreis, J., Jakobi, G., Orasche, J., Jing, L., Canonaco, F., Prevot, A.S.H., Zimmermann, R., 2016. Combustion process apportionment of carbonaceous particulate emission from a diesel fuel burner. *J. Aerosol Sci.* 100, 61–72. <http://dx.doi.org/10.1016/j.jaerosci.2016.06.003>.
- Munyeza, C.F., Dikale, O., Rohwer, E.R., Forbes, P.B.C., 2018. Development and optimization of a plunger assisted solvent extraction method for polycyclic aromatic hydrocarbons sampled onto multi-channel silicone rubber traps. *J. Chromatogr. A* 1555, 20–29. <http://dx.doi.org/10.1016/j.chroma.2018.04.053>.
- Nyström, R., Sadiktsis, I., Ahmed, T.M., Westerholm, R., Koegler, J.H., Blomberg, A., Sandström, T., Boman, C., 2016. Physical and chemical properties of RME biodiesel exhaust particles without engine modifications. *Fuel* 186, 261–269. <http://dx.doi.org/10.1016/j.fuel.2016.08.062>.
- Ortner, E.K., Rohwer, E.R., 1996. Trace analysis of semi-volatile organic air pollutants using thick film silicone rubber traps with capillary gas chromatography. *J. High Resolut. Chromatogr.* 19 (6), 339–344. <http://dx.doi.org/10.1002/jhrc.1240190607>.
- Peters, A., Döring, A., Wichmann, H.-E., Koenig, W., 1997. Increased plasma viscosity during an air pollution episode: a link to mortality? *Lancet* 349 (9065), 1582–1587. [http://dx.doi.org/10.1016/S0140-6736\(97\)01211-7](http://dx.doi.org/10.1016/S0140-6736(97)01211-7).
- Points, J., 2019. Global VOC standards to address a volatile global problem: Dr. Ehrenstrofer.
- Raza, N., Hashemi, B., Kim, K.-H., Lee, S.-H., Deep, A., 2018. Aromatic hydrocarbons in air, water, and soil: Sampling and pretreatment techniques. *TRAC Trends Anal. Chem.* 103, 56–73. <http://dx.doi.org/10.1016/j.trac.2018.03.012>.
- Schoonraad, G.-L., Forbes, P.B.C., 2019a. System and method for manufacturing graphene wool, SA provisional patent application 2019/00675. filed on 1 February 2019.
- Schoonraad, G.-L., Forbes, P.B.C., 2019b. Air pollutant trap, SA provisional patent application 2019/00674. filed on 1 February 2019.
- Schoonraad, G.-L., Madito, M.J., Manyala, N., Forbes, P.B.C., 2020. Synthesis and optimisation of a novel graphene wool material by atmospheric pressure chemical vapour deposition. *J. Mater. Sci.* 55, 545–564. <http://dx.doi.org/10.1007/s10853-019-03948-0>.
- Shen, G., Xue, M., Wei, S., Chen, Y., Zhao, Q., Li, B., Wu, H., Tao, S., 2013. Influence of fuel moisture, charge size, feeding rate and air ventilation conditions on the emissions of PM, OC, EC, parent PAHs, and their derivatives from residential wood combustion. *J. Environ. Sci.* 25 (9), 1808–1816. [http://dx.doi.org/10.1016/S1001-0742\(12\)60258-7](http://dx.doi.org/10.1016/S1001-0742(12)60258-7).
- Soriano, J.A., García-Contreras, R., Leiva-Candia, D., Soto, F., 2018. Influence on performance and emissions of an automotive diesel engine fueled with biodiesel and paraffinic fuels: GTL and biojet fuel farnesane. *Energy Fuels* 32 (4), 5125–5133. <http://dx.doi.org/10.1021/acs.energyfuels.7b03779>.
- United States Environmental Protection Agency, 1999. Compendium method TO-17 determination of volatile organic compounds in ambient air using active sampling onto sorbent tubes. [Online] Available at: <https://www3.epa.gov/ttnamti1/files/ambient/airtox/to-17r.pdf>.
- Yan, B., Liu, S., Zhao, B., Li, X., Fu, Q., Jiang, G., 2018. China's fight for clean air and human health. *Environ. Sci. Technol.* 52, 8063–8064. <http://dx.doi.org/10.1021/acs.est.8b03137>.
- Yu, C.W.F., Kim, J.T., 2010. Building pathology, investigation of sick buildings—VOC emissions. *Indoor Built Environ.* 19 (1), 30–39. <http://dx.doi.org/10.1177/1420326X09358799>.
- Zhou, S., Zhou, J., Zhu, Y., 2019. Chemical composition and size distribution of particulate matters from marine diesel engines with different fuel oils. *Fuel* 235, 972–983. <http://dx.doi.org/10.1016/j.fuel.2018.08.080>.
- Züttel, A., Sudan, P., Mauron, P., Wenger, P., 2004. Model for the hydrogen adsorption on carbon nanostructures. *Appl. Phys. A* 78 (7), 941–946. <http://dx.doi.org/10.1007/s00339-003-2412-1>.

Paper 6: Supplementary Information



Figure S1: Graphene wool sampler showing the GW of 60 mm bed length housed in a glass tube with glass end caps held in place by Teflon sleeves. Source: Adapted from (Schoonraad and Forbes, 2019b).



Figure S2: Photograph of the CAST generator sampling set-up.

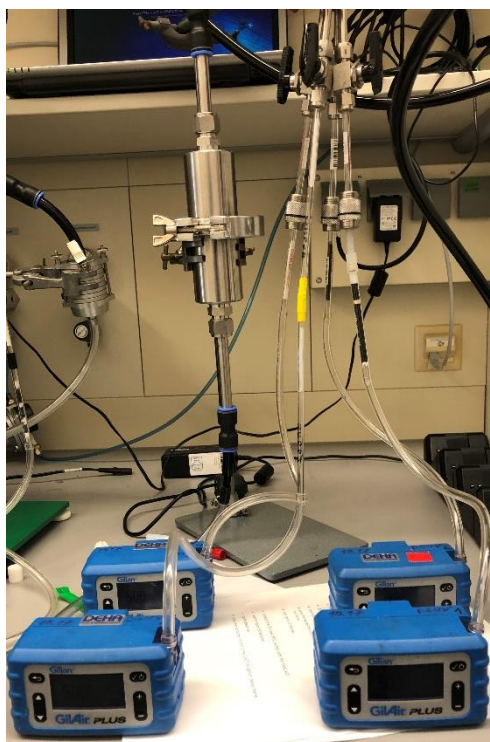


Figure S3: Photograph of the sampler setup for the activated charcoal, GW and PDMS samplers, respectively, during CAST sampling events. Note: The fourth sampling point was for another experiment and is not reported on here.

Table S1: Standards and internal standards used in this study.

| Standard | Supplier |
|---------------------------------|---------------|
| Naphthalene | Alfa Aesar |
| Fluorene | Fluka |
| Acenaphthene | Fluka |
| Acenaphthylene | Supelco |
| Phenanthrene | Alfa Aesar |
| Anthracene | Fluka |
| 1-Methylnaphthalene | Aldrich |
| 1,2-Dimethylnaphthalene | Alfa Aesar |
| 2-Methylnaphthalene | Supelco |
| Biphenyl | Supelco |
| 1-Methylfluorene | Aldrich |
| Fluoranthene | Fluka |
| Pyrene | Sigma-Aldrich |
| Benzene | Carl Roth |
| Toluene | Carl Roth |
| M-Xylene | Fluka |
| O-Xylene | Vwr |
| Ethylbenzene | Alfa Aesar |
| Benzaldehyde | Sigma Aldrich |
| Styrene | Fluka |
| Phenol | Merck |
| Indene | Aldrich |
| Indane | Fluka |
| Alkane Standard Solution C8-C20 | Sigma-Aldrich |

| | |
|-------------------|------------------------------------|
| Benzene D6 | Fluka |
| Toluene D8 | Sigma Aldrich |
| O-Xylene D10 | Sigma Aldrich |
| Naphthalene D8 | Sigma Aldrich |
| Biphenyl D10 | Cil - Cambridge Isotope Institute |
| Acenaphthylene D8 | Cil-Cambridge Isotope Laboratories |
| Acenaphthene D10 | Sigma Aldrich |
| Fluorene D10 | Supelco |
| Phenanthrene D10 | Cil-Cambridge Isotope Laboratories |
| Anthracene D10 | Cil - Cambridge Isotope Institute |
| N-Heptane D16 | Sigma Aldrich |
| N-Dodecane D26 | Sigma Aldrich |
| N-Hexadecane D34 | Aldrich |

Table S2: Ambient conditions at the start of sampling events for this study

| Measurement | Barometric Pressure (hPa) | Wet Bulb (°C) | Dry Bulb (°C) |
|--------------|---------------------------|---------------|---------------|
| B0 1 | 955.5 | 20.4 | 26.8 |
| GTL 1 | 955.8 | 20.4 | 26.8 |
| GTL 2 | 955.9 | 10.7 | 27.0 |
| RME 1 | 956.0 | 10.7 | 27.0 |
| RME 2 | 956.1 | 9.0 | 27.7 |
| B0 2 | 956.2 | 9.0 | 27.7 |

Table S3: Mean FTIR results for the sampling events of the undiluted fuel emissions over each 10 min sampling period.

| Sample | H ₂ O (%) | CO ₂ (%) | CO (ppm) | O ₂ (%) |
|--------|----------------------|---------------------|----------|--------------------|
| B0 1 | 0.58 | 0.58 | 9.51 | 10.30 |
| B0 2 | 0.57 | 0.58 | 9.48 | 10.30 |
| B0 3 | 0.65 | 0.58 | 9.40 | 10.20 |
| B0 4 | 0.66 | 0.58 | 9.42 | 10.20 |
| Mean | 0.62 | 0.58 | 9.45 | 10.25 |
| SD | 0.05 | 0.00 | 0.05 | 0.06 |
| %RSD | 7.42 | 0.13 | 0.55 | 0.56 |
| GTL 1 | 0.56 | 0.58 | 7.89 | 10.31 |
| GTL 2 | 0.56 | 0.58 | 7.86 | 10.31 |
| GTL 3 | 0.66 | 0.58 | 7.63 | 10.50 |
| GTL 4 | 0.65 | 0.58 | 7.65 | 10.45 |
| Mean | 0.61 | 0.58 | 7.76 | 10.39 |
| SD | 0.06 | 0.00 | 0.14 | 0.10 |
| %RSD | 9.10 | 0.21 | 1.77 | 0.94 |
| RME 1 | 0.62 | 0.60 | 7.25 | 10.26 |
| RME 2 | 0.62 | 0.60 | 7.30 | 10.28 |
| RME 3 | 0.67 | 0.60 | 7.32 | 10.45 |

| | | | | |
|-------|------|------|------|-------|
| RME 4 | 0.67 | 0.59 | 7.64 | 10.41 |
| Mean | 0.64 | 0.60 | 7.38 | 10.35 |
| SD | 0.03 | 0.00 | 0.18 | 0.10 |
| %RSD | 4.79 | 0.63 | 2.43 | 0.93 |

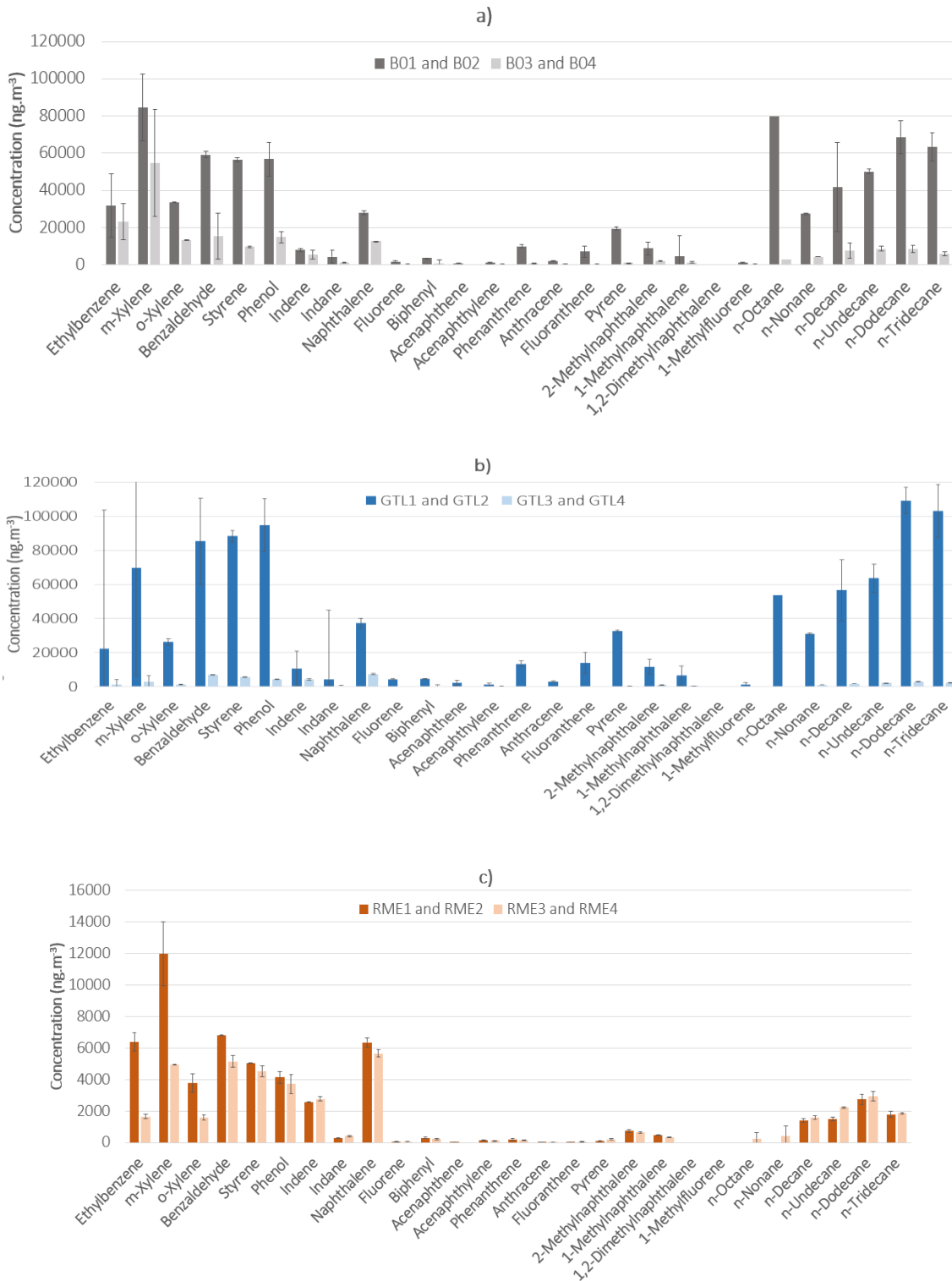


Figure S4: Comparison of sampling event replicates for B0 a), GTL b) and RME c)

Table S4: Concentrations of target analytes detected upon analysis of blank samplers. (n.d.) denotes that the specific target analyte was not detected.

| Analyte | Concentration detected (ng) | | |
|-------------------------|-----------------------------|------|--------------------|
| | PDMS | GW | Activated charcoal |
| Benzene | 6.72 | n.d. | 74.95 |
| Toluene | 35.60 | n.d. | 19.25 |
| Ethylbenzene | n.d. | n.d. | n.d. |
| m-Xylene | n.d. | n.d. | n.d. |
| o-Xylene | 0.01 | n.d. | n.d. |
| Benzaldehyde | n.d. | n.d. | n.d. |
| Styrene | n.d. | n.d. | n.d. |
| Phenol | n.d. | n.d. | n.d. |
| Indene | n.d. | n.d. | n.d. |
| Indane | n.d. | n.d. | n.d. |
| Naphthalene | 0.07 | n.d. | n.d. |
| Fluorene | n.d. | n.d. | n.d. |
| Biphenyl | 0.01 | n.d. | n.d. |
| Acenaphthene | n.d. | n.d. | n.d. |
| Acenaphthylene | n.d. | n.d. | n.d. |
| Phenanthrene | 0.01 | n.d. | n.d. |
| Anthracene | 0.01 | n.d. | n.d. |
| Fluoranthene | n.d. | n.d. | n.d. |
| Pyrene | n.d. | n.d. | n.d. |
| 2-Methylnaphthalene | n.d. | n.d. | n.d. |
| 1-Methylnaphthalene | n.d. | n.d. | n.d. |
| 1,2-Dimethylnaphthalene | n.d. | n.d. | n.d. |
| 1-Methylfluorene | n.d. | n.d. | n.d. |
| n-Octane | n.d. | n.d. | n.d. |
| n-Nonane | n.d. | n.d. | n.d. |
| n-Decane | 0.01 | n.d. | n.d. |
| n-Undecane | 0.01 | n.d. | n.d. |
| n-Dodecane | n.d. | n.d. | n.d. |
| n-Tridecane | n.d. | n.d. | n.d. |
| n-Tetradecane | 0.05 | n.d. | n.d. |
| n-Pentadecane | 0.07 | n.d. | n.d. |
| n-Hexadecane | 0.09 | n.d. | n.d. |
| n-Heptadecane | n.d. | n.d. | n.d. |
| n-Octadecane | n.d. | n.d. | n.d. |
| n-Nonadecane | n.d. | n.d. | n.d. |
| n-Eicosane | n.d. | n.d. | n.d. |

Table S5: Concentrations of target analytes detected upon thermal desorption of GW samplers after sampling the emissions of CAST combustion of different fuels with associated standard deviations between sampling duplicates. (n.d.) denotes that the specific target analyte was not detected for a specific analyte/sampler combination.

| Target analytes | Average concentrations of target analyte ($\mu\text{g}\cdot\text{m}^{-3}$) | | | %RSD of the duplicate measurements | | |
|---------------------------|--|---------------|---------------|------------------------------------|--------|--------|
| | B0 | GTL | RME | B0 | GTL | RME |
| Benzene | 96.63 | 21.65 | 26.57 | 10.09 | 12.28 | 5.96 |
| Toluene | 773.83 | 148.24 | 161.10 | 3.72 | 2.33 | 2.30 |
| Ethylbenzene | 23.19 | 1.36 | 6.39 | 0.63 | 14.06 | 9.05 |
| m-Xylene | 54.90 | 3.07 | 11.99 | 22.43 | 5.60 | 16.96 |
| o-Xylene | 13.36 | 1.12 | 3.79 | 2.91 | 8.52 | 15.63 |
| Benzaldehyde | 15.69 | 6.95 | 6.82 | 19.46 | 1.25 | 0.33 |
| Styrene | 9.78 | 5.62 | 5.03 | 24.03 | 10.74 | 0.52 |
| Phenol | 15.01 | 4.38 | 4.15 | 0.56 | 9.58 | 8.68 |
| Indene | 5.53 | 4.30 | 2.59 | 0.02 | 9.73 | 0.74 |
| Indane | 1.33 | 0.40 | 0.31 | 28.53 | 9.97 | 4.56 |
| Naphthalene | 12.83 | 7.40 | 6.37 | 13.75 | 12.64 | 4.89 |
| Fluorene | 0.28 | 0.07 | 0.07 | 61.87 | 141.11 | 31.98 |
| Biphenyl | 0.85 | 0.30 | 0.30 | 10.94 | 19.21 | 15.14 |
| Acenaphthene | 0.15 | 0.06 | 0.04 | 141.45 | 1.59 | 8.33 |
| Acenaphthylene | 0.42 | 0.23 | 0.16 | 84.21 | 1.13 | 11.05 |
| Phenanthrene | 0.81 | 0.21 | 0.22 | 34.41 | 0.37 | 30.69 |
| Anthracene | 0.07 | 0.04 | 0.01 | 24.32 | 63.85 | 142.59 |
| Fluoranthene | 0.44 | 0.12 | 0.05 | 28.34 | 34.07 | 7.66 |
| Pyrene | 1.18 | 0.29 | 0.09 | 38.74 | 10.01 | 29.98 |
| 2-Methylnaphthalene | 2.06 | 0.90 | 0.75 | 30.84 | 4.45 | 12.39 |
| 1-Methylnaphthalene | 1.46 | 0.52 | 0.47 | 29.26 | 15.43 | 4.34 |
| 1,2-Dimethylnaphthalene | n.d. | n.d. | n.d. | n.d. | n.d. | n.d. |
| 1-Methylfluorene | n.d. | n.d. | n.d. | n.d. | n.d. | n.d. |
| n-Octane | 2.90 | n.d. | n.d. | 141.42 | n.d. | n.d. |
| n-Nonane | 4.45 | n.d. | n.d. | 28.04 | 1.78 | n.d. |
| n-Decane | 7.90 | 1.63 | 1.43 | 24.32 | 1.24 | 9.17 |
| n-Undecane | 8.72 | 2.24 | 1.52 | 13.65 | 8.92 | 7.10 |
| n-Dodecane | 8.76 | 3.02 | 2.75 | 18.82 | 2.74 | 11.17 |
| n-Tridecane | 6.06 | 2.14 | 1.80 | 33.12 | 9.88 | 10.07 |
| n-Tetradecane | 10.74 | 5.81 | 4.71 | 58.44 | 4.16 | 16.36 |
| n-Pentadecane | 3.62 | 3.44 | 3.02 | 54.29 | 32.67 | 0.62 |
| n-Hexadecane | 5.22 | 6.34 | 4.06 | 59.61 | 20.35 | 23.37 |
| n-Heptadecane | 2.16 | 1.66 | 1.17 | 40.45 | 17.83 | 26.03 |
| n-Octadecane | 2.25 | 2.10 | 0.74 | 50.89 | 62.41 | 8.76 |
| n-Nonadecane | 2.78 | 0.91 | 0.51 | 76.23 | 2.11 | 21.29 |
| n-Eicosane | 1.82 | 0.57 | 0.30 | 69.41 | 8.14 | 22.08 |
| Total VOCs + SVOCs | 1097.16 | 237.09 | 259.29 | | | |

Table S6: Concentrations of target analytes detected upon thermal desorption of PDMS samplers after sampling the emissions of CAST combustion of different fuels with associated standard deviations between sampling duplicates. (n.d.) denotes that the specific target analyte was not detected for a specific analyte/sampler combination.

| Target analytes | Average concentrations of target analyte ($\mu\text{g}\cdot\text{m}^{-3}$) | | | %RSD of the duplicate measurements | | |
|---------------------------|--|---------------|---------------|------------------------------------|--------|--------|
| | B0 | GTL | RME | B0 | GTL | RME |
| Benzene | 374.65 | 76.74 | 71.51 | 8.72 | 8.89 | 7.15 |
| Toluene | 774.41 | 159.30 | 158.30 | 0.18 | 1.61 | 0.36 |
| Ethylbenzene | 7.91 | 2.07 | 2.57 | 18.31 | 1.64 | 29.13 |
| m-Xylene | 22.07 | 2.73 | 5.36 | 34.95 | 12.19 | 30.19 |
| o-Xylene | 7.31 | 1.01 | 2.38 | 17.10 | 38.32 | 19.83 |
| Benzaldehyde | 59.86 | 27.56 | 20.25 | 37.49 | 9.69 | 7.30 |
| Styrene | 6.53 | 5.14 | 3.79 | 16.97 | 17.68 | 11.63 |
| Phenol | 54.34 | 13.28 | 12.62 | 6.01 | 13.91 | 12.16 |
| Indene | 4.28 | 4.03 | 3.03 | 1.99 | 13.75 | 7.79 |
| Indane | 0.35 | 0.44 | 0.25 | 0.00 | 5.16 | 7.45 |
| Naphthalene | 13.45 | 8.96 | 6.55 | 23.13 | 3.17 | 6.07 |
| Fluorene | 0.66 | 0.09 | 0.09 | 61.04 | 141.31 | 50.64 |
| Biphenyl | 0.80 | 0.31 | 0.14 | 48.49 | 74.59 | 4.80 |
| Acenaphthene | 0.38 | 0.12 | 0.03 | 80.47 | 21.37 | 141.25 |
| Acenaphthylene | 0.21 | 0.31 | 0.27 | 141.26 | 7.57 | 4.26 |
| Phenanthrene | 1.07 | 0.22 | 0.21 | 71.78 | 76.52 | 52.34 |
| Anthracene | 0.25 | n.d. | 0.01 | 64.40 | n.d. | 142.86 |
| Fluoranthene | 0.61 | 0.05 | 0.05 | 5.45 | 5.17 | 30.53 |
| Pyrene | 0.51 | 0.16 | 0.10 | 119.65 | 47.45 | 2.00 |
| 2-Methylnaphthalene | 3.07 | 1.11 | 0.86 | 75.32 | 24.08 | 3.62 |
| 1-Methylnaphthalene | 2.10 | 0.78 | 0.55 | 32.75 | 14.58 | 7.71 |
| 1,2-Dimethylnaphthalene | 0.38 | n.d. | n.d. | 141.36 | n.d. | n.d. |
| 1-Methylfluorene | n.d. | n.d. | n.d. | n.d. | n.d. | n.d. |
| n-Octane | n.d. | n.d. | n.d. | n.d. | n.d. | n.d. |
| n-Nonane | n.d. | n.d. | n.d. | n.d. | n.d. | n.d. |
| n-Decane | 5.73 | 2.13 | 1.09 | 141.43 | 49.46 | 0.26 |
| n-Undecane | 8.19 | 3.25 | 1.52 | 141.42 | 38.41 | 10.44 |
| n-Dodecane | 16.44 | 4.42 | 3.92 | 72.83 | 64.28 | 66.00 |
| n-Tridecane | 16.87 | 4.56 | 1.66 | 97.65 | 84.11 | 2.39 |
| n-Tetradecane | 520.12 | 119.29 | 4.36 | 139.33 | 137.22 | 30.47 |
| n-Pentadecane | 150.05 | 31.72 | 2.20 | 131.22 | 130.84 | 0.39 |
| n-Hexadecane | 1672.63 | 12.29 | 9.82 | 140.53 | 55.46 | 96.35 |
| n-Heptadecane | 7.50 | 1.57 | 0.93 | 53.58 | 57.03 | 28.53 |
| n-Octadecane | 10.30 | 2.13 | 1.09 | 46.23 | 69.11 | 6.49 |
| n-Nonadecane | 18.57 | 1.16 | 0.89 | 26.85 | 27.60 | 6.40 |
| n-Eicosane | 6.44 | 1.02 | 0.64 | 12.58 | 33.06 | 12.86 |
| Total VOCs + SVOCs | 3768.03 | 487.96 | 317.03 | | | |

Table S7a: LODs and LOQs (ng) of target analytes for different samplers, namely PDMS, GW and activated charcoal. PDMS and GW samplers were directly thermally desorbed whilst the activated charcoal extract was first extracted with CS₂ and the extract was injected into the GC port. (-) denotes that content is unavailable for a specific analyte/sampler combination.

| Target analytes | Abr. | LOD (ng) | | | LOQ (ng) | | |
|-------------------------|-----------|----------|------|----------|----------|-------|----------|
| | | PDMS | GW | Charcoal | PDMS | GW | Charcoal |
| Benzene | - | 0.03 | 0.44 | 0.002 | 0.09 | 1.45 | 0.01 |
| Toluene | - | 0.001 | 0.01 | 0.002 | 0.004 | 0.04 | 0.01 |
| Ethylbenzene | - | 0.02 | 0.09 | 0.003 | 0.06 | 0.29 | 0.01 |
| m-Xylene | - | 0.05 | 2.27 | 0.004 | 0.15 | 7.58 | 0.01 |
| o-Xylene | - | 0.07 | 0.07 | 0.002 | 0.22 | 0.24 | 0.01 |
| Benzaldehyde | - | 0.07 | 0.13 | - | 0.22 | 0.42 | - |
| Styrene | - | 0.02 | 0.13 | 0.001 | 0.06 | 0.43 | 0.003 |
| Phenol | - | 0.04 | 0.09 | 0.003 | 0.14 | 0.31 | 0.01 |
| Indene | - | 0.05 | 0.06 | - | 0.15 | 0.19 | - |
| Indane | - | 0.03 | 0.06 | - | 0.11 | 0.19 | - |
| Naphthalene | Naph | 0.004 | 0.86 | 0.001 | 0.01 | 2.85 | 0.003 |
| Fluorene | FluE | 0.02 | 0.03 | - | 0.08 | 0.11 | - |
| Biphenyl | Biph | 0.01 | 0.01 | - | 0.04 | 0.04 | - |
| Acenaphthene | AceE | 0.02 | 0.04 | - | 0.07 | 0.13 | - |
| Acenaphthylene | AceY | 0.02 | 0.02 | - | 0.06 | 0.08 | - |
| Phenanthrene | Phe | 0.01 | 0.02 | - | 0.05 | 0.05 | - |
| Anthracene | Anth | 0.02 | 0.02 | - | 0.06 | 0.06 | - |
| Fluoranthene | FluA | 0.01 | 0.02 | - | 0.03 | 0.05 | - |
| Pyrene | Pyr | 0.01 | 0.01 | - | 0.03 | 0.05 | - |
| 2-Methylnaphthalene | 2-Mnap | 0.03 | 0.03 | - | 0.11 | 0.10 | - |
| 1-Methylnaphthalene | 1-MNap | 0.10 | 0.58 | - | 0.33 | 1.92 | - |
| 1,2-Dimethylnaphthalene | 1,2-DiMNa | 0.001 | 0.31 | - | 0.002 | 1.02 | - |
| 1-Methylfluorene | 1-MF | 0.03 | 0.05 | - | 0.10 | 0.16 | - |
| n-Octane | n-Oct | 4.00 | 3.95 | - | 13.33 | 13.16 | - |
| n-Nonane | n-Non | 0.79 | 3.95 | - | 2.63 | 13.16 | - |
| n-Decane | n-Dec | 0.19 | 0.63 | - | 0.62 | 2.10 | - |
| n-Undecane | n-Und | 0.07 | 0.26 | - | 0.24 | 0.87 | - |
| n-Dodecane | n-Dod | 0.05 | 0.07 | - | 0.17 | 0.24 | - |
| n-Tridecane | n-Tri | 0.06 | 0.05 | - | 0.21 | 0.17 | - |
| n-Tetradecane | n-Tet | 0.02 | 0.04 | - | 0.06 | 0.12 | - |
| n-Pentadecane | n-Pent | 0.03 | 0.03 | - | 0.09 | 0.12 | - |
| n-Hexadecane | n-Hex | 0.04 | 0.04 | - | 0.12 | 0.12 | - |
| n-Heptadecane | n-Hept | 0.02 | 0.03 | - | 0.07 | 0.10 | - |
| n-Octadecane | n-OctD | 0.03 | 0.04 | - | 0.10 | 0.14 | - |
| n-Nonadecane | n-NonD | 0.04 | 0.04 | - | 0.13 | 0.13 | - |
| n-Eicosane | n-Eic | 0.05 | 0.12 | - | 0.16 | 0.41 | - |

Table S7b: LODs and LOQs (ng.m^{-3}) of target analytes for different samplers, namely PDMS, GW and activated charcoal. PDMS and GW samplers were directly thermally desorbed whilst the activated charcoal extract was first extracted with CS_2 and 1 μL of the 3 mL extract was injected into the GC port. (-) denotes that content is unavailable for a specific analyte/sampler combination.

| Target analytes | Abr. | LOD ($\mu\text{g.m}^{-3}$) | | | LOQ ($\mu\text{g.m}^{-3}$) | | |
|-------------------------|------------|------------------------------|-------|----------|------------------------------|------|----------|
| | | PDMS | GW | Charcoal | PDMS | GW | Charcoal |
| Benzene | - | 0.01 | 0.09 | 0.99 | 0.02 | 0.29 | 3.31 |
| Toluene | - | 0.0002 | 0.002 | 1.10 | 0.00 | 0.01 | 3.66 |
| Ethylbenzene | - | 0.004 | 0.02 | 1.78 | 0.01 | 0.06 | 5.94 |
| m-Xylene | - | 0.01 | 0.45 | 2.26 | 0.03 | 1.52 | 7.55 |
| o-Xylene | - | 0.01 | 0.01 | 1.49 | 0.04 | 0.05 | 4.95 |
| Benzaldehyde | - | 0.01 | 0.03 | - | 0.04 | 0.08 | - |
| Styrene | - | 0.003 | 0.03 | 0.62 | 0.01 | 0.09 | 2.08 |
| Phenol | - | 0.01 | 0.02 | 1.50 | 0.03 | 0.06 | 5.01 |
| Indene | - | 0.01 | 0.01 | - | 0.03 | 0.04 | - |
| Indane | - | 0.01 | 0.01 | - | 0.02 | 0.04 | - |
| Naphthalene | Naph | 0.001 | 0.17 | 0.48 | 0.00 | 0.57 | 1.59 |
| Fluorene | FluE | 0.005 | 0.01 | - | 0.02 | 0.02 | - |
| Biphenyl | Biph | 0.002 | 0.003 | - | 0.01 | 0.01 | - |
| Acenaphthene | AceE | 0.004 | 0.01 | - | 0.01 | 0.03 | - |
| Acenaphthylene | AceY | 0.004 | 0.005 | - | 0.01 | 0.02 | - |
| Phenanthrene | Phe | 0.003 | 0.003 | - | 0.01 | 0.01 | - |
| Anthracene | Anth | 0.004 | 0.004 | - | 0.01 | 0.01 | - |
| Fluoranthene | FluA | 0.002 | 0.003 | - | 0.01 | 0.01 | - |
| Pyrene | Pyr | 0.002 | 0.003 | - | 0.01 | 0.01 | - |
| 2-Methylnaphthalene | 2-Mnap | 0.01 | 0.01 | - | 0.02 | 0.02 | - |
| 1-Methylnaphthalene | 1-MNap | 0.02 | 0.12 | - | 0.07 | 0.38 | - |
| 1,2-Dimethylnaphthalene | 1,2-DiMNap | 0.0001 | 0.06 | - | 0.00 | 0.20 | - |
| 1-Methylfluorene | 1-MF | 0.01 | 0.01 | - | 0.02 | 0.03 | - |
| n-Octane | n-Oct | 0.80 | 0.79 | - | 2.67 | 2.63 | - |
| n-Nonane | n-Non | 0.16 | 0.79 | - | 0.53 | 2.63 | - |
| n-Decane | n-Dec | 0.04 | 0.13 | - | 0.12 | 0.42 | - |
| n-Undecane | n-Und | 0.01 | 0.05 | - | 0.05 | 0.17 | - |
| n-Dodecane | n-Dod | 0.01 | 0.01 | - | 0.03 | 0.05 | - |
| n-Tridecane | n-Tri | 0.01 | 0.01 | - | 0.04 | 0.03 | - |
| n-Tetradecane | n-Tet | 0.003 | 0.01 | - | 0.01 | 0.02 | - |
| n-Pentadecane | n-Pent | 0.01 | 0.01 | - | 0.02 | 0.02 | - |
| n-Hexadecane | n-Hex | 0.01 | 0.01 | - | 0.02 | 0.02 | - |
| n-Heptadecane | n-Hept | 0.004 | 0.01 | - | 0.01 | 0.02 | - |
| n-Octadecane | n-OctD | 0.01 | 0.01 | - | 0.02 | 0.03 | - |
| n-Nonadecane | n-NonD | 0.01 | 0.01 | - | 0.03 | 0.03 | - |
| n-Eicosane | n-Eic | 0.01 | 0.02 | - | 0.03 | 0.08 | - |

Chapter 6: Conclusions and Recommendations for Future Work

6.1 Conclusions

There is a clear need for sustainable solutions to the major problems that modern society is facing, including the decline in the health of our environment. Greener energy sources, specifically biofuel as a replacement for petrogenic liquid fuels, was therefore a focus of this study. Sampling of airborne environmental markers, such as polycyclic aromatic hydrocarbons (PAHs), is a key component in evaluating the potential reductions in air pollutants upon such a transition. This further highlighted the need for additional sampling methodologies that are more practical and sustainable than what is currently commercially available. This work was carried out in a sector-based approach in order for findings to be as impactful as possible, so that realisation of the recommendations can be achieved in a developing country context.

One of the main environmental challenges in a developing country is that of combustion emissions from a generally aged and less technologically advanced vehicle fleet. To address this, a light duty diesel engine dynamometer study was conducted, as discussed in Chapter 2. This study allowed for the establishment of a “status quo” in terms of PAH air emissions from diesel vehicles which can be used to develop emission inventories and the EFs could be used in models to simulate scenarios in further investigating a transition to alternative fuels. Polydimethylsiloxane (PDMS) denuder devices were employed to quantify both gas and particle phase PAH emissions with an analytical method devoid of toxic solvents that can be considered to be more environmentally friendly and sustainable than solvent-based approaches. Total PAH emission factors (EFs) were determined to be 1181.14 and 592.10 $\mu\text{g kg}^{-1}$ for the idle and maximum power mode respectively and over 80 % of PAHs were found in the gas phase. This work emphasized the need for an adequate sampling methodology that accounts for partitioning of airborne analytes between phases to calculate more accurate emission inventories that can be used to guide air quality management plans as well as reduction and abatement strategies. It was for the first time that PAH EFs were determined for vehicles in SA and the developed methodology can be applied in future to assess alternative fuels.

Atmospheric pollutants emitted during biomass burning is another source of air pollution in South Africa, with the practice of traditional pre-harvest sugar cane burning contributing significantly to air pollution on a local and even global scale. The potential for sugar cane and its biomass to be used as feedstock for biofuel production is what drove the agenda for the

sampling campaign detailed in Chapter 3. Here, gaseous and particulate PAH emissions from various sugar cane burn events were simultaneously sampled using the same portable denuder sampling technology, which again proved to be a green approach to PAH monitoring which is well suited to in-field applications. This was the first study to fully characterise PAHs in both phases in emissions from sugar cane burning in South Africa. The PAH concentrations quantified during current pre-harvest burning can be compared to alternative practices and be used as motivation to transition to more sustainable solutions.

Individual and total PAHs detected in the sugar cane burn emissions ranged from two ring naphthalene to four ring pyrene and concentrations were increased 10-fold compared to background air samples. The total PAHs in the primary trap samples for all the burn events, (equating to $17.2 \mu\text{g m}^{-3}$) accounted for over 90% of total PAHs detected in the samples, signifying that the majority of PAHs were in the gas phase. This further iterates the need for gas phase PAH monitoring and abatement especially since the smaller, gas phase PAHs, having higher vapour pressures, undergo atmospheric oxidative conversions and aging reactions which contribute to the toxicity of the resulting secondary organic aerosols. The PAH fingerprints were substantially different between the various burn events indicating the vital role that prevailing weather conditions, as well as the nature of the burn and the crop, have on PAH emissions and the gas-particle partitioning thereof. Fast, contained burns resulted in lower PAH emissions due to more complete combustion while slow, smouldering burns resulted in higher PAH emissions. Higher relative humidity and lower ambient temperatures during burns favoured higher concentrations of particle phase PAHs with the opposite for high ambient temperatures and low humidities which favoured the gas phase. Crop varieties with abundant leaf matter contributed to efficient and contained combustion and thus lower PAH concentrations whilst bare stalk and resin rich varieties were conducive to a smouldering burn with higher PAH concentrations.

Realistically, a full transition to 'green harvesting' will not take place in the short term and pre-harvest burning is a practice that will still be adopted for many years to come due to its associated financial benefits. Thus, this study and the recommended future strategies can be used as a tool by the sugar industry to further optimise burn conditions to ensure more complete combustion, and thus lower PAH emissions.

Following findings and recommendations in Chapter 2 and 3, a sector specific feasibility study was conducted as discussed in Chapter 4. The platinum mining industry is one of the main

consumers of energy in the country and critical mining operations include the extensive use of trackless mobile diesel machinery, thus implying that this sector would have much to gain from a transition to more sustainable fuel. In this study, pollutants emitted from a load haul dump (LHD) engine exhaust in an underground platinum mine were compared when the vehicle was operated on pure diesel, rapeseed methyl ester (RME) and gas-to-liquid (GTL) fuel with the aim of determining the influence of PAH emissions on air quality in the mines. This was the first study in South Africa to report on and compare PAH emissions from an LHD using different fuels based on *in situ* sampling in the underground mining environment. Portable denuder sampling devices were used to sample PAHs and were found to be fit for use in this challenging underground mining environment. PAH combustion emissions from the LHD in high idling mode decreased dramatically when substituting the diesel fuel with GTL or RME fuels. Total PAH gas phase emissions of 42; 18 and 11 $\mu\text{g m}^{-3}$ were reported for diesel, GTL and RME respectively, and no substantial hinderance to engine performance or power was reported. After considering cost and sensitivity factors, it can be concluded that the production and use of biomass-to-liquid (BTL) and biodiesel fuels is a potentially feasible solution towards sustainability in SA underground platinum mines and could be implemented without excessive capital expenditure or government support. The findings of this study and adopted methodology may also further aid in the determination of a strategy to biofuel industrialisation in SA.

The PDMS denuder samplers that were used successfully throughout this project proved to be a practical, portable, robust and cost-effective solution to the collection of semi-volatile organic compounds in challenging environments, but these samplers did have limitations regarding the scope of analytes that could be sampled. This restriction sparked the investigation into a novel graphene wool (GW) material for use as an adsorbent medium. The *in situ* synthesis of GW onto quartz wool allowed the graphene to be directly synthesised into GW via non-catalytic chemical vapour deposition and avoided post-growth transfer and isolation steps. The resultant fibrous GW was flexible, malleable and compressible, allowing for a wealth of potential applications.

To address air pollutant monitoring capabilities of this novel material, a GW sampler was optimised in terms of sorbent mass, bed length and packing density and was tested for its use for a range of volatile and semi-volatile analytes. The GW sampler was compared to PDMS traps and commercial charcoal samplers to assess sampling efficacy. This was investigated by the adsorption of vaporized alkane standards on the different samplers using a condensation

aerosol generator in a temperature-controlled chamber and subsequent detection by FID. The gas phase collection efficiency of the GW sampler was found to be >90% for octane, dodecane, and hexadecane at ambient temperatures, which was comparable to that of activated charcoal. The humidity uptake onto GW was found to be insignificant (less than 1% (m/m)). Breakthrough studies showed the favourable adsorption of polar molecules on the GW, which was attributed to the defective nature of the graphene and its inhomogeneous coating. This suggested that the polar versus non-polar uptake potential of the GW may be tuned by varying the graphene layering on the quartz wool substrate during synthesis. The GW sampler was then tested by means of a combustion aerosol standard system (CAST) where it performed comparably to the PDMS trap in terms of sampling and thermal desorption of non-polar semi-volatile organic compounds, with total reported alkane concentrations after thermal desorption of GW and PDMS samplers being 17.96 ± 13.27 and $18.30 \pm 16.42 \mu\text{g m}^{-3}$ respectively.

In line with sustainability, GW is a novel adsorbent that overcomes limitations of commercially available sorbents, such as once-off usage and the need for solvent extraction which is time consuming and requires toxic solvents, and provides new, exciting possibilities for the monitoring of organic air pollutants. GW displays numerous advantages, including high sampling efficiencies, simple and cost-effective synthesis of the thermally stable GW, solvent-free and environmentally friendly analysis, and, importantly, the potential reusability of samplers. Another significant advantage of GW as a sorbent is the possibility of tailoring the surface chemistry for targeted polar or non-polar analytes by modifying the surface coverage of graphene.

Overall, this research has shed new light on current environmental and human health issues in South Africa, and of global interest, and provides a valuable basis for decision makers in both regulatory bodies and related industries, to take necessary action in planning long term bio-economical and sustainable resource management strategies. One such imperative is the transition to alternative fuels and the promotion of a circular economy, whereby a collaboration between the key sectors would close the loop between feedstock producers, the refining industry and fuel users in the country. An example of this would be the transition from the traditional pre-harvest sugar cane burning to green harvesting which will not only allow converting the unneeded waste biomass into fuel for the mining industry, but will also substantially decrease PAHs, PM and other hazardous air emissions resulting from open burning of agricultural wastes.

6.2 Recommendations for future work

The work presented in each chapter of this thesis could be expanded on further. It is suggested that PAH emission inventories, with EFs, be established for all studies with larger sample sets and more replicates for enhanced statistical significance. The scope of analytes should be increased to include oxygenated and nitrated PAH derivatives and methods for the analysis of these compounds should be developed and fully optimised. It is also recommended that the method for desorption of heavier particulate phase PAHs on QFFs also be fully optimised and specific component toxicity studies should be done with emphasis on benzo[a]pyrene.

The feasibility study focused on two key industries in SA that have great potential in promoting a circular economy. Future work should investigate the potential implementation of production and use of BTL fuel instead of diesel which would be facilitated by the completion of a more comprehensive feasibility study with additional input from the sugar cane and refining industries and include social studies to identify and assess any barriers to implementation and how they can be overcome. In order to further evaluate the reduction of emissions when transitioning to biofuel and add to the results reported on the PAH concentrations, it is recommended that a more comprehensive study be done whereby regulated combustion pollutants be measured in parallel which can be done by using a controlled dynamometer setup as described in Paper 1.

Further testing and optimisation of the GW sampler is required and a full validation should be performed. One such example is headspace gas sampling where the breakthrough of analytes can be determined by means of permeation tubes. A starting point would be the determination of breakthrough of naphthalene as this can be directly compared to the available validation data relating to PDMS sorbents. The thermal desorption of the GW samplers should be optimized and the samplers should be used in parallel with other sorbents during sampling campaigns to enable further comparative studies. Furthermore, an investigation into the effect of surface tuning and doping of GW during synthesis would expand on the current scope of applications and give a more fundamental understanding of the mechanisms at play during sorption. The GW samplers should be tested for additional matrices, such as water, to establish and optimise environmental monitoring methods.

Appendix A: Co-authored paper 1

This paper was published in Gefahrstoffe Reinhaltung Der Luft.

Geitner, V., Orasche, J., Dragan, G.C., Jakobi, G., Schnelle-Kreis, J., Geldenhuys, G.L., Forbes, P.B.C., Karg, E.W., Breuer, D. and Zimmermann, R. 2021. Feasibility study of portable sampling techniques for combustion related airborne particulates in a platinum mine. *Gefahrstoffe Reinhaltung Der Luft*. 81(9-10): 386-396

Feasibility study of portable sampling techniques for combustion related airborne particulates in a platinum mine

V. Geitner, J. Orasche, G. C. Dragan, G. Jakobi, J. Schnelle-Kreis, G.-L. Geldenhuys, P. B. C. Forbes, E. W. Karg, D. Breuer, R. Zimmermann

ABSTRACT Hazardous compounds such as airborne particulate polycyclic aromatic hydrocarbons (PAHs) and black carbon (BC) require special attention. The toxicological effects caused by the inhalation of such substances depend mainly on the concentration of each health relevant compound inhaled. In this feasibility study, portable aerosol samplers were utilised for the first time together with portable Aethalometers in different areas of a South African underground platinum mine. The preliminary results showed the highest mean toxicity equivalent (TEQ) values from 3.2 to 3.9 ng m⁻³ in the mechanised mining areas, indicating the largest extent of diesel exhaust emissions at those sampling sites. Furthermore, very high mean equivalent black carbon (eBC) concentrations from 264 to 1439 µg m⁻³ were found in the same areas and give therefore, a cause of concern regarding occupational health aspects. In summary, both, the aerosol samplers and the Aethalometers delivered valuable data regarding the occupational exposure to airborne pollutants originating from combustion sources in mining activities. For such mining activities, the exposure to eBC was shown to be of greater concern than the exposure to PAHs.

Machbarkeitsstudie zu personengetragenen Probenahmetechniken für Partikel aus Verbrennungsmotoremissionen in einer Platinmine

ZUSAMMENFASSUNG Luftgetragene Gefahrstoffe, wie partikelförmige polyzyklische aromatische Kohlenwasserstoffe (PAK) und Ruß (schwarzer Kohlenstoff, engl. black carbon, BC), erfordern unter arbeitsmedizinischen Gesichtspunkten besondere Aufmerksamkeit. Toxikologische Auswirkungen, verursacht durch die Einatmung dieser Substanzen, hängen im Wesentlichen von der Konzentration der gesundheitlich relevanten Verbindungen ab. In dieser Machbarkeitsstudie wurden erstmals personengetragene Aerosolsammler zusammen mit tragbaren Aethalometern in verschiedenen Bereichen einer südafrikanischen Platinmine angewendet. Die vorläufigen Ergebnisse zeigten die höchsten Toxizitätsäquivalent-Werte (TEQ-Werte) von 3,2 bis 3,9 ng m⁻³ in den mechanisierten Bergbaubereichen, welche auf die hohen Dieselabgasemissionen in diesen Minenbereichen zurückzuführen sind. Außerdem konnten in denselben Bereichen sehr hohe Ruß- bzw. BC-Konzentrationsmittelwerte von 264 bis 1439 µg m⁻³ festgestellt werden, was im Hinblick auf arbeitsmedizinische Aspekte ein Grund zur Besorgnis ist. Die mit den Aerosolsammlern und Aethalometern ermittelten Ergebnisse liefern wertvolle Daten hinsichtlich der berufsbedingten Exposition luftgetragener Schadstoffe aus Verbrennungsquellen bei Abbau- und Transportarbeiten unter Tage. Bei diesen Bergbauarbeiten konnte gezeigt werden, dass die Exposition mit Ruß bzw. BC besorgniserregender ist als die Exposition mit PAK.

1 Introduction

The health of underground workers in the mining sector worldwide is a matter of concern. Noise, thermal stress, whole body vibration, musculoskeletal disorders and the inhalation of hazardous substances such as coal dust, silica or diesel exhaust emissions are some examples for risks mine workers are confronted with [1; 2]. Severe occupational diseases might result in the case of continuous inhalation of polluted air over a long period of time. For instance, if heavy diesel powered vehicles are used for ore mining and transportation, diesel exhaust emissions above a threshold limit value should be considered as a potential trigger of cancer [3; 4]. More precisely, diesel engine exhaust was categorised by the International Agency for Research on Cancer (IARC) as carcinogenic to humans (Group 1) [4]. In general, particle-bound diesel engine emissions are considered of great concern as they can penetrate deep into the lungs. Therefore, in

addition to the implementation of technical and organisational protection measures, regular occupational monitoring of hazardous substances is vital to control the potential exposure of workers.

Diesel exhaust emissions consist of a complex mixture of gaseous substances and particulate matter (PM), resulting from unburned fuel, lubricant oil and combustion products [5]. Diesel emission PM comprises mainly elemental carbon (EC) as core and organic compounds adsorbed on the large surface area of the core [6]. These organic compounds in turn contain polycyclic aromatic hydrocarbons (PAHs) as well as methylated, nitrated and oxygenated PAHs [5]. Besides carcinogenic PAHs [7], the high quantity of carcinogenic EC also indicates a high health risk potential [8]. Furthermore, various metals from additives can be found in diesel exhaust [9]. If diesel exhaust is emitted to the surrounding environment, particle ageing additionally leads to mixed particles by coagulation of engine emission and dust particles

Table 1 Sampling parameters for the Aethalometer and aerosol sampling measurements in the platinum mine [22].

| | Sampling location | | |
|-----------------------------------|-------------------|------------------|---------------------|
| | Mechanised mining | | Conventional mining |
| | Tipping point | LHD vehicle area | |
| Aethalometer measurements | | | |
| Number of instruments N | 3 | 3 | 2 |
| Measurement duration [min] | 64, 32, 29 | 55, 27, 50 | 66, 65 |
| Mean air temperature [°C] | 33, 30, 32 | 34, 31, 33 | 31, 31 |
| Mean relative humidity [%] | 48, 49, 40 | 53, 47, 40 | 42, 40 |
| Flow rate [ml min ⁻¹] | 150, 50, 50 | 150, 50, 50 | 50, 50 |
| Time resolution [s] | 60 | 60 | 60 |
| Aerosol sampling | | | |
| Number of samples N | 4 | 4 | 5 |
| Flow rate [l min ⁻¹] | 0.5 | 0.5 | 0.5 |
| Sampling duration [min] | 31, 33, 45, 88 | 14, 20, 57, 60 | 7, 15, 28, 50, 60 |

from working activities. The discussion of the fate of those particles after lung deposition highlights the need for a single particle analysis to better assess potential health outcomes. A method to characterise individual particles is the aerosol time-of-flight (ATOF) mass spectrometer [10; 11], which is able to deliver for each single particle both the PAH profile and the inorganic composition. However, personal exposure data would be particularly beneficial for occupational or environmental health studies, which include ideally personal biomarkers of exposure (e.g. from blood [12] or urine [13; 14]).

The extent of adverse health effects depends on the concentration of the compounds inhaled as well as on their physico-chemical properties. While hygroscopic gases are predominantly deposited in the extrathoracic region like nose, larynx and upper airways due to their high diffusivity, non-hygroscopic gases can penetrate further into deep lung regions, depending on absorption, translocation and metabolism in the airway lining cells [15]. In contrast, particles are deposited mainly depending on their aerodynamic diameter [16]. Micron-sized particles mainly deposit on the air conducting extra thoracic and bronchial part of the respiratory tract by gravitational sedimentation and impaction at the airway bifurcations [17; 18]. There, they can be cleared by the mucus covering the airways and transported to the larynx by ciliated cell activity [19; 20]. If sub-micron-sized fine and ultrafine (<100 nm) particles reach the alveoli, an unspecific immune defence in the alveolar region is performed by freely moving macrophage cells, removing particles from the epithelium by phagocytosis. However, ultrafine particles from diesel emissions deceive this mechanism by their small size and by depositing widely spread over the alveolar surface with a local dose of up to several particles per pneumocyte (6,940 nm² [21]). Those particles could be taken up by the cells or could be translocated through the epithelium, for instance to the blood circulation.

The goal of our study was the analysis of the diesel emission PM fraction inside an underground platinum mine in the North West Province of South Africa. The mine was a perfect location

to compare different work exposures dominated by one combustion source, the load haul dump (LHD) vehicles. Since these LHD vehicles were operated without any emission reduction measures and were responsible for high emissions of soot particles. In order to assess the workers' exposure to PM in different areas of the mine, personal sampling was undertaken in the mechanised (i.e. diesel engine based) as well as conventional (i.e. electrical power based) mining areas. For this purpose, portable Aethalometers and personal aerosol samplers were carried by workers to measure their exposure for different tasks. The direct-reading portable Aethalometers provided online measurements of equivalent black carbon (eBC) originating from emitted soot particles. The particle mass collected by the personal aerosol samplers provided useful information towards the exposure against polycyclic aromatic hydrocarbons (PAHs), their oxygenated and methylated derivatives as well as aliphatic compounds with carbon ranges from C₁₂ to C₄₀. Applying these personal aerosol sampling techniques, concentrations of hazardous compounds as well as PAH toxicity equivalent (TEQ) values could be determined.

2 Materials and methods

2.1 Sampling sites

The field measurements took place in the underground shafts of a platinum mine in the North West Province of South Africa [22]. The underground platinum mine is one of approximately 17 Merensky Reef mines in the Bushveld Igneous Complex. The mined ore contains a wide range of various platinum- and palladium based compounds such as platinum sulphides, which can be found with a content of up to 74 % in some ore layers [23]. The depth of the mine, where our field studies were carried out, had a depth of between 620 and 1,290 m below surface.

In this mine, aerosol sampling and Aethalometer measurements were carried out in three different areas: two in mechanised mining areas and one in a conventional mining area. In the mechanised mining areas, heavy diesel powered LHD vehicles

were used. The LHD vehicles transported the mined platinum ore to a central location called the tipping point, where it was dumped by the tipping point operator above a conveyor belt that transferred the ore to the ground level. Workers who carried the personal samplers and Aethalometers in the mechanised mining area were LHD vehicle operators and the tipping point operator. These workers were not protected by any pressurised cabins, thus they were directly exposed to the diesel engine emissions. This means the LHDs had no cabins and there was also no housing around the control panel for the tipping point. Workers were only protected from getting injured due to impacts of larger objects by open cages.

At the tipping point, there was a steady but infrequent arrival of LHD vehicles to dump their load. In contrast, in the conventional mining area, no LHD vehicles were present (non-diesel shaft). Here, miners were collecting ore by means of electrically powered drilling and blasting operations. Compared to the mechanised mining area, no diesel exhaust emissions were expected here.

The conditions in the mine were characterised by high temperatures around 32 °C and a relative humidity around 45% (Table 1). All of the investigated areas had similar conditions. The non-diesel shaft was slightly cooler at around 31°C, whereas LHD vehicle drivers had to work at temperatures of up to 34 °C due to heat radiation from the engines.

2.2 Sampling of particles with personal aerosol samplers

For the purpose of this feasibility study, personal aerosol samplers were used to trap airborne particulate organic compounds found underground (Figure 1 a/b). A detailed description and characterisation of the samplers can be found elsewhere [22; 24].

For the purpose of this study, only the particle-bound hazardous compounds were considered. The particle phase was sampled on 13 mm quartz fibre filters. Before use, the commercially available quartz fibre filters (T293, Munktell, Sweden) were heated in an oven at 550 °C for 12 h and stored in sealed glass vials.

Inside the mine, 13 workers were equipped with personal aerosol samplers connected to GilAir Plus pumps (Sensidyne, USA) in order to perform workplace air measurements inside the platinum mine (Figure 1 d/e and Table 1). Four personal aerosol samplers were applied each in the tipping point area as well as in the LHD vehicle area, while five aerosol samplers were used in the conventional mining area. All filter samples were taken at a flow rate of 0.5 l min⁻¹. The sampling duration varied widely from 7 to 88 min. The reason for the different sampling durations was that portable aerosol samplers were attached to workers in the underground mine and it was not possible for them to return after a certain predetermined time. For example, every LHD operator had individual driving routes and therefore, varying distances which had to be covered. The variation in sampling time and thus sample volume was corrected for in the calculation of the analytical results from the aerosol samplers.

In addition to the portable filter samples, five field blank samples were taken underground and treated in the same way as the real samples except they were not connected to a sampling pump. The determined background levels of analysed organic compounds were finally subtracted from sample values. After sampling, all filters were stored in capped glass vials. The samples

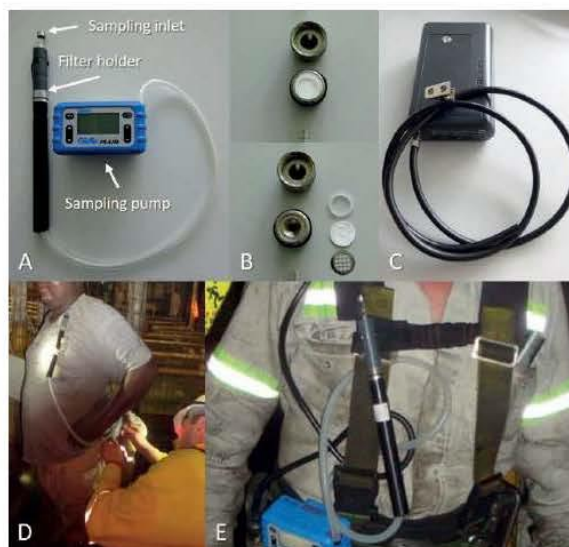


Figure 1 a: Portable aerosol sampling device; b: open filter holder (top) and disassembled filter holder; c: portable Aethalometer; d, e: sampling set up as carried by the workers. Photo: Authors

were transported in a cooler box to ground level and stored in a freezer until analysis.

The off-line analysis of the particulate matter from quartz fibre filters by thermal extraction was carried out with an OPTIC-4 (GL Sciences, Netherlands) direct thermal desorption injector. Prior to extraction, samples were spiked with internal standard (ISTD) mixtures (Table 2). For the first 50 s, the split flow was set at 50 ml min⁻¹, at a column flow rate of 1 ml min⁻¹. Afterwards the injector was switched to splitless mode for 20 min. After 135 s vent time the sample was heated up to 300 °C with a heating rate of 50 °C s⁻¹. Extracted compounds were trapped on the separation column at 40 °C. The gas chromatography (GC) column was a 25 m BPX-5 non-polar column (0.22 mm ID, 0.25 µm film thickness, SGE, Australia). After a sampling time of 15 min for thermal extraction, the column was heated at a rate of 20 °C min⁻¹ up to 150 °C, 5 °C min⁻¹ up to 350 °C followed by 10 min of isothermal operation. The mass spectrometer (MS) of the GC-MS-System (Shimadzu GCMS-QP2010 Ultra, Shimadzu, Japan) was operated in scan mode (m/z 35 to 500, scan rate 3.3 Hz). Quantification of analysed compounds was based on internal standard calibration of certain compounds using internal (ISTD) and a calibration standard mixture in toluene (Table 2).

2.3 Determination of the PAH based toxicity equivalent values

An estimation of potential carcinogenicity resulting from PAH exposure was achieved by the calculation of toxicity equivalent (TEQ) values based on an approach of the German Research Foundation [25] for occupational exposure. Briefly, the TEQ was calculated by summing up the multiplication products of the concentration of single compounds with a corresponding toxicity equivalent factor (TEF). The TEFs were set by a DFG expert commission (MAK commission for maximum work place concentrations). The toxicity of eleven PAHs is related to

Table 2 Overview of (isotope labelled) compounds used for the internal and calibration standard mixture for filters used underground. The precision processing was determined for the calibration and was given as the relative standard deviation (RSD) in % [22].

| Isotope labelled internal standard mixture | Calibration standard mixture | Precision in % RSD |
|---|-------------------------------------|--------------------|
| Naphthalene d ₈ | Naphthalene | 8 |
| Biphenyl d ₁₀ | Biphenyl | 11 |
| Acenaphthylene d ₈ | Acenaphthylene | 10 |
| Acenaphthene d ₁₀ | Acenaphthene | 10 |
| Fluorene d ₁₀ | Fluorene | 7 |
| Phenanthrene d ₁₀ | Phenanthrene | 5 |
| Anthracene d ₁₀ | Anthracene | 6 |
| Fluoranthene d ₁₀ | Fluoranthene | 7 |
| Pyrene d ₁₀ | Pyrene | 7 |
| Benz[a]anthracene d ₁₂ | Benzo[c]phenanthrene | 7 |
| Chrysene d ₁₂ | Benz[a]anthracene | 8 |
| sum Benzo[b,k]fluoranthene d ₁₂ | Chrysene | 7 |
| Benzo[e]pyrene d ₁₂ | 2,2'-Binaphthalene | 12 |
| Benzo[a]pyrene d ₁₂ | sum Benzo [b,j,k]fluoranthene | 15 |
| Perylene d ₁₂ | Benzo[e]pyrene | 12 |
| Indeno[1,2,3-cd]pyrene d ₁₂ | Benzo[a]pyrene | 13 |
| Dibenz[ah]anthracene d ₁₄ | Perylene | 15 |
| Benzo[ghi]perylene d ₁₂ | Indeno[1,2,3-cd]pyrene | 9 |
| Coronene d ₁₂ | Dibenz[ah]anthracene | 15 |
| Dibenzothiophene d ₈ | Picene | 13 |
| 9,10-Anthracenedione ¹³ C ₆ | Benzo[ghi]perylene | 15 |
| Benz[a]anthracene-7,12-dione d ₁₀ | Coronene | 18 |
| n-Hexadecane d ₃₄ | 1,4-Naphthoquinone | 30 |
| n-Octadecane d ₃₈ | 1-Naphthaldehyde | 13 |
| n-Docosane d ₄₆ | 1(2H)-Acenaphthylene | 13 |
| n-Tetracosane d ₅₀ | 9H-Fluoren-9-one | 12 |
| n-Triacontane d ₆₂ | 9H-Xanthen-9-one | 17 |
| | 9,10-Anthracenedione | 5 |
| | 1,8-Naphthalic anhydride | 30 |
| | 4H-Cyclopenta[def]phenanthren-4-one | 6 |
| | Benzo[b]naphtho[2,3-d]furan | 22 |
| | 11H-Benzo[a]fluoren-11-one | 9 |

| Isotope labelled internal standard mixture | Calibration standard mixture | Precision in % RSD |
|--|---------------------------------|--------------------|
| | 11H-Benzo[b]fluoren-11-one | 11 |
| | Benzo[b]naphtho[2,1-d]furan | 11 |
| | Naphtho[2,1,8,7-klmn]xanthene | 7 |
| | Benz[a]anthracene-7,12-dione | 17 |
| | 5,12-Naphthacenedione | 10 |
| | 1,2-Dimethylnaphthalene | 7 |
| | 1-Methylpyrene | 6 |
| | C ₁₂ H ₂₆ | 15 |
| | C ₁₃ H ₂₈ | 10 |
| | C ₁₄ H ₃₀ | 14 |
| | C ₁₅ H ₃₂ | 15 |
| | C ₁₆ H ₃₄ | 2 |
| | C ₁₇ H ₃₆ | 10 |
| | C ₁₈ H ₃₈ | 20 |
| | C ₁₉ H ₄₀ | 15 |
| | C ₂₀ H ₄₂ | 5 |
| | C ₂₁ H ₄₄ | 8 |
| | C ₂₂ H ₄₆ | 9 |
| | C ₂₃ H ₄₈ | 6 |
| | C ₂₄ H ₅₀ | 6 |
| | C ₂₅ H ₅₂ | 7 |
| | C ₂₆ H ₅₄ | 9 |
| | C ₂₇ H ₅₆ | 8 |
| | C ₂₈ H ₅₈ | 9 |
| | C ₂₉ H ₆₀ | 6 |
| | C ₃₀ H ₆₂ | 16 |
| | C ₃₁ H ₆₄ | 25 |
| | C ₃₂ H ₆₆ | 14 |
| | C ₃₃ H ₆₈ | 16 |
| | C ₃₄ H ₇₀ | 20 |
| | C ₃₅ H ₇₂ | 20 |
| | C ₃₆ H ₇₄ | 21 |
| | C ₃₇ H ₇₆ | 22 |
| | C ₃₈ H ₇₈ | 25 |
| | C ₃₉ H ₈₀ | 16 |
| | C ₄₀ H ₈₂ | 17 |
| | 2-Methylnaphthalene | 8 |
| | 1-Methylnaphthalene | 8 |
| | Cyclopenta[cd]pyrene | 7 |

benzo[a]pyrene (B[a]P, TEF = 1), due to higher or lower health risk potential compared to B[a]P [25].

In a number of European countries like Austria, Poland, Sweden and Switzerland, an occupational exposure limit of $2 \mu\text{g m}^{-3}$ is in place for benzo[a]pyrene. Other countries (Germany, Latvia, the Netherlands) have enforce even lower exposure limits for B[a]P [26].

2.4 Black carbon monitoring with portable Aethalometers

Black carbon (BC) is a product of incomplete combustion processes and is emitted for example by vehicles operated on diesel fuel, such as LHDs. Due to the large surface area thereof, BC is capable of absorbing various organic substances. In order to characterise BC, portable Aethalometers (microAeth®, MA 200 series, AethLabs, USA) were used during our field campaign (Figure 1 c). These Aethalometers enabled the online monitoring of carbonaceous aerosol particles within a sampling period. The instrument is operated with an internal pump, which allows continuous measurements over about 8 h with a time resolution between 1 s and 5 min. It measures the light attenuation (ATN) by aerosol particles continuously deposited on a polytetrafluoroethylene (PTFE) filter tape at five wavelengths (375, 470, 528, 625 and 880 nm) ranging from ultraviolet (UV) to near infrared (IR).

BC is characterised by its strong wavelength independent absorption of visible light, from near UV up to near IR and is defined by its absorbance at 880 nm [27]. The conversion of the attenuation to a mass concentration is done by an internal algorithm considering mass absorption cross section and different optical parameters, device design and filter material. The achieved values are given as equivalent black carbon (eBC) [28]. Another fraction of carbonaceous aerosols, excluding BC, which absorbs light primarily at the short visible wavelengths (UV-VIS) is called brown carbon (BrC). BrC can be calculated from the difference between the absorbance at 370 nm and 880 nm [27; 29; 30].

Because of the toxicological effects of elemental carbon, the European Commission has set a binding occupational exposure limit value (BOELV) of $50 \mu\text{g m}^{-3}$, which shall be adhered to in underground mining and tunnelling starting from February 2026. This quite low BOELV can raise issues for measurements using traditional personal filter sampling techniques, as long sampling times and high flowrates are necessary to achieve a low enough LOQ. On the other hand, portable Aethalometers are much more sensitive, which can be found very useful for occupational monitoring purposes. Beside shorter sampling times, exposure profiles can also be measured with such direct-reading instruments. Even though the BC measured by the Aethalometer doesn't directly translate into an EC concentration, validated calibration factors could be used for the purpose of workplace measurements. A similar device [31; 32] was successfully used to measure diesel particulate matter in underground mines. Because the particles emitted from diesel engines are below $1 \mu\text{m}$ in size [33], the portable Aethalometers could be operated without a size-selective inlet.

Here, in order to measure the ambient eBC concentrations online in different mine regions, eight workers in total were equipped with portable Aethalometers (Table 1). Six Aethalometers were worn by workers at the tipping point and the LHD ve-

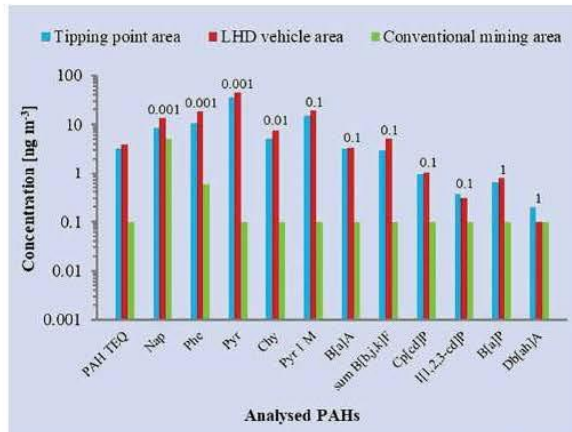


Figure 2 Mean PAHTEQ values and mean PM concentrations of health relevant PAHs. The health relevant PAHs are naphthalene (Nap), phenanthrene (Phe), pyrene (Pyr), chrysene (Chy), 1methylpyrene (Pyr 1 M), benz[a]anthracene (B[a]A), sum benzo[b,j,k]fluoranthenes (sum B[b,j,k]F), cyclopenta[cd]pyrene (Cp[cd]P), indeno[1,2,3-cd]pyrene (I[1,2,3-cd]P), benzo[a]pyrene (B[a]P) and dibenz[ah]anthracene (D[ah]A). The PAHs are listed from left to right with increasing TEFs [25]. TEFs of each PAH are shown on the top of the bars. Graphic: Authors

hicle area. In the conventional mining area, two workers were equipped with one Aethalometer each.

3 Results and discussion

3.1 Health relevant organic compounds found underground

The mean and median concentrations of aromatic analytes associated with PM in different areas of the underground platinum mine, as well as the calculated TEQ values are presented in Table 3. The mean TEQ values and mean PM concentrations of health relevant PAHs found underground are listed with increasing TEFs in Figure 2. The bar diagram represents the results determined for the tipping point (blue), LHD vehicle (red) and conventional mining (green) area. Here, the highest mean concentrations of up to 45 ng m^{-3} (median: 46 ng m^{-3}) could be found for pyrene, its methylated derivatives and for phenanthrene in the LHD vehicle area. This is due to the highest frequency of LHD vehicles passing by in this area and therefore the largest extent of diesel exhaust emissions. However, one exception was dibenz[ah]anthracene, a heavier PAH, for which much higher concentrations were found at the tipping point. In contrast, the LHD vehicle and conventional mining area, the dibenz[ah]anthracene concentrations found were below the limit of quantification (LOQ). Also the green bars starting with pyrene represent values below the LOQ.

In general, considering the sampled health relevant PAHs in this feasibility study, the highest mean TEQ value of 3.9 ng m^{-3} (median: 3.5 ng m^{-3}) was calculated for the LHD vehicle area. In the area of the tipping point, LHD vehicles were not continuously present and therefore, lower concentrations of health relevant PAHs were present in the surrounding air. Consequently, a lower mean TEQ value of 3.2 ng m^{-3} (median: 3.1 ng m^{-3}) was determined for that area. These measured TEQ values or B[a]P equivalents are several orders of magnitude below the OEL of $2 \mu\text{g/m}^3$ imposed in most European countries. These findings

Table 3 GC-MS quantification results for aromatic analytes found on filter samples as PM and calculated toxicity equivalent (TEQ) values. The toxicity equivalent factors (TEFs) for different PAHs are listed in the right column [25]. Less than (<) values were below the limit of quantification (LOQ).

| Aromatic analytes | Sampling location | | | | | | |
|-------------------------------|----------------------------|------------------------------|----------------------------|------------------------------|----------------------------|------------------------------|-------|
| | Mechanised mining PM | | | | Conventional mining PM | | |
| | Tipping point | | LHD vehicle area | | Mean [ng m ⁻³] | Median [ng m ⁻³] | TEF |
| | Mean [ng m ⁻³] | Median [ng m ⁻³] | Mean [ng m ⁻³] | Median [ng m ⁻³] | | | |
| TEQ | 3.2 | 3.1 | 3.9 | 3.5 | <0.1 | <0.1 | |
| Naphthalene | 8.6 | 7.8 | 13 | 14 | 5.1 | 4.3 | 0.001 |
| 1-Methylnaphthalene | 2.1 | 1.6 | 2.7 | 2.9 | 1.7 | 1.3 | |
| 2-Methylnaphthalene | 3.0 | 2.5 | 5.2 | 5.0 | 1.7 | 1.6 | |
| Biphenyl | 2.5 | 1.9 | 3.7 | 3.4 | 2.3 | 1.1 | |
| Acenaphthylene | 0.4 | 0.3 | 1.4 | 1.4 | <0.1 | <0.1 | |
| Acenaphthene | 0.1 | <0.1 | 33 | 2.3 | 1.8 | <0.1 | |
| Fluorene | 1.9 | 1.6 | 3.2 | 2.9 | 0.8 | <0.1 | |
| Phenanthrene | 11 | 9.4 | 19 | 13 | 0.6 | 0.2 | 0.001 |
| Anthracene | 4.8 | 4.7 | 11 | 7.9 | 0.5 | 0.3 | |
| Fluoranthene | 10 | 10 | 10 | 9.9 | <0.1 | <0.1 | |
| Pyrene | 36 | 34 | 45 | 46 | <0.1 | <0.1 | 0.001 |
| 1-Methylpyrene | 15 | 14 | 19 | 17 | <0.1 | <0.1 | 0.1 |
| 2-Methylpyrene | 21 | 20 | 29 | 27 | <0.1 | <0.1 | |
| 4-Methylpyrene | 20 | 18 | 26 | 24 | <0.1 | <0.1 | |
| Benzo[c]phenanthrene | 0.2 | <0.1 | 0.5 | <0.1 | <0.1 | <0.1 | |
| Benz[a]anthracene | 3.2 | 3.2 | 3.4 | 3.4 | <0.1 | <0.1 | 0.1 |
| Chrysene | 5.1 | 5.4 | 7.5 | 7.3 | <0.1 | <0.1 | 0.01 |
| 2,2'-Binaphthalene | 0.1 | 0.1 | 1.0 | 0.9 | <0.1 | <0.1 | |
| sum Benzo[b,j,k]fluoranthenes | 2.9 | 3.3 | 5.1 | 5.0 | <0.1 | <0.1 | 0.1 |
| Cyclopenta[cd]pyrene | 0.9 | 0.9 | 1.1 | 1.0 | <0.1 | <0.1 | 0.1 |
| Benzo[e]pyrene | 1.1 | 1.1 | 1.6 | 1.6 | <0.1 | <0.1 | |
| Benzo[a]pyrene | 0.6 | 0.7 | 0.8 | 0.8 | <0.1 | <0.1 | 1 |
| Perylene | 0.2 | 0.1 | 0.5 | 0.1 | <0.1 | <0.1 | |
| Indeno[1,2,3-cd]pyrene | 0.4 | 0.1 | 0.3 | 0.2 | <0.1 | <0.1 | 0.1 |
| Dibenz[ah]anthracene | 0.2 | 0.2 | <0.1 | <0.1 | <0.1 | <0.1 | 1 |
| Picene | 6.7 | 5.0 | 6.1 | 4.8 | <0.1 | <0.1 | |
| Benzo[ghi]perylene | 1.4 | 1.3 | 1.0 | 1.2 | <0.1 | <0.1 | |
| Coronene | 0.2 | <0.1 | <0.1 | <0.1 | <0.1 | <0.1 | |
| 1,4-Naphthoquinone | <0.1 | <0.1 | <0.1 | <0.1 | <0.1 | <0.1 | |
| 1-Naphthaldehyde | 1.2 | 1.5 | 2.4 | 2.6 | <0.1 | <0.1 | |
| 1(2H)-Acenaphthylene | 0.5 | 0.5 | 0.5 | 0.4 | <0.1 | <0.1 | |
| 9H-Fluoren-9-one | 2.1 | 1.8 | 3.3 | 2.5 | <0.1 | <0.1 | |
| 9H-Xanthen-9-one | 0.6 | 0.7 | 0.6 | 0.5 | <0.1 | <0.1 | |
| 9,10-Anthracenedione | 8.9 | 8.6 | 7.1 | 7.1 | <0.1 | <0.1 | |
| 1,8-Naphthalic anhydride | 7.5 | 3.8 | 5.1 | 6.1 | <0.1 | <0.1 | |

| | Sampling location | | | | | | |
|--------------------------------------|------------------------------|----------------------------|------------------------------|------|----------------------------|------------------------------|-----|
| | Mechanised mining PM | | | | Conventional mining PM | | |
| | Tipping point | | LHD vehicle area | | Mean [ng m ⁻³] | Median [ng m ⁻³] | TEF |
| Mean [ng m ⁻³] | Median [ng m ⁻³] | Mean [ng m ⁻³] | Median [ng m ⁻³] | | | | |
| 4-H-Cyclopenta[def]phenanthren-4-one | 2.3 | 2.0 | 4.0 | 2.8 | <0.1 | <0.1 | |
| Benzo[b]naph-to[2,3-d]furan | <0.1 | <0.1 | <0.1 | <0.1 | <0.1 | <0.1 | |
| 11H-Benzo[a]fluoren-11-one | 5.0 | 4.9 | 6.7 | 6.4 | <0.1 | <0.1 | |
| 11H-Benzo[b]fluoren-11-one | 4.3 | 4.1 | 13 | 13 | <0.1 | <0.1 | |
| Benzo[b]naph-to[2,1-d]furan | <0.1 | <0.1 | 0.3 | <0.1 | <0.1 | <0.1 | |
| Naph-to[2,1,8,7-klmn]xanthene | <0.1 | <0.1 | <0.1 | <0.1 | <0.1 | <0.1 | |
| Benz[a]anthracene-7,12-dione | 0.2 | <0.1 | 0.8 | <0.1 | <0.1 | <0.1 | |
| 5,12-Naphthacenedione | <0.1 | <0.1 | <0.1 | <0.1 | <0.1 | <0.1 | |
| 7-Isopropyl-1-methylphenanthrene | 1.6 | 1.7 | 7.3 | 6.4 | 0.7 | <0.1 | |

suggest that the exposure to PAHs is not a main concern in similar mining environments. Currently, no OELs are defined for PAHs in South Africa.

In contrast to the mechanised mining areas, no LHD vehicles were present in the conventional mining shaft at all. Therefore, with a few exceptions, almost all detected compounds were below the LOQ. Here, the low concentrations of health relevant components resulted in mean and median TEQ values below LOQ. One possibility for the occurrence of PAHs in a LHD vehicle free area could be wooden poles, which were utilised as roof supports underground. If these wooden poles were treated with PAH containing mixtures such as creosote before use, the release of PAHs such as naphthalene into the surrounding air is not unlikely [34]. However, the existence of trace amounts of PAHs in a section without any diesel emissions could also result from the transference of airborne compounds from the outer environment of the ground level via the air inlet [35]. Further investigations concerning airborne compounds, transmitted from the external environment via the air inlet, should be taken into account. In this way, the quantity of air pollutants found underground can be assigned to emission sources in the mine considering the incoming external air quality. The dispersion of gases and PM from diesel mechanised mining sections to conventional mining sections may be possible, depending on the configuration of the shafts and the ventilation system, thus the linkages between diesel engine emissions, ventilation system parameters and occupational exposure need to be considered in assessing potential health risks underground.

Besides aromatic compounds, aliphatic substances were also found on filters in all three sampling sites. The mean and median concentrations are listed in Table 4. In general, aliphatic substan-

ces found on filter samples originated from combustion aerosols and from aerosols generated by the evaporation of lubrication oil. Thus C₁₂ to C₂₄ aliphatics can be assigned to diesel exhaust emissions, while aliphatic compounds with carbon numbers higher than C₁₇ originate from the exhaust of unburned lubricant oil [36]. Our results revealed the highest mean concentrations in the range of 64 to 204 ng m⁻³ (median: 69 to 199 ng m⁻³) for C₂₁ to C₂₉ aliphatics found on filter samples taken in the LHD vehicle area. However, for carbon numbers greater than 30, higher concentrations could be found on filters applied in the conventional mining area. Here, the utilisation of greased pneumatic drills as conventional mining tools was considered as a potential source of aerosolised aliphatic components.

3.2 Equivalent black carbon concentrations

Table 5 shows all determined eBC concentrations as mean and median values, while Figure 3 represents the online concentrations of eBC measured by four portable Aethalometers in all three sampling locations. The measurements were not carried out simultaneously, except the two measurements illustrated in Figure 3c.

In the section of mechanised mining, fluctuating eBC concentrations, partially with high peak values could be observed (Figure 3 a/b). Very high eBC concentrations of up to 1.5 mg m⁻³ were measured particularly at the tipping point, where LHD vehicles arrived to dump the ore onto the conveyor belt (Figure 3a). The fluctuations in Figure 3a are the result of time slots, where LHD vehicles either arrived at the tipping point or were absent. The evaluation of the measurement data of all three devices worn in this area revealed a high mean concentration of 326 µg m⁻³ (median: 279 µg m⁻³) (Table 5). However, higher

Table 4 GC-MS quantification results for aliphatic analytes found on filter samples. Less than (<) values were below the limit of quantification (LOQ).

| Aliphatic analytes | Sampling location | | | | | |
|---------------------------------|----------------------------|------------------------------|----------------------------|------------------------------|----------------------------|------------------------------|
| | Mechanised mining PM | | | | Conventional mining PM | |
| | Tipping point | | LHD vehicle area | | Mean in ng m ⁻³ | Median in ng m ⁻³ |
| | Mean in ng m ⁻³ | Median in ng m ⁻³ | Mean in ng m ⁻³ | Median in ng m ⁻³ | Mean in ng m ⁻³ | Median in ng m ⁻³ |
| C ₁₂ H ₂₆ | 11 | 5.0 | 5.3 | 3.6 | <0.1 | <0.1 |
| C ₁₃ H ₂₈ | 6.4 | 6.4 | 6.6 | 5.1 | <0.1 | <0.1 |
| C ₁₄ H ₃₀ | 4.9 | 4.7 | 10 | 9.5 | <0.1 | <0.1 |
| C ₁₅ H ₃₂ | 5.0 | 5.4 | 9.7 | 7.6 | <0.1 | <0.1 |
| C ₁₆ H ₃₄ | 5.8 | 6.4 | 9.0 | 8.5 | <0.1 | <0.1 |
| C ₁₇ H ₃₆ | 12 | 13 | 21 | 21 | <0.1 | <0.1 |
| C ₁₈ H ₃₈ | 11 | 10 | 18 | 16 | <0.1 | <0.1 |
| C ₁₉ H ₄₀ | 13 | 10 | 18 | 16 | 4.4 | 2.8 |
| C ₂₀ H ₄₂ | 22 | 15 | 28 | 29 | 7.3 | 6.2 |
| C ₂₁ H ₄₄ | 44 | 30 | 64 | 69 | 13 | 11 |
| C ₂₂ H ₄₆ | 95 | 54 | 148 | 153 | 12 | 13 |
| C ₂₃ H ₄₈ | 113 | 67 | 204 | 199 | 15 | 11 |
| C ₂₄ H ₅₀ | 131 | 103 | 200 | 184 | 35 | 20 |
| C ₂₅ H ₅₂ | 97 | 91 | 146 | 144 | 36 | 14 |
| C ₂₆ H ₅₄ | 93 | 92 | 130 | 122 | 46 | 25 |
| C ₂₇ H ₅₆ | 70 | 79 | 99 | 85 | 54 | 25 |
| C ₂₈ H ₅₈ | 66 | 78 | 98 | 96 | 54 | 28 |
| C ₂₉ H ₆₀ | 54 | 60 | 103 | 102 | 52 | 23 |
| C ₃₀ H ₆₂ | 30 | 31 | 52 | 54 | 53 | 31 |
| C ₃₁ H ₆₄ | 25 | 28 | 32 | 30 | 50 | 23 |
| C ₃₂ H ₆₆ | 21 | 24 | 31 | 29 | 49 | 26 |
| C ₃₃ H ₆₈ | 22 | 25 | 33 | 30 | 46 | 23 |
| C ₃₄ H ₇₀ | 17 | 19 | 28 | 25 | 38 | 15 |
| C ₃₅ H ₇₂ | 21 | 22 | 22 | 19 | 34 | 18 |
| C ₃₆ H ₇₄ | 17 | 15 | 21 | 21 | 27 | 9.6 |
| C ₃₇ H ₇₆ | 12 | 13 | 18 | 17 | 22 | 8.3 |
| C ₃₈ H ₇₈ | 16 | 17 | 18 | 19 | 22 | 8.2 |
| C ₃₉ H ₈₀ | 17 | 19 | 14 | 10 | 24 | 14 |
| C ₄₀ H ₈₂ | 21 | 21 | 23 | 21 | 45 | 27 |

mean and median concentrations were found in the LHD vehicle area.

In the LHD vehicle area a high overall mean eBC concentration of 657 µg m⁻³ (median: 350 µg m⁻³) could be observed (Table 5). Here, the highest mean concentration overall of 1,439 µg m⁻³ (median: 450 µg m⁻³) was measured. The other instrument measured lower concentrations with a mean value of 307 µg m⁻³ (median: 295 µg m⁻³). The very high eBC concentrations observed in this area are the result of the direct exposure of miners to diesel exhaust emissions or their work was performed in areas with a steady operation of diesel engines. In view of this, Figure 3b shows the online eBC concentrations correlated to

the operating procedures of the LHD vehicle engine. It transpires that the engine loads were changing quickly depending on the three working steps load, haul and dump. In addition, these vehicles often reversed. This resulted in fluctuating peak values as well as the higher eBC concentrations the drivers were exposed to. The high eBC concentrations measured are of concern, when compared to the BOELV of 50 µg m⁻³ for EC, which will be in place in the European Union from 2026. Even though a calibration factor is needed to convert eBC measurements in EC equivalents, the high eBC concentrations measured in the mechanised mining area show that exposure to diesel exhaust can be an issue in mining environments.

Table 5 Mean and median eBC concentrations determined via online Aethalometer measurements in different mine areas [22].

| | eBC concentrations | |
|------------------------------|------------------------------|--------------------------------|
| | Mean in $\mu\text{g m}^{-3}$ | Median in $\mu\text{g m}^{-3}$ |
| Tipping point | | |
| Worker 1 | 334 | 336 |
| Worker 2 | 264 | 245 |
| Worker 3 | 379 | 231 |
| Overall mean / median values | 326 | 279 |
| LHD vehicle area | | |
| Worker LHD 1 | 1439 | 450 |
| Worker LHD 2 | 307 | 295 |
| Worker LHD 3 | 559 | 540 |
| Overall mean / median values | 657 | 350 |
| Conventional mining | | |
| Worker 1 | 2.0 | 1.9 |
| Worker 2 | 2.0 | 2.2 |
| Overall mean/median values | 2.0 | 2.1 |

Figure 3c shows the online eBC concentrations within the conventional mining section. Each of the two workers wore one instrument simultaneously. Compared to the mechanised mining area, these eBC concentration levels were much lower and rather constant during the whole measurement interval since no LHD vehicles were present at all. The total mean and median eBC concentrations in the conventional mining area were $2 \mu\text{g m}^{-3}$ (Table 5).

As expected, there was no BrC measured, neither in the conventional nor in the mechanised mining section. This is in agreement with Corbin et al. [37], who found that BrC is commonly negligible for diesel engine exhaust due to the high temperature of combustion. Moreover, the low concentrations of organic compounds, such as PAHs and alkanes, underline the huge disproportion of organic material to eBC emitted by diesel engines.

4 Conclusion

The objective of this feasibility study was to perform an assessment of the potential exposure of mine workers to health relevant particulate compounds, such as eBC and PAHs, using a portable Aethalometer and a personal aerosol sampler. The results obtained revealed that the area with the highest exposure measured by the personal samplers was the LHD vehicle area, followed by the tipping point. Compared to the conventional mining area, the eBC concentrations measured in the mechanised mining sections were much higher. Since BC is an emission product and has a large surface area, it is capable of adsorbing high concentrations of PAHs. Therefore, the calculated TEQ values assigned to the mechanised mining areas were much higher than those values

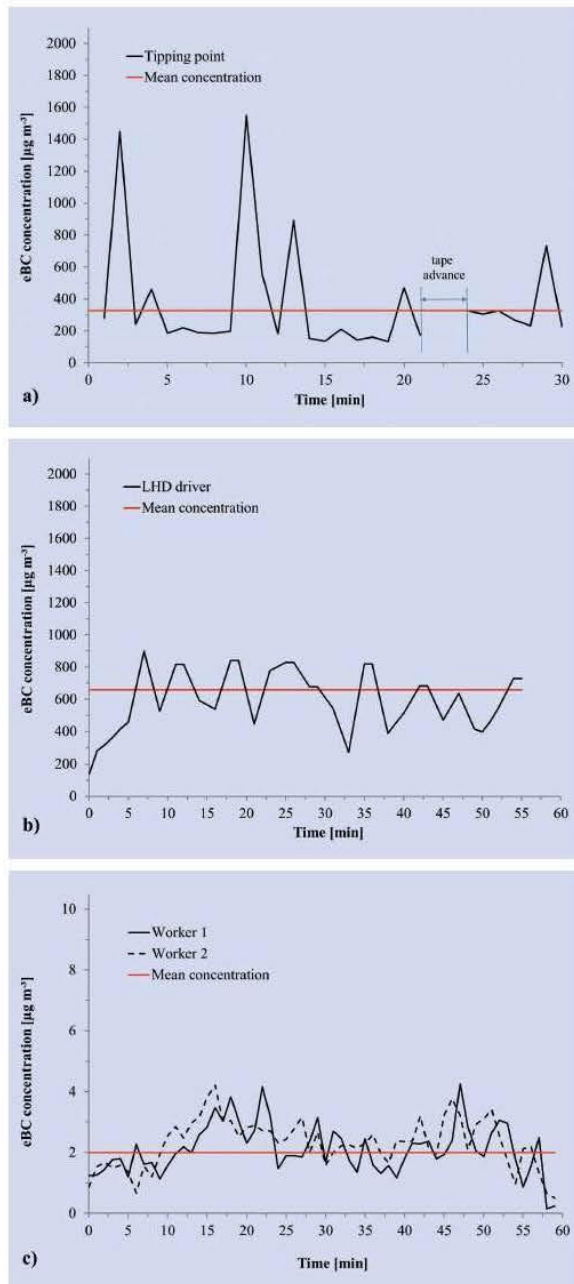


Figure 3 eBC_(880 nm) Concentrations measured online at three different sampling locations; 3a shows the eBC concentration at the tipping point; 3b shows the eBC concentration in the LHD vehicle area; 3c shows the eBC concentration in the conventional mining area. Here, two workers wore the instruments at the same time. The red straight lines indicate the mean eBC concentrations measured in each area. Graphic: Authors

determined for the non-diesel shaft, where no BC was emitted. However, compared to the eBC concentrations, the determined PAH concentrations were much lower by around four orders of magnitude.

Finally three main outcomes were found in this feasibility study which require further investigation:

1. Sampling duration for PM also requires further consideration, as variations in eBC concentration were detected by the Aethalometer, which infers large changes in organic compounds concentrations during a working shift as well.
2. The portable Aethalometer is well suited for occupational monitoring of soot emissions, as areas of high exposure and exposure peaks can be easily identified, given the direct-reading measurement principle. We showed in this feasibility study that the Aethalometer can be an appropriate instrument for measuring black carbon in underground metal mines. A calibration factor for diesel soot, between the eBC concentration measured by the Aethalometers and the concentration of elemental carbon, such as the established NIOSH 5040 [38] or DGUV Information 213–544 [39] methods could be very advantageous for occupational monitoring purposes. This parameter should be monitored in general in diesel mechanised underground working areas.
3. Last but not least, in further studies the number of workers wearing personal samplers should be increased. The sampling strategy should take into consideration that the sampling duration shall be representative for a work shift and personal sampling should be conducted over several working days/shifts in order to obtain a statistically reliable number of samples.

4.1 Study limitations

The eBC measurements with the portable Aethalometer without a size-selective inlet can only be performed in mines where interference from coal dust is not expected. Coal dust can interfere with the eBC reading of soot, making a particle size-selective inlet a prerequisite for coal mining environments. Occupational exposure limits for diesel emissions are usually set for the concentration of elemental carbon, as measured by the NIOSH 5040 or DGUV Information 213–544 [39] methods. For occupational studies, a conversion factor between eBC and elemental carbon would be necessary.

Our study did not consider the exposure against silica, metals, nitrogen oxides or volatile organic compounds, which may also be of concern in mining environments.

4.2 Conflicts of interest

There are no conflicts to declare.

ACKNOWLEDGEMENTS

This work was supported by the German Social Accident Insurance (DGUV), research contract FP-371 and the Federal Ministry of Education and Research (BMBF), research contract 01DG17023. The South African National Research Foundation (NRF) is acknowledged for joint funding of the project (grant 105877) via the German/South Africa Research Collaboration Programme. The excellent work (construction and machining of the aerosol samplers) of Mr. *Thomas Gerlach* and his team at the Helmholtz mechanical workshop is thankfully acknowledged. Assistance at the mine and of mine management is gratefully acknowledged including the workers who wore the devices.

References

- [1] *Cho, K. S.; Lee, S. H.*: Occupational health hazards of mine workers. Bulletin of the World Health Organization (1978) vol. 56, pp. 205-218.
- [2] Mining Review Africa 2019. Mining health safety – 7 common risks to protect yourself against. www.miningreview.com/features-analysis/mining-health-safety-7-common-risks-to-protect-yourself-against/
- [3] *Benbrahim-Tallaa, L.; Baan, R. A.; Grosse, Y.; Lauby-Secretan, B.; El Ghissassi, F.; Bouvard, V. et al.*: Carcinogenicity of diesel-engine and gasoline-engine exhausts and some nitroarenes. The Lancet Oncology (2012) vol. 13, pp. 663-664.
- [4] World Health Organization. IARC: Diesel engine exhaust carcinogenic. Press release N° 213 (2012). France. 4 pp.
- [5] *Ono-Ogasawara, M.; Smith, T. J.*: Diesel exhaust particles in the work environment and their analysis. Industrial Health (2004) vol. 42, pp. 389-399.
- [6] *Wichmann, H. E.*: Diesel exhaust particles. Inhalation Toxicology (2007) vol. 19, pp. 241-244.
- [7] *Xu, Y.; Zhang, J. S.*: Understanding SVOC. ASHRAE Journal (2011) vol. 53, pp. 121-125.
- [8] *Oeder, S.; Kanashova, T.; Sippula, O.; Sapcariu, S. C.; Streibel, T.; Arteaga-Salas, J. M. et al.*: Particulate matter from both heavy fuel oil and diesel fuel shipping emissions show strong biological effects on human lung cells at realistic and comparable in vitro exposure conditions. Plos One (2015) vol. 10, pp. 1-17.
- [9] *Okuda, T.; Schauer, J. J.; Olson, M. R.; Shafer, M. M.; Rutter, A. P.; Walz, K. A.; Morschauer, P. A.*: Effects of a platinum-cerium bimetallic fuel additive on the chemical composition of diesel engine exhaust particles. Energy & Fuels (2009) vol. 23, pp. 4974-4980.
- [10] *Passig, J.; Schade, J.; Oster, M.; Fuchs, M.; Ehlert, S.; Jäger, C. et al.*: Aerosol mass spectrometer for simultaneous detection of polyaromatic hydrocarbons and inorganic components from individual particles. Analytical Chemistry (2017) vol. 89, pp. 6341-6345.
- [11] *Schade, J.; Passig, J.; Irsig, R.; Ehlert, S.; Sklorz, M.; Adam, T. et al.*: Spatially shaped laser pulses for the simultaneous detection of polycyclic aromatic hydrocarbons as well as positive and negative inorganic ions in single particle mass spectrometry. Analytical Chemistry (2019) vol. 91, pp. 10282-10288.
- [12] *Rynning, I.; Arit, V. M.; Vrbova, K.; Neča, J.; Rossner, P.; Klema, J. et al.*: Bulky DNA adducts, microrna profiles, and lipid biomarkers in norwegian tunnel finishing workers occupationally exposed to diesel exhaust. Occupational and Environmental Medicine (2019) vol. 76, pp. 10-16.
- [13] *Wu, X.; Lintelmann, J.; Klingbeil, S.; Li, J.; Wang, H.; Kuhn, E. et al.*: Determination of air pollution-related biomarkers of exposure in urine of travellers between germany and china using liquid chromatographic and liquid chromatographic-mass spectrometric methods: A pilot study. Biomarkers (2017) vol. 22, pp. 525-536.
- [14] *Weiss, T.; Breuer, D.; Bury, D.; Friedrich, C.; Werner, S.; Aziz, M. et al.*: (Mono-) Exposure to Naphthalene in the Abrasives Industry: Air Monitoring and Biological Monitoring. Annals of Work Exposures and Health 64 (2020) vol. 9, pp. 982-992. [org/10.1093/annweh/wxaa062](https://doi.org/10.1093/annweh/wxaa062)
- [15] Human respiratory tract model for radiological protection. ICRP publication 66 (1994) vol. 24 (1-3).
- [16] *Heyder, J.*: Deposition of inhaled particles in the human respiratory tract and consequences for regional targeting in respiratory drug delivery. Proceedings of the American Thoracic Society (2004) vol. 1, pp. 315-320.
- [17] *Ferron, G. A.; Haider, B.; Kreyling, W. G.*: Inhalation of salt aerosol particles-I. Estimation of the temperature and relative humidity of the air in the human upper airways. Journal of Aerosol Science (1988) vol. 19, pp. 343-363.
- [18] *Ferron, G. A.; Upadhyay, S.; Zimmermann, R.; Karg, E.*: Model of the deposition of aerosol particles in the respiratory tract of the rat. II. Hygroscopic particle deposition. Journal of Aerosol Medicine and Pulmonary Drug Delivery (2013) vol. 26, pp. 101-119.
- [19] *Kreyling, W. G.; Hirn, S.; Schleh, C.*: Nanoparticles in the lung. Nature Biotechnology (2010) vol. 28, pp. 1275-1276.
- [20] *Kreyling, W. G.; Möller, W.; Semmler-Behnke, M.; Oberdörster, G.*: Particle dosimetry: Deposition and clearance from the respiratory tract and translocation towards extra-pulmonary sites. Particle toxicology (2007), pp. 47-74. CRC Press Taylor & Francis Group. Florida.
- [21] *Stone, K. C.; Mercer, R. R.; Gehr, P.; Stockstill, B.; Crapo, J. D.*: Allometric relationships of cell numbers and size in the mammalian lung. American Journal of Respiratory and Molecular Biology (1992) vol. 6, pp. 235-243.
- [22] *Kohlmeier, V.*: Development and Application of Novel Portable Personal Aerosol Samplers for Partitioned Sampling of Aerosolised Semi-

- Volatile Organic Compounds in Workplace Environments. Dissertation, Universität Rostock 2019.
- [23] Hutchinson, D.; Foster, J.; Prichard, H.; Gilbert, S.: Concentration of particulate platinum-group minerals during magma emplacement; a case study from the merensky reef, bushveld complex. *Journal of Petrology* (2015) vol. 56, pp. 113-159.
- [24] Dragan, G. C.; Kohlmeier, V.; Orasche, J.; Schnelle-Kreis, J.; Forbes, P. B. C.; Breuer, D.; Zimmermann, R.: Development of a Personal Aerosol Sampler for Monitoring the Particle-Vapour Fractionation of SVOC in Workplaces. *Annals of Work Exposures and Health* 64 (2020) vol. 8, pp. 903-908. 10.1093/annweh/wxaa059
- [25] DFG, German Research Foundation: Polycyclic aromatic hydrocarbons (PAH) – MAK value documentation. The MAK collection for occupational health and safety, pp. 1-216. Wiley-VCH, 2012.
- [26] Gestis International Limit Values Database. limitvalue.ifa.dguv.de/
- [27] Olson, M. R.; Garcia, M. V.; Robinson, M. A.; van Rooy, P.; Dietersberger, M. A.; Bergin, M.; Schauer, J. J.: Investigation of black and brown carbon multiple-wavelength-dependent light absorption from biomass and fossil fuel combustion source emissions. *Journal of Geophysical Research: Atmospheres* (2015) vol. 120, pp. 6682-6697.
- [28] Petzold, A.; Ogren, J. A.; Fiebig, M.; Laj, P.; Li, S. M.; Baltensperger, U. et al.: Recommendations for reporting „black carbon“ measurements. *Atmospheric Chemistry and Physics* (2013) vol. 13, pp. 8365-8379.
- [29] Feng, Y.; Ramanathan, V.; Kotamarthi, V. R.: Brown carbon: A significant atmospheric absorber of solar radiation? *Atmospheric Chemistry and Physics* (2013) vol. 13, pp. 8607-8621.
- [30] Lack, D. A.; Moosmüller, H.; McMeeking, G. R.; Chakrabarty, R. K.; Baumgardner, D.: Characterizing elemental, equivalent black, and refractory black carbon aerosol particles: A review of techniques, their limitations and uncertainties. *Analytical and Bioanalytical Chemistry* (2014) vol. 406, pp. 99-122.
- [31] Noll, J. D.; Janisko, S.: Evaluation of a Wearable Monitor for Measuring Real-Time Diesel Particulate Matter Concentrations in Several Underground Mines. *Journal of Occupational and Environmental Hygiene* 10 (2013) vol. 12, pp. 716-722. 10.1080/15459624.2013.821575
- [32] Noll, J.; Janisko, S.; Mischler, S. E.: Real-time diesel particulate monitor for underground mines. *Analytical methods: advancing methods and applications* (2013), vol. 5, pp. 2954-2963. 10.1039/C3AY40083B
- [33] Tsai, C. S.-J.; Shin, N.; Brune, J.: Evaluation of Sub-micrometer-Sized Particles Generated from a Diesel Locomotive and Jackleg Drilling in an Underground Metal Mine. *Annals of Work Exposures and Health* 64 (2020) vol. 8, pp. 876-889. 10.1093/annweh/wxaa069
- [34] Gallego, E.; Roca, F. J.; Perales, J. F.; Guardino, X.; Berenguer, M. J.: VOC and pahs emissions from creosote-treated wood in a field storage area. *Science of The Total Environment* (2008) vol. 402, pp. 130-138.
- [35] Geldenhuys, G., Rohwer, E. R., Naudé, Y. & Forbes, P. B. C.: Monitoring of atmospheric gaseous and particulate polycyclic aromatic hydrocarbons in south african platinum mines utilising portable denuder sampling with analysis by thermal desorption-comprehensive gas chromatography-mass spectrometry. *Journal of Chromatography A* (2015) vol. 1380, pp. 17-28.
- [36] Maricq, M. M.: Chemical characterization of particulate emissions from diesel engines: A review. *Journal of Aerosol Science* 38 (2007) vol. 11, pp. 1079-1118. 10.1016/j.jaerosci.2007.08.001
- [37] Corbin, J. C.; Pieber, S. M.; Czech, H.; Zanatta, M.; Jakobi, G.; Massabó, D. et al.: Brown and black carbon emitted by a marine engine operated on heavy fuel oil and distillate fuels: Optical properties, size distributions, and emission factors. *Journal of Geophysical Research: Atmospheres* (2018) vol. 123, pp. 6175-6195.
- [38] NIOSH Method 5040: Diesel Particulate Matter (as Elemental Carbon) NIOSH Manual of Analytical Methods (NMAM), Fourth Edition
- [39] DGUV Information 213-544: Verfahren zur Bestimmung von Kohlenstoff im Feinstaub – anwendbar für partikelförmige Dieselmotor-Emissionen in Arbeitsbereichen. Hrsg.: Deutsche Gesetzliche Unfallversicherung e.V. (DGUV), Berlin 1995.

Dr. Vesta Geitner

Dr. Juergen Orasche

Dr. Gert Jakobi

Dr. Juergen Schnelle-Kreis

Dipl. Met. Erwin W. Karg

Joint Mass Spectrometry Centre, Helmholtz Zentrum München, Oberschleißheim.

Dr. George C. Dragan

Bundesanstalt für Arbeitsschutz und Arbeitsmedizin (BAuA), Dortmund.

M.Sc. Genna-Leigh Geldenhuys

Prof. Dr. Patricia B. C. Forbes

University of Pretoria, South Africa.

Prof. Dr. Dietmar Breuer

Institut für Arbeitsschutz der Deutschen Gesetzlichen Unfallversicherung (IFA), Sankt Augustin.

Prof. Dr. Ralf Zimmermann

Joint Mass Spectrometry Centre, Universität Rostock, Rostock.

Appendix B: Co-authored paper 2

This paper was published in Air Quality, Atmosphere & Health.

Gawlitta; N., Orasche; J., Geldenhuys; G., Jakobi; G., Wattrus, M., Jennerwein; M., Michalke; B., Gröger; T., Forbes; P.B.C. and Zimmermann, R. 2022. A study on the chemical profile and the derived health effects of heavy-duty machinery aerosol with a focus on the impact of alternative fuels. *Air Quality, Atmosphere & Health* :1-17. DOI: <https://doi.org/10.1007/s11869-022-01287-9>.



A study on the chemical profile and the derived health effects of heavy-duty machinery aerosol with a focus on the impact of alternative fuels

Nadine Gawlitta^{1,2} · Jürgen Orasche¹ · Genna-Leigh Geldenhuys^{3,4} · Gert Jakobi¹ · Mark Wattrus⁵ · Maximilian Jennerwein⁶ · Bernhard Michalke⁷ · Thomas Gröger¹ · Patricia Forbes³ · Ralf Zimmermann^{1,2}

Received: 24 May 2022 / Accepted: 17 November 2022
© The Author(s) 2022

Abstract

The combustion of petroleum-based fossil fuels is associated with a high environmental burden. Several alternative fuels, including synthetic fuels (e.g., gas-to-liquid, GTL) and biofuels (e.g., rapeseed methyl ester, RME) have been studied in the last few years. While the advantages for the environment (sustainability of biofuels) are well known, research on the resulting health effects from combustion aerosols of these alternative fuels is still scarce. Consequently, we investigated the chemical combustion profile from three distinct fuel types, including a petroleum-based fossil fuel (B0) and two alternative fuels (GTL, RME) under real exposure conditions. We sampled particulate matter (PM_{2.5}, PM_{0.25}) and the gas phase from heavy-duty machinery and evaluated the general pattern of volatile and semi-volatile organic compounds, elemental and organic carbon as well as a range of transition metals in the size segregated PM and/or gas phase. The use of comprehensive two-dimensional gas chromatography time-of-flight mass spectrometry enabled us to classify distinct methylated PAHs in the PM samples and its high abundance, especially in the fine fraction of PM. We found that (methylated) PAHs were highly abundant in the PM of B0 compared to GTL and RME. Highest concentrations of targeted aromatic species in the gas phase were released from B0. In summary, we demonstrated that GTL and RME combustion released lower amounts of chemical compounds related to adverse health effects, thus, the substitution of petroleum-based fuels could improve air quality for human and the environment.

Keywords Alternative fuels · Combustion aerosol · (methylated) PAHs · Ultrafine particulate matter · Health effects

Introduction

Heavy-duty vehicles are in use on construction sites, in mines, and in other working environments and contribute to a considerable extent to the local air pollution (Traviss et al. 2010; Gautam et al. 2018; Salo et al. 2021). These heavy-duty vehicles are typically powered by fossil fuel. The increasing environmental burden resulting from petroleum-based fossil fuel combustion has led to the ongoing search for alternative fuels (Unosson et al. 2021). Several advantages can be discussed supporting a substitution of petroleum-based fuels by alternative fuels. CO₂ and greenhouse gas (GHG) emissions are lower for alternative fuels compared to petroleum-based fuel combustion (Moon et al. 2010; Zaharin et al. 2017), decreasing the environmental burden, e.g., in terms of its negative impact on climate. Regarding biofuel, several organic feedstocks are available enabling a sustainable way of fuel production. Therefore,

✉ Thomas Gröger
thomas.groeger@helmholtz-muenchen.de

- 1 Joint Mass Spectrometry Centre (JMSC), Cooperation Group Comprehensive Molecular Analytics, Helmholtz Zentrum München, Neuherberg, Germany
- 2 Joint Mass Spectrometry Centre (JMSC), Chair of Analytical Chemistry, University of Rostock, Rostock, Germany
- 3 Department of Chemistry, Faculty of Natural and Agricultural Sciences, University of Pretoria, Pretoria, South Africa
- 4 Processing Laboratory, Impala Platinum Limited, Rustenburg, South Africa
- 5 Energy Business, Sasol, Cape Town, South Africa
- 6 ASG Analytik-Service AG, Neusäß, Germany
- 7 Research Unit Analytical BioGeoChemistry, Helmholtz Zentrum München, Neuherberg, Germany

biofuels are a prominently discussed alternative to petroleum-based fuels (Traviss et al. 2010; Sakthivel et al. 2018; Unosson et al. 2021). Biofuels can be generated from oil-producing crops, and vegetable oils can be utilized in a pure or transesterified form into biodiesel. Other feedstocks are sugar or starch crops for the production of alcohols such as methanol or ethanol (Yasin et al. 2019). Biofuels from oil-producing crops can be separated in three different generations including vegetable oil (first generation), nonedible vegetable oil (second generation), and waste cooking oil (third generation) (Sakthivel et al. 2018). The chemical and physical properties of a biofuel are mostly dependent on the feedstock. For example, waste cooking oil is a widely used biofuel due to its low cost, but it has inferior cold-flow properties, which limits its use in winter months (Moon et al. 2010). Up to now, biofuels are mostly utilized as diesel–biodiesel blends to overcome difficulties in terms of cold-flow properties as well as long-term negative consequences of the use of pure biofuel such as injector coking, deposits, and ring sticking (Moon et al. 2010). Several studies have been conducted to increase the efficiency of biodiesel use compared to petroleum-derived diesel, but still, contradictory data is available on the emissions of biodiesel combustion and resulting health effects (Bluhm et al. 2012; Møller et al. 2020). A typical feedstock of vegetable oil widely used is rapeseed methyl ester (RME). This fuel is gained by the transesterification of rapeseed oil. RME is primarily composed of fatty acid methyl esters (FAMES) with different lengths of alkyl chains. As this fuel has no aromatic content, polycyclic aromatic hydrocarbons (PAHs) cannot be emitted by unburned fuel. Another alternative widely discussed in the substitution of petroleum-based fuel is the synthetic gas-to-liquid (GTL) fuel. It is gained by, e.g., the Fischer–Tropsch process from natural gas, leading to a fuel with negligible amounts of aromatic compounds and sulfur (Li et al. 2007; Moon et al. 2010). GTL can usually be used in conventional diesel engines without any engine hardware modifications (Moon et al. 2010). This fuel is primarily composed of long-chain alkanes and, thus, expected to emit lower amounts of PM, in particular, PAHs compared to fossil fuel combustion. Recently, an alternative to the synthetic GTL has gained more attention, the so-called biomass-to-liquid (BTL) fuel, which is produced in a similar way as the GTL after gasification from biomass (van Steen and Claeys 2008).

Generally, fuel combustion releases high quantities of particles. This particulate matter (PM) is physically characterized by its aerodynamic diameter (size distribution) and mass. Only particles with an aerodynamic diameter equal to or smaller than 2.5 μm are expected to deeply penetrate into the respiratory tract (Hussain et al. 2011). The particles themselves and the semi-volatile organic compounds (SVOCs) bound to the particles can be released into the

lung leading to acute and inflammatory effects (Salo et al. 2021). Recently, the WHO updated their guidelines in which they suggest even lower maximum exposure levels for $\text{PM}_{2.5}$ and other air pollutants due to their known adverse health effects, e.g., the increased risk of respiratory and cardiovascular diseases (Lin et al. 2015; World Health Organization 2021). Moreover, the importance of further characterizing specific PM such as ultrafine particles (UFP) was emphasized (World Health Organization 2021). UFP are particles with an aerodynamic diameter smaller than 0.1 μm . Due to their low size, UFP are physically not restricted to the respiratory tract but can also be translocated to other organs via the bloodstream (Hussain et al. 2011). Moreover, UFP have a high-specific surface area and, thus, vast amounts of organic compounds can be adsorbed onto these particles. The translocation and the intense loading are expected to have adverse health effects and highlight the need for further characterization of UFP (Kwon et al. 2020).

Aerosol from fossil fuel combustion is loaded with a plethora of different chemical components, of which polycyclic aromatic hydrocarbons (PAHs) are of specific health concern. Many PAHs are known to be carcinogenic and mutagenic (Abdel-Shafy and Mansour 2016). Due to their gas-to-particle equilibrium, they can occur particle-bound or in the gas phase. For single compounds, their presence in either of these phases mostly depends on their molecular weight and vapor pressure. For complex samples such as aerosol produced by combustion processes, the gas-to-particle partitioning is mostly influenced by the ambient air temperature and the total organic aerosol concentration (C_{OA}) (Shrivastava et al. 2006). At high C_{OA} and, thus, low dilution ratios the SVOCs are prone to be absorbed into the particle phase (Lipsky and Robinson 2006; Shrivastava et al. 2006). Working environments like construction sites and mines are using vehicles, which emit high amounts of combustion aerosol. During their working shifts, workers may be exposed to high amounts of potentially hazardous air pollutants when operating this kind of heavy-duty machinery. It is, thus, important to gain further insights on the combustion aerosol of distinct fuel types and their possible resulting health effects on employees.

In this study, we focused on the comparison of the chemical profile of the combustion aerosols from three distinct fuel types and their possible health-related effects on workers in a confined working environment. For this purpose, we sampled particles and gas phase of a heavy-duty (Load-Haul-Dump, LHD) vehicle fueled with petroleum-derived fossil fuel (B0), GTL, and RME in a South African platinum mine (1000 m underground). As ventilation may be insufficient and space limited, occupational exposure to combustion aerosols in mining environments is of specific concern (Salo et al. 2021). We aimed at comparing the exposure profile of the currently used diesel fuel to the alternative fuels (GTL,

RME) to enable a comprehensive characterization of the chemical compounds emitted and to estimate their possible health-related effects. Combustion aerosol of the three fuel types was sampled in terms of $PM_{2.5}$, size-segregated PM with an emphasis on $PM_{0.25}$, and the gas phase.

The analysis of PM samples focused on the chemical characterization of substituted and unsubstituted PAHs in the combustion aerosol of the different fuel types, and a comparative analysis of the different size fractions. We also investigated alkylated PAHs were classified based on their aromatic core and methylation pattern. Moreover, concentrations of seven distinct unsubstituted PAHs (phenanthrene, anthracene, fluoranthene, pyrene, benz(a)anthracene, benz(e)pyrene, benz(a)pyrene) were calculated, and toxic equivalents (TEQs) were determined. Additionally, the elemental composition of the PM samples regarding transition metals, alkaline metals, and other elements was performed and compared between the different combustion aerosols. The worker exposure to the gas phase was compared between B0, GTL, and RME highlighting their differences in aromatic carbon content. In particular, concentrations of benzene, toluene, o-xylene, naphthalene, and biphenyl were calculated and compared for the gas phase of the different combustion aerosols. Finally, the gaseous organic compounds, mainly volatile organic compounds (VOCs), were collected in two distinct sampling positions (engine operator and tailpipe), enabling a more comprehensive comparison of concentrations workers could be exposed to during working procedures.

Experimental section

Sampling site

Aerosol sampling was conducted in a platinum mine in South Africa 1000 m underground. The heavy-duty vehicle used in this sampling campaign was a load-haul-dump (LHD) vehicle typically used in this underground mine. The sampling station was 1.5 m from the tailpipe (TP) as well as 1 m above ground (Fig. 1a).

The following samples have been taken: $PM_{2.5}$, size-segregated PM (Sioutas, $n=3$), gas phase during test cycle (TeC), and gas phase in high idling (HI) mode of the LHD (Fig. 1b). Gas phase samples were additionally taken at the LHD operator position (OP) at human chest height during TeC and in HI mode (Fig. 1a). The complete sample set and the conducted chemical analysis are summarized in Table 1.

Engine operations

The LHD was equipped with a Deutz BF 6L 914C engine. Engine specifications are summarized in following Table 2.

The LHD was filled with the specific fuel type at the beginning of each sampling day. For that purpose, the remaining fuel was drained from the LHD, fuel filters and air filters were exchanged and the tank was flushed with 20 L of the test fuel before filling the tank. Lubrication oil was exchanged prior sampling. Afterwards, the LHD returned to work in production for 30 min before returning to the test site. For aerosol sampling, the LHD vehicle was parked at the common parking area of those vehicles at which the sampling was conducted without movement. A pre-conditioning cycle was performed for 10 min to ensure temperature

Table 1 Summary of samples taken and analysis carried out. EC elemental carbon, OC organic carbon

| | B0 | GTL | RME |
|---------------------|---|--------------------------|--------------------------|
| PM analysis | | | |
| EC/OC | $PM_{2.5}$, $PM_{0.25}$ | $PM_{2.5}$, $PM_{0.25}$ | $PM_{2.5}$, $PM_{0.25}$ |
| Elements by ICP-AES | $PM_{2.5}$, $PM_{0.25}$ | $PM_{2.5}$, $PM_{0.25}$ | $PM_{2.5}$, $PM_{0.25}$ |
| SVOC by GC×GC-MS | $PM_{2.5}$, $PM_{0.25}$, size-segregated PM | $PM_{2.5}$, $PM_{0.25}$ | $PM_{2.5}$, $PM_{0.25}$ |
| Gas phase analysis | | | |
| VOC by GC-MS | TP (TeC, HI) | TP (TeC, HI) | TP (TeC, HI) |
| VOC by GC-MS | OP (TeC, HI) | OP (TeC, HI) | OP (TeC, HI) |

Fig. 1 Underground sampling site of combustion aerosols. Sampling station and additional gas phase sampling at the operator are depicted (a). Main sampling station. Samples taken from left to right (b): $PM_{2.5}$, size-segregated PM, and gas phase

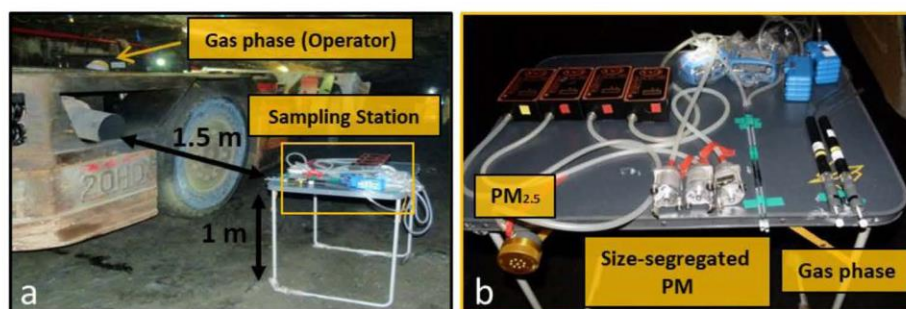


Table 2 Engine specifications of a Deutz BF 6L 914C engine

| Emission certification | Tier 2 |
|---------------------------|--|
| No. of cylinders | 6 |
| Bore/stroke | 102/132 mm |
| Displacement | 6.5 L |
| Compression ratio | 18 |
| Stroke | 132 mm |
| Rated power | 141 kW (herein de-rated to 118 kW) |
| Max. torque | 700 Nm at 1600 rpm |
| Induction | Charged air cooled |
| Fuel injection | Five-hole nozzle injection; high pressure in-line injector pump with mechanical centrifugal governor |
| Specific fuel consumption | 210 g (kWh) ⁻¹ |

stabilization prior aerosol sampling. Aerosol sampling was conducted in 10-min intervals in the two modes. High idling (HI) was conducted with full acceleration and 0% throttle. The test cycle (TC) was done including a bucket lift with a fixed mass (one tire) which should mimic a load test. More information on engine operations by LHD vehicles can be found in Watrus et al. (2016).

Fuel types

Three different fuels were used for sampling of the corresponding combustion aerosol: (1) a petroleum-derived diesel fuel with no biofuel content (B0), representing the reference diesel used in the working place, (2) a paraffinic fuel (GTL, ORYX, Qatar) compatible with EN15940, and (3) a biofuel (RME, SBE BioEnergie, Germany) according to EN14214 additivized with oxidation stabilizer. The organic composition of B0 and lubrication oil used in this study was characterized by GC×GC-ToFMS and the elemental composition of lubrication oil was also determined by ASG Analytik-Service AG. Fuel properties and composition of GTL and RME were analyzed by Sasol Limited. Further information on the composition and properties of fuel and lubrication oil used can be found in Tables S1–S6.

Sampling and analysis of PM

PM was sampled on quartz fiber filters (QFF) (Quartz-Microfibre Discs, Ahlstrom-Munksjö, Finland) with a deployable particulate sampler (DPS) (SKC Inc., USA) and a cut-off of 2.5 µm. These PM_{2.5} samples were continuously sampled for all three fuel types during TeC and HI mode at a flow of 10 L min⁻¹ for 21 min in total. In a similar manner, size-segregated PM was sampled with a Sioutas five-stage cascade impactor (SKC Inc., USA) at a flow of 9 L min⁻¹ for 21 min. The five size ranges include > 2.5, 2.5–1.0, 1.0–0.5, 0.5–0.25 and < 0.25 µm. Samples were collected on

a 25-mm QFF on the different stages and on a 37-mm QFF (Quartz-Microfibre Discs, Ahlstrom-Munksjö, Finland) on an after-filter (< 0.25 µm). PM samples were taken at the main sampling station solely (Fig. 1). Three experimental replicates were taken for the size-segregated samples for every fuel type (Fig. 1b). Filter samples were kept in the corresponding samplers for transport until filter exchange could be carried out under clean surrounding conditions at the same day. Samples were stored at – 20 °C until analysis.

PM samples were prepared on the day of analysis. QFF were cut by defined punches (*d* = 2 mm) and placed into glass inserts for the direct thermal desorption unit for analysis. These glass inserts were deactivated with trimethylchlorosilane (TMCS, Fisher Scientific, Germany) prior use. The analyzed filter corresponded to 1.64 × 10⁻² m³ for the stages, 7.47 × 10⁻⁴ m³ for PM_{0.25} and 8.10 × 10⁻⁴ m³ for PM_{2.5} samples of collected aerosol. 1 µL of an internal standard (ISTD) was applied to the QFFs by an autosampler (PAL 3 DHR, CTC Dual Head) prior to analysis (see Table S7 for ISTD).

Determination of SVOC on PM was conducted on a direct thermal desorption (DTD) comprehensive two-dimensional gas chromatography (GC×GC) time-of-flight mass spectrometer (ToF-MS, Pegasus BT 4D, LECO, USA). An OPTIC-4 inlet system (GL Sciences, Netherlands) was used. The GC column setup was as follows: A BPX5 capillary column (60 m, 0.25 mm i.d., 0.25 µm d_f, SGE, Australia) was installed as the first dimension and a BPX50 capillary column (1.4 m, 0.1 mm i.d., 0.1 µm d_f, SGE, Australia) was installed as the second dimension. A BPX5 capillary column (2 m, 0.25 mm i.d., 0.25 µm d_f, SGE, Australia) was additionally installed as a pre-column. A temperature gradient of 2 °C min⁻¹ in the temperature range of 40 to 330 °C was applied for GC analysis. More detailed information on the applied methodology for thermal desorption and gas chromatographic separation can be found in Tables S7–S9. The MS transfer line and ion source temperature were set to 300 °C and 250 °C, respectively. The mass acquisition was from 35 to 700 Da at an acquisition rate of 100 spectra/s. The electron energy applied was 70 eV.

Data acquisition and processing were carried out using the ChromaTOF software (Version 5.5, LECO, USA). Peak finding was conducted for the complete run with a signal-to-noise (S/N) set to 300. Total ion chromatogram (TIC) was used as a quantitation signal. The spectral match required for peak combination was 800. The spectral similarity was compared with the National Institute of Standards and Technology (NIST) library (version 2.3, 2017). The mass range compared for library search was 35 to 600 m/z. The relative abundance threshold was set to 10. The minimum similarity for matches was set to 700 before the hit was assigned. For the classification of alkylated PAHs, distinct retention time regions were marked and spectral filters specific to those PAHs were assigned. Unsubstituted PAHs were targeted using their molecular mass ion and their elution on the selected column with respect to their deuterated standard. Internal standards were applied for quantification (Table S10).

We applied ChromaToF Tile (version 0.27.2.0, Leco, USA) to perform a comparative analysis of the SVOC pattern of PM_{0.25} samples. Supervised principal component analysis (ANOVA-PCA) was conducted. A *p*-value of 0.05 was used for data comparison. F-ratios were calculated for the significant compounds. Only compounds with an average F-ratio larger than 100 were included in the PCA analysis. Additionally, we excluded the region (RT1: 8000–9000 s and RT2: 1.40–1.87 s) resulting from the column bleed of the instrument. More information on the comparison of the PM_{0.25} by ChromaTOF Tile can be found in the supplementary material (Table S11).

EC and OC contents were determined from the QFFs using a thermal–optical carbon analyzer (Desert Research Institute Model 2001A, Atmoslytic Inc., USA). The analysis was conducted following the IMPROVE_A protocol (Chow et al. 2007).

Elements were determined from the QFFs by inductively coupled plasma atomic emission spectroscopy (ICP-AES; Optima 7300 DV, Perkin Elmer, Germany). Samples were transferred into closed quartz vessels and digested with HNO₃ in a microwave system (Multiwave 300, Anton Paar, Austria). Afterwards, the solution was diluted to 30 mL with ultrapure H₂O. The following elements were determined from the emission samples: Al, As, B, Ba, Be, Bi, Ca, Cd, Co, Cr, Cu, Fe, Hg, K, Li, Mg, Mn, Mo, Na, Ni, P, Pb, S, Sb, Se, Sn, Sr, Ti, V, W, and Zn. Samples were introduced to the system with a peristaltic pump, connected to a micromist nebulizer and a cyclone spray chamber. The power of the radio frequency generator was set to 1400 W. Flow rate of the argon plasma gas and the argon nebulizer gas was 15 L min⁻¹ and 0.6 L min⁻¹, respectively. Three blank measurements and one control measurement of a certified standard (CPI, USA) were performed for all elements mentioned previously. Results were calculated with a computerized

lab-data management system using calibration curves, blank determinations, and control standards.

Sampling and analysis of gas phase

The gas phase was sampled for all three fuel types. Samples were taken at the tailpipe (main sampling station, Fig. 1) and at the operator during the test cycle (TeC) and in the idle mode of the heavy-duty vehicle. Samples were taken at a flow of 0.5 L min⁻¹ for approximately 5 min each. Additionally, the gas phase was taken at the operator during the test cycle as well as idle mode. Flow and sampling time corresponded to the gas phase samples taken at the main sampling station. Adsorber tubes were sampled with Gilian GilAir Plus Personal Sampling Pumps (Gilian, USA). A filter holder assembly made of stainless steel and equipped with a QFF was used for removing the particulate fraction and for protecting the adsorbers. Adsorber tubes consisted of three sublayers of graphitized carbon black (GCB) sorbents used to trap compounds of several volatility ranges (Table S12). At least one adsorber tube was kept closed and taken as field blank for every sampling day. Samples were stored at –20 °C until analysis.

The analysis of the adsorber tubes was done by thermal desorption (TD) with a Shimadzu TD-20 thermal desorption unit (Shimadzu, Japan), coupled to a GC–MS System (Shimadzu GCMS-QP2010 Ultra, Shimadzu, Japan). The analysis was done according to Mason et al. (2020), but modified to the applied GCB adsorbent material. An isotope-labelled standard mixture was applied to the sample prior to analysis (Table S13). The thermal desorption was performed at 345 °C and lasted 45 min. Extracted compounds were at first concentrated on a Tenax TD trap, cooled at 5 °C, and then redesorbed at 330 °C and transferred with a split ratio of 10 to the gas chromatograph. Separation was done on a 30-m-long VF-xMS, high arylene-modified phase column (0.25 mm ID × 0.25 μm d_f, Agilent Varian, USA). Further information on the temperature program of GC analysis and mass spectral parameters can be found in Table S14.

Raw data files were imported to OpenChrom (Lablicate, Edition 1.4.0.202110221400) as *cdf-files. Peak detection, integration, and identification were applied (Table S15). The 30 most abundant and reliable identified compounds found in the gas phase of the different fuel combustion aerosols were compared. An S/N ratio of 50 was applied as the threshold. Visual sample comparison as well as peak table comparison have been applied. The comparison was based on retention time and mass spectra. Identification was based on mass spectral comparison with the NIST library (version 2.3, 2017). Distinct aromatic compounds have been targeted and semi-quantified by the equivalent isotope-labelled standard compound (Table S13).

Results and discussion

Fuels

In this study, three different fuel types were investigated namely B0, GTL, and RME. B0 represented the petroleum-based reference fuel, that is usually used for the heavy-duty machinery in this platinum mine. GC×GC analysis of this reference fuel revealed dinaphthenes/olefins (22.1%), naphthenes/olefins (21.8%), and iso-paraffins (21.4%) as the most abundant compound classes found in the B0, followed by n-paraffins (16.0%), alkylbenzenes (7.8%), and naphthenobenzenes (6.1%, Table S10). These compound classes make up over 95% of the fuel composition. The remaining 5% can be attributed to indenes (1.6%), naphthalenes (1.6%), and several other aromatic compounds (~ 1.7%, Table S1). GTL and RME were chosen as alternative fuels. The production process for GTL results in a paraffinic fuel mostly consisting of n-alkanes (51.9%) and iso-alkanes (47.7%), making up over 99% of the fuel composition. (The GTL used in this study was produced from natural gas.) Relative amounts of compound classes were determined by GC×GC (Table S1). Only 0.2% of monocyclic as well as 0.2% of bi- and polycyclic paraffins were measured in this fuel and no aromatic compounds were detected. The composition of the RME was determined by standardized analysis methods. Its ester content was determined by EN 14103 and confirmed that the RME used is composed of at least 96.5% of FAMES (Table S1). Moreover, the RME was defined by maximum values for methanol and mono-, di- and triglyceride content (0.2%, 0.7%, 0.2%, 0.2%, respectively). The content of alkaline metals (Na, K) as well as earth alkali metals (Ca, Mg) was required to be below 5.0 mg kg⁻¹ for each of these groups (Table S2). For all three fuel types, distinct properties were determined using standardized analysis methods (ASTM, DIN, EN, ISO). These properties included among others the sulfur content, density, viscosity at 40 °C, flash point, and cetane-number of the respective fuel. The specific fuel properties measured can be found in Tables S1–S4.

Additionally, the lubrication oil utilized in this study was analyzed by GC×GC. We found alkanes (61.5%), followed by dinaphthenes/olefins (20.0%) and naphthenes/olefins (12.5%) add up to 94% of its composition. Furthermore, 2.8% of polynaphthenes/olefins, 1.9% of 2,6-di-tert-butylphenole, and 0.5% of benzenes were detected (Table S5). The elemental composition was measured by ICP-AES. We found that the main elements of the lubrication oil were calcium (Ca, 1710 mg kg⁻¹), zinc (Zn, 1300 mg kg⁻¹), and phosphorus (P, 1230 mg kg⁻¹, Table S6). These are typical additives used in lubrication

oil (Selby et al. 2005; Lin et al. 2015). Ca is commonly used as a detergent additive, while Zn and P are used as extreme pressure-additives as well as wear protection additives (Selby et al. 2005; Lin et al. 2015). Other abundant elements found in the lubrication oil were boron (B, 310 mg kg⁻¹), followed by sodium (Na, 47.6 mg kg⁻¹), silver (Ag, 11.6 mg kg⁻¹), magnesium (Mg, 8.9 mg kg⁻¹), potassium (K, 8.1 mg kg⁻¹), copper (Cu, 6.8 mg kg⁻¹), and silicon (Si, 5.0 mg kg⁻¹) (Table S15). Na can originate from the anti-corrosion agent NaNO₂, Mg is a known detergent additive and Cu is an additive used in high-temperature lubricant (Lin et al. 2015).

Particulate matter

The particulate matter (PM) in the exposure profile derived from the combustion aerosols of LHDs has been chemically characterized. To enable a comprehensive comparison, different techniques to determine the EC/OC ratio, elemental composition, and semi-volatile organic compounds have been applied. Table S16 shows the differences in total, elemental, and organic carbon (TC, EC, OC) content for the PM of the combustion aerosols. PM_{2.5} and PM_{0.25} samples have been analyzed. We found the EC/OC ratio of B0 compared to GTL was similar for PM_{2.5} (0.45 and 0.44, respectively) and PM_{0.25} (0.52 and 0.58, respectively). RME showed a four to five times lower EC/OC ratio (0.11) for PM_{2.5} and PM_{0.25} compared to B0 and GTL. Data recently published by Unosson et al. confirm lower EC/OC ratios for RME compared to B0 (Unosson et al. 2021). Although EC/OC is less for RME PM compared to B0 PM, we found similar TC values. This can be explained by higher OC content for RME compared to B0 PM (Table S16, Fig. 2). These results are consistent with other studies, where lower amounts of EC and higher amounts of OC were found for biodiesel PM compared to PM from fossil fuel combustion due to the higher oxygen content in biodiesel (Lu et al. 2012). Lowest TC and OC were measured for GTL (1.9 mg m⁻³ and 1.2 mg m⁻³, respectively, Table S16, Fig. 2). This can also be explained by the composition of the fuel as aromatic species and sulfur content are substantially lower compared to B0 fuel. These differences in the carbon content of the PM can be derived from the composition of the distinct fuel types. The different fractions of OC and EC content for PM_{2.5} and PM_{0.25} for all three fuels can be observed in Fig. 2.

The comparison of the distinct OC fractions indicated that the first OC fraction (OC1) differs the most from one fuel to another independent from the size fraction of the PM. OC1 reflects thermally desorbed carbon up to a temperature of 140 °C, thus, mainly VOCs are desorbed in this organic fraction (Chow et al. 2007). However, this fraction is also particularly susceptible to incorrect storage and handling of the sample material. The OC2 and OC3 fractions (up

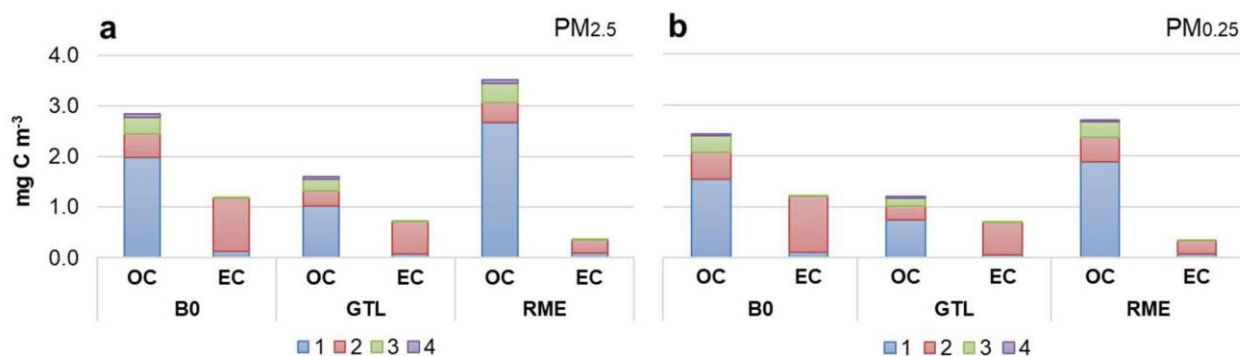


Fig. 2 Determination of the EC/OC-content of the combustion aerosols of the three distinct fuel types (B0, GTL, RME) by a thermal-optical carbon analyzer. OC and EC contents are divided in their distinct fractions. The numbers 1, 2, 3, and 4 represent the respective

OC and EC fractions. Data was normalized by m³. **a** EC/OC content of PM_{2.5} samples is displayed. **b** EC/OC content of PM_{0.25} samples is displayed

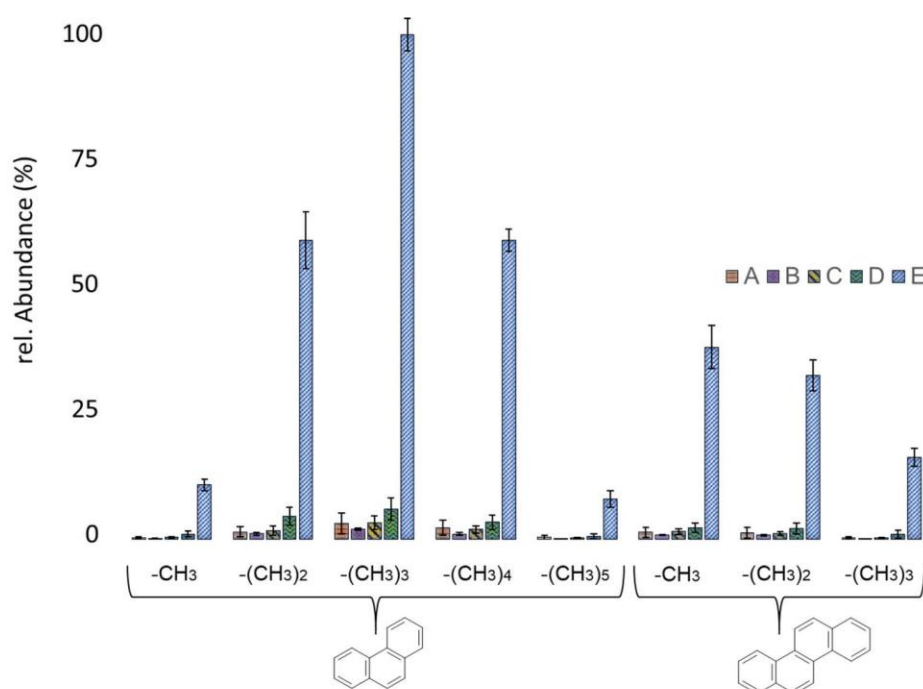
to 280 °C and 480 °C, respectively) are characteristic of the desorption of SVOCs (Chow et al. 2007). Additionally, pyrolysis products from compounds with higher molecular weight can be found in OC3 (Diab et al. 2015). Diab et al. demonstrated that the OC2 fraction was mainly composed of PAHs and alkylated PAHs (Diab et al. 2015). As PAHs are intensively discussed in the literature to induce adverse health effects, with some of them being known as potential carcinogens and mutagens and fossil fuel combustion is known to emit high amounts of these hazardous compounds (Boström et al. 2002; Kumar et al. 2014; Sun et al. 2014), we further focused on the analysis of PAHs.

Up to now, the potential toxicity of a sample is mostly conducted by the analysis of the 16 EPA PAHs. These EPA PAHs were selected back in 1976 when knowledge on PAH occurrence and the availability of standard material for identification and quantification purposes was limited (Andersson and Achten 2015). Nowadays, increasing research has been directed to the analysis of different PAH species including alkylated PAHs. Alkylated PAHs are highly abundant in crude oil products and dominate petrogenic sources (Czech et al. 2017). Although pyrogenic sources are dominated by their unsubstituted analogues, the abundance of alkylated PAHs due to unburned fuel as well as combustion processes cannot be neglected. Nevertheless, research on their potential toxicity in comparison to their unsubstituted analogues is still limited. Lam et al. focused on the comparison of the potency and aryl hydrogen receptor (AhR) activation of methylated PAHs compared to their unsubstituted analogues (Lam et al. 2018). They found that the relative potency factors (REPs) of monomethylated PAHs decreased faster than the ones of their parent compounds or other derivatives with increasing exposure time (Lam et al. 2018). This is in agreement with the study of Kang et al. showing a higher solubility of methylated PAHs and thus a higher biotransformation of the incorporated compounds (Kang et al.

2016). This can lead to higher excretion and detoxification of those compounds. Nevertheless, when comparing REPs of chrysene, benz(a)anthracene, and benzo(a)pyrene with their methylated analogues, significantly higher potencies were determined for their methylated analogues. Moreover, they presented higher potencies for PAHs with a methyl group attached to the core compared to ethyl, hydroxyl, and methoxy groups after 24-h exposure duration (Lam et al. 2018). The relative potency determined by the H4IIE-luc assay was, independent of the position of the methyl group attached to the PAH, higher compared to the unsubstituted PAHs (Lam et al. 2018). These studies emphasize the importance of monitoring methylated PAHs in a similar manner as unsubstituted PAHs. We, thus, focused on the classification of methylated three- and four-ring aromatics in the combustion aerosols by comprehensive GC×GC-ToFMS analysis in addition to the unsubstituted PAHs.

For B0, the overall PAH distribution in the samples was similar independent of the particle size (Figs. S1, 3). Most PAHs identified were three- and four-ring aromatics with different methylation patterns (Figs. S1, 3). Three-ring aromatics were found with up to four methyl groups and multiple alkyl groups attached to the ring structure. The abundance of the three-ring aromatics increased with increasing methylation having a maximum at the group of three times methylated (C₃) three-ring aromatics. For three-ring aromatics with higher methylation patterns, the abundance decreased again (Figs. S1, 3). The four-ring aromatics show a decrease in the abundance with an increase of methylation. A maximum of three times methylated four ring aromatics was identified. The abundance of two to four-times methylated three-ring aromatics is higher than the one found for the methylated four-ring aromatics. When comparing these PAH patterns to the literature, we found the distribution of methylated three-ring aromatics (bell-shape) is typical for PAHs originating from unburned fuel (Andersson and Achten 2015). In

Fig. 3 PAH distribution of B0 for the following particle sizes: A (> 2.5 μm), B (2.5–1.0 μm), C (1.0–0.5 μm), D (0.5–0.25 μm), and after-filter E (< 0.25 μm). Phenanthrene and chrysene are exemplary shown as reference compounds for the three- and four-ring aromatics, respectively. Degree of methylation is shown as the amount of $-\text{CH}_3$ groups substituted to the core. The highest abundance of PAHs can be found on the quasi-ultrafine particle after-filter E. Stages and after-filter were simultaneously sampled in triplicates and analyzed via TD-GC \times GC-ToFMS. Sample abundance is shown as an area normalized by m^3 . Standard deviation is depicted as error bars



contrast, the distribution found for the four-ring aromatics and a lower abundance with an increasing amount of methylation ($C_0 > C_1 > C_2 > C_3 > C_4$) is typical for PAHs arising from the combustion process (Andersson and Achten 2015). In this context, it is important to mention that PAHs can generally originate from three different sources. First, they can originate from unburned fuel or the lubrication oil (Kleeman et al. 2008; Czech et al. 2017). Second, they can be formed by the hydrogen abstraction- C_2H_2 addition (HACA) mechanism (Kislov et al. 2013; Czech et al. 2017). Third, they can be broken down to smaller PAHs by pyrolysis (Diab et al. 2015; Abdel-Shafy and Mansour 2016). In combustion engines, unsubstituted PAHs are noticeably formed by the HACA mechanism. The number of rings formed in this process depends on the combustion temperature. Czech et al. stated that in a homologue series of PAHs, usually the unsubstituted or (mono-) methylated PAH shows the highest abundance, but also higher alkylation degrees are visible especially for larger diesel engines due to a higher release of unburned fuel (Czech et al. 2017).

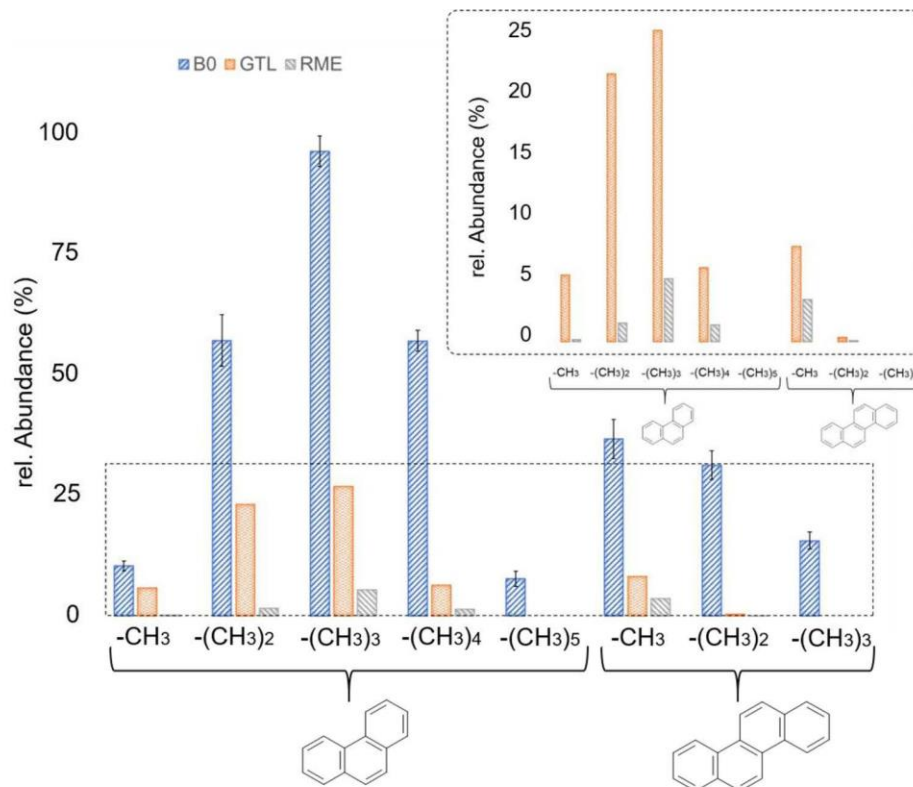
For the size-segregated PM, we used the Sioutas impactors, which enabled sampling of PM in the following size range: A (> 2.5 μm), B (2.5–1.0 μm), C (1.0–0.5 μm), D (0.5–0.25 μm), and after-filter E (< 0.25 μm). Ultrafine particles are defined as particles with an aerodynamic diameter equal or smaller than 100 nm. Due to the cut-off point of the Sioutas impactors, we could only sample particles with a diameter equal or smaller than 250 nm. Nevertheless, we assume that the collected combustion particles

will still mainly be ultrafine particles at this cut-off and, thus, this fraction will be referred to as “quasi”-ultrafine particles (qUFP) throughout the manuscript. We found that the “quasi”-ultrafine particles (qUFP, $\text{PM}_{0.25}$, after-filter E) show the highest abundance of PAH compared to all other size ranges (Fig. 3). The PAHs classified on these qUFP represent at least 80% of the PAHs classified on the total PM (Stage A–E). As the majority of PM released from diesel engine combustion is accounted to the ultrafine fraction (in terms of particle number) (Salo et al. 2021), the identification of more than 80% of the classified PAHs on the qUFP is plausible. The analysis of the several size ranges showed higher variances for samples from stages A to D compared to the after-filter (E). Although less pronounced as for the qUFP, we can still observe the typical PAH distribution described previously (Fig. 3 insert).

As the classified PAHs are certainly most abundant on the qUFP and UFP are of specific health concern, we further focused on the composition of the $\text{PM}_{0.25}$ samples when comparing the combustion aerosol of B0 to the combustion aerosols of the alternative fuels GTL and RME.

The PAHs classified are noticeably most abundant in the B0 combustion aerosol, followed by GTL and RME (Fig. 4). For most of the PAHs determined, we found that the abundance is at least twice as high in B0 compared to GTL. Multiply alkylated three-ring aromatics and three times methylated four-ring aromatics cannot be identified in GTL. The PAH distribution found for B0 can be confirmed for GTL. We found an increase of PAH abundance up to C_3 -PAH for

Fig. 4 PAH distribution analyzed from the “quasi”-ultrafine particles ($PM_{0.25}$) for B0, GTL, and RME. Phenanthrene and chrysene are exemplary shown as reference compounds for the three- and four-ring aromatics, respectively. Degree of methylation is shown as the amount of $-CH_3$ groups substituted to the core. B0 was simultaneously sampled in triplicates, whereas GTL and RME can only be shown as two experimental replicates. Sample abundance is shown as the area normalized by m^3 sampled. Standard deviation is depicted as error bars for samples measured in triplicates. Insert: Detailed view of PAH distribution of GTL and RME solely



the three-ring aromatics and a decline of abundance with increasing methylation for the four-ring aromatics.

The amount of PAHs classified in the combustion aerosol of RME is distinctly less compared to B0 and GTL (Fig. 4). The distribution of the PAHs, though, equals the distribution found for GTL and B0 combustion aerosol. The abundance of the PAHs on the RME $PM_{0.25}$ is at least twofold less compared to GTL. We determined an abundance four times lower for the C_3 -PAHs group in RME compared to GTL and twelve times lower compared to the B0 $PM_{0.25}$ samples. For the four-ring aromatics, we confirm the decrease of abundance with increasing methylation, which was already observed for B0 and GTL. The groups of multiply alkylated three-ring aromatics and three times methylated four-ring aromatics cannot be identified in the $PM_{0.25}$ samples of RME.

This aspect is important when discussing health aspects of distinct combustion aerosols. The exposure to (alkylated) PAHs is known to have adverse effects on human health. A change in fuel type could, thus, greatly decrease the amount of alkylated PAHs released. Moreover, the confirmation of PAHs mainly found on the qUFP is of great concern as these particles can deeply penetrate into the lung, enter the alveolar region, and can even be translocated to other organs (Hussain et al. 2011). Although they have a low particle mass, UFP have a very high particle number and, thus, a high surface area on which different chemical components

can be absorbed or adsorbed onto (Kwon et al. 2020). This is also explaining the high amount of alkylated PAHs (over 80% of total alkylated PAHs classified) found on the $PM_{0.25}$ fraction.

To enable a comparison to previous research results and to give a more comprehensive picture of the chemical profile of the PM from these distinct fuel types, we additionally targeted seven unsubstituted PAHs in the $PM_{0.25}$ of B0, GTL, and RME. We found that, independent of the targeted PAH, the combustion of B0 released highest PAH concentrations compared to GTL and RME. The comparison of GTL and RME combustion aerosol showed higher concentrations of smaller PAHs (phenanthrene, anthracene, fluoranthene, pyrene) for GTL. In contrast, higher molecular weight PAHs (benz(a)anthracene, benz(e)pyrene, benz(a)pyrene) were more prominent in the RME combustion aerosol compared to GTL. The prevalence in the formation of specific PAHs can be explained by the composition of the fuels and the resulting differences in the combustion process. While the paraffinic GTL is mainly consisting of smaller alkane and alkene compounds, which mostly leads to the formation of smaller PAHs by butadiene addition reactions (Kislov et al. 2013), RME mainly consists of FAMES of different lengths of alkyl chains. As stated by Llamas et al., FAMES are primarily consumed by the abstraction of the H atoms by $OH\cdot$ and $H\cdot$ radicals (Llamas et al. 2017). The

α -hydrogen atom in regard to the ester group is the most labile H atom due to resonance stabilization of the resulting radical. The more stable radical will decompose later to a stable acrylic ester molecule and a ($R-CH_2\bullet$) radical which can induce a chain reaction by β -elimination. This radical can form several PAH and soot precursor in the flame such as acetylene, ethylene and 1,3-butadiene. Ethylene and 1,3-butadiene could then form benzene, naphthalene, anthracene, and phenanthrene by Diels–Alder reaction followed by aromatization (Llamas et al. 2017). This would explain the detection of smaller PAHs in the RME combustion aerosol. The formation of larger PAHs could be explained by the Diels–Alder reaction of those lighter PAHs and ethylene followed by aromatization of the naphthenic-aromatic hydrocarbon formed. Herein, oxygen would serve as a hydrogen acceptor to produce water in the combustion process (Llamas et al. 2017).

Nisbet and Lagoy proposed toxicity equivalent factors (TEFs) for 16 individual PAHs (Nisbet and Lagoy 1992). These TEFs were based on previously conducted experiments on the toxicity and carcinogenic potential of distinct PAHs compared to the toxic effect of benz(a)pyrene (BaP) and are the basis for the calculation of toxic equivalents (TEQs) for different PM samples. The comparison of the resulting TEQ values shows that the sum of BaP_{TEQ} for the analyzed PAHs is the highest for B0, followed by RME and GTL. The overall higher concentrations of the targeted PAHs in B0, thus, also result in a higher sum of calculated TEQs. Intriguingly, while the concentration of the targeted PAHs is higher in the GTL $PM_{0.25}$, the overall BaP_{TEQ} value is lower compared to RME $PM_{0.25}$ (Table 3). This can be explained by the different TEFs taken into account for the TEQ calculations. Smaller molecular PAHs are known to show lower toxic effects and have, therefore, lower TEFs. This emphasizes the importance of monitoring different PAHs. Especially, higher molecular PAHs such as dibenzo(a,h)anthracene and indeno(123-c,d)pyrene (which were below the limit of quantification in our study) with TEF of 5 and 0.1, respectively (Nisbet and Lagoy 1992), can significantly contribute

to the total toxicity induced by PAHs. Moreover, the toxicity of alkylated PAHs should be further investigated to enable an assessment of their potential TEQ values. Recently, Richter-Brockmann and Achten highlighted the importance of alkylated PAHs, in particular 1-methylpyrene and 5-methylchrysene, on the overall toxicity of environmental samples and proposed their consideration in future risk assessments (Richter-Brockmann and Achten 2018). In summary, valuable TEF values for PAH derivatives are needed to achieve a more realistic estimation on the toxicity of complex aerosol samples. Nevertheless, we found higher abundances in the alkylated PAHs as well as higher concentrations of all targeted unsubstituted PAHs in the B0 in comparison to GTL and RME $PM_{0.25}$. Based on this data, the change in fuel type would not only lead to the use of more sustainable energy sources as well as to an independence of fossil fuel supply, but might additionally improve the exposure situation.

As alkylated PAHs showed the lowest abundance in the $PM_{0.25}$ of RME and also targeted PAHs showed lower concentrations compared to B0 $PM_{0.25}$, the higher OC measured for RME must derive from another source. We noted previously that RME consists of high amounts of FAMES in the fuel (Table S2). To evaluate whether FAMES contribute to the most distinct differences of PM between RME, GTL, and B0, we performed a supervised analysis of variances-principal component analysis (ANOVA-PCA) of the $PM_{0.25}$ of these three fuels (Fig. S2). A detailed look at the components with the greatest loadings towards the RME samples included FAMES of various lengths of alkane side chains as being the most significant components (Fig. S3, Table 4). Although this type of statistical analysis cannot state quantitative differences between the samples, Table 4 shows highest areas are clearly measured for the distinct FAMES, e.g., docosanoic acid methyl ester and tetracosanoic acid methyl ester, in comparison to the other significantly different compounds from RME to GTL and B0 $PM_{0.25}$ samples. This might be an explanation for the higher OC content of RME combustion aerosol compared to GTL and B0. Besides two unknown compounds, we found two cyclic

Table 3 Targeted PAHs in the $PM_{0.25}$ samples of B0, GTL, and RME. TEF values are based on the proposed TEF by Nisbet and Lagoy (Nisbet and Lagoy 1992). TEQ values were calculated by multiplying the concentration of a PAH by its proposed TEF. Concentrations are given in $ng\ m^{-3}$

| | B0 | GTL | RME | TEF | B0 BaP_{TEQ} | GTL BaP_{TEQ} | RME BaP_{TEQ} |
|-------------------|------------|------------|------------|-------|-------------------|--------------------|--------------------|
| Phenanthrene | 76.1 | 48.2 | 26.6 | 0.001 | 0.1 | <0.1 | <0.1 |
| Anthracene | 23.1 | 11.3 | n.d | 0.01 | 0.2 | 0.1 | n.d |
| Fluoranthene | 62.9 | 48.3 | 33.5 | 0.001 | 0.1 | <0.1 | <0.1 |
| Pyrene | 237 | 177.1 | 118.2 | 0.001 | 0.2 | 0.2 | 0.1 |
| Benz(a)anthracene | 21.5 | 1.7 | 13.2 | 0.1 | 2.2 | 0.2 | 1.3 |
| Benz(e)pyrene | 12.1 | 2.4 | 7.9 | 0 | 0 | 0 | 0 |
| Benz(a)pyrene | 15.7 | 0.2 | 11.6 | 1 | 15.7 | 0.2 | 11.6 |
| Σ | 449 | 289 | 211 | | 19 | 0.8 | 13 |

n.d. not detected

Table 4 Table content derived from supervised ANOVA-PCA (Figs. S2, S3). Components with highest loadings towards RME from the PM_{0.25}-bound combustion aerosol are listed and sorted from highest to lowest abundance. Identification and similarity calculations are based on NIST library hits

| Name | Compound class | F-ratio | Abundance rel. (%) | Similarity |
|--|-------------------|---------|--------------------|------------|
| Docosanoic acid, methyl ester | FAME | 542 | 100.00 | 883 |
| Tetracosanoic acid, methyl ester | FAME | 354 | 55.03 | 908 |
| Methyl 8-(2-furyl)octanoate | Ester | 415 | 12.15 | 966 |
| 15-Tetracosenoic acid, methyl ester | FAME | 124 | 10.16 | 898 |
| Cyclopentene, 1-butyl- | Naphthene | 1904 | 9.84 | 957 |
| 13-Docosenoic acid, methyl ester, (Z)- | FAME | 181 | 9.32 | 889 |
| Methyl 10-oxohexadecanoate | Ester | 695 | 6.48 | 798 |
| cis-Methyl 11-eicosenoate | Ester | 969 | 3.66 | 874 |
| 10-Oxodecanoic acid, methyl ester | FAME | 275 | 2.43 | 854 |
| Neophytadiene | Diterpene | 379 | 1.94 | 916 |
| 7-Nonynoic acid, methyl ester | FAME | 174 | 1.21 | 762 |
| 11,13-Eicosadienoic acid, methyl ester | FAME | 283 | 0.95 | 915 |
| Methyl 18-methylnonadecanoate | Ester | 1920 | 0.75 | 872 |
| Unknown (not identified) | - | 630 | 0.61 | - |
| Methyl 8-(5-hexyl-2-furyl)-octanoate | Ester | 172 | 0.56 | 855 |
| 2-n-Octylfuran | Furan | 377 | 0.40 | 965 |
| Nonadecanoic acid, methyl ester | FAME | 687 | 0.27 | 810 |
| Butylated Hydroxytoluene | Phenol derivative | 460 | 0.19 | 902 |
| Unknown (not identified) | - | 164 | 0.06 | - |
| 3-Methylene-7,11-dimethyl-1-dodecene | Alkene | 275 | 0.05 | 830 |

compounds (1-butyl-cyclopentene and 2-n-octylfuran), an alkene (3-methylene-7,11-dimethyl-1-dodecene), which is expected to have no influence on the toxicity of the aerosol, a diterpene (neophytadiene) and an aromatic compound (Butylated Hydroxytoluene, BHT). BHT is a known antioxidant and commonly used as an oxidation stabilizer in petroleum products (Ryu 2010). As RME is a biodiesel composed of many polar substances, it is important to ensure the stability of this fuel during use and storage. We, thus, propose that BHT was used as the oxidation stabilizer in this biofuel.

Besides, organic compounds also various metals are considered to have adverse health effects. Therefore, we compared the elemental composition of the ultrafine PM_{0.25} samples from B0, GTL, and RME by ICP-AES. We analyzed a wide range of elements, whereas the most hazardous group of elements measured were the transition metals (Table S17). Cu, Fe, Ni, Ti, and Zn were found in at least one of the combustion aerosols from the distinct fuels. Cu was only detectable in B0 (592 ng m⁻³), while it was below the limit of quantification (LOQ) for GTL and RME combustion samples. Cu is usually released by wear abrasion. As our sampling approach was conducted without moving of the vehicle, we did not expect significant amounts of copper being present in our samples. As Cu is also used as an additive in high-temperature lubricants and we confirmed Cu in the lubrication oil measured, we expect the Cu found in the B0 combustion aerosol derived from the lubrication oil. Although the lubrication oil was the same for all tested fuel

types, the fuel and the resulting combustion temperature can influence the release of unburned lubrication oil. Fe showed the highest concentration in the PM of B0 (7146 ng m⁻³) compared to GTL and RME (6963 ng m⁻³ and 5918 ng m⁻³, respectively).

The highest concentration of Ni was determined in the GTL samples (1047 ng m⁻³) compared to B0 (881 ng m⁻³) and RME (666 ng m⁻³). Al showed highest concentrations for GTL (9570 ng m⁻³) in comparison to B0 and RME (8585 ng m⁻³ and 4413 ng m⁻³, respectively). The higher concentrations of Ni and Al in the PM of GTL could be explained by the production process of the fuel. Nickel is a commonly used catalyst in the Fischer–Tropsch process and Al₂O₃ is a known support material used, i.e., to enhance the mechanical stability of the catalyst (van Steen et al. 2008). Zn concentration was highest for RME combustion aerosol (5631 ng m⁻³) compared to B0 (4375 ng m⁻³) and GTL (1588 ng m⁻³). Alkali (K, Na) and alkaline earth metals (Ba, Ca, Mg) showed highest concentrations for RME combustion aerosol compared to B0 and GTL (Table S18). The following concentrations were determined for the RME PM_{0.25} samples: K (88 µg m⁻³), Na (14 µg m⁻³), Ba (914 ng m⁻³), Ca (18 µg m⁻³), and Mg (2206 ng m⁻³). Mg concentrations were below the LOQ for B0 and GTL. For RME, we found mainly alkali and alkaline earth metals showing the highest abundance compared to the elemental composition of PM_{0.25} of B0 and GTL. The higher concentrations of alkali and alkaline earth metals in the PM of RME could be explained

by their expected occurrence in natural sources such as rape-seed oil and by their common use as catalysts in the transesterification process of biofuels (Arzamendi et al. 2008; Mohadesi et al. 2014; Tavizón-Pozos et al. 2021). Mohadesi et al. studied the catalytic reactivity of alkaline earth metal oxides including CaO/SiO_2 , BaO/SiO_2 , and MgO/SiO_2 (Mohadesi et al. 2014). Arzamendi et al. studied the catalytic reactivity and selectivity of several alkali and alkaline earth metals in the transesterification process, including among others Na, K, Ca, and Mg carbonites, Na and K bicarbonates, and Ca and Mg oxides (Arzamendi et al. 2008). Recently, Tavizón-Pozos et al. concluded that the combined use of alkaline earth oxides with alkaline metals might enhance their basicity so that more active sites would be available and a higher resistance to environmental factors could be achieved (Tavizón-Pozos et al. 2021). Ti concentrations were comparable between RME and B0 (287 ng m^{-3} and 253 ng m^{-3} , respectively), while it was below the LOQ for GTL $\text{PM}_{0.25}$. Sn concentrations were comparable for B0 (221 ng m^{-3}), GTL (208 ng m^{-3}), and RME (215 ng m^{-3}). Non-metals (B, P, S, Se) analyzed were found to be most abundant in B0 combustion aerosol (B, Se) or comparable to RME (P, S) while lowest for GTL (Table S18). Sulfur concentration was measured to be lowest for GTL combustion aerosol ($9 \text{ } \mu\text{g m}^{-3}$) which was expected as the fuel is characterized by a low sulfur content (Table S4).

Gas phase

To enable a comprehensive comparison of the complete combustion aerosol produced by the different fuels, the gas phase needs to be considered. As previously mentioned, VOCs and SVOCs are present in an equilibrium between the gas and particulate phase. Their gas-to-particle partitioning is depending on the exhaust temperature as well as the complete organic aerosol concentration (C_{OA}). The identification of VOCs and SVOCs in the gas phase was achieved using TD-GC-MS.

For the comparison of the gas phase from the distinct fuel types, we focused on the samples taken at the tailpipe during the test cycle. Differences in the SVOC and VOC composition of the gas phase between B0, GTL, and RME were assessed. We identified 164 different volatiles in B0 and in GTL and 100 volatiles in the RME gas phase with similar pre-processing conditions. We found that of the 30 most abundant compounds identified in the B0 gas phase, 25 can also be found in the GTL and 26 in the RME gas phase (Table 5). Aromatic compounds like xylene and other methylated benzene isomers are more abundant in the B0 gas phase, while alkanes can be found several orders of magnitude higher in GTL compared to B0 and RME gas phase (Table 5, Fig. S4). This resembles the results already gained by the chemical analysis of the PM samples. The higher

abundance of the aromatic species in the B0 gas phase compared to GTL and RME can again be explained by the differences in their fuel composition. The higher amount of aromatic hydrocarbons in the B0 fuel, leads to higher amounts of smaller aromatic compounds by pyrolysis of larger PAHs during the combustion process. The increased amount of alkanes in the GTL gas phase reflects the high abundance of n- and iso-paraffins in this fuel.

To consider whether other chemical compounds were highly abundant in GTL and RME but not found in the B0, we additionally summarized the 30 most abundant compounds found in GTL and RME gas phase (Table S18). The analysis confirmed that the GTL gas phase mainly consists of highly abundant alkane peaks. Most of the components found in the RME gas phase showed smaller abundances compared to GTL and B0, as can already be observed in Table 5. Besides alkanes and aromatic compounds, the presence of FAMES in the RME gas phase could be confirmed (Table S18).

The gas phase samples evaluated in the previous chapter considered only the sampling of volatiles at TP during TeC. To study in which extent the LHD operator is exposed to volatiles, known to have adverse health effects, we targeted distinct aromatic compounds and included different exposure scenarios which were addressed by our experimental design. Absolute concentrations were determined by equivalent isotope-labeled ISTDs.

The three main parameters for the exposure were as follows: (1) use of different fuels, (2) engine conditions, and (3) sampling position. First, we found that the concentration of the targeted mono- and diaromatic hydrocarbons in the gas phase of the three fuels was observed to be highest for B0 (Table 6). Second, the concentrations calculated during TeC and HI were higher during TeC for most of the compounds independent of fuel type and sampling position. Third, the concentrations measured at the main sampling position (TP) were found to be several times higher for most of the targeted compounds (except for toluene) in comparison to the OP sampling position.

The influence of the different fuel types will exemplarily be discussed for the TeC conditions at the tailpipe (TP). For benzene, we determined a concentration of $311 \text{ } \mu\text{g m}^{-3}$ for B0 in comparison to $286 \text{ } \mu\text{g m}^{-3}$ for GTL and $210 \text{ } \mu\text{g m}^{-3}$ for RME in the gas phase. Toluene concentrations could only be determined for B0 ($103 \text{ } \mu\text{g m}^{-3}$) and RME ($87.8 \text{ } \mu\text{g m}^{-3}$), as the isotope-labelled standard (toluene-d8) and, thus, the native toluene peak are co-eluting with a highly abundant alkane peak in the GTL samples. O-xylene could only be determined in the B0 gas phase with a concentration of $153 \text{ } \mu\text{g m}^{-3}$. Naphthalene concentrations were similar for B0 ($19.5 \text{ } \mu\text{g m}^{-3}$) and GTL ($22.7 \text{ } \mu\text{g m}^{-3}$) but four times less in RME ($3.78 \text{ } \mu\text{g m}^{-3}$). Biphenyl showed the lowest amount calculated for the targeted gas phase compounds for all fuel

Table 5 Table based on the 30 most abundant peaks found in the gas phase of the B0 during test cycle at the tailpipe. Retention time (RT) and mass spectra similarity was used for component identification

| Compound | Peak no. ¹ | Class | Rel. Abundance ² (%) | | |
|--------------------------------|-----------------------|-----------|---------------------------------|----------------|--------|
| | | | B0 | GTL | RME |
| Benzene | 1 | Aromatic | 48.05 | 4.92 | 100.00 |
| Undecane | 20 | Alkane | 100.00 | 82.10 | 26.90 |
| Decane | 12 | Alkane | 100.00 | 100.00 | 31.94 |
| Dodecane | 26 | Alkane | 73.00 | 33.11 | 15.32 |
| Nonane | 5 | Alkane | 43.02 | 85.23 | 24.31 |
| Toluene | 2 | Aromatic | 37.99 | - ³ | 76.21 |
| Tridecane | 29 | Alkane | 37.99 | 21.10 | 4.80 |
| Mesitylene | 13 | Aromatic | 35.70 | 2.17 | 3.33 |
| p-Xylene | 4 | Aromatic | 25.40 | 0.83 | 9.96 |
| Decane, 4-methyl- | 14 | Alkane | 24.49 | 2.53 | 3.39 |
| Tetradecane | 30 | Alkane | 23.11 | 6.13 | 23.23 |
| Benzene, 1,2,3-trimethyl- | 15 | Aromatic | 20.98 | - | 1.08 |
| Undecane, 3-methyl- | 25 | Alkane | 20.09 | 9.13 | 2.09 |
| Undecane, 2-methyl- | 24 | Alkane | 19.77 | 10.20 | 3.36 |
| Nonane, 3-methyl- | 9 | Alkane | 19.08 | 9.44 | 1.56 |
| Decane, 5-methyl- | 17 | Alkane | 17.73 | 8.61 | 3.86 |
| Undecane, 2,6-dimethyl- | 27 | Alkane | 16.32 | 1.98 | 0.62 |
| 9-Octadecen-1-ol, (Z)- | 19 | Alcohol | 16.18 | - | 1.44 |
| Nonane, 2-methyl- | 8 | Alkane | 15.56 | 8.37 | 1.93 |
| Decane, 4-methyl- | 18 | Alkane | 14.74 | 9.04 | 2.15 |
| Tetradecane, 2,6,10-trimethyl- | 28 | Alkane | 14.28 | 1.15 | 4.23 |
| Benzene, 1-ethyl-3-methyl- | 10 | Aromatic | 13.50 | 0.18 | 0.92 |
| Cyclohexane, butyl- | 16 | Naphthene | 12.65 | 0.55 | - |
| trans-Decalin, 2-methyl- | 22 | Naphthene | 12.59 | 0.25 | - |
| Octane, 4-methyl- | 3 | Alkane | 12.56 | 9.44 | 7.18 |
| o-Xylene | 6 | Aromatic | 12.27 | - | - |
| Octane, 2,6-dimethyl- | 7 | Alkane | 12.01 | 1.58 | - |
| trans-Decalin, 2-methyl- | 21 | Naphthene | 11.95 | 0.47 | 1.36 |
| Undecane, 5-methyl- | 23 | Alkane | 11.74 | 8.37 | 1.33 |
| Benzene, 1-ethyl-3-methyl- | 11 | Aromatic | 11.53 | - | 1.63 |

¹Peak no.: the numbering of the peaks refers to the statistical analysis (Fig. S4)

²Relative abundance was calculated based on the area using TIC

³Toluene-d8 is coeluting with a highly abundant alkane peak and, thus, native toluene might not be detectable

types. As biphenyl could not be determined for the TP-TeC condition for GTL, we compared the TP-HI concentrations for B0, GTL, and RME. The concentration of biphenyl found in B0 gas phase ($1.08 \mu\text{g m}^{-3}$) was twice as high compared to GTL ($0.432 \mu\text{g m}^{-3}$) and RME ($0.558 \mu\text{g m}^{-3}$).

The comparison of the different engine conditions (TeC, HI) showed higher compound concentrations during TeC for benzene, o-xylene, and naphthalene for GTL and RME (Table 6). The concentrations for toluene and naphthalene were comparable between TeC and HI in the B0 gas phase at the TP position. The concentration of biphenyl was higher during HI than during TeC at the TP but not at the OP position. As concentrations of the targeted compounds were up

to 23 times lower for the OP compared to the TP sampling site (e.g. O-xylene in B0 samples), we expect mainly dilution factors being responsible for this decrease. Although, we were able to confirm dilution effects due to the distance of the OP compared to the TP for the targeted compounds (except for toluene), we were still able to measure concentrations as high as $55.7 \mu\text{g m}^{-3}$ for benzene and $13.7 \mu\text{g m}^{-3}$ for o-xylene in the B0 gas phase. Concentrations of naphthalene and biphenyl were $0.535 \mu\text{g m}^{-3}$ and $0.245 \mu\text{g m}^{-3}$ at maximum at the OP.

As VOCs have a relatively high vapour pressure, their main exposure pathway is through inhalation. Benzene, toluene, and xylene (BTX) compounds have high potential for

Table 6 Targeted aromatic hydrocarbons in the gas phase samples of B0, GTL, and RME are summarized. Samples were taken at the tailpipe and at the operator level during test cycle and at high idling conditions. Concentrations were normalized to sampling volume in m³. Single measurements are listed if not stated differently

| | Benzene ($\mu\text{g m}^{-3}$) | Toluene ($\mu\text{g m}^{-3}$) | o-Xylene ($\mu\text{g m}^{-3}$) | Naphthalene ($\mu\text{g m}^{-3}$) | Biphenyl ($\mu\text{g m}^{-3}$) |
|---------------------|-------------------------------------|-------------------------------------|--------------------------------------|---|--------------------------------------|
| B0 | | | | | |
| TP-TeC ¹ | 311 | 103 | 153 | 19.5 | 0.648 |
| TP-HI ¹ | 226 | 108 | 115 | 21.2 | 1.08 |
| OP-TeC | 55.7 | - | 6.61 | 0.535 | 0.245 |
| OP-HI | 56.8 | 95.5 | 13.7 | 0.314 | 0.168 |
| GTL | | | | | |
| TP-TeC | 286 | ² | - | 22.7 | - |
| TP-HI | 138 | ² | - | 11.9 | 0.432 |
| OP-TeC | - | ² | - | 0.465 | 0.121 |
| OP-HI | 40.6 | ² | - | 0.395 | 0.079 |
| RME | | | | | |
| TP-TeC | 210 | 87.8 | - | 3.78 | 0.197 |
| TP-HI | 118 | 84.2 | - | 1.19 | 0.558 |
| OP-TeC | 7.10 | 15.8 | - | 0.294 | - |
| OP-HI | - | - | - | 0.185 | 0.128 |

¹Mean values ($n=2$) are depicted

²Toluene-d8 is coeluting with a highly abundant alkane peak and, thus, native toluene might not be detectable

TP tailpipe, OP operator, TeC test cycle, HI high idling

bioaccumulation and are implicated in cancer and tumour cases in humans (Kuranchie et al. 2019). Acute effects of BTX exposure could include eye, nose, and skin irritation as well as headaches, tiredness, and dizziness. A chronic exposure to these VOCs could consequently pose a risk for cancer as well as it could damage liver, kidneys, heart, lungs, and other organs (Kuranchie et al. 2019). Benzene is the most toxic component and has been confirmed to be carcinogenic to humans (group 1) by the US EPA (Kuranchie et al. 2019; Mihajlović et al. 2021). After inhalation, benzene is converted to toxic metabolites and can produce mutagenic properties (Kuranchie et al. 2019). Toluene is known to induce skin and eye irritations and operates depressant on the central nervous system (CNS). Xylenes are irritants for the eye, skin, and mucous membrane and can cause among others respiratory and gastrointestinal damage (Kuranchie et al. 2019). Naphthalene has been categorized as possibly carcinogenic to humans (group 2B) by the International Agency for Research on Cancer (IARC) (Yost et al. 2021). While epidemiological studies are limited to two occupational exposure studies which demonstrated limited evidence for effects on the nervous system of the workers by exposure to biphenyl above the occupational threshold limit value (1.3 mg m^{-3}), experimental animal studies of ingested biphenyl provided consistent evidence for renal and some evidence for liver toxicity (Li et al. 2016).

Moreover, carcinogenicity of biphenyl is summarized by the US EPA (2005a) as “suggestive evidence of carcinogenic potential” based on increased incidence of urinary bladder tumours in rats and liver tumours in mice after biphenyl exposure (Li et al. 2016).

In summary, we demonstrated that the concentrations calculated for these targeted aromatic compounds were higher in the B0 gas phase compared to GTL and RME gas phase. Thus, potentially hazardous air pollutants, in particular aromatic compounds, were determined with the highest concentrations in the gas phase and on the PM of B0 combustion aerosol. This implies the potential benefits of a change in fuel type from a health perspective.

Strengths and limitations

This study was carried out under realistic exposure conditions to gain important information on the exposure situation of the mine workers. The choice of this sampling place and the sampling itself has some limitations. The LHD vehicles used are optimized for the use of B0 fuel and, thus, exposure profiles of GTL and RME could be influenced by non-optimal engine settings. As the sampling was conducted without movement of the LHD vehicle the influence of abrasion of break and tire wear cannot be included in this study. An advantage of this setup is that the analysis of elemental composition of the combustion particles is not influenced by elements resulting from abrasion. Moreover, the sampling of $\text{PM}_{2.5}$, $\text{PM}_{0.25}$, and gas phase enabled a comprehensive characterization of the combustion aerosol of these fuels. The advanced data analysis and evaluation using GC×GC-ToFMS enabled a group-type comparison of methylated PAHs as well as a semi-quantification of targeted unsubstituted PAHs and, thus, the determination of BaP_{TEQ} values. Furthermore, gas phase was sampled at two sampling positions, including the position of the LHD operator, which enabled the assessment of a realistic exposure profile of VOCs for those operators. Based on the chemical characteristics, including the amount of metals and aromatic species released by the combustion of the different fuel types, which reflect compounds of potential health concern, we were able to identify B0 as fuel that released the highest amount of compounds of potential health concern in comparison to GTL and RME.

Conclusion

A decreased release of greenhouse gases, less environmental impact, and a reduced dependency of developing countries on fossil fuels are key factors of sustainable development. In this study, we wanted to evaluate a possible improvement of the exposure situation when exchanging fossil fuel with alternative fuels (GTL, RME). We demonstrated that

chemical compounds such as (methylated) PAHs, metal elements (Cu, Fe), and other aromatic species are released from heavy-duty machinery to a greater extent when fueled with B0 compared to GTL and RME. Moreover, the calculated BaP_{TEQ} value was highest for B0, followed by RME and GTL. Gas phase analysis of the different fuels showed highest concentrations for the targeted aromatic species (BTX, naphthalene, biphenyl) released from B0 followed by GTL and RME. The concentration of these compounds was still elevated at the position of the LHD operator. This implies potential adverse health effects for workers operating this heavy-duty machinery. The use of GTL and RME would release less (methylated) PAHs, metals, and other aromatic species compared to B0, which could consequently lead to a lower toxicological potential of the combustion aerosol. Nevertheless, the use of GTL and RME would still lead to substantial amounts of (methylated) PAHs and VOCs such as benzene and toluene, which should not be neglected.

Future studies should focus on the biological evaluation of these aerosols and their potential toxicological response, as research on the toxicological potential of distinct aerosol components such as methylated PAHs is still limited. Furthermore, we suggest the implementation of TEF values for methylated PAHs to ensure a more comprehensive toxicological evaluation of complex aerosol samples.

Supplementary Information The online version contains supplementary material available at <https://doi.org/10.1007/s11869-022-01287-9>.

Acknowledgements The authors thank LECO Europe for technical support and for providing the software ChromaTOF Tile for GC×GC data evaluation. Furthermore, we thank Dr. Philip Wenig for the support in data evaluation with the evaluation software OpenChrom (Lablicate). We thank Sasol Limited for the fuel supply and fuel characterization. We also thank ASG Analytik-Service for fuel and lube oil characterization. We further like to thank the management and staff at Impala Platinum Limited for assistance with sampling. The authors would like to thank Dr. Jürgen Schnelle-Kreis and Dr. Hendryk Czech for their fruitful discussions and ideas regarding this paper. Finally, we would like to thank Prof. Dr. Tuulia Hyötyläinen for her support as PhD thesis committee member.

Author contribution All authors, in particular PF, GLG, JO, and NG, contributed to the study conception and design. Material preparation, data collection, and analysis were performed by NG, JO, MW, MJ, GJ, and BM. Interpretation of results was performed by NG, JO, and TG. The concept for the manuscript was elaborated by NG, JO, TG, and RZ. The first draft of the manuscript was written by NG, and all authors commented on previous versions of the manuscript. All authors read and approved the final manuscript.

Funding Open Access funding enabled and organized by Projekt DEAL. We acknowledge the funding provided by the University of Pretoria and the National Research Foundation of South Africa (NRF, grant number 105807) and the support by the German Federal Ministry of Education and Research (BMBF, research contract 01DG17023).

Data availability The datasets used and/or analyzed during the current study are available from the first author on reasonable request. (Please contact nadine.gawlitta@helmholtz-muenchen.de).

Declarations

Ethics approval Not applicable.

Consent to participate Not applicable.

Consent for publication Not applicable.

Competing interests The authors declare no competing interests.

Open Access This article is licensed under a Creative Commons Attribution 4.0 International License, which permits use, sharing, adaptation, distribution and reproduction in any medium or format, as long as you give appropriate credit to the original author(s) and the source, provide a link to the Creative Commons licence, and indicate if changes were made. The images or other third party material in this article are included in the article's Creative Commons licence, unless indicated otherwise in a credit line to the material. If material is not included in the article's Creative Commons licence and your intended use is not permitted by statutory regulation or exceeds the permitted use, you will need to obtain permission directly from the copyright holder. To view a copy of this licence, visit <http://creativecommons.org/licenses/by/4.0/>.

References

- Abdel-Shafy HI, Mansour MSM (2016) A review on polycyclic aromatic hydrocarbons: source, environmental impact, effect on human health and remediation. *Egypt J Pet* 25(1):107–123 <https://doi.org/10.1016/j.ejpe.2015.03.011>
- Andersson JT, Achten C (2015) Time to say goodbye to the 16 EPA PAHs? Toward an up-to-date use of PACs for environmental purposes. *Polycyclic Aromat Compd* 35(2–4):330–354 <https://doi.org/10.1080/10406638.2014.991042>
- Arzamendi G, Arguñarena E, Campo I, Zabala S, Gandía LM (2008) Alkaline and alkaline-earth metals compounds as catalysts for the methanolysis of sunflower oil. *Catal Today* 133–135:305–313 <https://doi.org/10.1016/j.cattod.2007.11.029>
- Bluhm K, Heger S, Seiler T-B, Hallare AV, Schäffer A, Hollert H (2012) Toxicological and ecotoxicological potencies of biofuels used for the transport sector—a literature review. *Energy Environ Sci* 5(6):7381–7392
- Boström CE, Gerde P, Hanberg A, Jernström B, Johansson C, Kyrklund T, Rannug A, Törnqvist M, Victorin K, Westerholm R (2002) Cancer risk assessment, indicators, and guidelines for polycyclic aromatic hydrocarbons in the ambient air. *Environ Health Perspect* 110 Suppl 3(Suppl 3):451–488 <https://doi.org/10.1289/ehp.110-1241197>
- Chow JC, Watson JG, Chen LWA, Chang MCO, Robinson NF, Trimble D, Kohl S (2007) The IMPROVE_A temperature protocol for thermal/optical carbon analysis: maintaining consistency with a long-term database. *J Air Waste Manag Assoc* 57(9):1014–1023. <https://doi.org/10.3155/1047-3289.57.9.1014>
- Czech H, Stengel B, Adam T, Sklorz M, Streibel T, Zimmermann R (2017) A chemometric investigation of aromatic emission profiles from a marine engine in comparison with residential wood combustion and road traffic: implications for source apportionment inside and outside sulphur emission control areas. *Atmos Environ* 167:212–222. <https://doi.org/10.1016/j.atmosenv.2017.08.022>
- Diab J, Streibel T, Cavalli F, Lee SC, Saathoff H, Mamakos A, Chow JC, Chen LWA, Watson JG, Sippula O, Zimmermann R (2015) Hyphenation of a EC/OC thermal–optical carbon analyzer to photo-ionization time-of-flight mass spectrometry: an off-line aerosol mass spectrometric approach for characterization of primary

- and secondary particulate matter. *Atmos Meas Tech* 8(8):3337–3353. <https://doi.org/10.5194/amt-8-3337-2015>
- Gautam S, Patra AK, Sahu SP, Hitch M (2018) Particulate matter pollution in opencast coal mining areas: a threat to human health and environment. *Int J Min Reclam Environ* 32(2):75–92 <https://doi.org/10.1080/17480930.2016.1218110>
- Hussain M, Madl P, Khan A (2011) Lung deposition predictions of airborne particles and the emergence of contemporary diseases, Part-I. *Health* 2(2):51–59
- Kang HJ, Lee SY, Kwon JH (2016) Physico-chemical properties and toxicity of alkylated polycyclic aromatic hydrocarbons. *J Hazard Mater* 312:200–207. <https://doi.org/10.1016/j.jhazmat.2016.03.051>
- Kislov VV, Sadovnikov AI, Mebel AM (2013) Formation mechanism of polycyclic aromatic hydrocarbons beyond the second aromatic ring. *J Phys Chem A* 117(23):4794–4816. <https://doi.org/10.1021/jp402481y>
- Kleeman MJ, Riddle SG, Robert MA, Jakober CA (2008) Lubricating oil and fuel contributions to particulate matter emissions from light-duty gasoline and heavy-duty diesel vehicles. *Environ Sci Technol* 42(1):235–242. <https://doi.org/10.1021/es071054c>
- Kumar AV, Kothiyal NC, Kumari S, Mehra R, Parkash A, Sinha RR, Tayagi SK, Gaba R (2014) Determination of some carcinogenic PAHs with toxic equivalency factor along roadside soil within a fast developing northern city of India. *J Earth Syst Sci* 123(3):479–489. <https://doi.org/10.1007/s12040-014-0410-7>
- Kuranchie FA, Angnunavuri PN, Attiogbe F, Nerquaye-Tetteh EN (2019) Occupational exposure of benzene, toluene, ethylbenzene and xylene (BTEX) to pump attendants in Ghana: implications for policy guidance. *Cogent Environ Sci* 5(1):1603418
- Kwon H-S, Ryu MH, Carlsten C (2020) Ultrafine particles: unique physicochemical properties relevant to health and disease. *Exp Mol Med* 52(3):318–328. <https://doi.org/10.1038/s12276-020-0405-1>
- Lam MM, Bülow R, Engwall M, Giesy JP, Larsson M (2018) Methylated PACs are more potent than their parent compounds: a study of aryl hydrocarbon receptor-mediated activity, degradability, and mixture interactions in the H4IIE-luc assay. *Environ Toxicol Chem* 37(5):1409–1419. <https://doi.org/10.1002/etc.4087>
- Li X, Huang Z, Wang J, Zhang W (2007) Particle size distribution from a GTL engine. *Sci Total Environ* 382(2–3):295–303. <https://doi.org/10.1016/j.scitotenv.2007.04.032>
- Li Z, Hogan KA, Cai C, Rieth S (2016) Human health effects of biphenyl: key findings and scientific issues. *Environ Health Perspect* 124(6):703–712. <https://doi.org/10.1289/ehp.1509730>
- Lin YC, Tsai CJ, Wu YC, Zhang R, Chi KH, Huang YT, Lin SH, Hsu SC (2015) Characteristics of trace metals in traffic-derived particles in Hsuehshan Tunnel, Taiwan: size distribution, potential source, and fingerprinting metal ratio. *Atmos Chem Phys* 15(8):4117–4130. <https://doi.org/10.5194/acp-15-4117-2015>
- Lipsky EM, Robinson AL (2006) Effects of dilution on fine particle mass and partitioning of semivolatile organics in diesel exhaust and wood smoke. *Environ Sci Technol* 40(1):155–162. <https://doi.org/10.1021/es050319p>
- Llamas A, Al-Lal A-M, García-Martínez M-J, Ortega MF, Llamas JF, Lapuerta M, Canoira L (2017) Polycyclic aromatic hydrocarbons (PAHs) produced in the combustion of fatty acid alkyl esters from different feedstocks: Quantification, statistical analysis and mechanisms of formation. *Sci Total Environ* 586:446–456 <https://doi.org/10.1016/j.scitotenv.2017.01.180>
- Lu T, Huang Z, Cheung CS, Ma J (2012) Size distribution of EC, OC and particle-phase PAHs emissions from a diesel engine fueled with three fuels. *Sci Total Environ* 438:33–41. <https://doi.org/10.1016/j.scitotenv.2012.08.026>
- Mason YC, Schoonraad G-L, Orasche J, Bisig C, Jakobi G, Zimmermann R, Forbes PBC (2020) Comparative sampling of gas phase volatile and semi-volatile organic fuel emissions from a combustion aerosol standard system. *Environ Technol Innov* 19:100945 <https://doi.org/10.1016/j.eti.2020.100945>
- Mihajlović V, Grba N, Sudi J, Eichert D, Krajinović S, Gavrilov MB, Marković SB (2021) Assessment of occupational exposure to BTEX in a petrochemical plant via urinary biomarkers. *Sustainability* 13(13):7178
- Mohadesi M, Hojabri Z, Moradi G (2014) Biodiesel production using alkali earth metal oxides catalysts synthesized by sol-gel method. *Biofuel Res J* 1(1):30–33
- Møller P, Scholten RH, Roursgaard M, Kraiss AM (2020) Inflammation, oxidative stress and genotoxicity responses to biodiesel emissions in cultured mammalian cells and animals. *Crit Rev Toxicol* 50(5):383–401 <https://doi.org/10.1080/10408444.2020.1762541>
- Moon G, Lee Y, Choi K, Jeong D (2010) Emission characteristics of diesel, gas to liquid, and biodiesel-blended fuels in a diesel engine for passenger cars. *Fuel* 89:3840–3846. <https://doi.org/10.1016/j.fuel.2010.07.009>
- Nisbet IC, Lagoy PK (1992) Toxic equivalency factors (TEFs) for polycyclic aromatic hydrocarbons (PAHs). *Regul Toxicol Pharmacol* 16(3):290–300
- Richter-Brockmann S, Achten C (2018) Analysis and toxicity of 59 PAH in petrogenic and pyrogenic environmental samples including dibenzopyrenes, 7H-benzo[c]fluorene, 5-methylchrysene and 1-methylpyrene. *Chemosphere* 200:495–503 <https://doi.org/10.1016/j.chemosphere.2018.02.146>
- Ryu K (2010) The characteristics of performance and exhaust emissions of a diesel engine using a biodiesel with antioxidants. *Biore-sour Technol* 101(Suppl 1):S78-82. <https://doi.org/10.1016/j.biortech.2009.05.034>
- Sakthivel R, Ramesh K, Purnachandran R, Shameer PM (2018) A review on the properties, performance and emission aspects of the third generation biodiesels. *Renew Sustain Energy Rev* 82:2970–2992
- Salo L, Rönkkö T, Saarikoski S, Teinilä K, Kuula J, Alanen J, Arffman A, Timonen H, Keskinen J (2021) Concentrations and size distributions of particle lung-deposited surface area (LDSA) in an underground mine. *Aerosol Air Qual Res* 21:200660. <https://doi.org/10.4209/aaqr.200660>
- Selby TW, Bosch RJ, Fee DC (2005) Phosphorus additive chemistry and its effects on the phosphorus volatility of engine oils. *J ASTM Int* 2(9) <https://doi.org/10.1520/JAI12977>
- Shrivastava MK, Lipsky EM, Stanier CO, Robinson AL (2006) Modeling semivolatile organic aerosol mass emissions from combustion systems. *Environ Sci Technol* 40(8):2671–2677. <https://doi.org/10.1021/es0522231>
- Sun Y, Miller III CA, Wiese TE, Blake DA (2014) Methylated phenanthrenes are more potent than phenanthrene in a bioassay of human aryl hydrocarbon receptor (AhR) signaling. *Environ Toxicol Chem* 33(10):2363–2367 <https://doi.org/10.1002/etc.2687>
- Tavizón-Pozos JA, Chavez-Esquivel G, Suárez-Toriello VA, Santolalla-Vargas CE, Luévano-Rivas OA, Valdés-Martínez OU, Talavera-López A, Rodríguez JA (2021) State of art of alkaline earth metal oxides catalysts used in the transesterification of oils for biodiesel production. *Energies* 14(4):1031
- Traviss N, Thelen BA, Ingalls JK, Treadwell MD (2010) Biodiesel versus diesel: a pilot study comparing exhaust exposures for employees at a rural municipal facility. *J Air Waste Manag Assoc* (1995) 60(9):1026–1033 <https://doi.org/10.3155/1047-3289.60.9.1026>
- Unosson J, Kabéle M, Boman C, Nyström R, Sadiqtsis I, Westerholm R, Mudway IS, Purdie E, Raftis J, Miller MR, Mills NL, Newby DE, Blomberg A, Sandström T, Bosson JA (2021) Acute cardiovascular effects of controlled exposure to dilute

- petrodiesel and biodiesel exhaust in healthy volunteers: a crossover study. *Part Fibre Toxicol* 18(1):22. <https://doi.org/10.1186/s12989-021-00412-3>
- van Steen E, Claeys M (2008) Fischer-Tropsch catalysts for the biomass-to-liquid (BTL)-process. *Chem Eng Technol Ind Chem-Plant Equip-Process Eng-Biotechnol* 31(5):655–666
- Wattrus MC, Biffi M, Pretorius CJ, Jacobs D (2016) Assessing stationary laboratory test methods for underground mining vehicles to determine their suitability in replicating real-world emissions. *Mine Ventilation Society of South Africa 2016 Conference: The increasing relevance of the mine ventilation profession in a highly regulated and cost constrained environment*, 1–2 September 2016, Emperors Palace, Johannesburg, p 37–44
- World Health Organization (2021) WHO global air quality guidelines: particulate matter (PM_{2.5} and PM₁₀), ozone, nitrogen dioxide, sulfur dioxide and carbon monoxide. Geneva, World Health Organization
- Yasin MHM, Ali MA, Mamat R, Yusop AF, Ali MH (2019) Chapter 11 - Physical properties and chemical composition of biofuels. In: Basile A, Dalena F (eds) *Second and Third Generation of Feedstocks*. Elsevier, pp 291–320
- Yost EE, Galizia A, Kapraun DF, Persad AS, Vulimiri SV, Angrish M, Lee JS, Druwe IL (2021) Health effects of naphthalene exposure: a systematic evidence map and analysis of potential considerations for dose–response evaluation. *Environ Health Perspect* 129(7):076002. <https://doi.org/10.1289/EHP7381>
- Zaharin MSM, Abdullah NR, Najafi G, Sharudin H, Yusaf T (2017) Effects of physicochemical properties of biodiesel fuel blends with alcohol on diesel engine performance and exhaust emissions: a review. *Renew Sustain Energy Rev* 79:475–493 <https://doi.org/10.1016/j.rser.2017.05.035>

Publisher's note Springer Nature remains neutral with regard to jurisdictional claims in published maps and institutional affiliations.

Appendix C: Certificate of Analysis of the PAH Mix

Certificate of Analysis

QTM PAH MIX 1X1ML,2000UG/ML,DICHLOROMETHANE

*Certified
Reference
Material*

Product ID CRM47930
 Lot LRAC0500
 Expiration Date October 2021
 MFG Date October 2018
 Storage Conditions Refrigerate
 Solvent/Matrix DICHLOROMETHANE

| Analyte | Units | Certified Value ^{1,4} | Analytical Value | Raw Material Purity,% | Raw Material lot | Elution order | CAS |
|--------------------------|-------|--------------------------------|------------------|-----------------------|------------------|---------------|----------|
| NAPHTHALENE | µg/ml | 2000 ± 191 | 2070 | 99.9 | 16412TN | 1 | 91-20-3 |
| ACENAPHTHENE | µg/ml | 2000 ± 200 | 2130 | 99.9 | MKCC8329 | 2 | 83-32-9 |
| 2-BROMONAPHTHALENE | µg/ml | 2000 ± 441 | 2020 | 99.9 | LB94855 | 3 | 580-13-2 |
| ACENAPHTHYLENE | µg/ml | 2000 ± 196 | 2080 | 99.6 | LC20622 | 4 | 208-96-8 |
| FLUORENE | µg/ml | 2000 ± 200 | 2110 | 99.4 | LC19126 | 5 | 86-73-7 |
| PHENANTHRENE | µg/ml | 2000 ± 200 | 2070 | 99.1 | LB92396 | 6 | 85-01-8 |
| ANTHRACENE | µg/ml | 2000 ± 199 | 2070 | 99.9 | LC14310 | 7 | 120-12-7 |
| FLUORANTHENE | µg/ml | 2000 ± 199 | 2090 | 98.2 | LC08645 | 8 | 206-44-0 |
| PYRENE | µg/ml | 2000 ± 207 | 2180 | 91.6 | LB70761 | 9 | 129-00-0 |
| BENZO (A) ANTHRACENE | µg/ml | 2000 ± 193 | 2040 | 99.9 | LC19271 | 10 | 56-55-3 |
| CHRYSENE | µg/ml | 2000 ± 200 | 2090 | 99 | 21L74 | 11 | 218-01-9 |
| BENZO (B) FLUORANTHENE | µg/ml | 2000 ± 204 | 2100 | 99.5 | LB95773 | 12 | 205-99-2 |
| BENZO (A) PYRENE | µg/ml | 2000 ± 194 | 2040 | 100 | SLBV8459 | 14 | 50-32-8 |
| INDENO (1,2,3-CD) PYRENE | µg/ml | 2000 ± 198 | 2080 | 99.5 | ER082107-02 | 15 | 193-39-5 |
| DIBENZ (A,H) ANTHRACENE | µg/ml | 2000 ± 198 | 2080 | 99.7 | LC18254 | 15 | 53-70-3 |
| BENZO (G,H,I) PERYLENE | µg/ml | 2000 ± 195 | 2050 | 98.8 | LC11626 | 16 | 191-24-2 |



SIGMA-ALDRICH®
 2931 Soldier Springs Rd. Laramie, Wyoming 82070 USA
 307-742-5452
 r1techgroup@sial.com www.sigma-aldrich.com